

**ISTANBUL TECHNICAL UNIVERSITY ★ GRADUATE SCHOOL OF SCIENCE**  
**ENGINEERING AND TECHNOLOGY**

**FIELD TESTING AND  
MODEL UPDATING OF TYPICAL  
RC BUILDINGS FOR DAMAGE IDENTIFICATION**



**Ph.D. THESIS**

**Pınar İNCİ KOÇAK**

**Department of Civil Engineering**

**Structure Engineering Programme**

**DECEMBER 2017**



**ISTANBUL TECHNICAL UNIVERSITY ★ GRADUATE SCHOOL OF SCIENCE**  
**ENGINEERING AND TECHNOLOGY**

**FIELD TESTING AND  
MODEL UPDATING OF TYPICAL  
RC BUILDINGS FOR DAMAGE IDENTIFICATION**

**Ph.D. THESIS**

**Pınar İNCİ KOÇAK  
501112011**

**Department of Civil Engineering**

**Structure Engineering Programme**

**Thesis Advisor: Prof. Dr. Alper İLKI**  
**Thesis Co-Advisor: Prof. Dr. F. Necati ÇATBAŞ**

**DECEMBER 2017**



**İSTANBUL TEKNİK ÜNİVERSİTESİ ★ FEN BİLİMLERİ ENSTİTÜSÜ**

**TİPİK BETONARME YAPILARDA HASAR TESPİTİ ÜZERİNE  
SAHA DENEYLERİ  
VE MODEL GÜNCELLEMESİ**

**DOKTORA TEZİ**

**Pınar İNCİ KOÇAK  
501112011**

**İnşaat Mühendisliği Anabilim Dalı**

**Yapı Mühendisliği Programı**

**Tez Danışmanı: Prof. Dr. Alper İLKİ  
Eş Danışman: Prof. Dr. F. Necati ÇATBAŞ**

**ARALIK 2017**



Pinar INCI KOCAK, a Ph.D. student of ITU Graduate School of Science Engineering and Technology student ID 501112011, successfully defended the thesis/dissertation entitled “FIELD TESTING AND MODEL UPDATING OF TYPICAL RC BUILDINGS FOR DAMAGE IDENTIFICATION”, which she prepared after fulfilling the requirements specified in the associated legislations, before the jury whose signatures are below.

**Thesis Advisor :**     **Prof. Dr. Alper İLKİ** .....  
ISTANBUL Technical University

**Co-advisor :**       **Prof. Dr. F. Necati ÇATBAŞ** .....  
University of Central Florida

**Jury Members :**    **Prof. Dr. Erdal ŞAFAK** .....  
Boğaziçi University

**Assoc. Prof. Dr. Baki ÖZTÜRK** .....  
Hacettepe University

**Assoc. Prof. Dr. Ufuk YAZGAN** .....  
Istanbul Technical University

**Prof. Dr. Metin AYDOĞAN** .....  
Istanbul Technical University

**Prof. Dr. Kutlu DARILMAZ** .....  
Istanbul Technical University

**Date of Submission : 31 October 2017**

**Date of Defense : 15 December 2017**





## **FOREWORD**

First, I would like to express my deepest gratitude and my thanks to my co-supervisors, Dr. Alper İlki and Dr. F. Necati Çatbaş for their unending supports, guidance, recommendations, and friendships throughout the PhD study.

I am thankful to Dr. Çağlar Göksu and Uğur Demir for their valuable contributions. Besides, I would like to greatly appreciate Ali Osman Ateş, Ali Naki Şanver, Dr. Burak Barutçu, Dr. Mustafa Cömert, Dr. Cem Demir, Dr. Ufuk Yazgan, Dr. Kutay Orakçal, Dr. Yavuz Durgun, Erkan Töre, Özgün Özeren, Alvand Mosfeghi and Süheyl Khoshkholghi for their helps and recommendations.

I would like to express my gratefully thanks to my family for their supports and my gratitude and appreciation to my spouse Mehmet Koçak for his endless support, patience, and encouragement throughout this study.

December 2017

Pınar İNCİ  
Civil Engineer, MSc



## TABLE OF CONTENTS

	<u>Page</u>
<b>FOREWORD</b> .....	<b>vii</b>
<b>TABLE OF CONTENTS</b> .....	<b>ix</b>
<b>ABBREVIATIONS</b> .....	<b>xi</b>
<b>SYMBOLS</b> .....	<b>xiii</b>
<b>LIST OF TABLES</b> .....	<b>xv</b>
<b>LIST OF FIGURES</b> .....	<b>xvii</b>
<b>SUMMARY</b> .....	<b>xxiii</b>
<b>ÖZET</b> .....	<b>xxvii</b>
<b>1. INTRODUCTION</b> .....	<b>1</b>
1.1 Damage Identification .....	3
1.1.1 Natural frequency based methods .....	5
1.1.2 Mode shape based methods.....	7
1.1.3 Flexibility matrix based methods.....	9
1.1.4 Model updating based methods.....	9
1.1.5 Wavelet transform methods .....	11
1.1.6 Statistical methods .....	11
1.2 Research motivation and objective .....	13
<b>2. EXPERIMENTAL STUDY</b> .....	<b>17</b>
2.1 Description of the Test Site.....	17
2.2 Description of the Test Buildings.....	19
2.2.1 Test building 1 .....	19
2.2.2 Test building 2 .....	21
2.3 Instrumentation of the Buildings.....	22
2.4 Vibration Based Test Program .....	25
2.5 Damage States of the Buildings at the Time of Vibration Based Test.....	27
2.5.1 Damage States of the Building TB-1 .....	27
2.5.2 Damage states for the building TB-2 .....	31
2.6 Vibration Based Tests .....	33
2.6.1 Ambient vibration test survey.....	33
2.6.1.1 Theoretical background.....	34
2.6.1.2 System identification results .....	35
2.6.2 Forced vibration test survey.....	40
2.6.2.1 System identification results .....	44
2.7 Conclusion.....	55
<b>3. FRF BASED DAMAGE IDENTIFICATION METHOD</b> .....	<b>57</b>
3.1 Theoretical Background .....	57
3.2 Two-step damage identification algorithm .....	60
3.2.1 Updating [K] and [M] (Step 1) .....	62
3.2.1.1 Establishing FEM of the buildings.....	62
3.2.1.2 Determining the mass and stiffness matrices of the buildings.....	65
3.2.1.3 Calculation of analytical FRF .....	67

3.2.1.4 Comparison of analytically determined and experimentally obtained FRFs .....	70
3.2.2 Updating damping ratio (Step 2) .....	77
3.2.2.1 Curve fitting .....	79
3.2.2.2 Sine analysis .....	87
3.2.2.3 Calculation of analytical FRF .....	89
3.2.2.4 Comparison of analytically determined and experimentally obtained FRFs .....	90
3.3 Conclusion .....	92
<b>4. DAMAGE IDENTIFICATION .....</b>	<b>95</b>
4.1 Damage identification of the building TB-1 .....	95
4.1.1 Updating [K] (Step 1) .....	96
4.1.1.1 Comparison of analytically determined and experimentally obtained FRFs .....	104
4.1.2 Updating damping ratio (Step 2) .....	105
4.1.2.1 Curve fitting .....	105
4.1.2.2 Sine analysis and Calculation of analytical FRF .....	110
4.2 Damage identification of the building TB-2 .....	111
4.2.1 Updating [K] (Step 1) .....	112
4.2.1.1 Grouping of unknown parameters and FRF sensitivity .....	112
4.2.1.2 Comparison of analytically determined and experimentally obtained FRFs .....	117
4.2.2 Updating damping ratio (Step 2) .....	123
4.2.2.1 Curve fitting .....	123
4.2.2.2 Sine analysis and Calculation of analytical FRF .....	130
4.3 Conclusion .....	131
<b>5. DEMONSTRATION OF EFFICIENCY OF SIMPLIFIED FINITE ELEMENT MODEL FOR DAMAGE IDENTIFICATION .....</b>	<b>135</b>
5.1 Simplified modelling approach .....	135
5.2 Model updating for baseline model .....	137
5.3 Damage identification .....	143
5.4 Conclusion .....	156
<b>6. PERFORMANCE BASED DAMAGE ASSESSMENT IN COMBINATION WITH FRF BASED DAMAGE IDENTIFICATION .....</b>	<b>157</b>
6.1 Simulation of the Field Tests .....	157
6.1.1 Prediction of pushover curve .....	157
6.1.2 Prediction of member damage states .....	159
6.2 Dynamic data generation .....	166
6.3 Utilizing of performance Based Damage Limits on Vibration Based Damage Identification .....	168
6.3.1 Plastic hinge modification factor .....	169
6.3.2 Determination of rotation demand .....	170
6.4 Conclusion .....	176
<b>7. CONCLUSION .....</b>	<b>179</b>
<b>REFERENCES .....</b>	<b>183</b>
<b>APPENDICES .....</b>	<b>189</b>
APPENDIX A .....	190
<b>CURRICULUM VITAE .....</b>	<b>201</b>

## ABBREVIATIONS

<b>A1</b>	: Accelerometer 1
<b>A2</b>	: Accelerometer 2
<b>A3</b>	: Accelerometer 3
<b>A4</b>	: Accelerometer 4
<b>A5</b>	: Accelerometer 5
<b>A6</b>	: Accelerometer 6
<b>API</b>	: Application Programming Interface
<b>COMAC</b>	: Coordinate Modal Assurance Criterion
<b>d.r.</b>	: Drift ratio
<b>DC1</b>	: Damaged Case 1
<b>DC2</b>	: Damaged Case 2
<b>DC3</b>	: Damaged Case 3
<b>DC4</b>	: Damaged Case 4
<b>DC5</b>	: Damaged Case 5
<b>DOF</b>	: Degree of Freedom
<b>FRF</b>	: Frequency Response Function
<b>FEM</b>	: Finite Element Model
<b>IDFT</b>	: Inverse Discrete Fourier Transform
<b>MAC</b>	: Modal Assurance Criterion
<b>MUP</b>	: Modal Updating Program
<b>PSD</b>	: Power Spectral Density
<b>RC</b>	: Reinforced Concrete
<b>SDOF</b>	: Single Degree of Freedom
<b>SS<sub>E</sub></b>	: Sum of Square Error
<b>SS<sub>T</sub></b>	: Sum of Square Total
<b>St-Id</b>	: Structural Identification
<b>SVD</b>	: Singular Value Decomposition
<b>TB-1</b>	: Test Building 1
<b>TB-2</b>	: Test Building 2
<b>TSDC</b>	: Turkish Seismic Design Code
<b>UC</b>	: Undamaged Case



## SYMBOLS

<b>A</b>	: Dynamic stiffness matrix
<b>C</b>	: Damping matrix
<b>e</b>	: Shaker eccentricity
<b>E(p)</b>	: Error function
<b>E<sub>c</sub></b>	: Young's modulus of concrete
<b>f<sub>cm</sub></b>	: Concrete compressive strength
<b>f</b>	: Natural frequency
<b>F<sub>q</sub></b>	: Input force
<b>M</b>	: Mass matrix
<b>m</b>	: Total number of modes
<b>G<sub>xx</sub>(<math>\omega</math>)</b>	: Power spectral density of inputs
<b>G<sub>yy</sub>(<math>\omega</math>)</b>	: Power spectral density of outputs
<b>H<sub>c</sub></b>	: Effective depth of the cross-section
<b>H(<math>\omega</math>)</b>	: Frequency response function matrix
<b>H<sub>pq</sub></b>	: Frequency response function (p: excitation point, q: response point)
<b>J(p)</b>	: Scalar objective function
<b>K</b>	: Stiffness matrix
<b>k<sub>x</sub></b>	: Lateral stiffness of the member due to relative unit displacement in x direction
<b>N</b>	: Number of degrees of freedom
<b>p<sub>1</sub></b>	: Unknown properties of the system
<b>p<sub>2</sub></b>	: Unknown properties of the system
<b>R<sub>x</sub></b>	: Rotational stiffness of end-spring (x direction)
<b>R<sub>y</sub></b>	: Rotational stiffness of end-spring (y direction)
<b>s</b>	: Laplace constant
<b>q</b>	: SComplex frequency response vector
<b>S<sub>i</sub></b>	: Diagonal matrix containing the scalar singular values
<b>S<sub>ij</sub></b>	: Scalar singular values
<b>U<sub>i</sub></b>	: Unitary matrix containing the singular vectors
<b>u<sub>ij</sub></b>	: Singular values
<b>u</b>	: Displacement vector
<b><math>\gamma_c</math></b>	: Unit weight of concrete
<b><math>\Omega</math></b>	: Frequency of excitation load
<b><math>\psi_k</math></b>	: Mode shape
<b><math>\lambda_k</math></b>	: Pole of the $k^{th}$ mode
<b><math>\sigma_k</math></b>	: Modal damping constant
<b><math>\theta_y</math></b>	: Yield rotation
<b><math>\xi</math></b>	: Modal damping ratio
<b><math>\omega</math></b>	: Angular frequency
<b><math>\omega_{dk}</math></b>	: Damped natural frequency





## LIST OF TABLES

	<u>Page</u>
<b>Table 2.1</b> : Program of the vibration test.....	27
<b>Table 2.2</b> : Identified modal frequencies and corresponding modal damping ratios of the building TB-2.....	39
<b>Table 2.3</b> : Identified modal frequencies and damping ratios of the buildings at different damage states.....	54
<b>Table 3.1</b> : Updated values of young modulus and unit weight of concrete.....	77
<b>Table 3.2</b> : Second-order differential equation of FRFs of updated FEM of the building TB-1.....	83
<b>Table 3.3</b> : Second-order differential equation of FRFs of updated FEM of the building TB-2.....	84
<b>Table 3.4</b> : Second-order differential equation of FRFs of updated FEM of the building TB-1.....	85
<b>Table 3.5</b> : Second-order differential equation of FRFs of updated FEM of the building TB-2.....	86
<b>Table 3.6</b> : Updated damping ratios for each DOFs.....	92
<b>Table 4.1</b> : Grouping the unknown parameters.....	99
<b>Table 4.2</b> : Updated values of rotational stiffness values of the end springs (Step 1).....	107
<b>Table 4.3</b> : Second order differential equations of updated FEM FRFs (Step 1) - curve fitting results-.....	108
<b>Table 4.4</b> : Second order differential equations of updated FEM FRFs (Step 1)....	109
<b>Table 4.5</b> : Updated values of damping ratio.....	111
<b>Table 4.6</b> : Grouping the unknown parameters.....	114
<b>Table 4.7</b> : Updated values of rotational stiffness values of the end springs (Step 1).....	121
<b>Table 4.8</b> : Change of the rotational stiffness values for the columns S11 and S14 (Updated stiffness/Initial stiffness) (Step 1).....	122
<b>Table 4.9</b> : Change of the rotational stiffness values for the columns S12 and S13 (Updated stiffness/Initial stiffness) (Step 1).....	122
<b>Table 4.10</b> : Second order differential equations of updated FEM FRFs (Step 1) – Damaged Case 1.....	124
<b>Table 4.11</b> : Second order differential equations of updated FEM FRFs (Step 1) - Damaged Case 2.....	125
<b>Table 4.12</b> : Second order differential equations of updated FEM FRFs (Step 1) - Damaged Case 3.....	126
<b>Table 4.13</b> : Second order differential equations of updated FEM FRFs (Step 1) - Damaged Case 4.....	127
<b>Table 4.14</b> : Second order differential equations of updated FEM FRFs (Step 1) - Damaged Case 4.....	129
<b>Table 4.15</b> : Updated values of damping ratio.....	130
<b>Table 5.1</b> : Second-order differential equation of FRFs of updated simple FEM..	141

<b>Table 5.2</b> : Second-order differential equation of FRFs of updated simple FEM (Algebraic summation).....	<b>142</b>
<b>Table 5.3</b> : Updated values of rotational stiffness values of the end springs (kNm/rad) (Step 1). .....	<b>147</b>
<b>Table 5.4</b> : Change of the rotational stiffness values (Updated stiffness/Initial stiffness) .....	<b>147</b>
<b>Table 5.5</b> : Ratio of the updated rotational stiffness values (Simple FEM/Full-Scale FEM). .....	<b>148</b>
<b>Table 5.6</b> : Updated values of damping ratio. ....	<b>155</b>
<b>Table 6.1</b> : Damage limits for RC columns for nonlinear procedures (plastic rotation). .....	<b>161</b>
<b>Table 6.2</b> : Condition to be used for columns in Table 6.1. ....	<b>162</b>
<b>Table 6.3</b> : Columns damage states. ....	<b>165</b>
<b>Table 6.4</b> : Modelling criteria for damaged plastic hinges. ....	<b>170</b>
<b>Table 6.5</b> : Comparison of the plastic rotations of the members. ....	<b>171</b>
<b>Table 6.6</b> : Comparison of member damage levels (S11). ....	<b>172</b>
<b>Table 6.7</b> : Comparison of member damage levels (S12). ....	<b>173</b>
<b>Table 6.8</b> : Comparison of member damage levels (S13). ....	<b>174</b>
<b>Table 6.9</b> : Comparison of member damage levels (S14). ....	<b>175</b>

## LIST OF FIGURES

	<u>Page</u>
<b>Figure 2.1</b> : Fikirtepe district.....	18
<b>Figure 2.2</b> : (a) Existing RC building, (b) TB-1, TB-2 and reaction wall at the same site. ....	18
<b>Figure 2.3</b> : Layout plan of the test site (units in meter). ....	19
<b>Figure 2.4</b> : Plan view and reinforcement cage of the columns and beams of TB-1 (dimensions in cm).....	21
<b>Figure 2.5</b> : Plan view and reinforcement cage of the columns and beams of TB-2 (dimensions in cm).....	23
<b>Figure 2.6</b> : Instrumentation of the buildings.....	24
<b>Figure 2.7</b> : Eccentric mass shaker.....	24
<b>Figure 2.8</b> : Structure of eccentric mass shaker (a) disks, (b) components of disks. ....	25
<b>Figure 2.9</b> : Attachment of the actuators. ....	26
<b>Figure 2.10</b> : Base shear-1 <sup>st</sup> story drift relationship of the building TB-1. ....	28
<b>Figure 2.11</b> : Flexural cracks observed at column S13 and the beam K11.....	29
<b>Figure 2.12</b> : Buckling of bottom longitudinal bars of the beam K12. ....	29
<b>Figure 2.13</b> : Buckling of longitudinal bars of the column. ....	30
<b>Figure 2.14</b> : Slight damage on the columns S12. ....	30
<b>Figure 2.15</b> : Base shear force-1 <sup>st</sup> story drift relationship and the vibration based testing stages of the building TB-2. ....	31
<b>Figure 2.16</b> : The first observed flexural cracks (a) Column S12 (the 1 <sup>st</sup> story), (b) Column S14 (the 2 <sup>nd</sup> story). ....	32
<b>Figure 2.17</b> : Damage propagation on the 1 <sup>st</sup> story column S11 of the building TB-2 . ....	32
<b>Figure 2.18</b> : Test site and sources of vibrations.....	33
<b>Figure 2.19</b> : Modal frequencies and mode shapes of building TB-2 in x direction, a) undamaged state, b) after %0.5 d.r. and c) after 3% d.r. ....	36
<b>Figure 2.20</b> : Modal frequencies and mode shapes of building TB-2 in y direction, a) undamaged state, b) after 3% d.r. ....	37
<b>Figure 2.21</b> : Coherence functions of the building TB-2 in x direction, a) undamaged state, b) after %0.5 d.r. and c) after 3% d.r. ....	38
<b>Figure 2.22</b> : Coherence functions of the building TB-2 in y direction, (a) undamaged state, (b) after 3% d.r. ....	38
<b>Figure 2.23</b> : Change in modal damping ratio as a function of achieved maximum drift ratio (damage state).....	40
<b>Figure 2.24</b> : Shaker force.....	41
<b>Figure 2.25</b> : Spectrogram views for TB-1 undamaged case – x direction testing, (a) shaker frequency range as 1.5-8Hz, (b) shaker frequency range as 8-15 Hz. ....	42
<b>Figure 2.26</b> : Spectrogram view for TB-1 undamaged case – y direction testing, shaker frequency range as 1.5-15 Hz.....	43

<b>Figure 2.27</b> : Sheme of FRF calculation. ....	<b>44</b>
<b>Figure 2.28</b> : Notations of the points, where the force was applied and the vibration response of the buildings against the force were measured...	<b>46</b>
<b>Figure 2.29</b> : Frequency response functions of the building TB-1 in x direction (a) undamaged and (b) after 1.5 % d.r.....	<b>46</b>
<b>Figure 2.30</b> : Frequency response functions of the building TB-1 in y direction (a) undamaged and (b) after 1.5 % d.r.....	<b>47</b>
<b>Figure 2.31</b> : Frequency response functions of the building TB-2 in x direction (a) undamaged, (b) after 0.5 % d.r., (c) after 1.0 % d.r., (d) after 1.5 % d.r., (b) after 2.0 % d.r. and (b) after 3.0 % d.r. ....	<b>48</b>
<b>Figure 2.32</b> : Frequency response functions of the building TB-2 in y direction (a) undamaged and (b) after 3.0 % d.r.....	<b>49</b>
<b>Figure 2.33</b> : Frequency response functions of the building TB-1 in x direction (a) undamaged and (b) after 1.5 % d.r.....	<b>50</b>
<b>Figure 2.34</b> : Frequency response functions of the building TB-1 in y direction (a) undamaged and (b) after 1.5 % d.r.....	<b>50</b>
<b>Figure 2.35</b> : Frequency response functions of the building TB-2 in x direction (a) undamaged, (b) after 0.5 % d.r., (c) after 1.0 % d.r., (d) after 1.5 % d.r., (b) after 2.0 % d.r. and (b) after 3.0 % d.r. ....	<b>51</b>
<b>Figure 2.36</b> : Frequency response functions of the building TB-2 in y direction (a) undamaged and (b) after 3.0 % d.r.....	<b>52</b>
<b>Figure 2.37</b> : Modal frequencies of the building TB-2 (x direction) at considered the first story drift ratio, (a) modal frequencies, (b) normalized modal frequencies with respect to the undamaged state. ....	<b>52</b>
<b>Figure 2.38</b> : Identification of modal damping ratios using half-power bandwidth method for building TB-1 for undamaged case in x direction.....	<b>53</b>
<b>Figure 2.39</b> : Modal damping ratios of the building TB-2 (x direction) at considered the first story drift ratio, (a) modal damping ratios, (b) normalized modal damping ratios with respect to the undamaged state. ....	<b>54</b>
<b>Figure 2.40</b> : Obtained modal damping ratios for the identified modal frequencies of the building TB-2.....	<b>55</b>
<b>Figure 3.1</b> : Schematic view of two- step damage identification algoritm, (a) Step 1, (b) Step 2. ....	<b>61</b>
<b>Figure 3.2</b> : FEM of the buildings in SAP2000, (a) TB-1, (b) TB-2 ....	<b>62</b>
<b>Figure 3.3</b> : DOF a ridig body.....	<b>63</b>
<b>Figure 3.4</b> : Definition of DOFs .....	<b>64</b>
<b>Figure 3.5</b> : Global axis.....	<b>65</b>
<b>Figure 3.6</b> : Analytically determined FRFs through initial FEM of the building TB-1, (a) x direction, (b) y direction. ....	<b>70</b>
<b>Figure 3.7</b> : Analytically determined FRFs through initial FEM of the building TB-2, (a) x direction, (b) y direction. ....	<b>70</b>
<b>Figure 3.8</b> : Comparison of analytically determined FRF (from initial FEM) and the experimental FRF of the building TB-1, (a) x direction, (b) y direction.....	<b>71</b>
<b>Figure 3.9</b> : Comparison of analytically determined FRF (from initial FEM) and the experimental FRF of the building TB-2, (a) x direction, (b) y direction.....	<b>72</b>
<b>Figure 3.10</b> : FRF sensitivity to changes in $E_c$ (the building TB-1). ....	<b>73</b>
<b>Figure 3.11</b> : FRF sensitivity to changes in $E_c$ (the building TB-2).....	<b>73</b>

<b>Figure 3.12</b> : FRF sensitivity to changes in unit weight of concrete (the building TB-1).....	<b>74</b>
<b>Figure 3.13</b> : Model updating results for the building TB-1 (Step 1: [K] and [M]).	<b>75</b>
<b>Figure 3.14</b> : Model updating results for the building TB-2 (Step 1: [K] and [M]).	<b>76</b>
<b>Figure 3.15</b> : Schematic view of revised algorithm for the Step-2. ....	<b>79</b>
<b>Figure 3.16</b> : Application of curve fitting (the building TB-1). ....	<b>80</b>
<b>Figure 3.17</b> : Application of curve fitting (the building TB-2). ....	<b>80</b>
<b>Figure 3.18</b> : FRF of the system (the building TB-1). ....	<b>81</b>
<b>Figure 3.19</b> : FRF of the system (the building TB-2). ....	<b>82</b>
<b>Figure 3.20</b> : Input force in sine analysis, (a) shaker sinusoidal force, (b) zoomed view.....	<b>87</b>
<b>Figure 3.21</b> : Response of the DOFs to sine analysis (The building TB-1).....	<b>88</b>
<b>Figure 3.22</b> : Response of the DOFs to sine analysis (The building TB-2).....	<b>89</b>
<b>Figure 3.23</b> : Analytical FRF (The building TB-1).....	<b>90</b>
<b>Figure 3.24</b> : Analytical FRF (The building TB-2).....	<b>90</b>
<b>Figure 3.25</b> : Model updating results of the building TB-1 (Step 2: Damping ratio).....	<b>91</b>
<b>Figure 3.26</b> : Model updating results of the building TB-2 (Step 2: Damping ratio).....	<b>92</b>
<b>Figure 4.1</b> : Baseline and damaged FRFs of the building TB-1. ....	<b>96</b>
<b>Figure 4.2</b> : Moment-rotation relationship of the columns, (a) S11, (b) S12, (c) S13 and (d) S14. ....	<b>99</b>
<b>Figure 4.3</b> : FRF sensitivity to change in rotational stiffness (Rx and Ry), Group 1.....	<b>101</b>
<b>Figure 4.4</b> : FRF sensitivity to change in rotational stiffness (Rx and Ry), Group 2.....	<b>101</b>
<b>Figure 4.5</b> : FRF sensitivity to change in rotational stiffness (Rx and Ry), i-end springs in Group 3. ....	<b>102</b>
<b>Figure 4.6</b> : FRF sensitivity to change in rotational stiffness (Rx and Ry), j-end springs in Group 3. ....	<b>103</b>
<b>Figure 4.7</b> : FRF sensitivity to change in rotational stiffness (Rx and Ry), Group 8.....	<b>104</b>
<b>Figure 4.8</b> : Model updating results for the building TB-1 (Step 1: [K]). ....	<b>105</b>
<b>Figure 4.9</b> : Application of curve fitting. ....	<b>106</b>
<b>Figure 4.10</b> : FRF of the system.....	<b>110</b>
<b>Figure 4.11</b> : Model updating results of the building TB-1 (Step 2). ....	<b>111</b>
<b>Figure 4.12</b> : Moment-rotation relationship of the columns, (a) S11-S14 for x direction and S12-S13 for y direction, (b) S12-S13 for x direction and S11-S12 for y direction. ....	<b>113</b>
<b>Figure 4.13</b> : FRF sensitivity to change in rotational stiffness (Rx and Ry), i-end springs in Group 1.....	<b>114</b>
<b>Figure 4.14</b> : FRF sensitivity to change in rotational stiffness (Rx and Ry), j-end springs in Group 1.....	<b>115</b>
<b>Figure 4.15</b> : FRF sensitivity to change in rotational stiffness (Rx and Ry), i-end springs in Group 2.....	<b>116</b>
<b>Figure 4.16</b> : FRF sensitivity to change in rotational stiffness (Rx and Ry), j-end springs in Group 2.....	<b>117</b>
<b>Figure 4.17</b> : FRF sensitivity to change in rotational stiffness (Rx and Ry), Group 3. ....	<b>117</b>

<b>Figure 4.18</b> : Model updating results for the building TB-2 for DC1 (Step 1: [K]).	118
<b>Figure 4.19</b> : Model updating results for the building TB-2 for DC2 (Step 1: [K]).	118
<b>Figure 4.20</b> : Model updating results for the building TB-2 for DC3 (Step 1: [K]).	118
<b>Figure 4.21</b> : Model updating results for the building TB-2 for DC4 (Step 1: [K]).	119
<b>Figure 4.22</b> : Model updating results for the building TB-2 for DC5 (Step 1: [K]).	119
<b>Figure 4.23</b> : Application of curve fitting (Damaged Case 1).	123
<b>Figure 4.24</b> : FRF of the system - Damaged Case 1.	124
<b>Figure 4.25</b> : Application of curve fitting (Damaged Case 2).	124
<b>Figure 4.26</b> : FRF of the system - Damaged Case 1.	125
<b>Figure 4.27</b> : Application of curve fitting (Damaged Case 3).	125
<b>Figure 4.28</b> : FRF of the system - Damaged Case 3.	126
<b>Figure 4.29</b> : Application of curve fitting (Damaged Case 4).	126
<b>Figure 4.30</b> : FRF of the system - Damaged Case 4.	127
<b>Figure 4.31</b> : Application of curve fitting (Damaged Case 5).	128
<b>Figure 4.32</b> : FRF of the system - Damaged Case 5.	128
<b>Figure 4.33</b> : Model updating results of the building TB-2 (Step 2) - DC1.	131
<b>Figure 4.34</b> : Model updating results of the building TB-2 (Step 2) – DC2.	131
<b>Figure 4.35</b> : Model updating results of the building TB-2 (Step 2) – DC3.	131
<b>Figure 4.36</b> : Model updating results of the building TB-2 (Step 2) – DC4.	132
<b>Figure 4.37</b> : Model updating results of the building TB-2 (Step 2) – DC5.	132
<b>Figure 5.1</b> : Schematic view of simplified FEMs.	136
<b>Figure 5.2</b> : Rigid floor diaphragms and corresponding DOFs of 1-story shear frame.	136
<b>Figure 5.3</b> : Updated FRF of the simple model of the building TB-2 (Step 1: [K] and [M]).	138
<b>Figure 5.4</b> : Application of curve fitting (the simple model of building TB-2).	139
<b>Figure 5.5</b> : FRF of the system (the simple model of building TB-2).	140
<b>Figure 5.6</b> : Model updating results of the building TB-2 for the simple model (Step 2: Damping ratio).	140
<b>Figure 5.7</b> : Model updating results for the building TB-2 for DC1 (Simple FEM).	143
<b>Figure 5.8</b> : Model updating results for the building TB-2 for DC2 (Simple FEM).	144
<b>Figure 5.9</b> : Model updating results for the building TB-2 for DC3 (Simple FEM).	144
<b>Figure 5.10</b> : Model updating results for the building TB-2 for DC4 (Simple FEM).	144
<b>Figure 5.11</b> : Model updating results for the building TB-2 for DC5 (Simple FEM).	145
<b>Figure 5.12</b> : Application of curve fitting (DC1-Simple FEM).	149
<b>Figure 5.13</b> : FRF of the system - DC1-Simple FEM.	149
<b>Figure 5.14</b> : Model updating results (Step 2) - DC1-Simple FEM.	150
<b>Figure 5.15</b> : Application of curve fitting (DC2-Simple FEM).	150
<b>Figure 5.16</b> : FRF of the system – DC2-Simple FEM.	150
<b>Figure 5.17</b> : Model updating results (Step 2) – DC2-Simple FEM.	151

<b>Figure 5.18</b> : Application of curve fitting (DC3-Simple FEM). .....	<b>151</b>
<b>Figure 5.19</b> : FRF of the system – DC3-Simple FEM. ....	<b>151</b>
<b>Figure 5.20</b> : Model updating results (Step 2) – DC3-Simple FEM. ....	<b>152</b>
<b>Figure 5.21</b> : Application of curve fitting (DC4-Simple FEM). ....	<b>152</b>
<b>Figure 5.22</b> : FRF of the system – DC3-Simple FEM. ....	<b>152</b>
<b>Figure 5.23</b> : Model updating results (Step 2) – DC4-Simple FEM. ....	<b>153</b>
<b>Figure 5.24</b> : Application of curve fitting (DC5-Simple FEM). ....	<b>153</b>
<b>Figure 5.25</b> : FRF of the system – DC5-Simple FEM. ....	<b>154</b>
<b>Figure 5.26</b> : Model updating results (Step 2) – DC5-Simple FEM. ....	<b>155</b>
<b>Figure 6.1</b> : Stress-strain relationships, (a) concrete, (b) reinforcement. ....	<b>158</b>
<b>Figure 6.2</b> : Quasi-static test – loading protocol. ....	<b>159</b>
<b>Figure 6.3</b> : Base shear force-first story drift ratio relationship. ....	<b>159</b>
<b>Figure 6.4</b> : Damage limits and response behavior of RC members. ....	<b>160</b>
<b>Figure 6.5</b> : Moment-Column end rotations (Perform 3D) (the first story), (a) S11, (b) S12, (c) S13 and (d) S14. ....	<b>163</b>
<b>Figure 6.6</b> : Moment-Column end rotations (Perform 3D) (the second story), (a) S11, (b) S12, (c) S13 and (d) S14. ....	<b>165</b>
<b>Figure 6.7</b> : White noise signal as dynamic input force. ....	<b>166</b>
<b>Figure 6.8</b> : CPSD functions of the generated vibration signal, (a) undamaged case, (b) damaged case. ....	<b>167</b>
<b>Figure 6.9</b> : Experimentally obtained and updated FRFs of the building TB-1. ....	<b>168</b>
<b>Figure 6.10</b> : Modelling criteria for damaged plastic hinges. ....	<b>169</b>





# **FIELD TESTING AND MODEL UPDATING OF TYPICAL RC BUILDINGS FOR DAMAGE IDENTIFICATION**

## **SUMMARY**

A great portion of existing building stock of Turkey consists of reinforced concrete (RC) structures. A significant amount of these RC structures, which were constructed several years ago, do not satisfy the requirements of the modern seismic design codes. Although majority of these structures are legally engineered structures, even some of them are not, due to the lack of an official control mechanism, these structures mostly do not fulfil the requirements of the seismic design codes, which were in force during their construction time. Accordingly, these buildings have basic structural weaknesses such as low concrete strength, insufficient reinforcement detail, etc. and represent a significant risk in case of any seismic action. Thereby, the condition assessment of the existing structures after an earthquake is crucial for determining the residual performance of the building. Up to the present, condition assessment of the buildings after a major earthquake has been immediately carried out based on visual inspection. Although this is a required and an essential method for making decision the current situation of the buildings, some damages could not be identified through visual inspection. For example, internal cracking or slip of the lap-splice can be hidden from view, however, their effects on the load bearing capacity of the building can be crucial and vital. From this point of view, the vibration signature of the building, which is obtained through St-Id methods, can provide significant information about the condition of the buildings.

In this dissertation, it is aimed to present an automated damage identification algorithm through field testing and model updating of typical RC buildings. For this purpose, first, a series of field testing was carried out for quantifying the influence of different types and extents of structural damage on the dynamic characteristics of typical existing RC buildings. In the context of the field testing, vibration-based tests were performed before and after quasi-static reversed lateral loading cycles as well as at certain damage levels. Since the test buildings (the buildings TB-1 and TB-2) are representative of large number of substandard RC buildings, the test results would be useful for the seismic performance assessment of existing RC buildings. At the end of the field tests, it was found that the modal frequencies decreased, and the modal damping ratios increased significantly up to the elastic limit. However, the progressing of damage beyond the elastic limit was not accompanied with a similar significant change in the modal frequencies and the modal damping ratios. Furthermore, despite a significant degradation in lateral load bearing capacity, as approximately 20%, induced by quasi-static lateral loading at around 3% lateral d.r., no intensified structural damage could be observed by visual inspection in case of building TB-2. However, the forced vibration test results presented that the modal frequencies and the damping ratios changed due to lateral loading in comparison with its undamaged state. These findings indicate a serious risk about the missing the structural damages during visual inspections after earthquakes. Hence, utilization of dynamic testing

accompanying with visual inspection could be a promising method for more realistic assessment of structural damages after seismic events.

Second, an automated damage identification algorithm was proposed using the results of the experimental study. A model based automated algorithm relies on the updating of Finite Element Model (FEM) of the test buildings was introduced. Different than the majority of the damage identification methods introduced in literature, two existing RC structures accompanied with different extent of damage were considered. By means of the presented damage identification algorithm, first the initial FEM of the buildings were successfully updated via changes stiffness, unit weight and damping parameters and the baseline model, which was taken as reference for damage identification, were obtained. Subsequently, the revision in the two-step algorithm in terms of updating the damping parameters provided to obtain the mathematical description of the buildings. Significantly, curve fitting clearly became a useful and practical part of the model updating algorithm and found to be a promising tool in case of the dynamic measurements including noisy components. Followingly, the FRF based model updating algorithm, which was introduced by updating the initial FEM of the buildings, was adopted for damage detection, localization and quantification using experimentally collected data from the building TB-1 and TB-2. At the end of the application of algorithm, it was found that the first step of the algorithm (Step 1) provided a successful damage detection, localization and quantification process. Although the second step (Step 2) also provided to match the experimental FRFs and FEM FRFs in terms of their amplitudes, it is basically have not any contribution for Level 3 damage identification purpose. Subsequently, the damage identification algorithm was computed by considering a simplified FEM of the test building TB-2 to examine the efficiency of utilizing a simple model. At the end of the process, a damage detection was provided in terms of story level not member level. Although this can not be classified as a Level 3 damage identification since it did not address the damage location, it could be a practical and rapid approach for assessing a multi-story building after earthquake.

Third, the Level 3 damage identification method was extended in order to predict the serviceability of the structure after damage. For this purpose, the nonlinear model of the building TB-1 was established, and the model was then subjected to the same lateral loading reversals with the quasi-static tests. Following to calibrating the nonlinear model with regard to experimental base shear force-1<sup>st</sup> story drift relationship, a set of dynamic data was generated from the model for both undamaged and damaged case. After verifying the dynamic results obtained from field tests (and updated ones) and estimated through generated signal are matching, the performance based assessment results of the building, which were obtained using ASCE 41-13, were compared with the vibration based damage identification results. By this way, the damage identification algorithm was not only examined in terms of efficiency and validity, but also extended to investigate the residual capacity of damaged structures. Most importantly, an additional step for algorithm was suggested so that nonlinear moment-rotation based damage state of the member can be obtained through vibration data.

Based on the literature survey, variation of dynamic characteristics with respect to increasing seismic structural damage and followingly a damage identification process was for the first time presented for the full-scale RC structures. Furthermore, the utilization of nonlinear moment-rotation based damage criteria for vibration based damage detection could provide practical and result-oriented assessment tool for

engineers. Both experimental and analytical results present the importance of utilization of the vibration based methods for condition assessment of RC structures.





## TİPİK BETONARME YAPILARDA HASAR TESPİTİ ÜZERİNE SAHA DENEYLERİ VE MODEL GÜNCELLEMESİ

### ÖZET

Ülkemizde, mevcut bina stoğunun büyük bir kısmı betonarme yapılardan oluşmaktadır. Çoğunluğu 1990 öncesi inşa edilmiş olan bu betonarme yapıların önemli miktarı güncel tasarım standartlarının gerekliliklerini karşılamamaktadır. Bu yapıların çoğunluğu yasal olarak mühendislik hizmeti almış yapılar olmasına rağmen, resmi denetim mekanizmalarının bulunmaması nedeniyle sadece güncel tasarım standartlarını değil, yapıldıkları dönemde yürürlükte olan standartların da gerekliliklerini karşılamamaktadır. Dolayısı ile, bu binalarda dayanımı düşük beton, yetersiz enine donatı detayı vb. gibi temel yapısal zayıflıklar vardır ve herhangi bir deprem etkisi altında önemli bir risk oluşturmaktadır. Bu sebeplerle, deprem sonrasında mevcut yapıların durum değerlendirmesi, binanın kalan ömründeki performansının belirlenmesinde çok önemlidir. Günümüzde, büyük bir deprem sonrasında binaların durum değerlendirmesi görsel incelemeye dayanarak gerçekleştirilmektedir. Binaların mevcut durumu hakkında karar vermek için gerekli ve pratik bir yöntem olmasına rağmen, bazı hasarların görsel inceleme yoluyla tespit edilememesi durumu olabilir. Örneğin, elemanlarda bulunan içsel çatlaklar veya bindirme donatısının sıyrılması gibi hasarlar, görsel inceleme ile farkedilemeyebilir, ancak binanın yük taşıma kapasitesi üzerindeki etkileri hayati olabilir. Bu açıdan bakıldığında, Yapısal Tanılama (St-Id) metodları ile elde edilen binanın titreşim karakteristikleri, binaların mevcut durumu hakkında önemli bilgiler sağlayabilir.

Bu tez çalışması kapsamında, tipik betonarme yapılarda dinamik karakteristiklerin yapısal sismik hasarla değişimi sayısal olarak ortaya koyulmuştur. Bununla beraber, tipik betonarme binalar için otomatik hasar tespit algoritması sunulmuştur. Bu amaçla, önce, tipik mevcut betonarme yapıların dinamik özelliklerinin farklı derecede ve tipte yapısal hasarla beraber değişimini incelemek için bir dizi saha testi gerçekleştirilmiştir. Saha çalışması kapsamında, yarı-statik tersinir tekrarlı yatay yükleme döngüleri öncesinde ve sonrasında ve bazı hasar düzeylerinde zorlanmış titreşim testleri yapılmıştır. Testler, iki adet üç katlı tam ölçekli betonarme yapıda, 3 adet hidrolik yük veren kullanılarak yapıların x doğrultusunda, tersinir tekrarlı yatay yer değiştirme adımları şeklinde gerçekleştirilmiştir (Test binaları TB-1 ve TB-2). Titreşim testleri ise, eksantrik kütleli sarsıcı ile zorlanan yapının titreşim cevabının ivmeölçerler ile toplanması şeklinde gerçekleştirilmiştir. Test binalarından TB-1, 1990'lı yıllarda inşa edilmiş ve 2013 yılında Kentsel Dönüşüm yasası kapsamında boşaltılmış gerçek bir binanın parçasıdır. Mevcut yapı stoğundaki tipik betonarme yapıların aksine, test binası TB-1, güçlü kolon-zayıf kiriş mekanizmasına sahiptir. Bu sebeple, mevcut yapı stoğunu daha iyi temsil etmesi açısından, bir bina (test binası TB-2) zayıf kolon-güçlü kiriş mekanizmasına sahip olacak şekilde tasarlanarak test binası TB-1 ile aynı alanda inşa edilmiştir. Tıpkı mevcut yapı stoğundaki birçok binada olduğu gibi, her iki test binasında da düşük dayanımlı beton, düz donatı, yetersiz enine donatı detayı gibi

eksiklikler mevcuttur. Saha çalışmalarının sonunda, yapısal frekansların ve sönüm oranlarının, yapısal hasarın akma sınırının ötesine geçmediği yüklemelerde, artan hasarla beraber ciddi mertebede değiştiği, akma sınırının ötesinde ise, artan hasarla beraber akma öncesinde sergilediği belirgin değişimi göstermediği ortaya konulmuştur.

Saha çalışmalarının akabinde, test sonuçlarını kullanarak otomatik hasar tespit algoritması içeren model-esaslı MATLAB tabanlı bir program yazılmıştır (Model Updating Program: MUP). Sonlu eleman modeli (FEM) güncellemesine dayanan program, deneysel olarak elde edilen frekans davranış fonksiyonu (FRF) ile sonlu eleman modelinden elde edilen FRF (bundan sonra analitik FRF olarak bahsedilecek) arasındaki farkı minimize edecek parametreleri tekrarlı olarak değiştirilerek hasar tespiti yapılmasına olanak tanımaktadır. İki-adımlı otomatik hasar tespit algoritması, test binalarının hasarsız durumunu temsil etmesi için (başlangıç modeli) SAP2000'de kurulan yapı sonlu eleman modelinin güncellenmesi ile doğrulanmıştır. Daha detaylı anlatmak gerekirse, algoritmanın ilk adımında sonlu eleman modelinin rijitlik ve kütle matrisleri güncellenerek analitik FRF'in frekans bileşenleri, deneysel olarak elde edilen FRF'in (bundan sonra deneysel FRF olarak bahsedilecek) frekans bileşenleri ile örtüştürülmeye çalışılmıştır. Algoritmanın ikinci adımında ise, sönüm oranı değerleri güncellenerek, analitik FRF ile deneysel FRF, fonksiyonların büyüklük bileşenleri açısından örtüştürülmüştür. Bu güncelleme işlemi MUP tarafından, analitik FRF ve deneysel FRF arasındaki farkı ifade eden hata fonksiyonunu minimuma indiren kadar, önceden seçilmiş parametrelerin tekrarlı olarak değiştirilmesi şeklinde yapılmıştır. Sonuç olarak, ilk etapta kurulan başlangıç modelleri güncellenerek, yapıların hasarsız durumunu temsil eden 'referans model' elde edilmiştir.

Bu işlemin akabinde, yapıların başlangıç modellerinin güncellenmesi işlemi ile tanıtılan ve doğrulanan iki-adımlı hasar tespit algoritması, yarı-statik testlerle erişilmiş hasarın otomatik olarak tespiti işlemine adapte edilmiştir. Hasar tespiti, bir önceki adımda elde edilen ve yapıların hasarsız durumunu temsil eden referans modele ait analitik FRF ile çeşitli hasar seviyelerinde (test binası TB-1 için %1.5 birinci kat yatay öteleme oranında, test binası TB-2 için %0.5, %1.0, %1.5, %2 ve %3 birinci kat yatay öteleme oranlarında) deneysel olarak elde edilmiş FRF'ler arasındaki farkın, tüm hasar seviyeleri için ayrı ayrı minimuma indirilmesi şeklinde gerçekleştirilmiştir. Test binalarının kolon-kiriş kesit özelliklerine bakılarak yapılan hızlı bir değerlendirme ve mühendislik tecrübesi ile, algoritmada değiştirilecek parametrelerin eleman başlangıç ve sınır koşullarında rijitlik değişimini temsil edecek şekilde seçilmesine karar verilmiştir. Dolayısıyla kolon ve kiriş uç bölgelerine eleman-uç yayları atanmış ve bu yaylara ait rijitliklerin tekrarlı değiştirilmesi ile algoritmanın ilk adımı tamamlanmıştır. Bu adımda güncellenen modelde sönüm parametreleri tekrarlı olarak değiştirilerek hasar tespit algoritmasının ikinci adımı da tamamlanmıştır. Bu sayede, yapısal hasarın varlığı, yeri ve mertebesi otomatik bir algoritma ile tespit edilmiştir.

Hasarın varlığı, yeri ve mertebesini tespit edebilen bu tür bir algoritma, literatürde 3. seviye hasar tespiti olarak sınıflandırılmıştır. Bu sınıflandırmaya göre 1. seviye, hasar varlığının tespitini, 2. seviye hasar varlığının ve yerinin tespitini, 3. seviye hasar varlığının, yerinin ve mertebesinin tespiti sağlayabilmektedir. Otomatik hasar tespiti algoritmalarında ulaşılması istenen nokta ise, hasarın varlığının, yerinin ve mertebesinin tespitine ek olarak, hasar gören yapının kalan servis ömrünün de tespit edilebilmesi yönündedir. Dolayısıyla ile bu çalışmada, 3. seviye hasar tespiti, bu şekilde tam ölçekli betonarme yapılar için ilk olarak sunulmuştur.

Geleneksel titreşim tabanlı hasar tespit algoritmalarından farklı olarak ayrıca, test binası TB-1 üzerinde yapılan analitik bir çalışma ile, yapının hasar gördükten sonraki kullanım düzeyi ile ilgili bilgiye erişilebilmesini sağlayan pratik bir algoritma, ilk kez sunulmuştur. Söz konusu analitik çalışma kapsamında, ilk olarak test binası TB-1'e ait doğrusal olmayan yapı modeli Perform-3D yapısal analiz programında kurulmuştur. Akabinde yapının saha testlerinde maruz kaldığı tersinir tekrarlı yatay yükleme patronu, söz konusu yapısal analiz programında simüle edilmiştir. Yarı-statik saha testleri sonucunda ulaşılan hasar ile uyumlu sonuçlar veren doğrusal olmayan yapı modeli esas alınarak, hasarlı ve hasarsız durumlar için titreşim verileri üretilmiştir. Dahası, hasar tespit algoritması, saha testlerini temsil eden bilgisayar simülasyonundan elde edilen bu verilere uygulanmıştır. Elde edilen sonuçlar, doğrusal olmayan modele uygulanan performans dayalı değerlendirme (ASCE 41-13) sonuçları ile kıyaslanmış ve uyumlu sonuçlar elde edilmiştir. Bu sayede, yapı elemanlarının performans düzeyleri belirlenmiştir. Söz konusu bu analitik çalışma ile, hem hasar tespit algoritmasının doğruluğu bir kez daha test edilmiş hem de 4. Seviye hasar tespiti yapabilmek konusunda ciddi bir ilerleme kaydedilmiştir. Yapının hasarlı durumuna ait titreşim cevabı kullanılarak, elemanlardaki hasar, doğrusal olmayan dönme değeri cinsinden ifade edilmiş, ve böylece hasarın seviyesi ile ilgili uluslararası kodlarda belirtilen limitler, titreşim tabanlı hasar tespiti için kullanılabilir hale gelmiştir.

Tez kapsamında gerçekleştirilmiş literatür çalışmasına dayanarak belirtmelidir ki, artan yapısal hasarla dinamik karakteristiklerin değişimi, bu boyutta betonarme yapılar için ilk olarak ortaya koyulmuştur. Ayrıca, titreşime dayalı hasar tespiti için doğrusal olmayan moment-dönme esaslı hasar ölçütlerinin kullanılması önerisinin, mühendisler için pratik ve sonuç odaklı değerlendirme aracı olduğuna inanılmaktadır. Deneysel ve analitik sonuçlar, betonarme yapılarının durum değerlendirmesi için titreşime dayalı yöntemlerin kullanılmasının önemini ortaya koymaktadır. Bu sebeple, sonuçların, daha farklı tipte ve boyutta yapıda doğrulanması önem arz etmektedir.





## 1. INTRODUCTION

At present, there are robust computers and powerful modeling tools that have the ability to design the structures or model the existing ones and subsequently simulate their behavior precisely under service loadings and/or successive loading such as earthquakes, blasts, wind etc. However, there are several cases that show even very detailed models may miss critical mechanisms within a complex structure (Catbas et al. 2013). For instance, modelling the existing structures may include uncertainties such as boundary and continuity conditions, change in the material characteristics due to aging, etc. Similarly, reliably modelling the historical structures requires to rise even more challenges such as predicting the material characteristics without destructive testing, determining the boundary conditions between structural members or considering the structural interventions which were made using different construction materials. Another big challenge for structural engineers is that modelling of force distributions in complex structures, such as suspension bridges, stadiums, tall buildings which may cause mistakes in simulating the local or global behavior of these structures. This understanding has displayed the need to verify and also improve the model predictions using experimental response data through St-Id. St-Id provides a link between the engineering profession and the structural systems they design, construct, operate and preserve by developing reliable estimates using experimental observations and data. Obviously, St-Id have provided a major contribution to understand, interpret and to control many structural problems existing in practice (Catbas et al. 2013). Therefore, St-Id, including both field tests for data acquisition and its processing, has gained recognition extensively for bridges, tall buildings, RC residential buildings, cultural heritages, etc with the aim of not only model calibration, but also condition assessment and damage identification.

For example, modal characteristics of bridges has been investigated utilizing measured dynamic properties with the aim of verifying the physics-based models (e.g., finite element model) of these bridges to reliably simulate their responses under various loading conditions (owing to wind and traffic-induced loads) (Abdel-Ghaffar and

Scanlan 1985; Chang et al. 2001; Huffman et al. 2006; Gentile and Gallino 2008; Picozzi et al. 2010; Apaydin et al. 2012). In the case of model updating and calibration issues; Abdel-Ghaffar and Scanlan 1985 carried out a series of tests on Golden Gate Bridge to determine the modal characteristics of bridge (such as effective damping, the three-dimensional mode shapes, and the associated modal frequencies). By taking into consideration the major interest as wind and earthquake problems, they aimed to make a comparison between measured modal characteristics and those obtained from the finite element model (FEM) of the bridge. Chang et al. 2001 studied the dynamic characteristics of a long cable-stayed bridge in Hong Kong utilizing FEM analysis and ambient vibration test results. Although the comparison results showed a total of 31 modes of the bridge were in good correlation, the frequency differences of the higher modes varied between 15-30%. This result of their study showed the necessity of FEM updating using test results. Gentile and Gallino 2008 conducted ambient vibration test of an historical suspension footbridge after its retrofitting. The dynamic test results were used to adjust some parameters of FEM of the bridge which were accepted to be used as the baseline model for simulating and evaluating the long-term behavior of bridge under the service and/or excessive loads. Apart from the alluded model calibration studies, St-Id provided a valuable information about the condition of the bridge under service loadings. Apaydin et al. 2012 studied the vibration amplifications under heavy-traffic as opposed to no-traffic conditions on the Fatih Sultan Mehmet suspension bridge in Istanbul. In order to obtain the response of the bridge to diverse traffic conditions, they performed two full-scale ambient vibration tests on two different days and found that heavy-traffic loads intensified the vibration response of the bridge and shifted the predominant frequencies. They also presented that any movement which induces vibration on the bridge was carried and amplified along its length.

In just the same way as the bridges, St-Id applications have attracted great deal of attention of worldwide researchers to extract the dynamic characteristics of the cultural heritage structures since these applications meet the preservation needs of these structures (Ivorra and Pallares 2006, D'ambrisi et al. 2012, Asteris et al. 2014; Votsis et al. 2012). Some of these studies were performed in order to provide a reliable FEM of the structure which was considered for the retrofitting/rehabilitation studies. For example, Ivorra and Pallares 2006 investigated the characterization of the dynamic structural behavior of the bell tower of Nuestra Sra. De la Misericordia Church in

Valencia, Spain. They calibrated different FEMs of the bell tower based on the dynamic tests and analyzed the inertia forced induced by bell swinging. Besides, D'ambrisi et al. 2012 extracted dynamic characteristics of masonry towers and bell-towers in Italy which were particularly vulnerable against seismic actions using dynamic tests in order to calibrate their analytical model to carry out nonlinear static and dynamic analysis.

In the case of the RC structures, St-Id plays a significant role in order to simulate the behavior of the structures during earthquakes or provides significant information for examining the effects of the applied retrofitting (Brownjohn 2003, Michel et al. 2010; Celik et al. 2013, Soyoz et al. 2013). Among these studies, Brownjohn 2003 showed that vibration test results which were obtained even with small amount of data, could provide reliable information about the dynamic characteristics of RC buildings. Celik et al. 2013 applied forced vibration tests to an existing typical nine-story reinforced concrete flat plate-wall building in order to establish its three-dimensional linear elastic FEM. They presented the importance of considering the impact of door and window openings in the shear walls, which were common in tunnel form buildings, during establishing FEM have the most significant impact on dynamic properties.

Since civil structures are prone to damage and deterioration due to not only excessive loadings such as earthquake, wind, but also service loadings and aging during their lifespan, all these alluded St-Id applications gained recognition in civil structures for the form of 'damage identification' by various researchers.

### **1.1 Damage Identification**

Structural damage identification is a promising research area for (i) preventing unpredicted structural failure which may cause serious economic and human life loss, (ii) reducing repairing and maintenance costs of civil infrastructure investments (bridges, wind turbines, nuclear power plants, etc). Therefore, monitoring a structure and detecting the damage at the earliest possible stage has gained significant attention from not only researchers but also from engineering communities (Catbas et al. 2013). As it was clearly stated in the comprehensive literature survey for the damage identification methods of Doebling et al. 1996, the commonly used damage identification methods are based on visual or localized experimental methods such as acoustic or ultrasonic methods, magnetic field methods, radiography or thermal field

methods which cannot be easily or practically adopted for most of the civil engineering structures (Fan and Qiao, 2011). All of these nondestructive experimental techniques require that the localization of the damage is known before applying the technique and most importantly are able to provide a limited part of the structure being inspected (Doebling et al. 1996). This situation clearly indicates that a quantitative global damage detection method, which can be applied to complex structures, is required. At that point, since the various reasons came together such as devastating failures resulting significant loss in life and its economic concerns after earthquakes or different than the civil structures, airplane loss, etc, the public, media and politicians focused the sensing and monitoring issues. Furthermore, the conditions of aging civil infrastructures which can cause repairing and maintenance costs have also been encouraging factors for the development of methods that can be used to detect the onset of damage or deterioration at the earliest possible stage (Catbas et al. 2013). Finally, with the increasing in technology (which fueled the increasing in cost-effective computing memory and speed, advances in measurement devices) and developments in scientific field like advancements in experimental techniques such as modal testing, have contributed to recent improvements in vibration-based damage detection (Doebling et al. 1996).

The main idea behind vibration-based damage identification methods is based on that modal parameters (frequencies, mode shapes, and modal damping ratios) are functions of the physical properties of the structure (mass, damping, and stiffness). Accordingly, any changes in the physical properties of the structure causes identified changes in the modal properties. For example, the onset of cracks cause reduction in stiffness. Therefore, this is the motivation which fueled the researches that damage can be identified by analyzing the changes in vibration features of the structure.

Before discussing the damage identification methods, it could be clarified that the effects of damage on a structure can be classified as linear and nonlinear (Doebling et al. 1996). The linear damage means the initially linear-elastic structure remains linear-elastic after damage. Although the changes in modal properties are induced by the changes in the geometry and/or the material properties and these are the possible results of any damage, the structural response can still be modeled using linear equation of motion (Doebling et al. 1996). And this is the type of damage which will be considered within the context of these thesis. Accordingly, linear methods can be

classified based on two main approaches: (a) non-model-based approach and (b) model-based approach (Farrar and Worden 2007). There are many researches and also real practices which both approaches have been successfully applied for damage detection. The non-model-based approach relies on the signal processing of experimental data and the model-based approach relies on mathematical descriptions of structural systems (Barthorpe 2011). Non-model-based approaches typically seek to identify damage from changes in structural vibration characteristics (response measurements, natural frequencies, mode shapes, etc.) (Saadat et al. 2004). However, the model-based approaches are usually implemented by using a computer model of the concerned structure (a FEM), to detect damage based on the measured test data. Accordingly, in the model-based method, the first step is to establish the FEM of the structure based on the design calculations (initial model). Apart from the alluded model and non-model based damage classification, Rytter 1993 defined a worldwide accepted classification system for damage identification based on the achieved items as detecting, localization, quantification of damage and predicting of remaining life of the structure:

- Level 1: Detection of damage,
- Level 2: Detection and localization of damage,
- Level 3: Detection, localization and quantification of damage,
- Level 4: Detection, localization, quantification of damage and prediction of remaining life.

Many damage identification methods concentrated on Levels 1 to 3 and most of them developed by studying on laboratory structures or controlled damage to field structures. Furthermore, they unfortunately did not estimate the remaining service life of a structure which means Level 4 damage identification. Followingly, a brief survey about the damage identification methods are given by following closely the comprehensive literature survey carried out by Doebling et al. 1996 and Carden and Fanning, 2004.

### **1.1.1 Natural frequency based methods**

In literature, there are significant number of research related to damage identification based on shifts in natural frequencies. For most of the cases, direct relation between

stiffness, mass and natural frequency and the relatively practical ways of experimentally obtaining the natural frequencies has been the motivation behind the studies which focus natural frequency shifts for damage identification (Carden and Fanning, 2004).

Although effectiveness of this method was questioned by various researchers (Chen et al. 1995, Farrar et al. 1994, Law et al. 1995a and 1995b) with the argument that shift of the lower frequencies would not necessarily be useful damage indicators, De Roeck et al. (2000) presented a successful result using this method in Z24 Bridge in Switzerland. According to this study, stiffness degradations could be detected if the corresponding frequency shifts were more than just 1%. It should be noted that this result could be demonstrated once the effects of environmental influences (air temperature, humidity, rain, wind speed and direction) were filtered out.

Messina et al. (1998) presented a method based on the sensitivity of each resonant frequency to damage in each location. The method defined a statistical correlation between the analytical predictions of the frequency changes  $\delta f$  and the measured frequency changes  $\Delta f$ : The multiple damage location assurance criterion (MDLAC). The analytically determined frequency change ( $\delta f$ ) can be written as a function of the damage extent vector ( $\delta D$ ). The interested damage state is calculated by calling the value of the damage extent vector ( $\delta D$ ) maximizing the MDLAC value (Eq 1.1).

$$MDLAC(\{\delta D\}) = \frac{|\{\Delta f\}^T \cdot \{\delta f(\{\delta D\})\}|^2}{(\{\Delta f\}^T \cdot \{\Delta f\}^T) \cdot (\{\delta f(\{\delta D\})\}^T \cdot \{\delta f(\{\delta D\})\})} \quad 1.1$$

Both the numerical and experimental test results showed that if changes in a few of natural frequencies of the structure between the undamaged and damaged conditions is known, the MDLAC approach provides good predictions of both the location and absolute size of damage at one or more sites.

Although the usage of frequency shifts for damage identification methods has been extensively studied in the past three decades, it generally provides identification limited with a few locations and has been mostly implemented on small laboratory structures.

### 1.1.2 Mode shape based methods

The damage identification methods based on change in modal extractions have been attracted by various researchers. In comparison to using natural frequency shift for damage identification, the use of mode shape based methods (mode shape and/or its derivatives), have significant advantages. Since the mode shapes include local information, they are prone to be affected from local damages and this make them enable to be used directly in multiple damage detection (Fan and Qiao 2011). Moreover, ambient, and environmental effects have very limited influence on the mode shapes (Farrar and James 1997). However, in contrary to the frequency shift based methods which can be applied even one sensor, capturing of the mode shapes requires a series of sensors and more critically, the measured mode shapes are more vulnerable to include noisy components than natural frequencies (Fan and Qiao 2011). In last three decades, two very commonly used methods were presented: (i) Modal Assurance Criterion, MAC (Allemann and Brown, 1982), and (ii) Coordinate Modal Assurance Criterion, COMAC (Lieven and Ewins, 1988).

The MAC value was introduced as a measure of the similarity of two mode shapes which were extracted for 2 different damage states (or undamaged and damaged states). A MAC value can vary between 0 and 1. The value 1 represent a perfect match of 2 mode shapes while a value of 0 means they are completely different than each other. Accordingly, the variation of the value from 1 to 0 may represent the damage. Salawu and Williams (1995) showed the efficiency of the method comparing to the frequency shift method. They tested a reinforced concrete bridge before and after repair. The MAC value for the first seven mode shapes showed significant change which indicated damage, while the first seven modal frequencies shifted by less than just 3%. However, Huth et al. 2005 investigated the performance of several damage identification methods based on experimental modal data, which was obtained from tests performed on a prestressed reinforced concrete bridge subjected to incremental artificial damage. The modal data obtained from the bridge monitoring over 8 months indicated that MAC value showed better performance as damage indicator than the frequency shifts did.

In the case of COMAC, since it is a pointwise measure of the difference between two mode shapes and it could be possible to detect and localize damage, as well. Like MAC, COMAC also takes a value between 0 and 1 and from 1 to 0, possibility of

discordance at a point increases (Carden and Fanning (2004). Fryba and Pirner (2001) used the COMAC method for understanding the effectiveness of a repair to a prestressed concrete segment bridge, which was damaged because a part of the superstructure had spontaneously slid off its bearings. COMAC analysis showed consistency between the repaired segment responses and undamaged segment.

However, there are lots of study which showed the efficiency of traditional mode shape changes methods, it is also clearly indicated that they are not sensitive to damage and are subjected to some limitations. For example, there are significant difficulties with full-scale structures and they are only sensitive to damage in a certain area such as mid-span of a clamped-clamped beam. The most importantly, without any further signal processing or pattern recognition technique, they can not provide accurate localization or quantification of damage (Fan and Qiao 2011).

As an alternative to direct use of mode shape changes in damage identification, the usage of mode mode shape curvature has been also attracted by various researchers. It is a method based on the assumption that changes in the mode shape curvatures are well indicator for detection of the region of damage. The mode shape curvature can be calculated using a central difference approximation to the displacement mode shapes ( $\phi$ ) (Eq. 1.2). In Eq. 1.2,  $i, j$  and  $L$  refers mode shape number, node number and distance between the nodes, respectively (It should be noted that the equation 1.2 is taken from the study of Alampalli et al.)

$$\phi''_{ji} = \frac{\phi_{(j+1)i} - 2\phi_{ji} + \phi_{(j-1)i}}{L^2} \quad 1.2$$

Wahab and De Roeck (1999) implemented the mode shape curvature method to a real structure, the Z24 Bridge in Switzerland. In this study, they presented a damage indicator named as curvature damage factor (CDF), which equals to the difference in curvature before and after damage averaged over a number of modes. They presented modal curvature based methods are promising method for damage identification in terms of locating damage.

After an extensive literature survey, it can be concluded that some studies indicate that mode shape based methods (direct usage or its derivatives such as mode shape curvature) are more robust than those based on natural frequency shifts [Kim and



Stuccs 1995, Salawu and Williams 1995, Shi et al. 2000]. However, Ren and De Roeck (2002) discuss these methods usefulness structures.

### **1.1.3 Flexibility matrix based methods**

As it is well known, flexibility is the inverse of the stiffness matrix and therefore depends the applied static force to the corresponding structural displacement. Accordingly, the dynamically measured flexibility matrix  $[F]$ , can be found using Eq. 1.3;

$$[F] = [\phi][\Delta]^{-1}[\phi]^T \quad 1.3$$

where  $[\phi]$  and  $[\Delta]$  represents the matrix of measured mode shapes and the diagonal matrix of associated measured modal frequencies squared, respectively. Li et al. (1999) suggested a method for damage identification of tall buildings and chimneys which are relatively slender structures. According to proposed method, structures were modeled as cantilevers which provide the opportunity as utilizing the flexibility matrix in a least squares solution approach. The damage in each story represented by two variables and therefore the number of required modes were limited and successfully identified. However, they did not apply the model to more complex structural models or verified it using experimental measurements which obtained from complex structures. The effectiveness of the dynamically measured flexibility matrix method was discussed by Zhao and DeWolf (1999) by comparing the sensitivity coefficients for natural frequencies, mode shapes and also dynamically measured flexibility. A series of numerical application on a simulated five DOF spring mass system, it was found that the dynamically measured flexibility was the most sensitive to damage. On the other hand, another comparative study presented by Farrar and Doebling (1999) on a real structure (I-40 bridge over the Rio Grande, America) stated different results for dynamically measured flexibility based method. It was found that only the localization of the damage could be detected by using flexibility matrix based method in the most intensified damage scenario.

### **1.1.4 Model updating based methods**

There are various algorithms which follow model updating approach for damage identification. In the model updating based method, the first step is to establish the FEM of the structure based on the design calculations suggested by design codes in

force (initial model). For most of the cases, the initial model, which is created considering the design calculations, can not accurately predict the actual parameters and represent the responses of the interested structure, which is an obvious result of the simplifications and assumptions in the modeling process. At this point, the measured responses of the structure play a major role in order to validate the initial structural model and to update the parameters of the initial model (Sanayei et al. 2015). This model updating procedure has provided a rich source of algorithms, which are adaptable to damage identification issues, and has been attracted by various number of researchers.

Gola et al. (2001) studied the number of parameters which could be identified using sensitivity based model updating methods. They found that the theoretical number of parameters obtained by the matching of eigenvalues is equal to the number of measured resonant frequencies. However, in the case of using mode shapes instead of resonant frequencies, there is an upper limit for identifiable parameters as the number of modes times the number of degrees of freedom measured. Like Gola et al. (2001), many of the model updating based damage identification algorithms follow a procedure to match natural frequencies and mode shapes. On the other hand, damping is generally neglected due to the difficulty in well modelling it accurately. In accordance with this issue, Casas and Aparicio (1994) investigated the identification of cracking in laboratory concrete beams using a model updating technique. They found that damping was not significantly different in the cracked beams compared to the uncracked beams. Furthermore, not only using the damping but also using the mode shapes are not as much as attractive than using natural frequencies in model updating based damage identification. Furthermore, using the natural frequencies provide the type, number and also location of damage (Level 1 and 2) (Wahab et al. 1999, Jang et al. 2002, Cobb and Liebst 1997).

As a model updating method, usage of FRF measurements instead of direct modal properties has been attracted by various researchers (Esfandiari et al. 2009, Rahmatalla et al. 2012, Chesné and Deraemaeker 2013, Gang et al. 2014). It provides an important advantage is that the FRF based methods do not require the extraction of modal properties. Moreover, FRF data provides more information in a certain desired frequency range.

However, FRF based algorithm has some disadvantages that it is more complex mathematically and such methods could be computationally very expensive for large–

scale structures Palencia et al (2015). Garcia–Palencia and Santini–Bell 2013 and Garcia-Palencia et al. 2014 presented FRF based model updating procedure using even the damping matrix for not only damage localization and but also quantification (Level 1 to 3).

### **1.1.5 Wavelet transform methods**

As aforementioned above, damage identification using shifts in natural frequencies and modeshapes is very popular method. However, the shifts are mostly quite small, and the method performs poorly in the case of noise contaminations of the measurements (Pakrashi et al 2007). At this point, damage identification using wavelet transform provides a better and more robust methodology. Since wavelet transform methods are associated with the detection of singularities in a function or in any of its derivatives, information about the structural member in its undamaged state is not required (Pakrashi et al 2007). For the last decades, wavelet based methods are studied by various researchers but many of them focused on laboratory scale members (Liew and Wang 1998, Hou et al. 2000 and Lu and Hsu 2002).

Pakrashi et al. (2007) presented a numerical study, which targeted Level 3 damage identification as detection of the presence, location and the extent of damage of a beam element. The first natural modeshape of the beam was obtained under the simulated condition of the beam with an open crack using smeared, lumped and continuous crack model. Furthermore, a static deflected shape of the same beam under vertical static loading was also simulate. Subsequently they performed a wavelet analysis on the simulated modeshape and the static deflected shape for locating the damage. They proposed a new wavelet–kurtosis based calibration of the extent of damage for different crack depth ratios and crack positions including the effects of varying signal to noise ratio. After an experimental validation on a damaged aluminium beam with open cracks of different extent, they showed that wavelet analysis in combination with a kurtosis based damage calibration can be useful in the identification of damage to structures.

### **1.1.6 Statistical methods**

Farrar and Doebling (1999) suggested that in order to proceed in vibration based damage identification, the classical model based methods require to be support with non-model based pattern recognition methods. This understanding fueled the studies

for using novelty detection for damage identification which is concerned with the determination of any deviations in measured data. That is to say, the features derived from the measured data have a distribution with an associated mean and variance and a change in the mean and/or the variance may be an indicator for damage. Hence statistical methods provide identification of the inconsistency of new data comparing to the previous 'outlier data' (Carden and Fanning, 2004). In literature, there are lots of studies focus on damage identification any kind of methods (such as shifts in modal characteristics, neural networks etc) in combination with statistical pattern recognition. For example, Hu and Afzal (2006) concentrated change in mode shapes due to damage on timber beam structures. They proposed a statistical algorithm and showed that the algorithm is reliable for the identification of local damage under different severities, locations, and also counts.

The short review of vibration based damage identification methods showed that there is not a worldwide accepted method for using measured vibration data for damage detection, location and/or quantification. Although, many forward problems can be listed here, some of them very tough ones, which will be the concern of these dissertation, are significantly expressed below:

First, according to the literature survey carried out in the context of dissertation, there is not any algorithm which attempts to predict the remaining service life of a structure (it is so called Level 4 identification).

Second, except very limited number of algorithms, most of them are capable to detect the limited in the number of damage locations. Furthermore, a vast majority of the researches alluded above focused damage identification on laboratory scale tests and numerical simulations. Although these tests and simulations are beneficial in terms of testing proposed damage detection algorithms, they obviously would not be representative the environmental effects to which real structures are subjected to.

Although it was not directly indicated above, the algorithms can be classified based on the number of sensors they required. As it was stated by Carden and Fanning (2004), some methods used data from a large number of sensors were generally successful and the ones considering on a single or limited number of sensors, such as natural frequency based methods, were not successful for all cases. Nevertheless, the statistical pattern recognition methods can be dealt as promising in terms of using few sensors while the ambition of these pattern recognition techniques is still limited to Level 1 identification.

Although there is clearly no suspect that more sensors, and consequently more measured data, provide a better success in damage detection, the optimization of number of required sensors could be one of the most important decision-making constraints facing the structural health monitoring community.

## **1.2 Research Motivation and Objective**

A great portion of existing building stock of Turkey consists of reinforced concrete (RC) structures. A significant amount of these RC structures, which were constructed several years ago, do not satisfy the requirements of the modern seismic design codes. Although majority of these structures are legally engineered structures, even some of them are not, due to the lack of an official control mechanism, these structures mostly do not fulfil the requirements of the seismic design codes, which were in force during their construction time. Accordingly, these buildings have basic structural weaknesses such as low concrete strength, insufficient reinforcement detail, etc. and represent a significant risk in case of any seismic action. Thereby, the condition assessment of the existing structures after an earthquake is crucial for determining the residual performance of the building. Up to the present, condition assessment of the buildings after a major earthquake has been immediately carried out based on visual inspection. Although this is a required and an essential method for making decision for the current situation of the buildings, some damages could not be identified through visual inspection. For example, internal cracking or slip of the lap-splice can be hidden from view, however, their effects on the load bearing capacity of the building can be crucial and vital. From this point of view, the vibration signature of the building, which is obtained through St-Id methods, can provide significant information about the condition of the buildings.

Accordingly, in this dissertation, it is aimed to present an automated damage identification algorithm through field testing and model updating of typical full-scale 3-story existing RC buildings. In addition to that the suggested damage identification algorithm was extended in order to predict the serviceability of the structures after damage.

The dissertation is organized followingly;

In Chapter 1, literature survey on the structural identification and significantly vibration based damage identification was conducted. The significance of the dissertation was stated.

Chapter 2 presents details of the full-scale test buildings and the field tests with their results. In the context of this chapter, a series of field testing was carried out for quantifying the influence of different types and extents of structural damage on the dynamic characteristics of typical existing RC buildings. In the context of the field testing, vibration-based tests were performed before and after quasi-static reversed lateral loading cycles as well as at certain damage levels. Since the test buildings are representative of large number of substandard RC buildings, the test results would be useful for the seismic performance assessment of existing RC buildings.

In Chapter 3, a model updating based iterative damage identification was developed. In this chapter, the algorithm was examined by updating the initial model of the test structures.

In Chapter 4, the model based algorithm was adapted in order to detect, localize and quantify the damage in the buildings TB-1 and TB-2. Therefore, a Level 3 damage identification process was achieved.

In Chapter 5 Since the damage identification algorithm, introduced above, follows a model-based approach, efficiency of a simplified FEM for damage identification algorithm was discussed.

In Chapter 6, automated damage identification procedure was extended by combining with moment-rotation based nonlinear performance assessment method. By this means, it was achieved to estimate the damage levels of the members by using vibration based damage identification method. This could provide to estimate the serviceability of the structure after damage.

Finally, Chapter 7 presents the conclusions and recommendation along with the summary of the dissertation. The consequences from the field tests clearly showed the risk about the missing the structural damages during visual inspections after earthquake and utilization of dynamic testing accompanying with visual inspection could be a promising method for more realistic assessment of structural damages after seismic events. Followingly, it was presented that eventhough noise components in the signal and technical limitations resulted missing the first natural frequencies of the

buildings, the FRF based damage identification process provided successful damage identification. The method estimates the rotational stiffness degradation on the members due to damage. Although the updating of initial and boundary conditions (stiffness degradation) is crucial to figure out the residual performance of the building after damage, this requires to re-analyse the model after damage identification. Instead of that, a practical tool was suggested as the extension of the damage identification process. The nonlinear moment-rotation based damage assessment procedure was adapted to the damage identification algorithm and by this means, the member damage level and accordingly serviceability of the structure after damage could be estimated.







## **2. EXPERIMENTAL STUDY**

### **2.1 Description of the Test Site**

Experimental phase of the study, which includes vibration-based tests in combination with the quasi-static reversed cyclic loading tests of 2 full-scale RC buildings, was carried out in Fikirtepe district, Kadikoy, Istanbul (Figure 2.1). The existing building stock in Fikirtepe consists of thousands of sub-standard RC and masonry structures, which were constructed several years ago without an appropriate engineering design, practice, and control. Moreover, according to Turkish Seismic Design Code (TSDC) (2007), Fikirtepe district lies in seismically active zone of the country and the effective ground acceleration is 0.4g. Considering these factors, Fikirtepe district had been declared as a high seismic risk area and was abandoned for reconstruction process on mass scale by the Urban Transformation Law (Law No.6306 on the Transformation of Areas Under Disaster Risk) (UTL) (2012). Existing of hundreds number of evacuated sub-standard RC buildings promoted the research team of the project for implementing the field tests on available the RC buildings in Fikirtepe district. After a short-term investigation in the district, due to the various condition of the building such as its location, structural characteristics, meet the requirements of the field tests, the RC building shown in Figure 2.2a was selected for implementing the test program.

Due to the technical limitations of the test equipment, including the limitations of the load capacities of the hydraulic actuators and the load cells used for quasi-static loading, limited number of the sensors, etc., the existing building was demolished partially, and the remaining part was introduced as Test Building 1 (TB-1) (as shown in Figure 2.2b). As seen in Figure 2.2b, non-structural walls were also demolished, and plaster layers of the columns and beams were then scraped off not to interfere with the structural system. Subsequently, the test site was arranged for construction of the reaction wall and Test Building 2 (TB-2), as shown in Figure 2.2b. Since the TB-1 had unreinforced column footings with approximately 0.15 m thickness, a 0.60 m thick mat foundation not only supported the reaction wall and TB-2, but also TB-1 was

constructed. The reaction wall with a 7.0 m high, 0.50 m thick and W-shaped cross-section in plan was designed and constructed as so providing the sufficient stiffness and lateral load capacity for the buildings to be tested consecutively, only by repositioning of three hydraulic actuators (Comert et al. 2016).

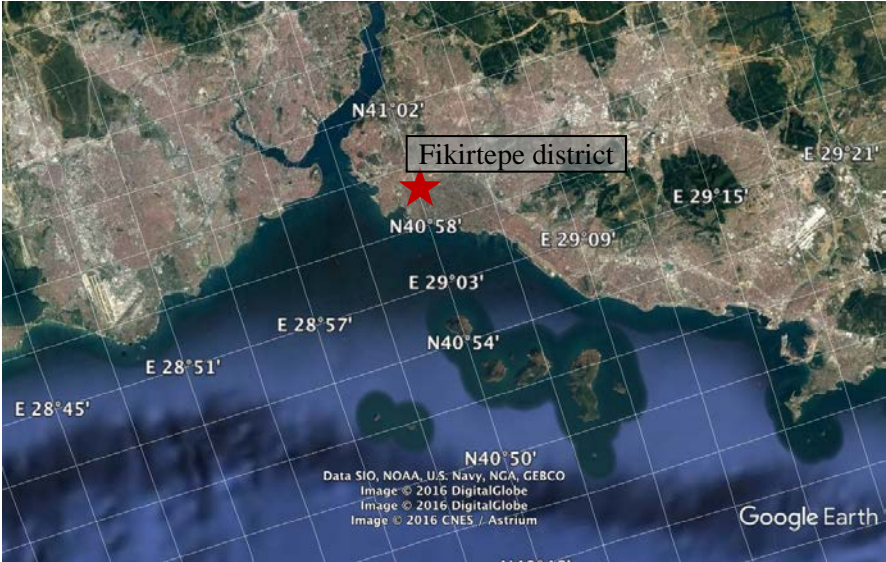
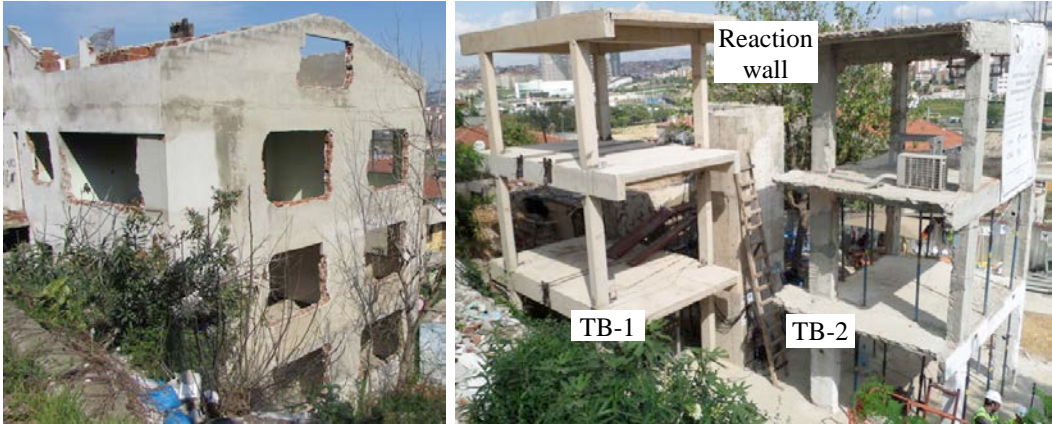


**Figure 2.1 :** Fikirtepe district.

Layout plan of the test site is shown in Figure 2.3. More detailed information about designing of the TB-2, mat foundation and reaction wall, arrangement of the test site and construction process can be found in companion studies of Comert et al. 2016 and the Comert 2017.



(a)

(b)

**Figure 2.2 :** (a) Existing RC building, (b) TB-1, TB-2 and reaction wall at the same site (Goksu et al. 2015).



column surfaces while the adjacent bay of the building was demolishing. Average concrete compressive strength ( $f_c$ ) was obtained as 13 MPa by uniaxial loading test of 100mm  $\times$  200mm cylindrical cores taken from each story. The reinforcement of the building consisted of plain reinforcing bars. The average yield stress of the longitudinal and transverse reinforcing bars, which were obtained by uniaxial tensile tests of the steel samples extracted from demolishing part of the building, were 280 MPa and 370 MPa, respectively.

The beams had two 10mm diameter longitudinal bars at the top and one 14mm diameter and two 12mm diameter longitudinal bars at the bottom of the support cross-sections. The cross-section dimensions of the columns of the third story were different than the given in Figure 2.4 and were approximately 250mm  $\times$  400mm. The Column S11 in the third story had a different reinforcement cage as four number of 16mm diameter longitudinal bar then the others as four number of 16mm diameter longitudinal bar. The beams and the columns had 8mm diameter stirrups at approximate spacing of 300mm. As commonly observed in the sub-standard existing structures, there were not any confinement region at potential plastic hinge locations of the columns and beams and the hooks were bent at 90° instead of 135°. In addition to these poor reinforcement detailing, formation of the cover concrete, significantly around the reinforcing bars, alignment of the reinforcing bars throughout the structural members and the concrete compaction was also problematic (Comert et al. 2016).

The average axial load level of the first story columns was approximately 6-10 % of the axial load capacity of the columns without the consideration of longitudinal reinforcing bars. As an unusual situation for sub-standard existing RC structures, the columns were slightly stronger than beams. These characteristics of the RC frames lead to the strong column-weak beam type of failure mechanism under seismic actions. This failure mechanism is a favorable mechanism compared to its alternative, the weak column-strong beam mechanism, which tends to sustain much more severe damages compared to others (Ilki and Celep 2012; Tapan et al. 2013).

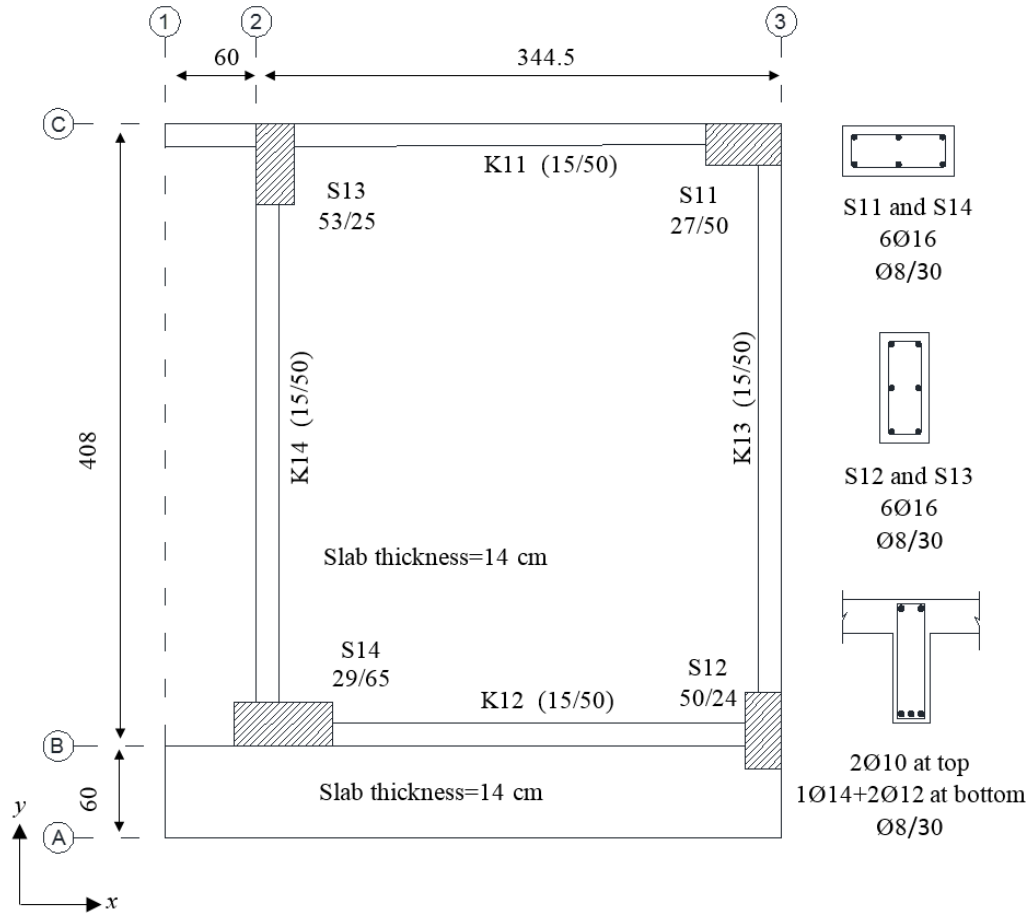


**Figure 2.4 :** Plan view and reinforcement cage of the columns and beams of TB-1 (dimensions in cm).

### 2.2.2 Test building 2

Test Building 2 was designed and constructed at the same test site with TB-1 to represent the sub-standard buildings in Turkey. Accordingly, TB-2 was designed with smaller cross-sections of columns to be achieved the intended weak column-strong beam type of failure mechanism which observed in existing sub-standard RC structures after major earthquakes. The typical plan view and the reinforcement cages of the beams and columns are given in Figure 2.5. As seen in this figure, dimensions of the typical floor plan were 4.30m × 3.70m. In order to increase the axial load level of the columns, slabs were intentionally designed to be a thickness of 0.18m. Furthermore, the slabs and the beams with 200mm × 500mm cross-sections were elongated as 1m long overhangs on both sides of the building, as well. The height of each story was 3 m.

The average concrete compressive strength ( $f_{cm}$ ) of 10 MPa was obtained through uniaxial testing of 150mm  $\times$  300mm cylinders on 28th day after pouring. The reinforcement of the building consisted of plain reinforcing bars and had an average yield stress of 350 MPa obtained by uniaxial tensile tests. In addition, poor reinforcement detailings, including starter bars of the columns with 180° hooks at the end, closed stirrups with 90° hooks and lack of confinement region at potential plastic hinge locations, were intentionally chosen with the same object of designing and constructing a sub-standard RC structure.

### **2.3 Instrumentation of the Buildings**

Test setup of the vibration based tests consisted of accelerometers, data acquisition system and an eccentric-mass shaker. The vibration response of the buildings was monitored through 6 uniaxial piezoelectric voltage accelerometers. The accelerometers had a wide frequency and acceleration range (DC to 1000 Hz and  $\pm 0.5g$ , respectively) and could capture accelerations as low as  $1.10^{-7}$  g. from 0.2 Hz and higher. The data logger, which provides signal conditioning, 24-bit analog-to-digital conversion with anti-aliasing filter, and GPS time stamping for synchronization across multiple nodes, were used for data acquisition. The data logger was required a computer connection to monitor the real-time data, and to record the data.

A uniaxial accelerometer was mounted at the center of each story as well as mat foundation (A2, A4, A5 and A6). Two additional accelerometers were mounted on 2 opposite corners of the third story (A1 and A3) (Figure 2.6). This instrumentation scheme provided to identify the only translational modes. The configuration given in Figure 2.6 was illustrated for capturing the acceleration response of the buildings in  $x$  direction. For capturing the acceleration response of the buildings in  $y$  direction, only the shaker and the accelerometers at the centers of the slabs (i.e. A2, A4, A5 and A6) were rotated 90°. As seen in Figure 2.6, each accelerometer was mounted on the buildings through high strength metal cubes. First, the metal cubes were firmly mounted on the floor of the buildings by means of high modulus resin. Accelerometers were then fixed to one face of the metal cube by means of a screw (Figure 2.7).

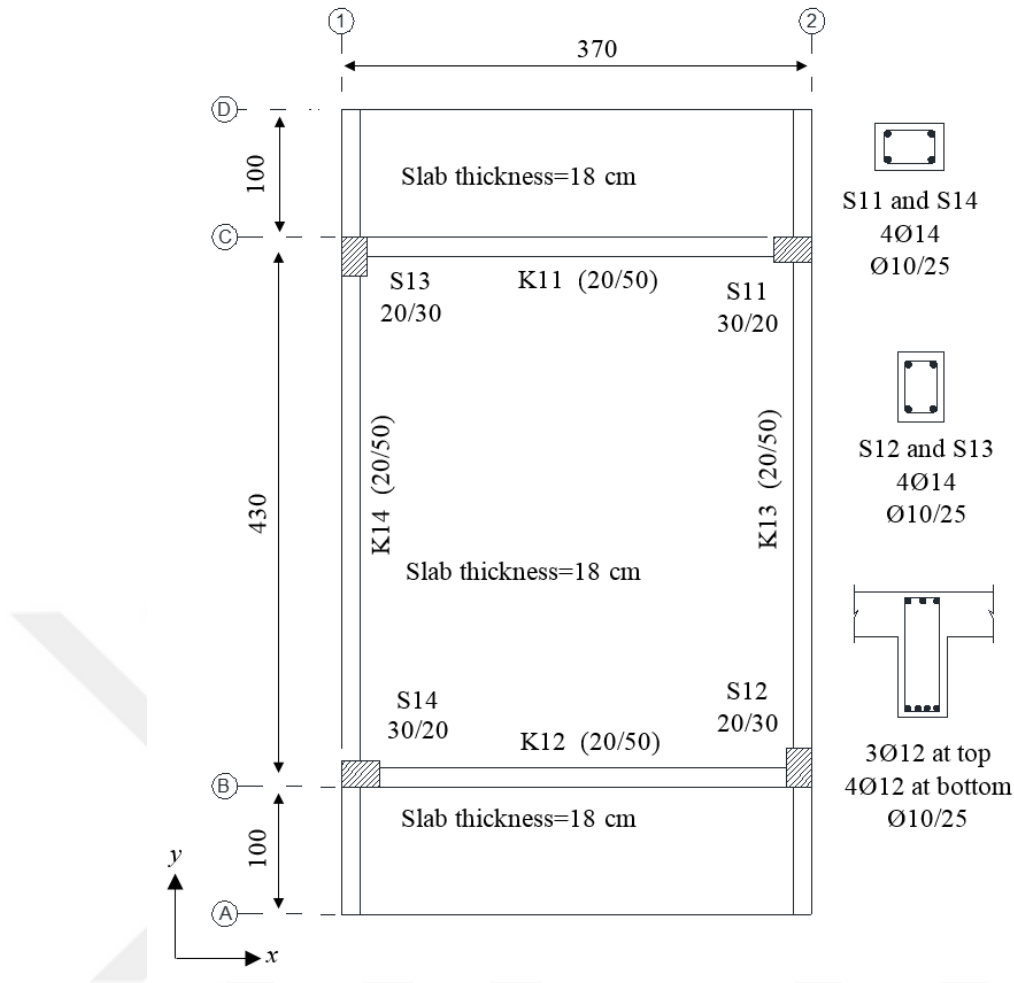


**Figure 2.5 :** Plan view and reinforcement cage of the columns and beams of TB-2 (dimensions in cm).

An eccentric-mass shaker was used to excite the buildings during the forced vibration tests (Figure 2.7 and Figure 2.8). As seen in this figure, the shaker, had 150 kg weight, consisted of three main components as servo engine, 8 disks and drive belt mechanism. Four out of eight disks were situated on the front shaft and the other four were situated on the back shaft. Each disk was made of integration of two different semi-circle cross-sectional materials. Figure 2.8 displays the different materials of the disk. Since these two different materials had different density values, the mass center of each disk had an eccentricity from the center of shaft (Figure 2.8a). Each disk was designed to be had 0.0625 kgm eccentricity value ( $8 \text{ disk} \times 0.0625 \text{ kgm} = 0.5 \text{ kgm}$  in total). The counter rotation of front and back shafts provided a sinusoidal force ( $F$ ) in a horizontal plane to the test structures in proportion to the eccentricity ( $e$ ) and square of the its operating rotational frequency ( $w$ ) in rad/s ( $F = e \times w^2$ ).

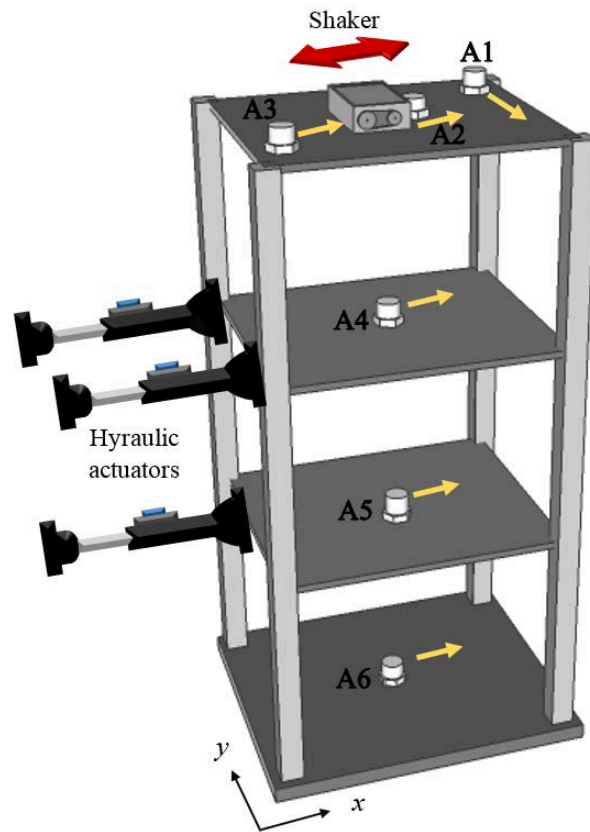


**Figure 2.6 :** Instrumentation of the buildings.

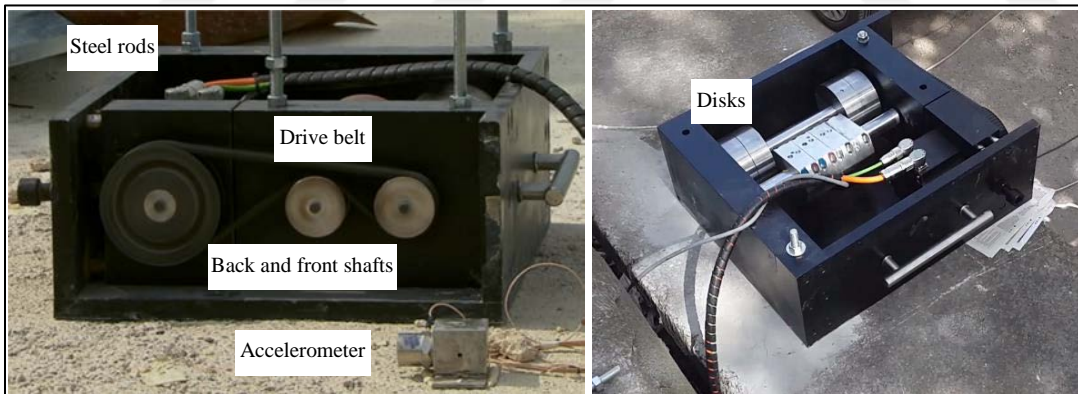
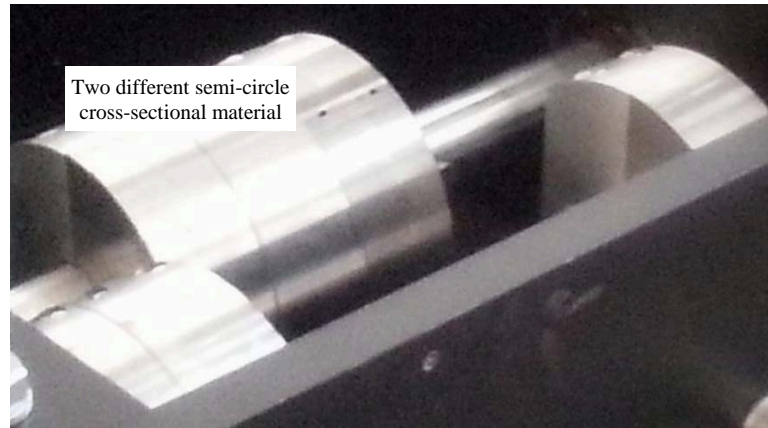


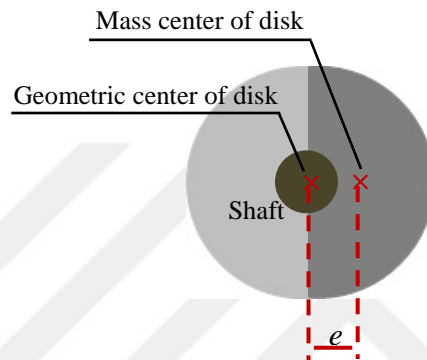
**Figure 2.7 :** Eccentric mass shaker (Goksu et al. 2015).

The shaker has a control unit and the control unit was connected a computer via ethernet cable. Hence the shaker was contolled through a software, which provides the user to operate the shaker at certain frequency values in its operating frequency range (1 to 100 Hz) for certain time periods. According to the maximum operating frequency value of 100 Hz., maximum force capacity of the shaker was 200 kN. It should be noted that the shaker was strongly anchored to the slab by means of high-strength steel rods (Figure 2.7).





(a)



(b)

**Figure 2.8 :** Structure of eccentric mass shaker (a) disks, (b) components of disks.

## 2.4 Vibration Based Test Program

Ambient and forced vibration tests were carried out before and after quasi-static lateral loading cycles. The ambient vibration tests were implemented for the building TB-2 before and after quasi-static reversed cyclic loading in both  $x$  and  $y$  directions and also at a certain damage state for only in  $x$  direction. The forced vibration tests were carried out for both buildings before and after quasi-static loading in both  $x$  and  $y$  directions. Additionally, for the building TB-2, forced vibration test (in  $x$  direction) were also performed at a set of certain damage levels with the aim of quantifying the rate of change of dynamic characteristics with gradually increasing structural seismic damage. The quasi-static loading was implemented to the buildings only in  $x$  direction in terms of incrementally increasing reversed lateral displacement cycles. These cycles were performed using three servo-controlled hydraulic actuators. The actuators, which had 300 kN load and 800 mm displacement capacities, were mounted on the reaction wall and attached to the buildings at first and second story slab levels (Figure 2.6). This configuration of the actuators, using two actuators on the second story slab level

instead of using one actuator at each story level, were preferred in order to prevent any possible torsional effects during lquasi-static loading. Attachment of the actuators to each slab was achieved by bolting the plate of the actuator swivel-head to one of two steel plates, which were located at outer faces of the beams spanning in transverse direction of the loadings. The steel plates were connected using post-tensioned threaded steel rods, which run top and bottom of the slab and pass through holes drilled on beams (Comert et al. 2016), (Figure 2.9). This demountable connection system of the actuators was intentionally designed since the vibration based tests required to detach of the hydraulic actuators from the building. This was done to provide that the dynamic characteristics of the buildings would not be affected from the presence of actuators. It should be noted that the buildings had been unloaded, before the hydraulic actuators were demounted. Targeted damage levels, at which the vibration based test were conducted, were accomplished by pushing and pulling the buildings to specific displacements. These displacement cycles were applied considering specific drift ratio levels, which were defined as the ratios of the lateral displacement of the first story to the height of this story.



**Figure 2.9 :** Attachment of the actuators.

Table 2.1 presents the details of the vibration based test program including the drift ratios (d.r.) where the ambient and forced vibration tests were performed and orientation, operating frequency range, and frequency increments of shaker, which were considered during the forced vibration tests. Since, the first 6 modal frequencies

of the buildings were expected to be in the range of 1–8 Hz, the frequency increment steps of the shaker were set to be low (0.05 Hz) up to around 8 Hz, in order to assure scanning these frequencies more sensitively.

It should be noted that the vibration tests were carried out at certain damage states after the buildings were unloaded. This was intentionally done to capture the vibration response of the buildings at their new linear limits.

**Table 2.1 : Program of the vibration test.**

Building	Damage situation	Testing direction	Forced vibration test		Ambient vibration test
			Shaker operating frequency range (Hz)	Increment steps (Hz)	
TB-1	Undamaged	<i>x</i>	1.5-8	0.05	-
		<i>y</i>	8-15	0.10	-
	Damaged (1.5 % d.r.)	<i>x</i>	1.5-15	0.05	-
		<i>x</i>	1.5-8	0.05	-
		<i>x</i>	8-15	0.10	-
		<i>y</i>	1.5-8	0.05	-
TB-2	Undamaged	<i>x</i>	8-15	0.10	✓
		<i>y</i>	1.5-8	0.05	✓
	Damaged (0.5 % d.r.)	<i>x</i>	8-15	0.10	✓
		<i>x</i>	1-10	0.05	✓
	Damaged (1.0 % d.r.)	<i>x</i>	1-5	0.05	-
		<i>x</i>	5-8	0.10	-
	Damaged (1.5 % d.r.)	<i>x</i>	1-5	0.05	-
		<i>x</i>	5-8	0.10	-
	Damaged (2.0 % d.r.)	<i>x</i>	1-5	0.05	-
		<i>x</i>	5-8	0.10	-
	Damaged (3.0 % d.r.)	<i>x</i>	1-8	0.05	✓
		<i>x</i>	8-15	0.10	✓
		<i>y</i>	1-8	0.05	✓
		<i>y</i>	8-15	0.10	✓

## 2.5 Damage States of the Buildings at the Time of Vibration Based Test

The structural damage due to quasi-static reversed cyclic loading was observed at all target 1<sup>st</sup> story drift levels that vibration based test were implemented. The damages were examined before the vibration based test were initiated.

### 2.5.1 Damage States of the Building TB-1

The quasi-static cyclic loading was implemented to the building up to 1.5% d.r. due to the safety reasons. The base shear-1<sup>st</sup> story drift ratio relationship of the building TB-1 is given in Figure 2.10. The vibration based test stages were also marked in this figure. During the quasi-static loading, owing to the significant contribution of

concrete to shear capacity that was higher than the subjected shear forces, any shear damage was not experienced on the building despite the 300 mm stirrup spacing. Hence, the overall response of the building was governed by nonlinear flexural behavior at the critical end regions of beams and columns (Comert et al. 2016). At the beginning of the quasi-static loading, bending cracks was first observed at the support regions of the first-story beams parallel to the loading direction (K11 and K12 in Figure 3.4). Afterwards, bending cracks started to accumulate upper and lower ends of the first-story columns S11 and S14 (at around 0.5 % d.r.) (Figure 2.11). With the following displacement cycles, the level of damage at the beam support regions was intensified and, wide bending cracks, crushing of concrete and subsequently spalling of concrete cover were observed. This is due to the extremely poor thickness of concrete cover of the beams, which was at around 5 mm (Comert et al. 2016). Consequently, buckling of the lower longitudinal reinforcing bars of the beams which were parallel to the loading direction (K11 and K12) were occurred (at around 1.0% d.r.) (Figure 2.12).

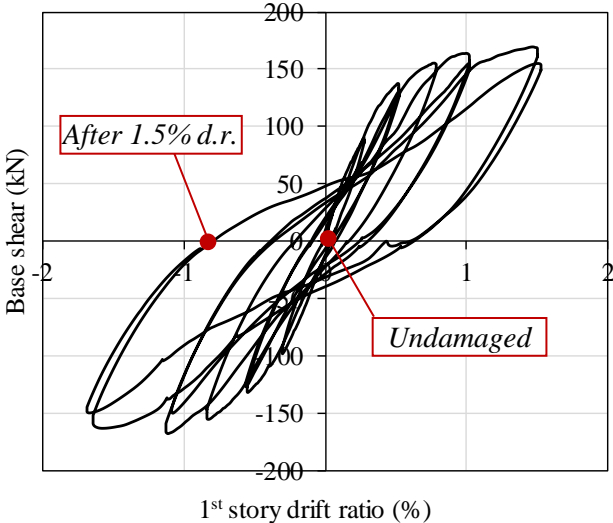


**Figure 2.10 :** Base shear-1<sup>st</sup> story drift relationship of the building TB-1.



**Figure 2.11** : Flexural cracks observed at column S13 and the beam K11 (Comert 2016).



**Figure 2.12** : Buckling of bottom longitudinal bars of the beam K12.

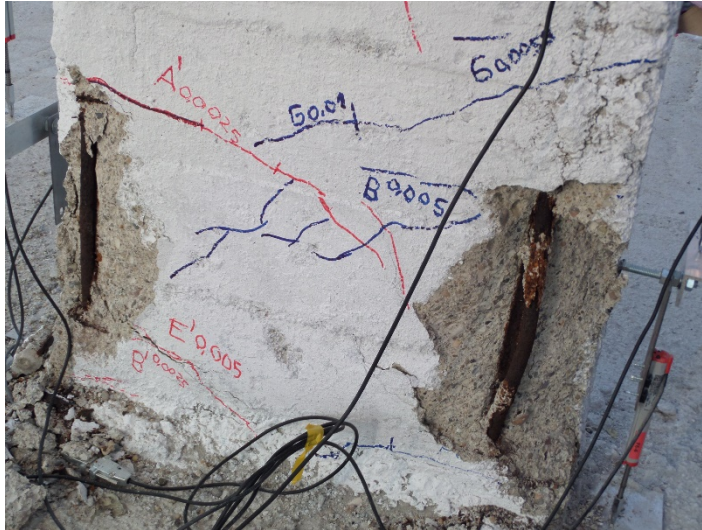


**Figure 2.13 :** Buckling of longitudinal bars of the column.

Right after the buckling of the longitudinal bars of the beams K11 and K12, extensive damage at the bottom ends of the 1<sup>st</sup> story columns S11 and S14 was started to observe and subsequently buckling of the longitudinal reinforcing bars were occurred (Figure 2.13). Just to clarify the damage state of the building, wide spacing of transverse reinforcing bars, which were around 300 mm, and the poor quality of the concrete cover in the columns and beams would have be reason for buckling of the longitudinal reinforcing bars. Moreover, it is worth to say that the columns S11 and S14 were stiffer and stronger in the loading direction due to their layout on the plan of the building (Figure 2.4).



**Figure 2.14 :** Slight damage on the columns S12 (Comert 2016).

Hence, no significant damage apart from flexural cracking was observed on the 1<sup>st</sup> story columns S12 and S13 (Figure 2.14). Similarly, any significant damage was

experienced on the beams and columns of the 2<sup>nd</sup> and the 3<sup>rd</sup> stories. Consequently, as seen in Figure 2.10, at the end of the loading, approximately 15% strength degradation was observed. More detailed information about the damage states of the buildings can be found at the study of Comert et al. 2016.

### 2.5.2 Damage states for the building TB-2

The quasi-static cyclic loading was implemented to the building up to 4% d.r., however, the vibration based test were terminally performed at 3% d.r. due to the safety reasons. The base shear force-1<sup>st</sup> story drift ratio response is given in Figure 2.15. Additionally, the vibration based test stages were also marked in this figure.

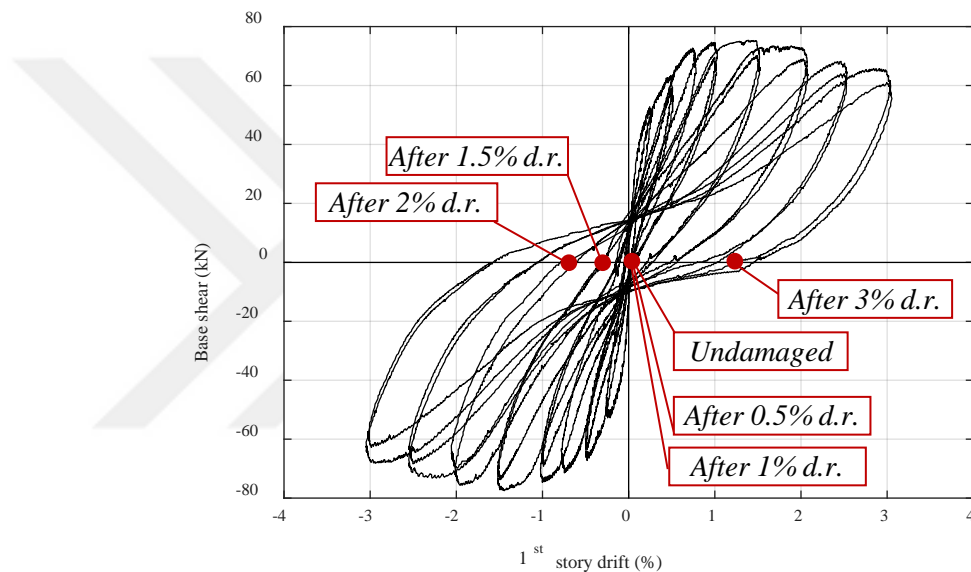


**Figure 2.15 :** Base shear force-1<sup>st</sup> story drift relationship and the vibration based testing stages of the building TB-2.

As experienced in the building TB-1, mainly due to the significant contribution of concrete to shear capacity, the building failed as a result of flexural effects. The first flexural cracks started at upper and lower ends of the 1<sup>st</sup> and 2<sup>nd</sup> story columns at around 0.25% and 0.5% drift ratio, respectively (Figure 2.16). With the following loading cycles, the crack widths increased, and concrete crushing were observed on column S11 at around 1.5 % drift ratio and subsequently cover spalling was experienced on the 1<sup>st</sup> story columns S11 and S13 at around 2.5% d.r. Throughout the quasi-static loading, almost no damage without minor flexural cracking was observed on the columns and beams of the 2<sup>nd</sup> story and beams of the 1<sup>st</sup> story, while no damage was observed on the columns and the beams of the 3<sup>rd</sup> story. All columns in the 1<sup>st</sup> story failed due to flexural effects. Inbrief, a distributed damage evolution occurred in

the building and the lateral load bearing capacity of the building was degraded approximately 40%. The damage propagation throughout the loading in the 1<sup>st</sup> story column S11 is presented in Figure 2.17. The intensified damage at the lower end of the columns can be seen in this figure.



**Figure 2.16 :** The first observed flexural cracks (a) Column S12 (the 1<sup>st</sup> story), (b) Column S14 (the 2<sup>nd</sup> story), (Comert 2016).



**Figure 2.17 :** Damage propagation on the 1<sup>st</sup> story column S11 of the building TB-2 (Goksu et al. 2015).



## 2.6 Vibration Based Tests

### 2.6.1 Ambient vibration test survey

As aforementioned, modal characteristics of the building TB-2 were determined through ambient vibration testing. As it is well-known, the basic idea for this testing method is that to identify the structure on the basis of measurements of the response of the structure to the natural loading instead of excited the structure artificially. The natural loading, which causes the continuous motion and vibrations on the all buildings, includes the ground-borne vibrations, wind load, traffic loads etc. For the buildings TB-2, the main sources of the vibrations were various construction projects, the closest one was 50m far away, a very busy highway passing approximately 350m far away from the test site and certainly the tremor of the plates. Figure 2.18 shows the test sites and the vibration sources.



**Figure 2.18 :** Test site and sources of vibrations.

As given in Table 2.1, ambient vibration tests were carried out for only the building TB-2 before and after quasi-static loading for both in  $x$  and  $y$  directions and at a certain damage state for only in  $x$  direction, as well.

System identification of the building for the undamaged and damaged states was carried out in frequency domain using the enhanced frequency domain decomposition (EFDD) method introduced by Brincker et al. (2001a,b). As it is very well-known, the EFDD follows an output-only modal identification algorithm and yields natural frequencies, modal damping ratios and mode shapes, as well. Before giving the

analysis results of the ambient vibration tests, a brief summary of frequency domain analysis was presented followingly.

### 2.6.1.1 Theoretical background

The following mathematical manipulations were intoruced by Brincker et al. (2001a,b). EFDD method basically computes singular value decomposition (SVD) of the power spectral density (PSD) matrix of output channels at discrete frequencies. Accordingly, the first step of the method is to implement a Discrete Fourier Transform (DFT) on the raw time data (output channels) to obtain the Power Spectral Density Matrices (Equation 2.1).

$$G_{yy}(\omega) = H(\omega)^* G_{yy}(\omega) H(\omega)^T \quad 2.1$$

where  $G_{xx}(\omega)$  is the PSD matrix of the inputs,  $G_{yy}(\omega)$  is the PSD matrix of the outputs,  $H(\omega)$  is the frequency response function (FRF) matrix, and the superscripts \* and  $T$  denote the complex conjugate and transpose, respectively. The FRF matrix can be defined in terms of poles,  $\lambda$  and residues,  $R$ ;

$$H(\omega) = \sum_{k=1}^m \frac{[R_k]}{j\omega - \lambda_k} + \frac{[R_k]^*}{j\omega - \lambda_k^*} \quad 2.2$$

$$\lambda_k = -\sigma_k + j\omega_{dk} \quad 2.3$$

where  $m$  is the total number of modes,  $\lambda_k$  is the pole of the  $k^{th}$  mode,  $\sigma_k$  the modal damping constant and  $\omega_{dk}$  the damped natural frequency of the  $k^{th}$  mode. It should be noted that the theoretical background of the FRF is explained briefly in following chapters. The PSD matrix in equation (2.1) can be expressed as in equation 3.4 using Heaviside partial fraction theorem for polynomial expansions. It is assumed that the input is a zero-mean white noise and random in both time and space which means it is PSD function is a constant.

$$G_{yy}(\omega) = \sum_{k=1}^m \frac{[A_k]}{j\omega - \lambda_k} + \frac{[A_k]^*}{j\omega - \lambda_k^*} + \frac{[B]}{-j\omega - \lambda_k} + \frac{[B_k]^*}{-j\omega - \lambda_k^*} \quad 2.4$$

In the case of a lightly damped, the output PSD matrix can be written as the following final form;

$$G_{yy}(\omega) = \sum_{k \in Sub(\omega)}^m \frac{[d_k \psi_k \psi_k^T]}{j\omega - \lambda_k} + \frac{[d_k^* \psi_k^* \psi_k^{*T}]}{j\omega - \lambda_k^*} \quad 2.5$$

where  $k \in \text{Sub}(\omega)$  is the set of modes that contribute at the frequency and where  $\psi_k$  is the mode shape and  $d_k$  is a scaling factor for the  $k^{\text{th}}$  mode. This form of the output PSD matrix,  $G_{yy}(\omega)$  at discrete frequencies  $\omega = \omega_i$ , is then decomposed through the SVD technique (Equation 2.6).

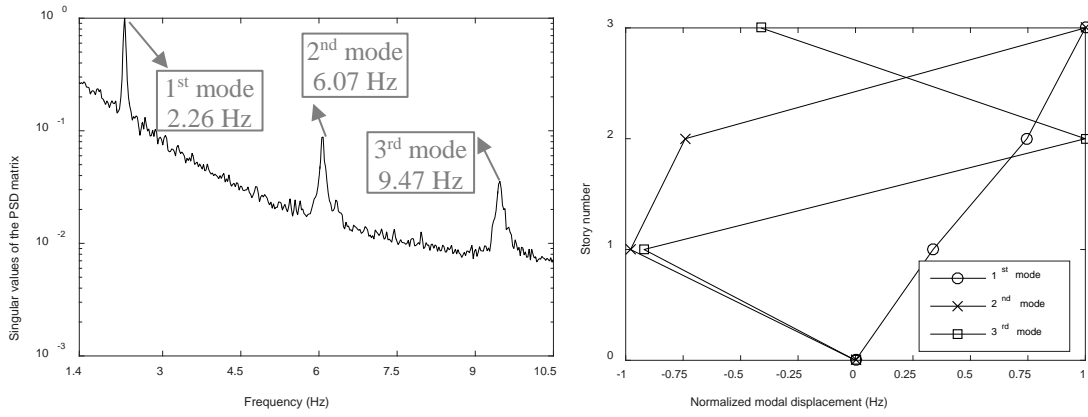
$$G_{yy}(\omega) = U_i S_i + i U_i^H \quad 2.6$$

Where  $S_i$  is a diagonal matrix containing the scalar singular values  $s_{ij}$  and the matrix  $U_i = [u_{i1}, u_{i2}, \dots, u_{im}]$  is a unitary matrix containing the singular vectors  $u_{ij}$ . The singular vectors in equation (2.6) is an estimation of the mode shapes, and the corresponding singular values are the auto spectral densities of the SDOF system introduced in equation (2.5).

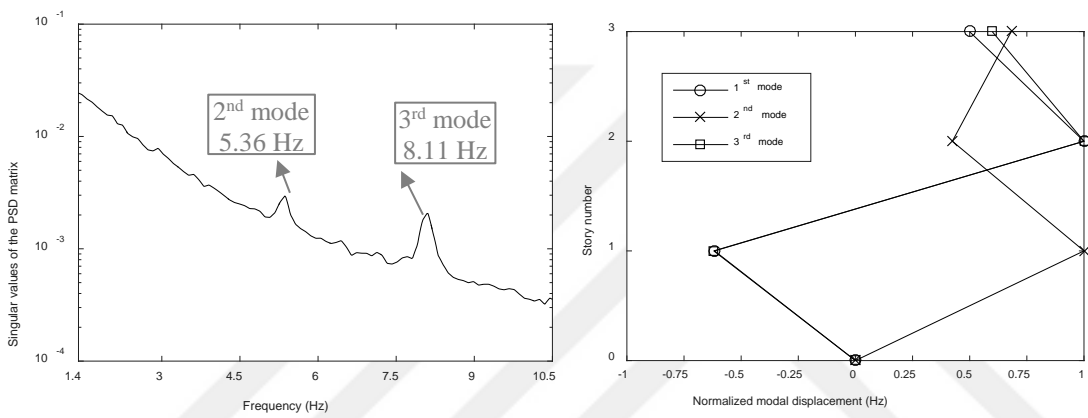
The SDOF Power Spectral Density function identified around a peak of resonance is taken back to the time domain using the Inverse Discrete Fourier Transform (IDFT) and the auto and cross-correlation functions are then derived. Hence, the frequency and the damping are estimated from the logarithmic decrement of the corresponding SDOF autocorrelation functions. More detailed information can be found (Brincker et al 2001a,b).

### 2.6.1.2 System identification results

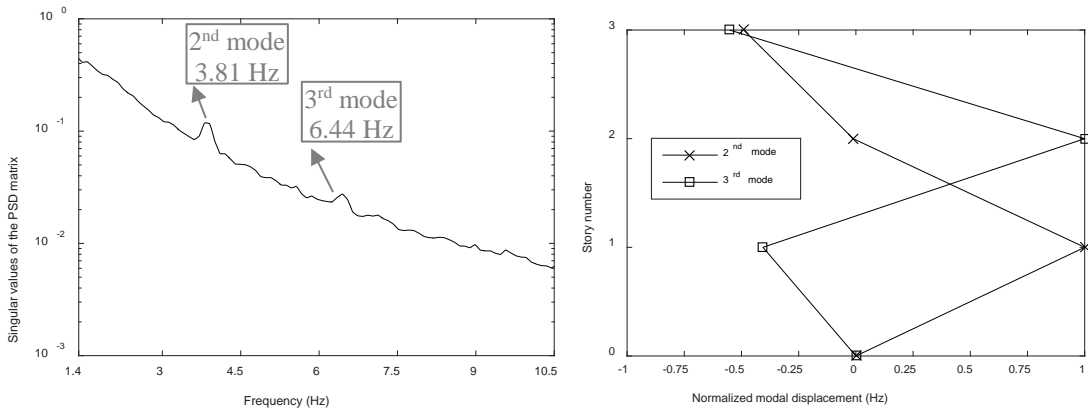
For the present case, the sampling frequency of the data was selected to be 100 Hz. The PSD relationships of the output channels were obtained utilizing a hanning window to minimize the leakage effects and number of the fast fourier transform points as 1024. Hence, the singular values of the PSD matrix of the response were obtained for undamaged and damaged states of the building in Figure 2.19 and Figure 2.20. In addition to that the mode shapes in  $x$  and  $y$  directions are also displayed. Peaks corresponding to the modal frequencies of the building were shown on these figures.



(a)

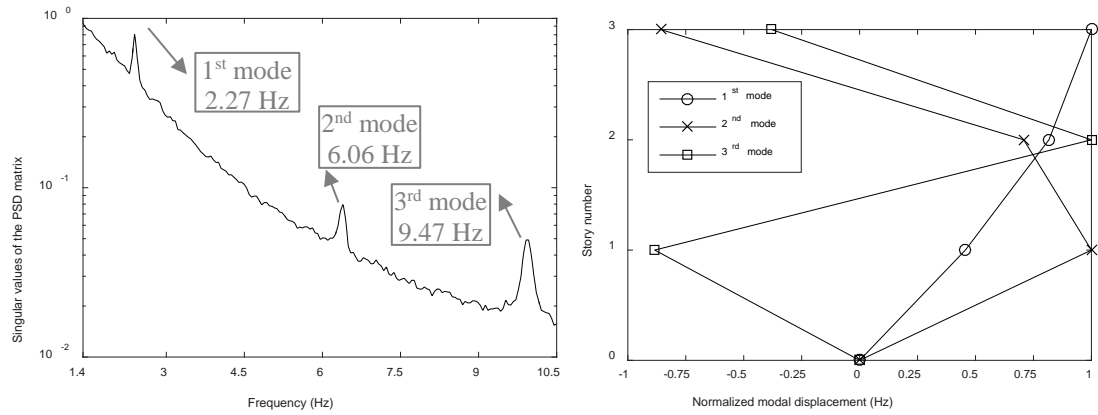


(b)

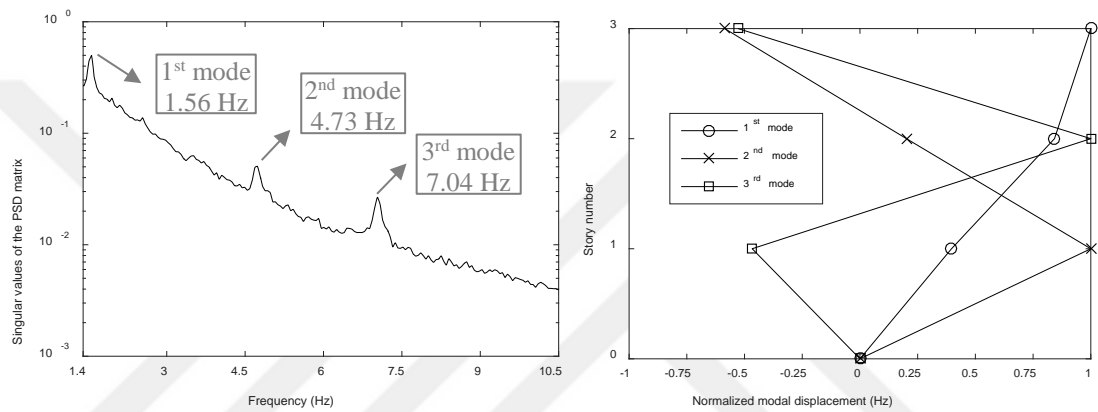


(c)

**Figure 2.19 :** Modal frequencies and mode shapes of building TB-2 in x direction, a) undamaged state, b) after %0.5 d.r. and c) after 3% d.r.



(a)



(b)

**Figure 2.20 :** Modal frequencies and mode shapes of building TB-2 in y direction, a) undamaged state, b) after 3% d.r.

However, the magnitudes of the peaks displayed in Figure 2.19 and Figure 2.20 for the damaged cases were significantly weak. This can be attributed the increasing damping forces of the building due to the increasing damage, for instance, increase in friction between the crack interfaces (Inci et al. 2017). Therefore, this complication in the identification of resonant frequencies was discarded by examining the coherence function of the responses (Figure 2.21, Figure 2.22). As seen in these figures, the resonant frequencies can be noticed with ease through coherence functions and were well-matched with the ones determined through EFDD algorithm. It should be noted that the first frequency peaks for some of the damaged cases decreased under the frequency value of 1.4 Hz and could not be captured due to technical limitations (Inci et al. 2017 and Goksu et al. 2015).

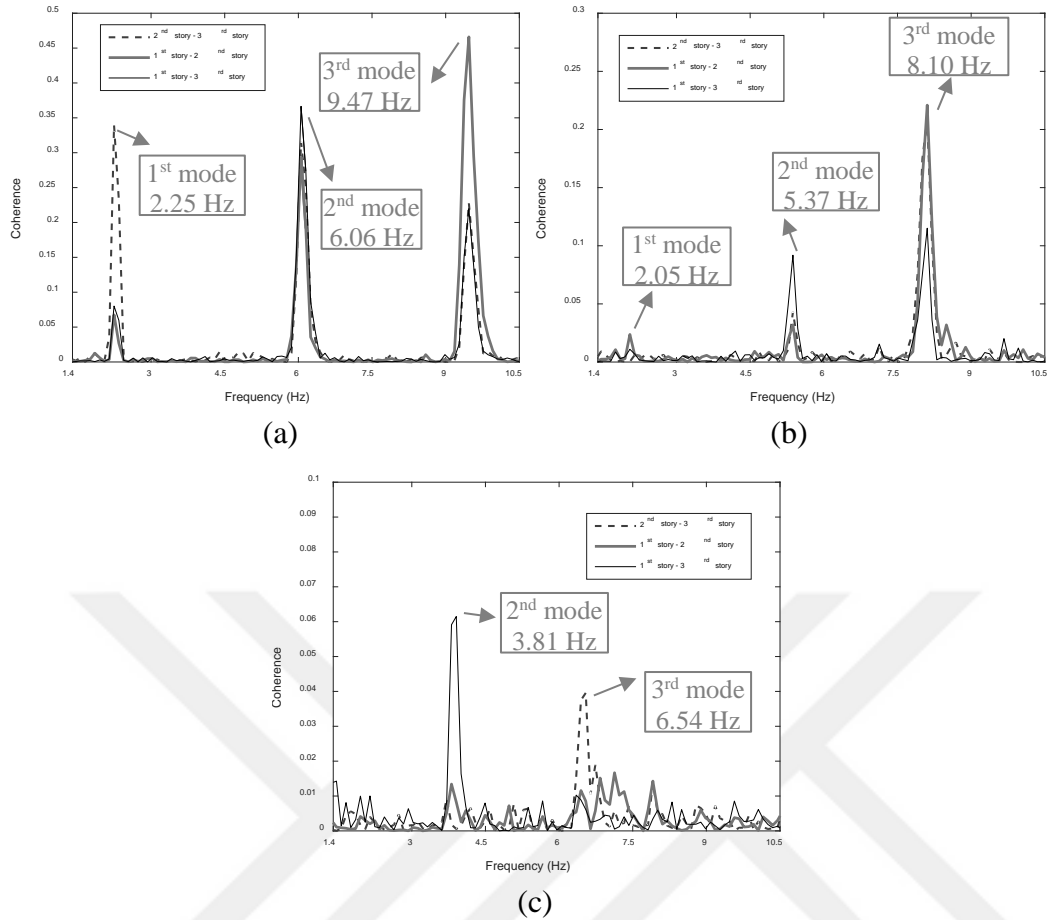


**Figure 2.21 :** Coherence functions of the building TB-2 in x direction, a) undamaged state, b) after %0.5 d.r. and c) after 3% d.r.

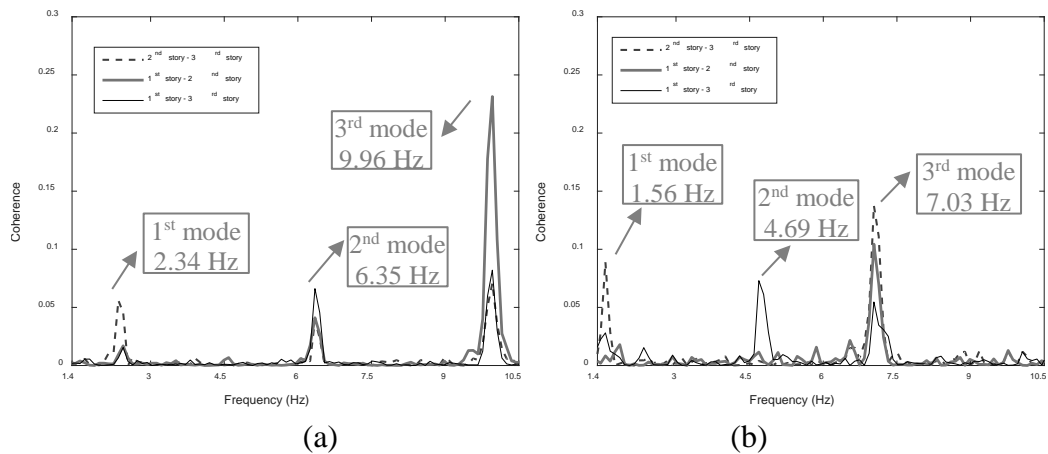


**Figure 2.22 :** Coherence functions of the building TB-2 in y direction, (a) undamaged state, (b) after 3% d.r.

The shifting of the resonant frequencies toward lower frequency values with the increasing seismic structural damage was presented in Figure 2.19, Figure 2.20, Figure 2.21 ve Figure 2.22. As it was expected, the stiffness of the structural members and accordingly the modal frequency values were decreased since the building was

enforced to exhibit lateral deformations beyond its elastic limit. Although, the quasi-static cyclic loading was implemented only in  $x$  direction, resonant frequencies decreased not only in  $x$  direction, but also in  $y$  direction as a result of the coupled nature of the response of the buildings along these directions (Goksu et al. 2015). However, the reduction of resonant frequencies due to structural damage observed in  $y$  direction was smaller than those observed in  $x$  direction (Table 2.2). For the sake of example, the third frequency peak as 9.47 Hz for both  $x$  and  $y$  directions at undamaged state shifted to the values as 6.44 and 7.04 Hz for  $x$  and  $y$  directions, respectively, when the building was enforced to 3 % d.r. at the 1<sup>st</sup> story.

**Table 2.2 :** Identified modal frequencies and corresponding modal damping ratios of the building TB-2.

Damage states	Modal frequencies (Hz)						Modal damping ratios					
	$x$ direction			$y$ direction			$x$ direction			$y$ direction		
	1 <sup>st</sup>	2 <sup>nd</sup>	3 <sup>rd</sup>	1 <sup>st</sup>	2 <sup>nd</sup>	3 <sup>rd</sup>	1 <sup>st</sup>	2 <sup>nd</sup>	3 <sup>rd</sup>	1 <sup>st</sup>	2 <sup>nd</sup>	3 <sup>rd</sup>
Undamaged	2.26	6.07	9.47	2.27	6.06	9.47	0.018	0.028	0.033	0.048	0.047	0.045
0.5 % d.r.	-	5.36	8.11	No test			-	0.048	0.039	No test		
3% d.r.	-	3.81	6.44	1.56	4.73	7.04	-	0.050	0.047	0.049	0.048	0.046

Besides, the modal damping ratios identified through EFDD increased with increasing seismic structural damage. The increasing in modal damping ratio as a function of attained lateral drift of the 1<sup>st</sup> story is given in Figure 2.23. As seen in this figure, the modal damping ratio in  $x$  direction increased significantly with increasing in damage comparing to the increasing of modal damping ratio in  $y$  direction (for the second and third mode: approximately 78% and 42% increase in  $x$  direction). This was attributed by more significant damage in  $x$  direction due to quasi-static loading only in  $x$  direction. Moreover, it is worth to note that the increasing in damping ratio with the onset of cracking (0.5% d.r.) did not follow the same trend for the following increasing damage.

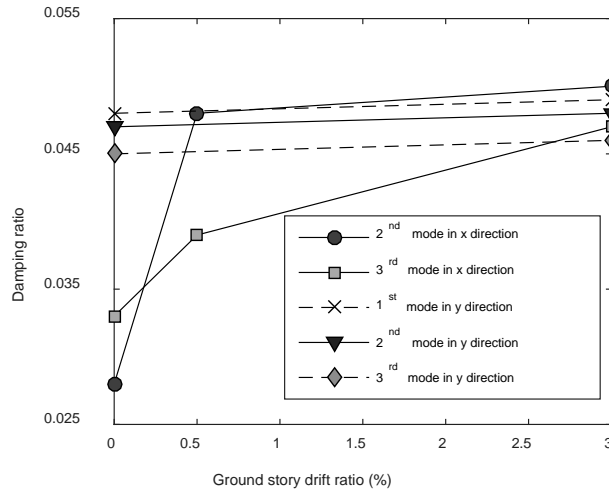


**Figure 2.23 :** Change in modal damping ratio as a function of achieved maximum drift ratio (damage state).

### 2.6.2 Forced vibration test survey

As aforementioned, forced vibration tests were implemented before and after quasi-static reversed cyclic loading for the buildings TB-1 and TB-2, and were also carried out at a set of damage levels for the building TB-2. Different than the ambient vibration tests, forced vibration tests requires to measure the excitation and the corresponding response of the excited structure, as well, so that the basic equations of frequency response function (FRF) can be used for system identification. Accordingly, in the case of force vibration test survey, FRF of the buildings were obtained by applying sinusoidal horizontal forces using eccentric mass shaker at various frequencies and measuring the corresponding vibration response of the buildings at steady state. Modal frequencies of the buildings were then obtained from FRF of the buildings by peak picking method. Subsequently, the modal damping ratios ( $\zeta$ ) corresponding to each peak were determined using half-power bandwidth method (Chopra 2001).

During the forced vibration tests, each discrete frequency steps were applied for 30 seconds and as seen in Table 2.1, the maximum operating frequency ( $f$ ) of the shaker was 15 Hz. Therefore, the corresponding horizontal force in proportion to eccentricity of shaker ( $0.0625 \times 8 \text{ kg.m}$ ) and rotational frequency squared ( $2\pi f^2$ ) was approximately  $\pm 4.44 \text{ kN}$ . This maximum horizontal force value was within the linear elastic limits of the structure. Figure 2.24 displays the relationships between the shaker force versus the shaker operating frequency and the base shear force response of the buildings.



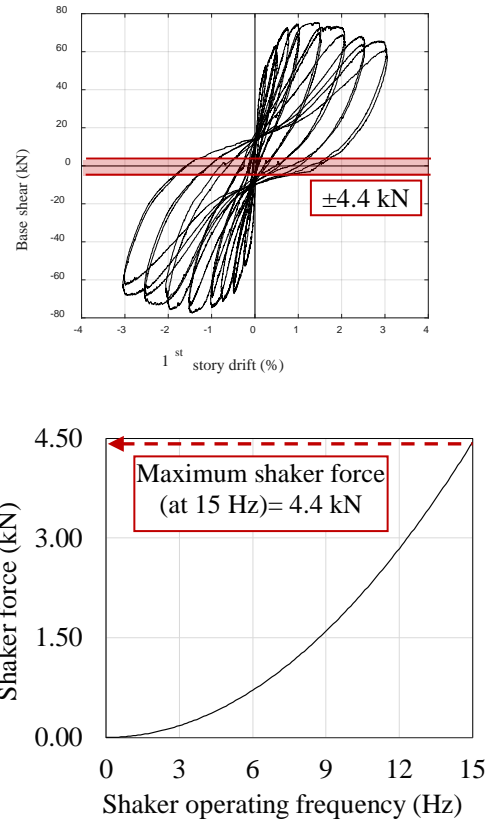
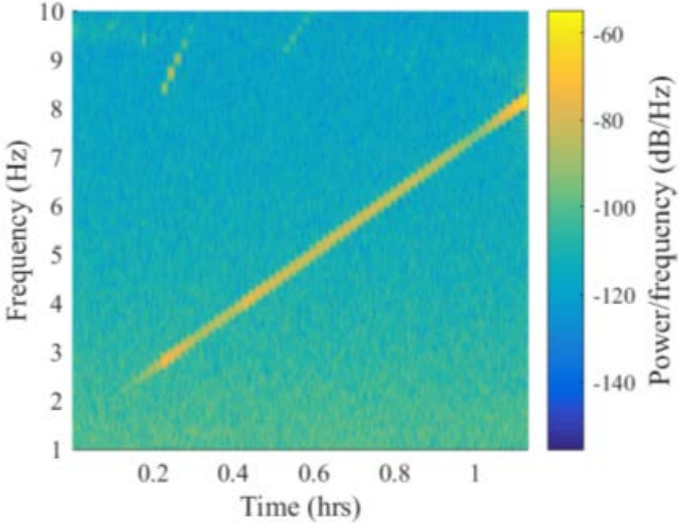


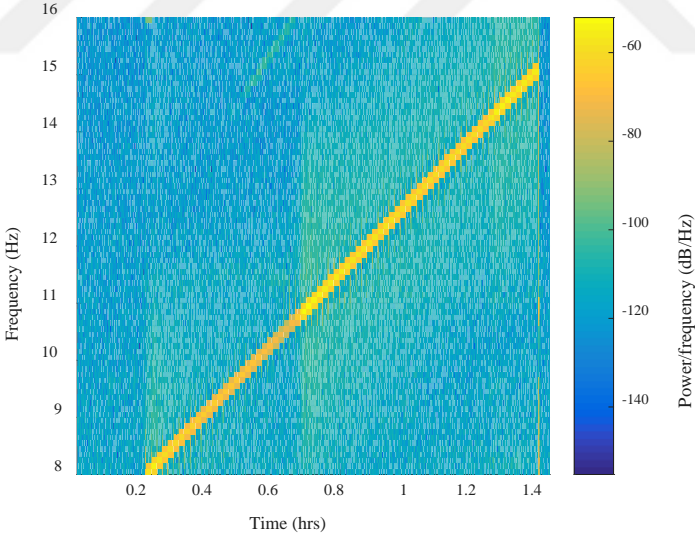
**Figure 2.24 : Shaker force.**

To examine the variations of the energy content of the recorded signals with time during the forced vibration test, the spectrogram of the data recorded by accelerometer A2 (which is the closest one to the shaker) was calculated. Spectrogram is a visual representation of the short-time fourier transform and consists of absolute values of each discrete power spectrums in successive time frames. Hence, spectrogram is calculated by windowing the time series signal into segments and taking its fourier transform. In this study, MATLAB spectrogram command is used. Since the shaker was operated so as sweeping a frequency range with certain frequency increment steps for certain time periods (Table 2.1), a spectrogram view of the vibration data captured by the accelerometer A2 could be useful to understand the frequency content of the data. Moreover, most of the forced vibration tests were applied as 2-phases (e.g.: 1.5-8 Hz and 8-15 Hz for TB-2 undamaged case) and data recording has been initiated approximately 1-5 minutes before the shaker started and continued 1-5 minutes after the shaker stopped. Hence, the spectrogram view was utilized to determine the starting and finishing point of the forced vibration tests and merge the data captured in 2 different phases of the test. The spectrogram views of the vibration data captured by

the A2 accelerometer during the forced vibration test at undamaged case of the building TB-1 were given in Figure 2.25 and Figure 2.26. The spectrogram views at damaged case of the building TB-1 and at undamaged and damaged cases of the building TB-2 are given in Appendix A.



(a)



(b)

**Figure 2.25 :** Spectrogram views for TB-1 undamaged case – x direction testing, (a) shaker frequency range as 1.5-8Hz, (b) shaker frequency range as 8-15 Hz.

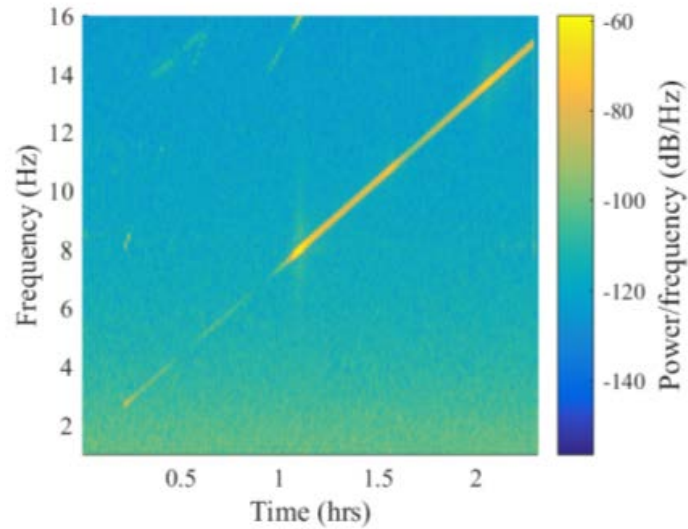


**Figure 2.26 :** Spectrogram view for TB-1 undamaged case – y direction testing, shaker frequency range as 1.5-15 Hz.

As seen in Figure 2.25 and Figure 2.26, the absolute values of the power spectrums as a function of frequency are given in right vertical axis in terms of a color palette. The absolute values of the power densities (between approximately -80 dB to -60 dB) corresponding to the frequency values swept by shaker can be clearly noticed throughout the diagonal path on the figures. In addition to the vibration content induced by sinusoidal force of the shaker, the signal captured by accelerometer A2 were also embedded gaussian noise induced by ambient vibration sources during the forced vibration test. As expected, the absolute values of the power densities of the vibrations induced by gaussian noise was found to be much smaller than those induced by forced vibration tests (at around -100 dB to -150 dB). Furthermore, the absolute power density values of lower frequencies (1.5 Hz-2.5 Hz) swept by shaker was found to be significantly smaller than those found at higher frequencies. In fact, the absolute power density values of the lower frequencies (1.5 Hz-2.5 Hz) varied around around -100 dB to -150 dB. This can be attributed to the extremely small excitation force applied by shaker at lower frequencies. Since the horizontal force provided by the shaker is in proportion to the eccentricity of shaker and rotational frequency squared, it reached approximate value of 0.04 kN and 0.12 kN at 1.5 Hz and 2.5 Hz, respectively. This level of shaker horizontal force remained relatively low comparing to the force levels at higher frequencies. As a result of this situation, as seen in the figures, the horizontal force applied by shaker between the frequencies 1-1.5 Hz to

approximately 3-4 Hz caused a vibration magnitude which was not much more than any ambient vibration.

**2.6.2.1 System identification results**

In the present case, since there was not a force sensor capturing the force implemented by shaker to the building, some assumptions were required for determining the excitation force, which was considered as input in the FRF calculations. Hence, 2 different methods were followed for determining the input force so that FRF of the buildings can be developed. For the 1<sup>st</sup> method, excitation force was defined as the shaker sinusoidal force. The shaker force corresponding to each implemented frequency steps given in Table 2.1 were calculated as explained above and substituted in the basic equation of FRF. A basic sheme for the 1<sup>st</sup> method is given in Figure 2.27. Unlike the 1<sup>st</sup> methods, the 2<sup>nd</sup> method does not follow a FRF algorithm which relies on the basic relationship between excitation force and the corresponding response of the building. Alternatively, in this method, the FRF were calculated dividing the recorded steady-state acceleration data to the squared values of shaker operating frequencies (Soyoz et al 2013).

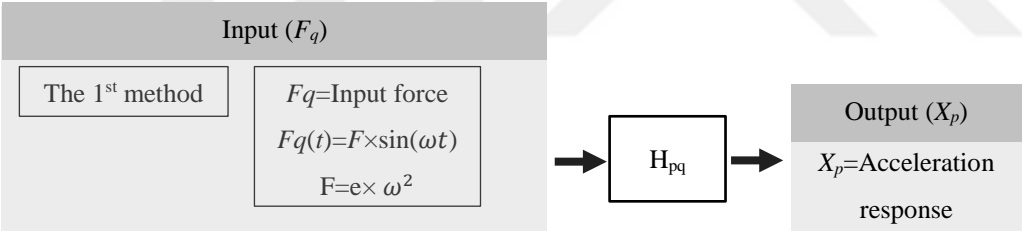


**Figure 2.27 :** Sheme of FRF calculation.

Hence the FRFs were obtained for two configurations of the shaker and the uniaxial piezoelectric sensors: *x* direction and *y* direction are presented in separate plots as indicated in the captions of the figures. In order to represent the obtained FRFs in *x* and *y* directions, the excitation points of input force and measurement points of response data were numbered considering both directions in each dynamic degree of freedom (1<sup>st</sup>, 2<sup>nd</sup> and 3<sup>rd</sup> story): Nodes 1, 4, 7 and 7c for *x* direction while Nodes 2, 5, 8 and 8c for *y* direction, where the letter ‘c’ refers corner (Figure 2.28). In this figure, the bracketed nodes represent the points in *y* direction while others represent the nodes in *x* direction. Accordingly, the FRF relationships developed using the 1<sup>st</sup> method for the nodes given in Figure 2.27 were presented in the Figure 2.29, Figure 2.30, Figure

2.31, and Figure 2.32, while that of developed using the 2nd method is given in the Figure 2.33, Figure 2.34, Figure 2.35 and Figure 2.36. In these figures, for the notation of FRF curves ( $H_{pq}$ ), the first term of the subscript ( $p$ ) refers excitation point and the second one ( $q$ ) represent the response (accelerometer) point (e.g.:  $H_{77c}$ , excitation point is the node 7 and the response point: 7c in the Figure 2.28). Consequently, each series in the figures represent the FRF relationship between 2 dynamic degree of freedoms. As it can be seen in the figures, because of the electronic and ambient noise and sensitivity problems of piezoelectric type sensors, experimental FRF curves obtained using the 1st method have a lot of unwanted, noise-like frequency peaks which have small energies. In fact, this was the underlain reason to be required for another FRF curve calculation methodology (So called the 2<sup>nd</sup> method). The modal frequencies of the both buildings for each undamaged and damaged cases were then determined making use of FRFs by peak picking method.

The testing setup utilized in the investigation provided a detailed picture of the FRFs for the frequency range from 2 to 50 Hz. However, in both buildings, it was not required to call for natural frequencies for the value higher than 15 Hz for undamaged case and 10 Hz for damaged cases. For the vibration frequencies below 2 Hz, FRFs could not be reliably identified due to the high pass filter (1.4 Hz) which was embedded on the data acquisition system. As seen in the figures, except a few minor differences between the natural frequencies of the building TB-1, those matched well for the building TB-2.

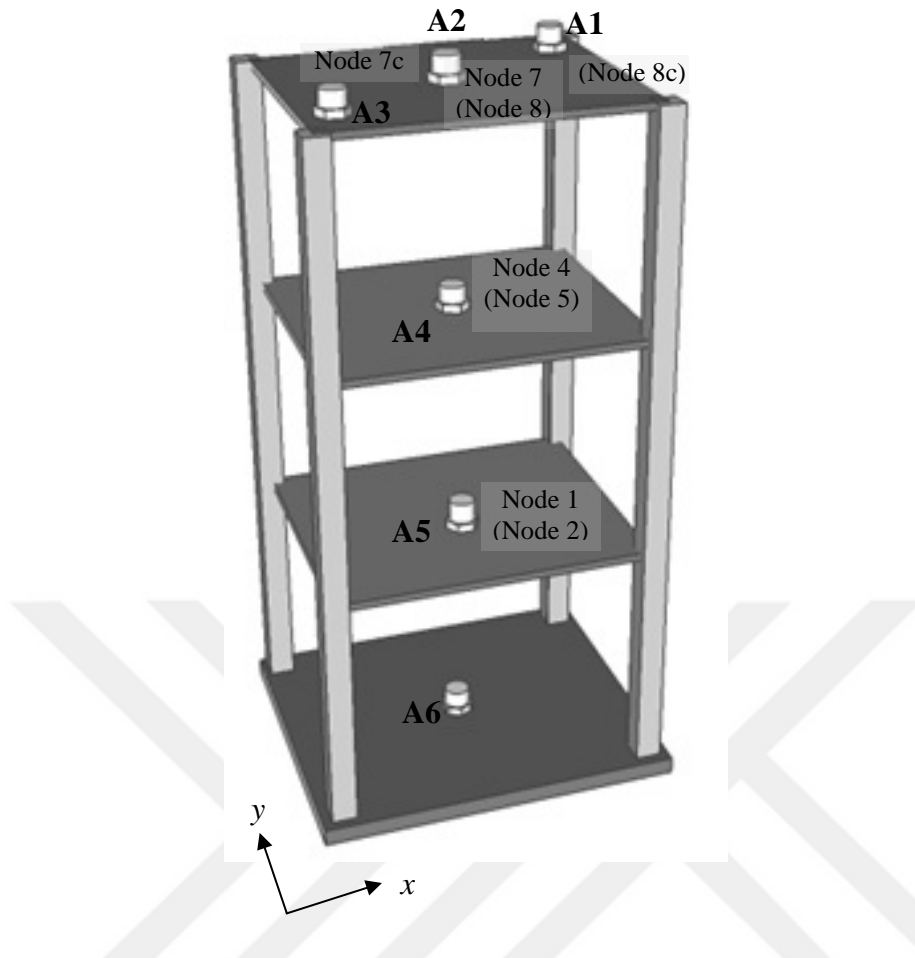


**Figure 2.28 :** Notations of the points, where the force was applied and the vibration response of the buildings against the force were measured.

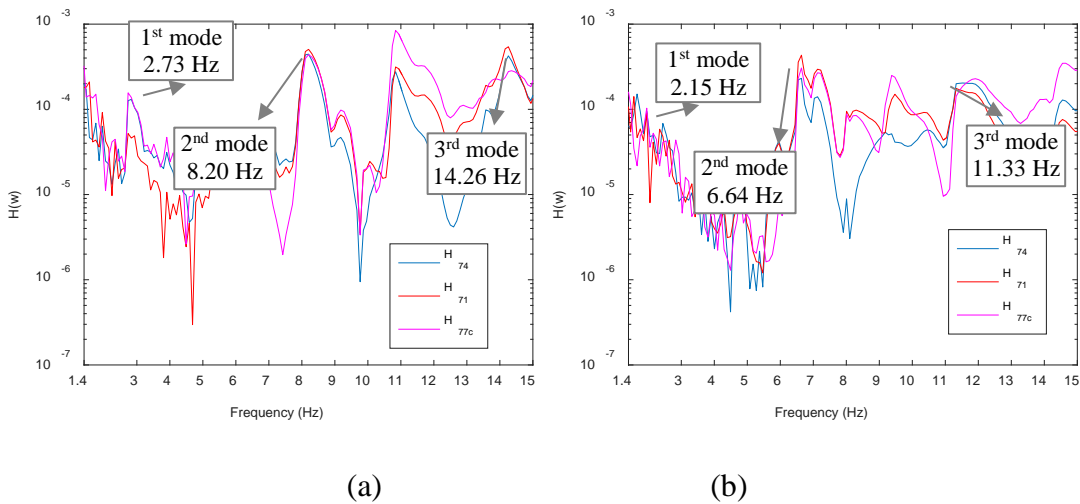


**Figure 2.29 :** Frequency response functions of the building TB-1 in x direction (a) undamaged and (b) after 1.5 % d.r.

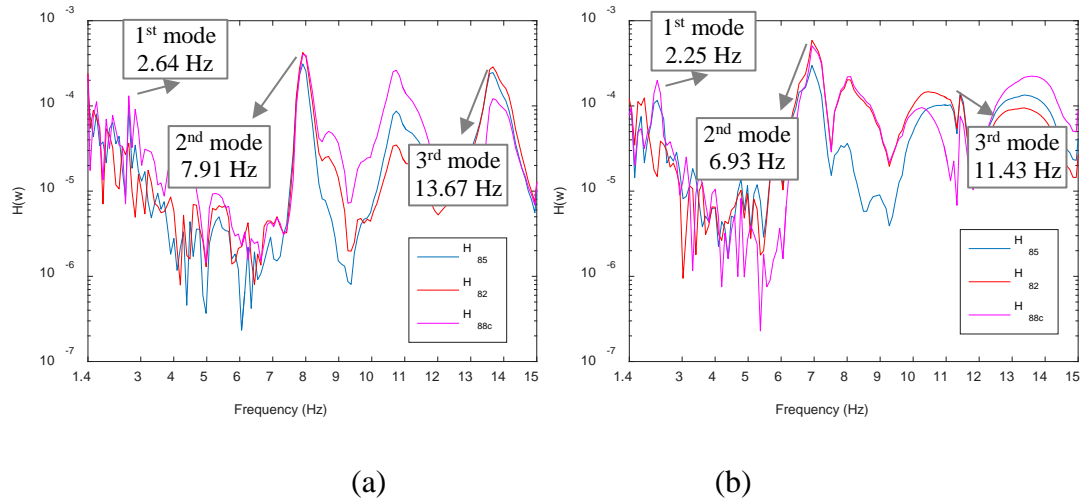


**Figure 2.30 :** Frequency response functions of the building TB-1 in y direction (a) undamaged and (b) after 1.5 % d.r.

The shifting of the natural frequency peaks of FRF toward lower frequencies with the increasing damage can be easily followed in Figure 2.29 to Figure 2.36. This shifting of the natural frequencies was the expecting result of the the stiffness degradation of the buildings since they were subjected to lateral deformations via quasi-static cyclic loading beyond their elastic limits. For example, the resonant frequency value determined at 8.65 Hz and 14.20 Hz for building TB-1 in x direction for its undamaged state decreased to the values at 6.60 Hz and 11.20 Hz, respectively, since the building was enforced to lateral displacement as 1.5 % drift ratio at the 1<sup>st</sup> story (Figure 2.33). For the case of building TB-2, the resonant frequency value determined at 9.10 Hz at undamaged state decreased to 5.95 Hz at the damaged state when the building was enforced to lateral displacement cycles of 3 % drift ratio at the 1<sup>st</sup> story (Figure 2.35). Due to the configuration of the test setup, the buildings were enforced to inelastic displacements in the x direction during the quasi-static reversed cyclic loading, and negligible displacements were experienced along the y direction. However, due to the coupled nature of the response of the buildings along x and y directions, not only the modal frequencies of the buildings in the x direction but also that of in y direction decreased in the identified FRFs (Goksu et al 2015). Nonetheless, as it was expected, the decrease in modal frequencies due to stiffness degradation observed in the y direction was smaller than those observed in the x direction (Table 2.3).

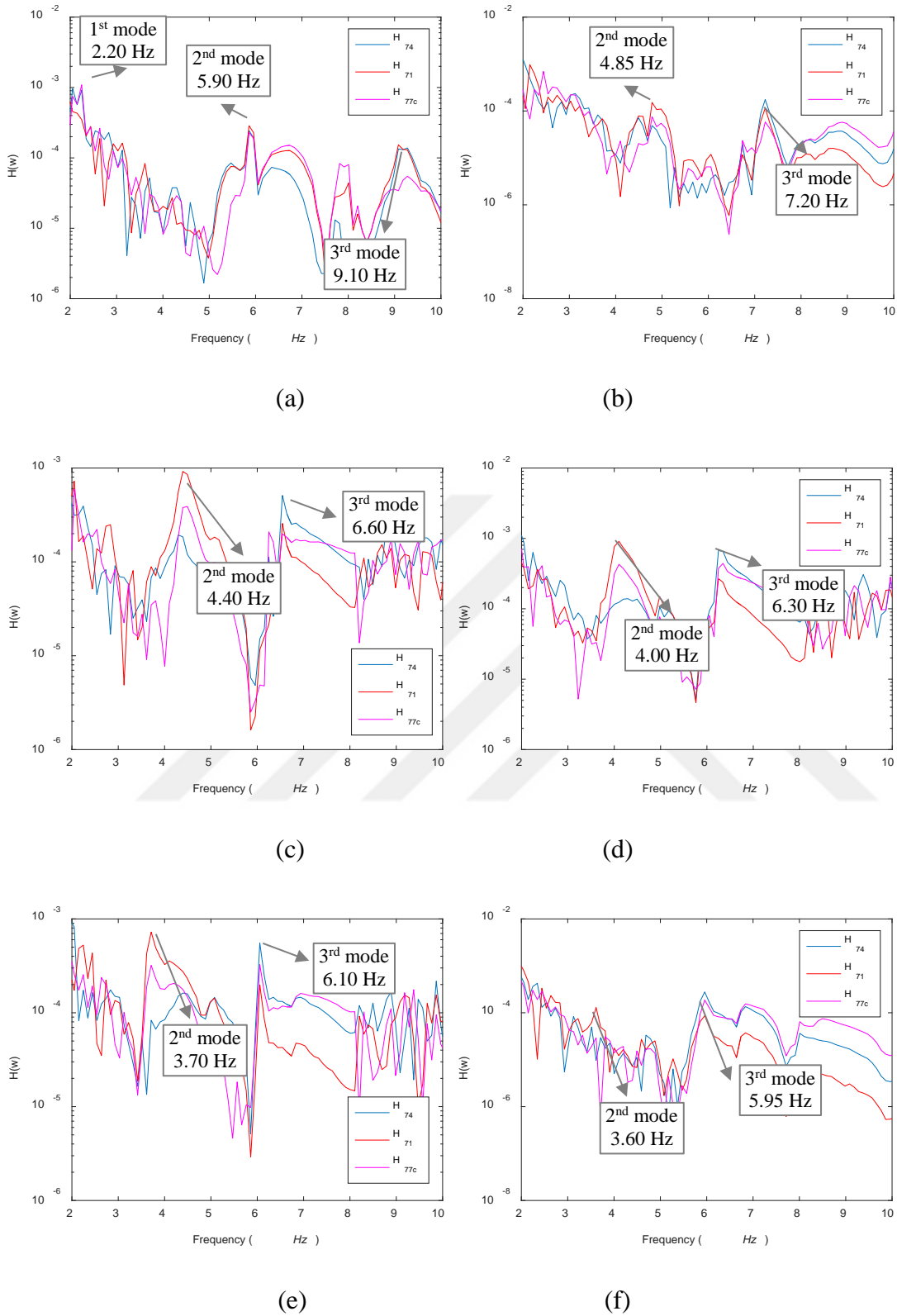


**Figure 2.31 :** Frequency response functions of the building TB-2 in  $x$  direction (a) undamaged, (b) after 0.5 % d.r., (c) after 1.0 % d.r., (d) after 1.5 % d.r., (e) after 2.0 % d.r. and (f) after 3.0 % d.r.



For the sake of example, the peaks observed at 7.80 Hz and 13.60 Hz (the second and the third natural frequencies in  $y$  direction) at the FRF of building TB-1 in at its undamaged state shifted to the peak at 6.95 Hz and 11.40 Hz, respectively, on the FRF of the building after the building was subjected to displacement cycles at 1.5 % drift ratio at the 1<sup>st</sup> story (Figure 2.33 and Figure 2.34). In a similar manner, for the case of building TB-2, the peak observed at 9.30 Hz at undamaged state shifted to 6.55 Hz (the third natural frequency in  $y$  direction) at the damaged state after the building was subjected to displacement cycles of 3 % drift ratio at the ground story (Figure 2.35 and 2.36). As seen in these figures, the shifting of the FRFs towards zero value could not be displayed due to the high-pass filter embeded in data acquisition system (as 1.4 Hz).

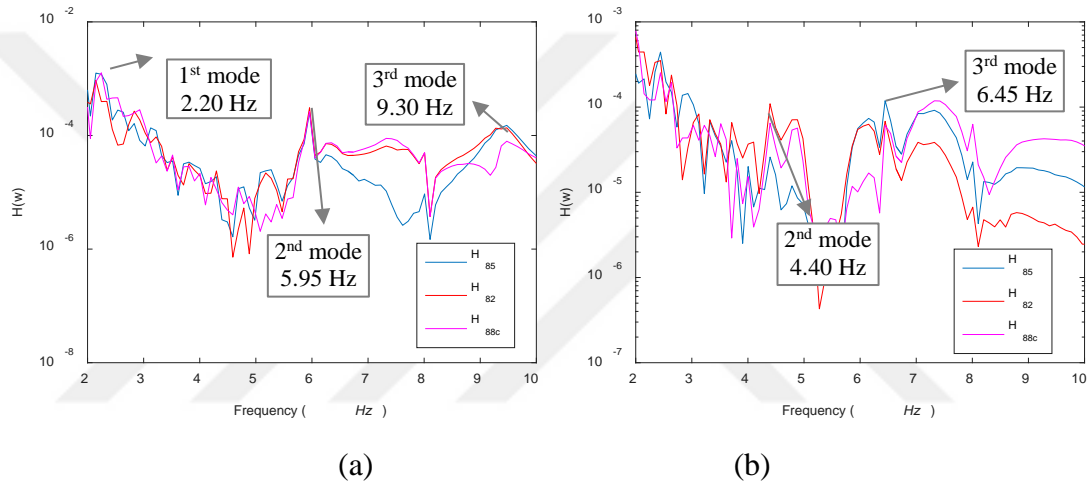


**Figure 2.32 :** Frequency response functions of the building TB-2 in  $y$  direction (a) undamaged and (b) after 3.0 % d.r.

The evolution of modal frequencies with increasing damage for building TB-2 is plotted in Figure 2.37. As shown in this figure, the modal frequencies were observed to decrease up to yield limit (around 1 % the first story drift). When the modal frequencies identified for each damaged state ( $f_i$ ) were normalized using the modal frequency obtained for the undamaged state ( $f_0$ ), the relationships between these normalized ratios and the first story drift ratio were found to follow a similar trend for the both second and third peaks (Goksu et al. 2015). This may be useful in estimating the evolution of the first modal frequency of building TB-2 with further increase of damage, which could not be captured due to technical limitations.

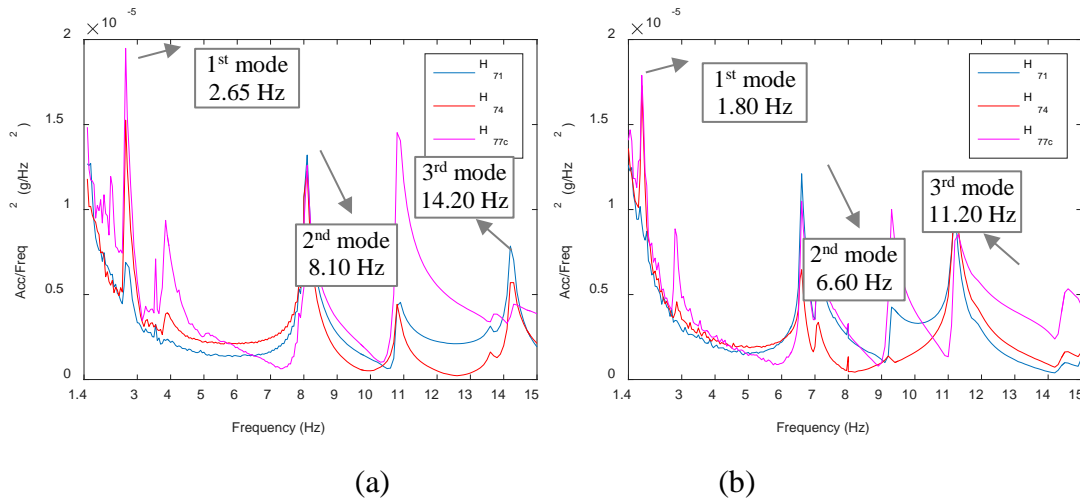


**Figure 2.33 :** Frequency response functions of the building TB-1 in  $x$  direction (a) undamaged and (b) after 1.5 % d.r.

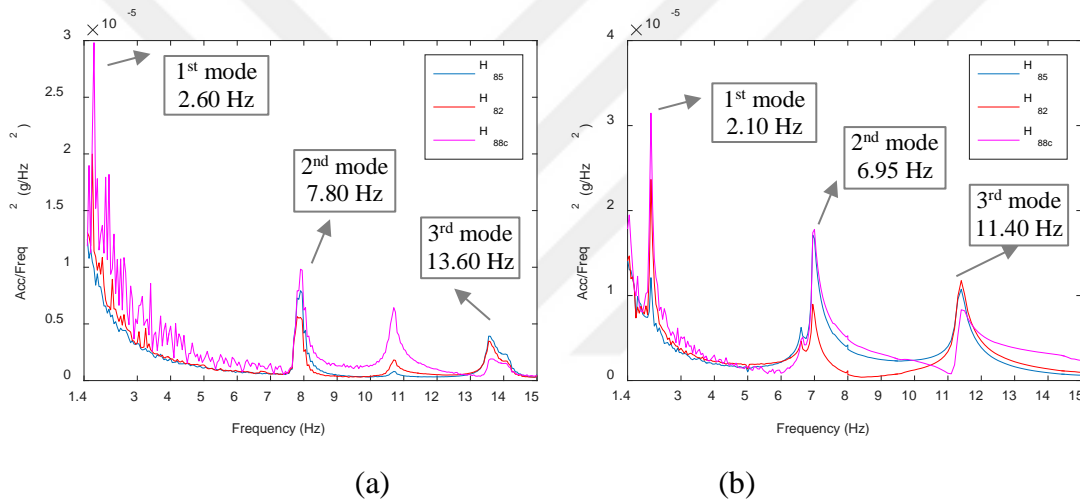


**Figure 2.34 :** Frequency response functions of the building TB-1 in  $y$  direction (a) undamaged and (b) after 1.5 % d.r.

As aforementioned, the modal damping ratios are calculated using half power bandwidth method. According to this method, first, the pair of frequencies (i.e.  $f_1$  and  $f_2$ ) corresponding to  $1/\sqrt{2}$  amplitude of a peak at a given resonant frequency  $f_n$  are determined. Subsequently, the damping ratio is obtained using Eq. (2.7). The modal damping ratios are calculated using the frequency peaks in FRF curve obtained using the 2<sup>nd</sup> method explained above.

$$\zeta = \frac{f_2 - f_1}{2 \cdot f_n} \quad (2.7)$$

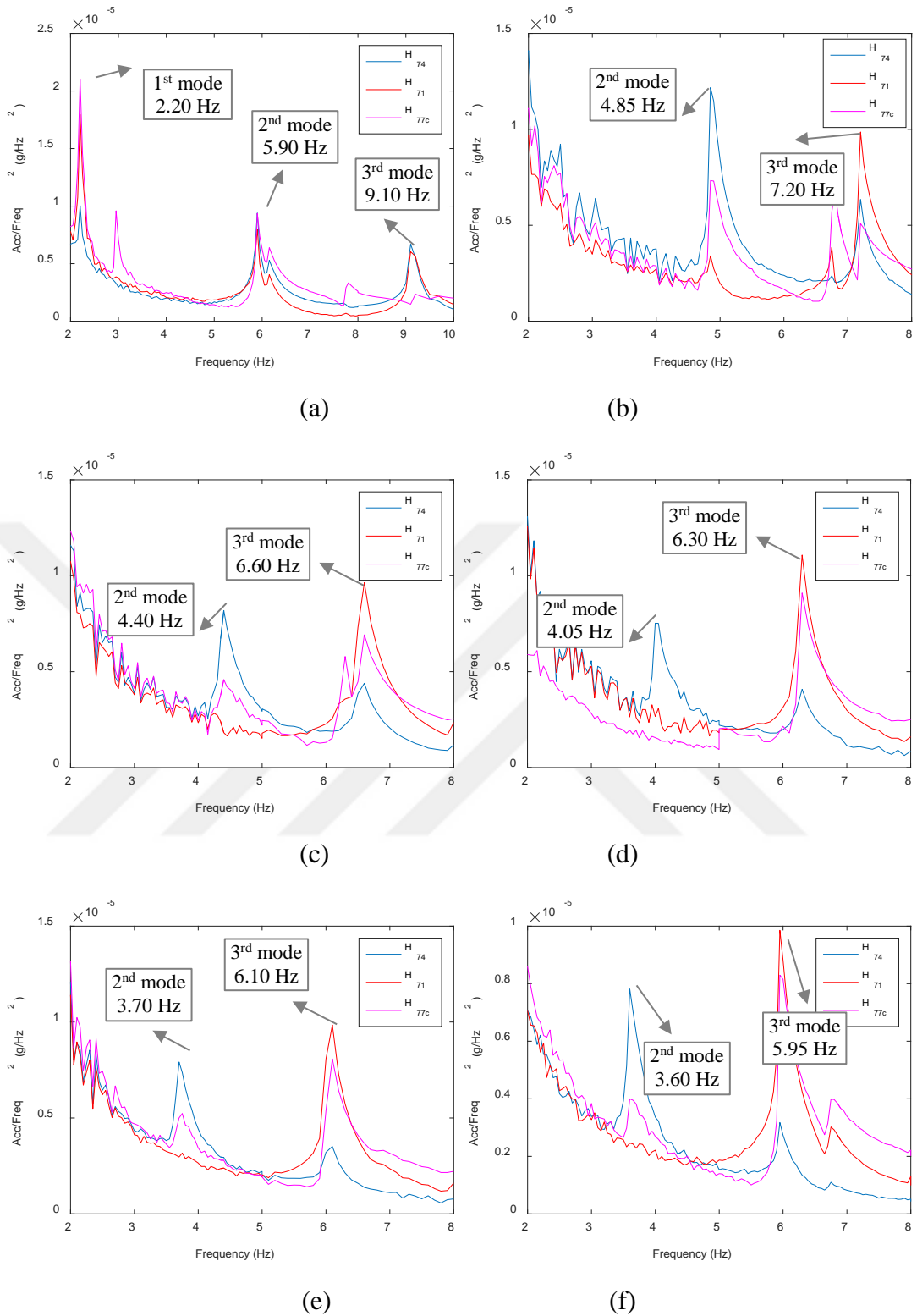


**Figure 2.35 :** Frequency response functions of the building TB-2 in x direction (a) undamaged, (b) after 0.5 % d.r., (c) after 1.0 % d.r., (d) after 1.5 % d.r., (e) after 2.0 % d.r. and (f) after 3.0 % d.r.

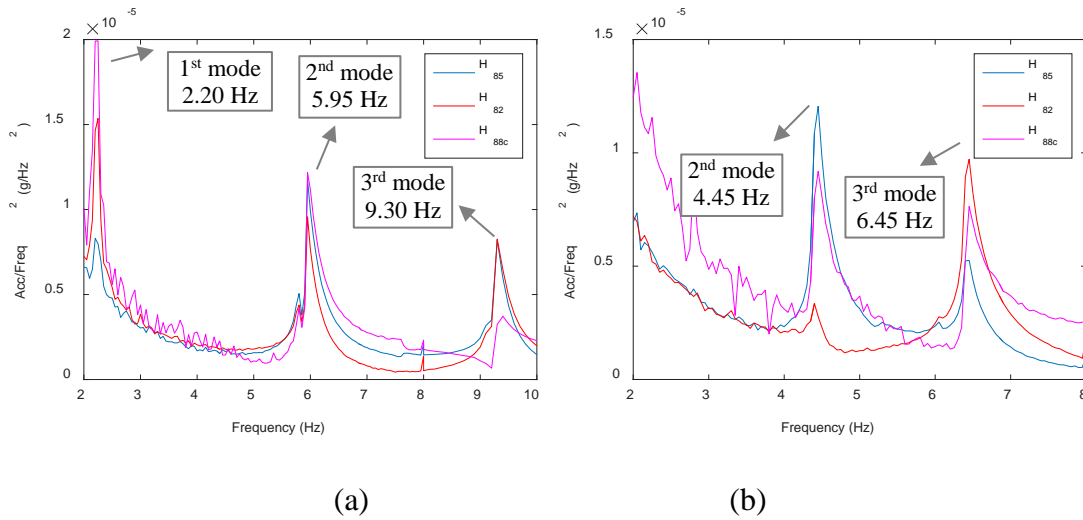


**Figure 2.36 :** Frequency response functions of the building TB-2 in y direction (a) undamaged and (b) after 3.0 % d.r.

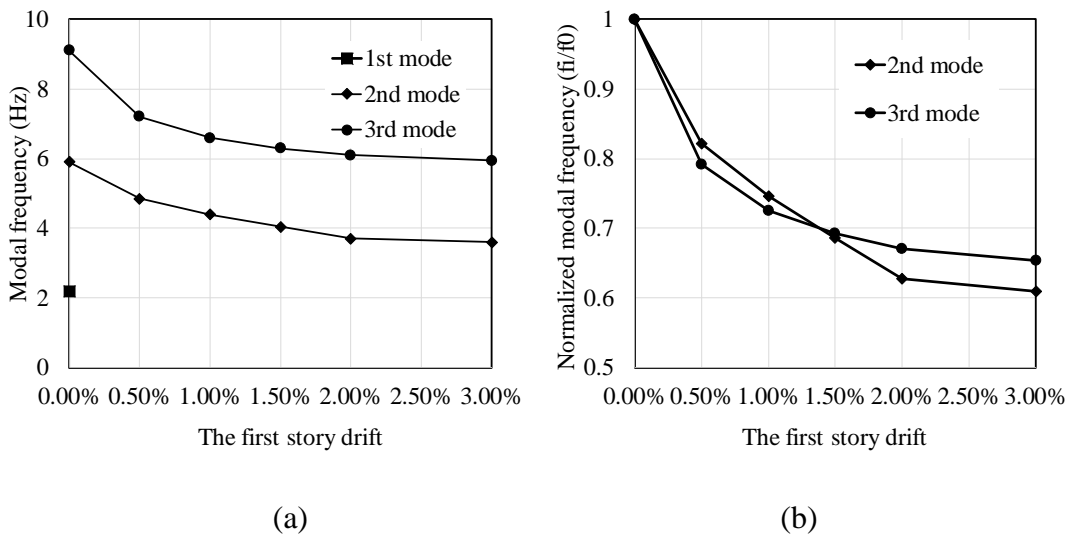


**Figure 2.37 :** Modal frequencies of the building TB-2 (*x* direction) at considered the first story drift ratio, (a) modal frequencies, (b) normalized modal frequencies with respect to the undamaged state.

As an example, Figure 2.38 displays the identification of modal damping ratio for the second mode in *x* direction of the building TB-1 for undamaged case. The natural frequencies and the corresponding modal damping ratios are given in Table 2.3. In the Table 3.3, the damage state 1.5% d.r. for the building TB-1 was referred as Damage Case 1 (DC1) and similarly, the damage states 0.5% d.r., 1.0% d.r., 1.5% d.r., 2.0% d.r. and 3.0% d.r. for the building TB-2 were referred as Damage Case 1 (DC1), Damage Case 2 (DC2), Damage Case 3 (DC3), Damage Case 4 (DC4) and Damage Case 5 (DC5), respectively. Furthermore, the undamage situation of both buildings

was referred as Undamaged Case (UC). These notations for the damage states where the forced vibration tests were applied will be followed for the remaining part of this thesis.

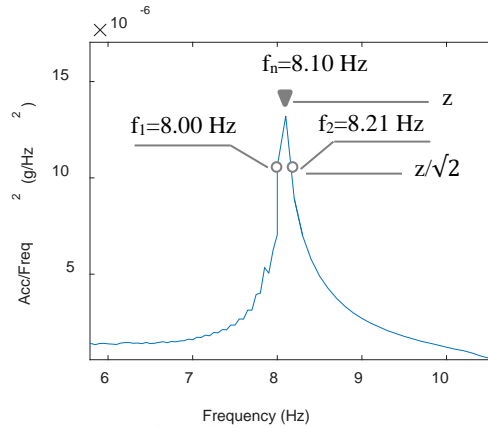


**Figure 2.38 :** Identification of modal damping ratios using half-power bandwidth method for building TB-1 for undamaged case in x direction.

In the case of building TB-1, the modal damping ratios for the undamaged state were in the range from 1.3 to 3.9 % and 1.4% to 2.0% for x and y directions respectively. The modal damping ratio corresponding to third peak (and for y direction, also 1st peak) increased significantly with the increasing damage while, contrary to expectations, that of corresponding to second peak decreased with the increasing damage (Table 2.3). In the case of the building TB-2, the modal damping ratios for the undamaged case were found to be in the range from 0.6 to 1.6 % and those increased significantly with the increasing damage. The modal damping ratios obtained for different damage states and the ones normalized with the damping ratio of the undamaged state are given in Figure 2.39. As seen in this figure, the normalized modal damping ratio corresponding to second and third peaks increased up to approximately 85% and 140% of its initial value at the onset of cracking, respectively (i.e. 0.5 % the first story drift). The increasing in modal damping ratio corresponding to both second and third peaks followed the approximately same increasing path till the building was enforced 1% dr. However, with the subsequent lateral displacement cycles, the change in modal damping ratio corresponding to the second peak was very limited. Even those corresponding to the third peak displayed occasionally decreasing with increasing damage. This pattern can be attributed that although the building was subjected to increasing lateral displacement cycles, the existing cracks occurred

beginning of the quasi-static loading did not significantly propagate, and width of these cracks did not widen critically with increasing lateral displacement cycles.

**Table 2.3 :** Identified modal frequencies and damping ratios of the buildings at different damage states.

Building	Damage situation	Modal frequencies (Hz)						Modal damping ratios					
		x direction			y direction			x direction			y direction		
TB-1	UC	2.65	8.10	14.20	2.60	7.80	13.60	4.00	1.40	1.70	2.00	1.40	1.50
	DC1	-	6.60	11.20	2.10	6.95	11.40	-	0.90	2.40	2.80	1.40	2.10
TB -2	UC	2.20	5.90	9.10	2.20	5.95	9.30	1.60	1.30	0.60	2.20	1.30	0.70
	DC1	-	4.85	7.20	*	*	*	-	2.40	1.40	*	*	*
	DC2	-	4.40	6.60	*	*	*	-	3.40	1.50	*	*	*
	DC3	-	4.05	6.30	*	*	*	-	3.60	1.40	*	*	*
	DC4	-	3.70	6.10	*	*	*	-	3.60	1.20	*	*	*
	DC5	-	3.60	5.95	-	4.45	6.45	-	3.50	1.40	-	2.20	1.20

\* Buildings were not tested at these configurations  
 - Could not be identified due to technical limitations  
 UC: Undamaged Case, DC: Damaged Case

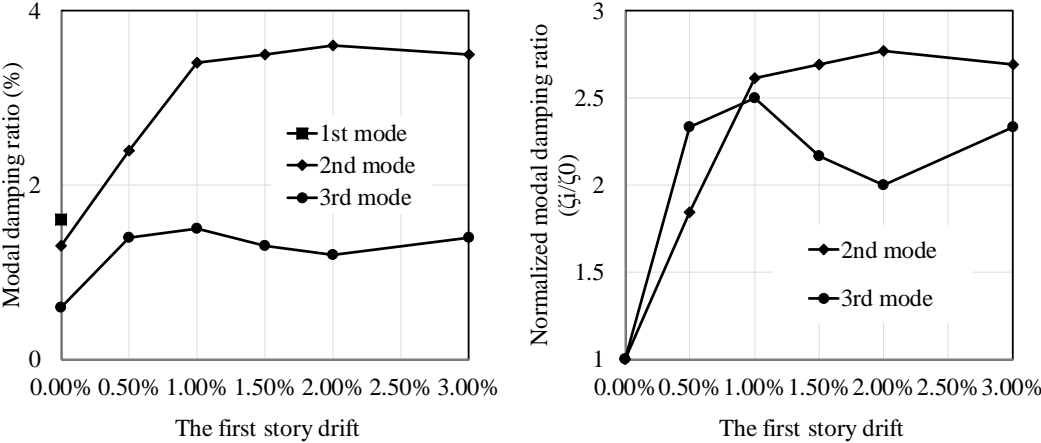


**Figure 2.39 :** Modal damping ratios of the building TB-2 (x direction) at considered the first story drift ratio, (a) modal damping ratios, (b) normalized modal damping ratios with respect to the undamaged state.

The modal frequencies are plotted against the corresponding modal damping ratios, it is found that small initial decreases in modal frequencies due to cracking are accompanied by quite significant jumps in damping ratio for all the peaks of building TB-2 (Figure 2.40). This identified relationship between modal frequencies and the corresponding modal damping ratios given in Figure 2.40 follows a trend that is

noticeably different than the behavior assumed in the commonly adopted damping models (e.g. Rayleigh damping, Wilson-h damping) (Goksu et. al 2015).

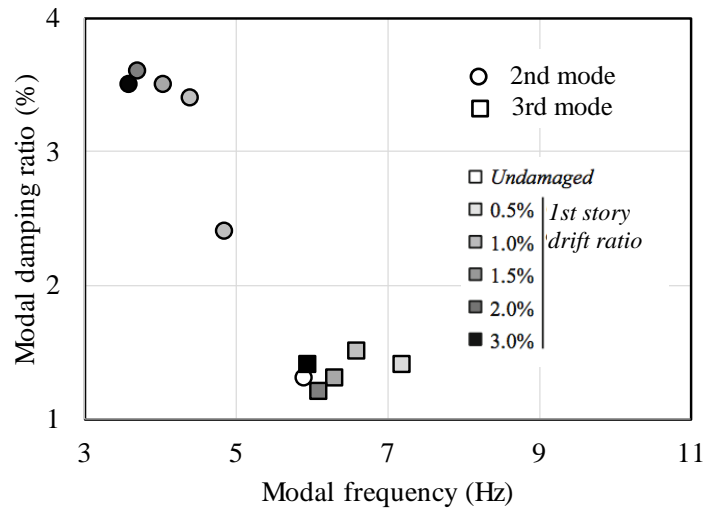


**Figure 2.40 :** Obtained modal damping ratios for the identified modal frequencies of the building TB-2.

Moreover, as it was given in Figure 2.15, the lateral load bearing capacity of the building TB-2 was degraded by approximately 20% of its maximum induced by the lateral displacement reversals. In the contrary to this degradation, any intensive structural damage which indicates this degradation, could not be detected during the detailed visual inspection after it is unloaded from 3% d.r. However, forced vibration test results clearly indicate that modal frequencies of building TB-2 decreased significantly while the modal damping ratios increased (Table 2.3). Hence, it can be extracted that the vibration based test results could indicate that the building subjected to significant structural damage even while very few indications could be identified through visual inspection. This result of experimental phase of the study is remarkably noticeable in terms of post-earthquake damage inspection of structures. After a catastrophic earthquake, vibration based signature of damaged structures could make enable the inspector to perform a more reliable damage assessment compared to visual inspection.

## 2.7 Concluding Remarks

The change on dynamic characteristics of two full-scale, three story substandard RC buildings with the seismic structural damage induced by quasi-static reversed cyclic loading were identified through forced vibration tests. The tests were implemented

before and after quasi-static loading as well as at a set of damage levels in terms of the 1<sup>st</sup> story drift ratio.

The modal frequencies, which were obtained by peak picking in the FRFs, decreased and the modal damping ratios, which were obtained using half power bandwidth method, increased significantly up to the elastic limit of the buildings are exceeded. However, the progressing of damage beyond the elastic limit was not accompanied with a similar significant change in the modal frequencies and the modal damping ratios.

Although a significant degradation in lateral load bearing capacity (around 20%) of the building TB-2 were achieved at around 3 % lateral d.r., no intensified structural damage could be observed by visual inspection. However, the forced vibration test results proved the modal frequencies and the damping ratios changed due to structural damage. These findings indicate a risk about the missing the structural damages during visual inspections carried out after earthquakes. Hence, utilization of dynamic testing accompanying with visual inspection could be a promising method for more realistic assessment of structural damages after seismic events.



### 3. FRF BASED DAMAGE IDENTIFICATION METHOD

In this chapter, a model updating based iterative damage identification algorithm using FRF based error function was developed. The algorithm provides damage detection, localization and quantification using experimentally obtained FRF data. Before explaining the algorithm and result of the damage identification survey for the target buildings TB-1 and TB-2, the theoretical background utilized throughout the calculations will be explained followingly.

#### 3.1 Theoretical Background

Thyagarajan *et al.* (1998) has been previously proposed a model updating based damage detection procedure including a FRF-based error function. According to this procedure, the equation of motion of a viscously damped system subjected to a harmonic force was expressed as shown in Eq. (3.1);

$$[M]\{\ddot{u}\} + [C]\{\dot{u}\} + [K]\{u\} = Re(\{F\}e^{j\Omega t}) \quad (3.1)$$

where  $[K]$ ,  $[M]$  and  $[C]$  refers the stiffness, mass and damping matrices, respectively.  $\{u\}$  refers the displacement vector,  $\Omega$  refers the frequency of the excitation load,  $\{F\}$  refers a vector that contains the amplitude of the applied forces.  $j=\sqrt{-1}$  and  $t$  refers the time. A solution for equation (3.1) is given in Eq. (3.2);

$$\{u(t)\} = Re(\{q\}e^{j\Omega t}) \quad (3.2)$$

where  $\{q\}$  refers a complex frequency response vector. When the equation 3.2 substitutes into equation 3.1, equation 3.3 can be obtained and a solution for equation 3.3 is given in equation 3.4;

$$Re\{([K] - \Omega^2[M] + j\Omega[C])\{q\} - \{F\}\}e^{j\Omega t} = 0 \quad (3.3)$$

$$([K] - \Omega^2[M] + j\Omega[C])\{q\} - \{F\} = 0 \quad (3.4)$$

It is assumed that (i) modal testing is performed on the structure and (ii) complex frequency response vector is  $\{q_e\}$ , the measured displacements. Additionally, let the

dynamic stiffness matrix  $[A] = [K] - \Omega^2[M] + j\Omega[C]$  and FRF vector  $\{q_e\} = \{q_a q_b\}^T$ , where  $q_a$  and  $q_b$  refer degrees of freedom (dofs) on the real structure where the FRFs are measured and not measured respectively. The matrix  $[A]$  can also be partitioned accordingly as given in equation (3.5);

$$[A] = \begin{bmatrix} A_{aa} & A_{ab} \\ A_{ba} & A_{bb} \end{bmatrix} = \begin{bmatrix} K_{aa} - \Omega^2 M_{aa} + j\Omega C_{aa} & K_{ab} - \Omega^2 M_{ab} + j\Omega C_{ab} \\ K_{ba} - \Omega^2 M_{ba} + j\Omega C_{ba} & K_{bb} - \Omega^2 M_{bb} + j\Omega C_{bb} \end{bmatrix} \quad (3.5)$$

Accordingly, at the end of some set of mathematical calculations, the FRF-based two-step error function  $\{e_{FRF}(p_1, p_2)\}$  for any frequency  $\Omega_r$  is obtained by equation (3.6). Garcia-Palencia and Santini-Bell 2013 presented the details of these process.

$$\{e_{FRF}(p_1, p_2)\} = [(A_{aa}) - (A_{ab})[A_{bb}]^{-1}(A_{ba})]\{q_a\} - (\{F_a\} - [A_{ab}][A_{bb}]^{-1}\{F_b\})_{\Omega=\Omega_r} \quad (3.6)$$

In this equation,  $\{p_1\}$  and  $\{p_2\}$  refer the unknown parameters of the system; the first one includes the unknown properties of the system related to stiffness and mass matrices ( $[K]$  and  $[M]$ , respectively) such as modulus of elasticity and mass density, the latter one includes the damping parameters related to damping matrix  $[C]$  and  $\{F_a\}$  and  $\{F_b\}$  are the result of partitioning the vector of applied forces  $\{F\}$ .

Since the solution of equation (3.6) requires multiple inverse calculations, a single object-oriented solver called *Factorize* is embedded into the model updating algorithm. *Factorize* improves how rank-deficient systems are handled by incorporating a complete orthogonal decomposition, and the singular value decomposition (Davis 2013).

Different segments of the frequency response function (such as frequency content and magnitude) provide meaningful information about different parameter groups, specifically (1) stiffness and mass and (2) damping (Palencia et al. 2015). This characteristic of FRF enables to perform the model updating procedure in two steps:

- Step 1: Only the mass and stiffness matrices will be updated. Hence  $\{p_1\}$  is set as the vector of unknown parameters and  $\{p_2\}$  is kept constant in error function. To put it differently, the modal damping ratios remain unchanged from the initial numerical model throughout the model updating process.
- Step 2: The damping matrix will be updated. Therefore  $\{p_2\}$  is set as the new vector of unknown parameters and the updated parameters from Step 1  $\{p_1\}^{updated}$  kept as constants.

It should be noted that within this two-step model updating protocol, frequency points can be selected to provide the most well-conditioned model updating scenario for each target structure (Palencia et al. 2015). Consequently, the two-step error function given in Equation (3.6) can be rewritten as shown in equations (3.7) and (3.8). In Equation (3.6),  $\{p_2\}^*$  refers the initial damping parameter vector which will be kept constant for Step 1 and in equation (3.7),  $\{p_1\}^{\text{updated}}$ , the updated version of  $\{p_1\}$  in Step 1, refers the updated mass and stiffness parameters in Step 1.

$$\{e_{FRF}(p_1, p_2^*)\} = [(A_{aa}] - [A_{ab}][A_{bb}]^{-1}[A_{ba}])\{q_a\} - (\{F_a\} - [A_{ab}][A_{ab}]^{-1}\{F_b\})_{\Omega=\Omega_r} \quad (3.7)$$

$$\{e_{FRF}(p_1^{\text{updated}}, p_2)\} = [(A_{aa}] - [A_{ab}][A_{bb}]^{-1}[A_{ba}])\{q_a\} - (\{F_a\} - [A_{ab}][A_{ab}]^{-1}\{F_b\})_{\Omega=\Omega_r} \quad (3.8)$$

The stacked residual error for the  $k$ th dynamic test  $\{E_I(p)_k\}$  can be found using equation (3.9);

$$\{E_I(p)_k\} = \begin{Bmatrix} e_{FRF}(p)_{\Omega_1} \\ \vdots \\ e_{FRF}(p)_{\Omega_{r-1}} \\ e_{FRF}(p)_{\Omega_r} \end{Bmatrix} \quad (3.9)$$

In this equation,  $\{e_{FRF}(p)_{\Omega_r}\}$  denotes the error vector for the  $r$ th updating frequency  $\Omega_r$ , and is a function of the unknown parameters  $\{p\}$ , which can be either  $\{p_1\}$  or  $\{p_2\}$  depending on the the step. And so, the stacked error vector  $\{E_{FRF}(p)\}$  that accounts for different load locations  $\{E_I(p)_k\}$  is shown in equation 3.10;

$$\{E_{FRF}(p)\} = \{E(p)\} \begin{Bmatrix} E_I(p)_1 \\ \vdots \\ E_I(p)_{k-1} \\ E_I(p)_k \end{Bmatrix} \quad (3.10)$$

It should be noted that, as in the scope of experimental part of this study explained in previous chapter, there is 1 or 2 load locations where the eccentric mass shaker was applied.

In brief, the parameter estimation through model updating became a constrained minimization problem. Accordingly, the error function  $\{E(p)\}$  has to be expressed as a scalar objective function  $J(p)$  which is given in equation (3.11) (Palencia et al. 2015);

$$J(p) = \{E(p)\}^* \{E(p)\} \quad (3.11)$$

The minimization problem can be expressed as given in equation (3.12);

$$\min J(p) \text{ subject to } \{p_{\min}\} < \{p\} \leq \{p_{\max}\} \quad (3.12)$$

In this equation,  $\{p_{min}\}$  and  $\{p_{max}\}$  refers the predefined constraints based on engineering judgment.

In the context of this dissertation, the error function was represented in terms of r-squared ( $R^2$ ) which is a measure of correlation between the predicted and actual outcomes (constant, not model dependent) and determined between 0 and 1 (Equation 3.13). The denominator of the equation ( $SS_T$ : sum of square total) is the total sum of squares of the actual outcomes. The numerator ( $SS_E$ : sum of square of error) is the residual sum of squares (square of the difference between predicted and actual outcomes) (Montgomery et al. 2007).

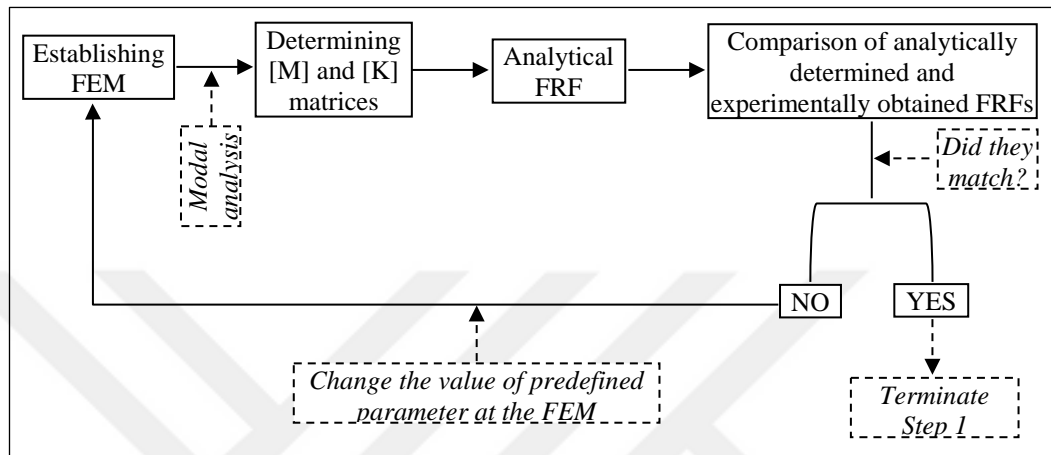
$$R^2 = 1 - \frac{SS_E}{SS_T} \quad (3.13)$$

The values close to 0 represents the predicted outcome does not mirror the actual outcome well, while the values close to 1 represents the predictions mirror the true outcome, tightly. R-squared measure was preferred since it gives the normalized results that means the results independent from the magnitudes of the different parameters compared. It should be noted that as it was suggested by Palencia et al. 2015, frequency points selected in the FRF were selected to provide the most well-conditioned model updating scenario for each updating procedure.

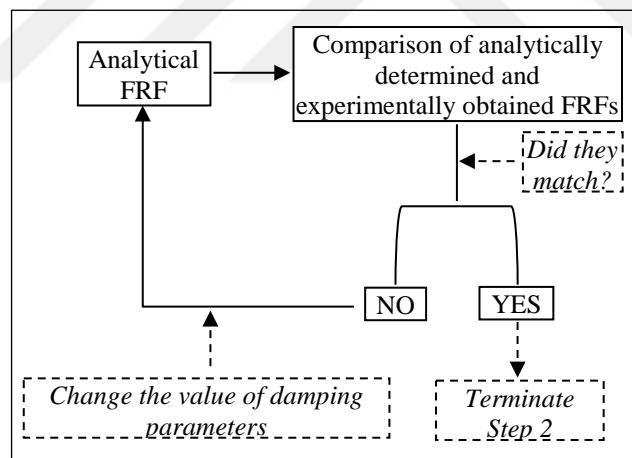
### **3.2 Two-step damage identification algorithm**

As aforementioned, a model updating based iterative damage identification algorithm using FRF based error function was developed in order to detect, localize and quantify the damage in target structures. For this purpose, a Model Updating Program (MUP), which runs a MATLAB (MathWorks Inc., 2011) based iterative algorithm, is developed to perform a damage identification process for the RC structures by minimizing error function. This program, MUP, is linked to SAP2000 (Computers and Structures, Inc., 2011) via Application Programming Interface (API) and allows to carry out model updating at predefined groups of elements which are determined through parameter sensitivity process. The schematical view of the two-step damage identification algorithm is shown in Figure 3.1. The two-step algorithm is iteratively run by MUP for different segments of the FRF. If the algorithm is computed for Step 1, MUP will run till frequency segment of the analytically determined and experimentally obtained FRFs match (by iteratively changing the parameters related

to stiffness and mass and keeping the damping constant). It will then start to run for Step 2 (by iteratively changing the damping and keeping constant the updated parameters in Step 1) and will terminate the algorithm while experimentally obtained and analytically determined FRFs match. Each sub-step (establishing FEM, analytical FRF, etc.) of the algorithm will be explained in detail through presenting the updating process of the initial FEMs of the buildings TB-1 and TB-2.



(a)



(b)

**Figure 3.1 :** Schematic view of two- step damage identification algorithm, (a) Step 1, (b) Step 2.

### 3.2.1 Updating [K] and [M] (Step 1)

#### 3.2.1.1 Establishing FEM of the buildings

The initial FEM of the test buildings TB-1 and TB-2 were created in SAP2000 (Figure 3.2). The  $x$ ,  $y$  and  $z$  axis in the FEMs are compatible with the axis given in Chapter 2.

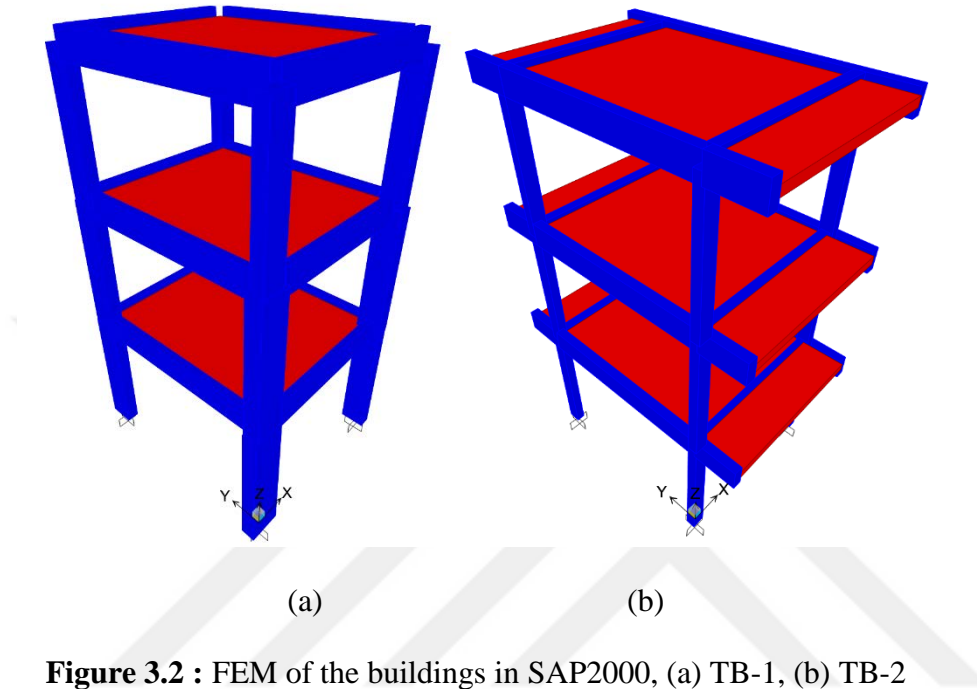


**Figure 3.2 :** FEM of the buildings in SAP2000, (a) TB-1, (b) TB-2

In the FEM, both columns and beams were modeled as frame elements based on a three-dimensional elastic beam-column formulation that considers the effects of bending, axial deformation, shear and torsion (Bathe and Wilson 1976) while slabs were modeled as shell elements. Owing to the buildings have 600 mm thick mat foundation, the connections of ground story columns were modeled as fixed support. The Young's modulus of the concrete ( $E_c$ ) was calculated using Eq. 3.13 based on the TS 500 (2000), (25710 MPa and 24270 MPa for the building TB-1 and TB-2, respectively). For the both buildings, the self-weight of the concrete ( $\gamma_c$ ) was taken as 25 kN/m<sup>3</sup>. Rigid diaphragms were assigned at all floor levels throughout the  $z$  direction.

$$E_c = 14000 + 3250\sqrt{f_{cm}} \quad (3.13)$$

Active DOFs in the FEM of the buildings were intentionally designed to be compatible with the dynamic test. Before giving more details about this choice while modelling, the basic concept underlying the theoretical DOFs and measurable DOFs is explained

in brief. Because, the development of any theoretical concept in the area of vibrations depends upon an understanding of the concept of the number of degrees of freedom ( $N$ ) of a system (Allemang 1999). This concept is extremely critical to the field of modal analysis since the number of modes of vibration of a system is equal to the number of degrees of freedom. At that point, the difference between the theoretical definition of the number of DOF and the number of measurement DOF ( $N_o, N_i$ ) should be explained first. The definition, which is normally associated with the concept of the number of DOF, is that the number of DOF for a mechanical system is equal to the number of independent coordinates (or minimum number of coordinates) which is required to locate and orient each mass in the mechanical system at any instant in time. Accordingly, in the case of a point mass, three DOFs are required since the location of the point mass includes the  $x$ ,  $y$ , and  $z$  translations of the center of gravity of the point mass. As in the case of a rigid body mass, in addition to the  $x$ ,  $y$ , and  $z$  translations,  $R_x$ ,  $R_y$ , and  $R_z$  rotations are also required in order to define both the orientation and location of the rigid body mass at any instant in time (Figure 3.3).

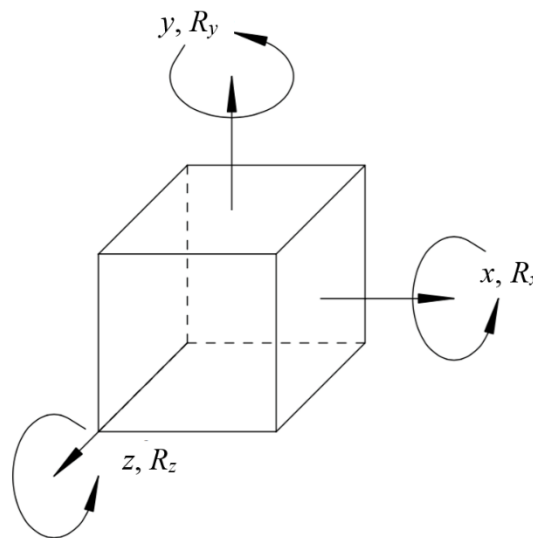


**Figure 3.3 :** DOF a rigid body.

When this definition is extended to any FEM, it is obvious that the number of DOF would be of infinite, however, due to a definite number of physical points of interest with six DOFs, the infinite number of DOF can be reduced to a large but finite number. When measurement limitations are taken into considerations (limited number of measurement DOF), the number of DOF of this system that are of interest is now reduced from infinity to a reasonable finite number. This can be considered as a

practical way if the limited frequency range that is of interest to the analysis is provided. For example, most dominant structural modes of vibration for a 4-story RC structure would be located between 0 and 20 Hz. When this limitation is considered, the number of DOF of this structure can be now reduced from infinity to a reasonable finite number. Therefore, the number of DOF ( $N$ ) can be assumed as the number of modes of vibration that are of interest. From this point of view, in the dynamic tests, as aforementioned, the accelerometers were mounted approximately the geometric center of each floor and the eccentric mass shaker excited the building at also the geometric center of the top floor. Therefore, the measurement DOFs were limited with the number of 9 ( $x$ ,  $y$  and  $R_z$  for each story). Therefore, the rigid body mass and centroidal mass moments of inertia values (centroidal mass for  $x$ ,  $y$  directions and mass moment of inertia for  $z$  direction) were assigned to the joints defined at the geometric centers of each floor levels. By this way, the analytical FRFs, which will be considered for model updating of the initial FEM, were determined for the points defined at the geometric center of each floor level as it was done in the experimental study. Figure 3.4 displays these joints named as ‘joint 1’, ‘joint 2’ and ‘joint 3’ which each of them includes 3 DOFs as U1, U2 and R3. The three DOFs U1, U2 and R3 are labeled as the nodes 1, 2 and 3, respectively for the 1<sup>st</sup> story, 4, 5 and 6, respectively for the 2<sup>nd</sup> story and 7, 8 and 9, respectively for the 3<sup>rd</sup> story.

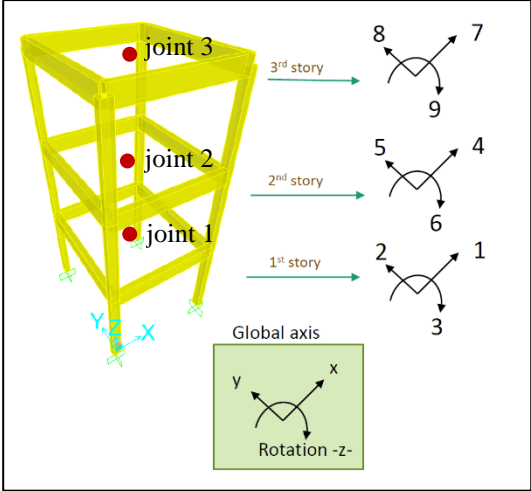


**Figure 3.4 :** Definition of DOFs



### 3.2.1.2 Determining the mass and stiffness matrices of the buildings

Afterward establishing the FEM of the buildings, modal analysis was performed so that the dynamic equation of motion can be written for each degree of freedoms (DOFs) at each joint and accordingly the stiffness and mass matrices of the system can be obtained. The general mathematical representation of dynamic equation of motion for single degree of freedom system is expressed using Newton's second law in equation 3.14. In this equation,  $\dot{x}$  and  $\ddot{x}$  refers the first and second derivative with respect to time of dependent variable  $x$ .

$$M\ddot{x}(t) + C\dot{x}(t) + Kx(t) = f(t) \quad (3.14)$$

After reminding this very well-known information, the definition and calculation of the mass and and stiffness matrices were explained:

SAP2000 assigns 6 DOFs ( $U1$ ,  $U2$ ,  $U3$ ,  $R1$ ,  $R2$  and  $R3$ ) for each joint defined throughout establishing the FEM. The notations  $U1$ ,  $U2$ ,  $U3$ ,  $R1$ ,  $R2$  and  $R3$  are DOFs for the global axis  $x$ ,  $y$ ,  $z$ ,  $Rx$ ,  $Ry$  and  $Rz$ , respectively (Figure 3.4 and Figure 3.5). A rigid diaphragm definition restrains 3 DOFs ( $U1$ ,  $U2$  and  $R3$ ) for each story and obviously the existing of fix support restrains all 6 DOFs.

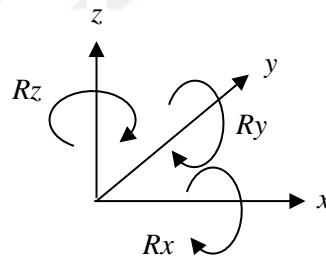


**Figure 3.5 :** Global axis

In the case of building TB-1, the number of the regular joints (available physical points alluded above) were 19, which includes 15 joints (4 of them for columns-beam joints + 1 of them is the joint defined to assign the mass = 5 joints  $\times$  3 stories = 15 joints) and 4 joints for the connections of the first story columns to fixed supports. Under these conditions, the number of the equations, and accordingly, size of the stiffness and mass matrices can be calculated as follows;

- 19 joints (regular joints)  $\times$  6 DOFs=114 equations,
- 4 joints (restrained)  $\times$  6 DOFs=24 (will be extracted),
- 3 constraints  $\times$  5 joints at each story  $\times$  3 DOFs=45 (will be extracted),

- 3 constraints  $\times$  3 DOFs=9 (additional equations arising from constraint definition),

Total number of the dynamic equation of motion is obtained as 54 (114-24-45+9=54). Accordingly, the size of the stiffness and mass matrices (m $\times$ n) are found to be 54 $\times$ 54. In the case of the building TB-2, the numbers of regular, restrained and constraint joints and the number of equations were calculated followingly;

- 31 joints (regular joints)  $\times$  6 DOFs=186 equations,
- 4 joints (restrained)  $\times$  6 DOFs=24 (will be extracted),
- 3 constraints  $\times$  9 joints at each story  $\times$  3 DOFs=81 (will be extracted),
- 3 constraints  $\times$  3 DOFs=9 (additional equations arising from constraint definition),

Accordingly, the dynamic equation of motion was obtained to be 90. Therefore, the size of the stiffness and mass matrices (m $\times$ n) of the building TB-2 are found to be 90 $\times$ 90.

Hence, MUP automatically computes SAP2000 for running the modal analysis so that the stiffness and mass matrices can be extracted. Subsequently, MUP reads the stiffness and mass matrices that are 54 $\times$ 54 and 90 $\times$ 90 lower half symmetrical matrices for the buildings TB-1 and TB-2, respectively. Afterwards MUP reads the stiffness and mass matrices, it computes a matrix condensation process in order to obtain a reduced mass and stiffness matrices with the size of 9 $\times$ 9 considering the DOFs given in Figure 3.4. General form of the lower half symmetrical mass and stiffness matrices are shown in equations 3.15 and 3.16. It should be noted that any experimental FRFs were obtained between the nodes 9 and 6 and/or 9 and 3 because no accelerometer setup was arranged to capture the vibration response of the buildings in rotational modes.

$$[M] = \begin{bmatrix} M_{11} & 0 & 0 & 0 & 0 & 0 & 0 & 0 & 0 \\ & M_{22} & 0 & 0 & 0 & 0 & 0 & 0 & 0 \\ & & M_{33} & 0 & 0 & 0 & 0 & 0 & 0 \\ & & & M_{44} & 0 & 0 & 0 & 0 & 0 \\ & & & & M_{55} & 0 & 0 & 0 & 0 \\ & & & & & M_{66} & 0 & 0 & 0 \\ & & & & & & M_{77} & 0 & 0 \\ & & & & & & & M_{88} & 0 \\ & & & & & & & & M_{99} \end{bmatrix}_{9 \times 9} \quad (3.15)$$

$$[K] = \begin{bmatrix} K_{11} & K_{12} & K_{13} & K_{14} & K_{15} & K_{16} & K_{17} & K_{18} & K_{19} \\ & K_{22} & K_{23} & K_{24} & K_{25} & K_{26} & K_{27} & K_{28} & K_{29} \\ & & K_{33} & K_{34} & K_{35} & K_{36} & K_{37} & K_{38} & K_{39} \\ & & & K_{44} & K_{45} & K_{46} & K_{47} & K_{48} & K_{49} \\ & & & & K_{55} & K_{56} & K_{57} & K_{58} & K_{59} \\ & & & & & K_{66} & K_{67} & K_{68} & K_{69} \\ & & & & & & K_{77} & K_{78} & K_{79} \\ & & & & & & & K_{88} & K_{99} \\ & & & & & & & & K_{99} \end{bmatrix}_{9 \times 9} \quad (3.16)$$

### 3.2.1.3 Calculation of analytical FRF

In this chapter, the derivation of numerical FRF was explained using well-known theoretical applications. Before that, the basic assumptions, which are considered throughout the model updating process, are giving in detail;

- The first assumption is that the buildings TB-1 and TB-2, even before and after quasi-static reversed cyclic loading, are linear systems whose dynamics equation of motion may be represented by a set of linear, second order, differential equations (Equation 3.14).
- The second assumption is that the buildings during the dynamic tests can be considered as time invariant, which means the coefficients in the linear, second order, differential equation of motion are constants and do not vary with time.
- The third assumption is that a FRF measured (or calculated) between points  $p$  and  $q$  by exciting at  $p$  and capturing the response at  $q$  equal to the one obtained by exciting by exciting at  $q$  and capturing the response at  $p$  ( $H_{pq}=H_{qp}$ ).

In order to derive the system transfer function, an equivalent equation of motion given in equation 3.14 was determined for the Laplace or  $s$  domain. The representation of equation of motion in Laplace domain has the advantage of converting a differential equation to an algebraic equation. Hence, this is accomplished by taking the Laplace transform of equation 3.14. The mathematical manipulations for taking the Laplace transform is given in equation 3.17.

$$L\{M\ddot{x} + C\dot{x} + Kx\} = M(s^2X(s) - sx(0) - \dot{x}(0)) + C(sX(s) - x(0)) + KX(s) \quad 3.17a$$

$$L\{M\ddot{x} + C\dot{x} + Kx\} = (Ms^2 + Cs + K)X(s) - Msx(0) - M\dot{x}(0) - Cx(0) \quad 3.17b$$

$$L\{f(t)\} = F(s)$$

After taking the laplace transform, equation 3.14 becomes;

$$[Ms^2 + Cs + K]x(s) = F(s) + (Ms + C)x(0) + M\dot{x}(0) \quad (3.18)$$

where  $x(0)$  is the initial displacement at time  $t = 0$  and  $\dot{x}(0)$  is the initial velocity at time  $t = 0$ . In case of the initial conditions are zero, equations 3.18 becomes as shown equation 3.19.

$$[Ms^2 + Cs + K]X(s) = F(s) \quad (3.19)$$

Let first part of equation 3.19 is referred as the system impedance ( $B(s)$ ), the equation 3.19 becomes;

$$B(s)X(s) = F(s) \quad (3.20)$$

Consequently, equation 3.20 is the equivalent representation of dynamic equation of motion given in equation 3.14. The Laplace domain ( $s$  domain) can be thought of as complex frequency ( $s = \sigma + j\omega$ ), where the  $\sigma$  refers variable of damping and the  $\omega$  refers variable of frequency (angular frequency). Therefore, the quantities in equation 3.20 can be considered of as follows;

- $F(s)$ : The Laplace domain (complex frequency) representation of the forcing function  $f(t)$ ,
- $X(s)$ : The Laplace domain (complex frequency) representation of the system response  $x(t)$ .

As it is shown in equation 3.20, the system response  $X(s)$  is directly related to the system forcing function  $F(s)$  through the quantity  $B(s)$  (Allemang 1999). If the system forcing function  $F(s)$  and considering its response  $X(s)$  are known,  $B(s)$  can be calculated as given in equation (3.21);

$$B(s) = \frac{F(s)}{X(s)} \quad (3.21)$$

When the system frequency response function is defined as  $H(s)=1/B(s)$ , it can be represented in Laplace domain as shown in equation (3.22);

$$H(s) = \frac{X(s)}{F(s)} = \frac{1/M}{s^2 + \left(\frac{C}{M}\right)s + (K/M)} \quad (3.22)$$

The denominator term of the equation 3.22 is the system characteristic equation and the roots of the characteristic equation are given in equation (3.23).

$$\lambda_{1,2} = -\left(\frac{c}{2M}\right) \pm \sqrt{\left(\frac{c}{2M}\right)^2 - (K/M)} \quad (3.23)$$

In the case of multi degree of freedom systems, the system impedance matrix ( $B(s)$ ) become as given in equation (3.24).

$$[B(s)] = s^2[M] + s[C] + [K] \quad (3.24)$$

Since  $[H(s)]=[B(s)]^{-1}$ , the inverse of the impedance matrix can be calculated using equation 3.25.

$$[H(s)] = [B(s)]^{-1} = \frac{Adjoint(B(s))}{\det[B(s)]} \quad (3.25)$$

When the equation (3.25) derives for two DOFs system for the sake of example as given in equation (3.26);

$$[H(s)] = \begin{bmatrix} H_{11} & H_{12} \\ H_{21} & H_{22} \end{bmatrix} = \frac{\begin{matrix} s^2 M_{22} + s C_{22} + K_{22} & -(s^2 M_{12} + s C_{12} + K_{12}) \\ -(s^2 M_{21} + s C_{21} + K_{21}) & s^2 M_{11} + s C_{11} + K_{11} \end{matrix}}{(s^2 M_{11} + s C_{11} + K_{11})(s^2 M_{22} + s C_{22} + K_{22}) - (s^2 M_{12} + s C_{12} + K_{12})(s^2 M_{21} + s C_{21} + K_{21})} \quad (3.25)$$

As aforementioned for equation 3.22, the denominator term of the equation 3.25 is also the system characteristic equation and the roots of the characteristic equation are given in equation (3.26).

$$\det[B(s)] = E(s - \lambda_1)(s - \lambda_1^*)(s - \lambda_2)(s - \lambda_2^*) \quad (3.26)$$

where the  $\lambda_1$ ,  $\lambda_1^*$ ,  $\lambda_2$  and  $\lambda_2^*$  are the roots of the characteristic equation and poles of the transfer function.  $E$  is the constant coefficient of the highest order term in the polynomial (product/sum of the mass terms). Details can be found in Allemang 1999.

Hence, the analytical FRF of the buildings TB-1 and TB-2 were calculated for the initial FEM by substituting the mass and stiffness matrices, which were obtained by MUP, into equation 3.24. (Figure 3.6 and Figure 3.7). It should be noted that while the numerical FRF (algebraic) was calculated, any terms related to damping was initially ignored, it means damping matrix  $[C]$  was taken as zero matrix in the equations.

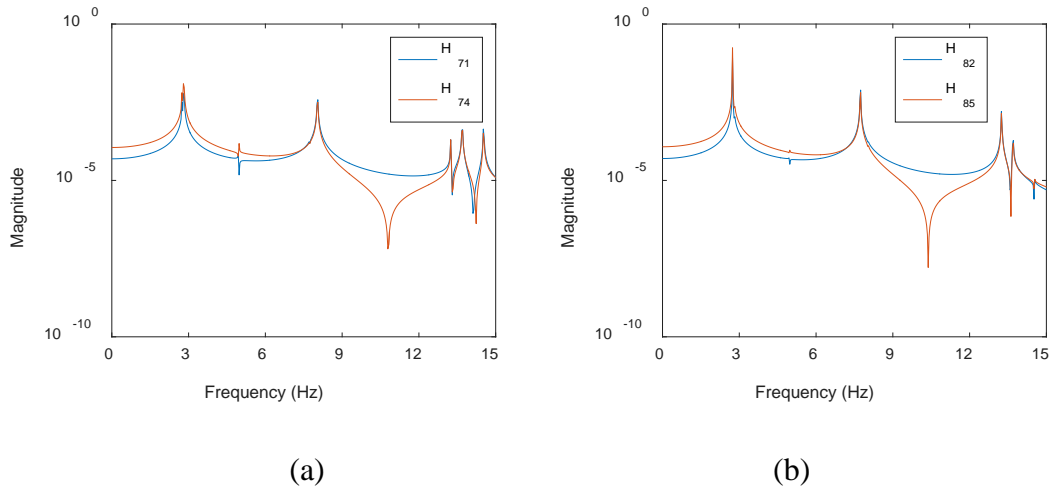


**Figure 3.6 :** Analytically determined FRFs through initial FEM of the building TB-1, (a)  $x$  direction, (b)  $y$  direction.

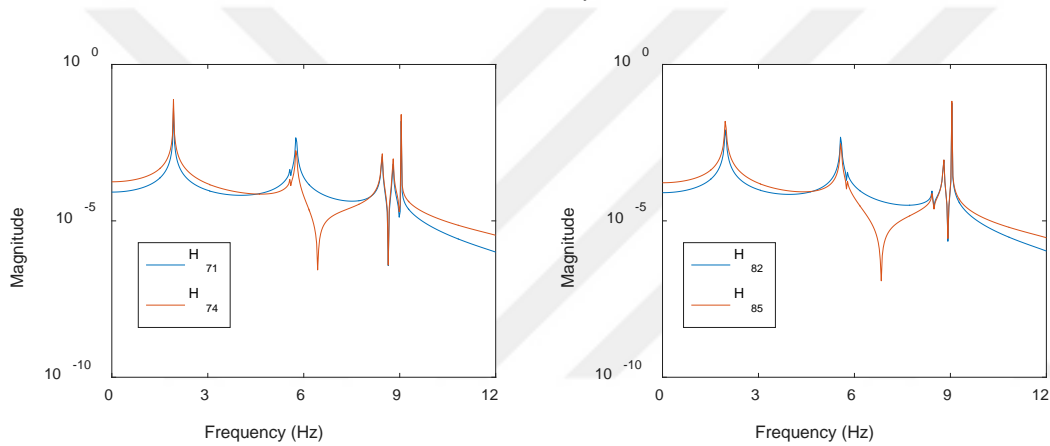


**Figure 3.7 :** Analytically determined FRFs through initial FEM of the building TB-2, (a)  $x$  direction, (b)  $y$  direction.

Following the calculation of analytical FRF of the buildings, MUP just pass to the next step that is the comparison of the analytically determined and experimentally obtained FRFs.

### 3.2.1.4 Comparison of analytically determined and experimentally obtained FRFs

In this sub-step of the damage identification algorithm, the analytically determined FRF, that is the output of the previous sub-step, were compared with the experimentally obtained FRF. As seen in the Figure 3.1, if the analytically determined and experimentally obtained FRFs do not match, the pre-defined parameters are changed in the FEM (sub-step: *establishing FEM*) and then  $[M]$  and  $[K]$  matrices are read again (sub-step: *determining  $[M]$  and  $[K]$  matrices*) and subsequently a new

analytical FRF are calculated (sub-step: *analytical FRF*) in order to re-compare with the experimentally obtained FRF (current sub-step). This process is computed by iteratively changing the pre-defined parameters till minimizing the error function which was introduced in terms of  $R^2$  measure. Hence, the comparison of the analytically determined and experimentally obtained FRFs are given in the Figure 3.8 and Figure 3.9.

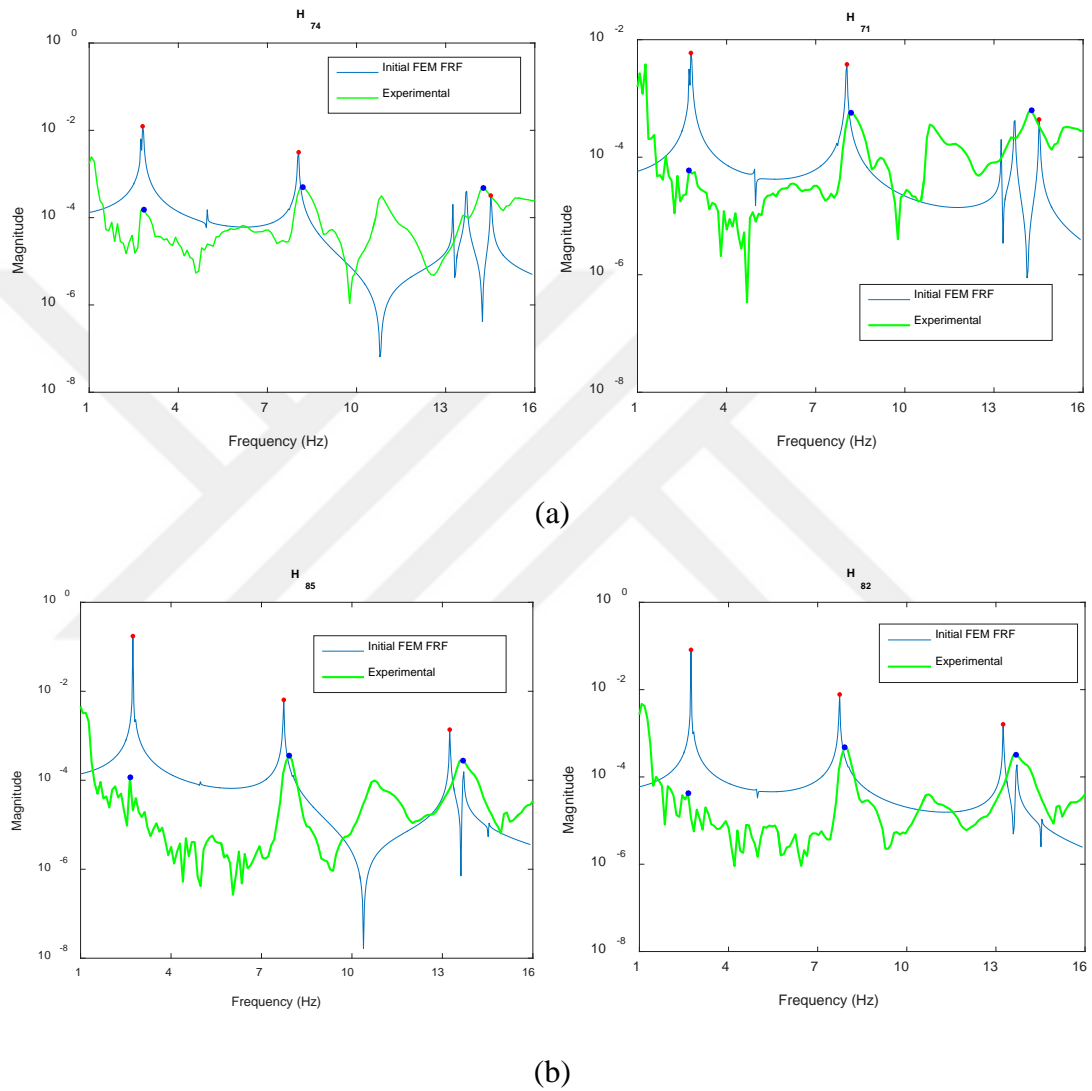


**Figure 3.8 :** Comparison of analytically determined FRF (from initial FEM) and the experimental FRF of the building TB-1, (a)  $x$  direction, (b)  $y$  direction.

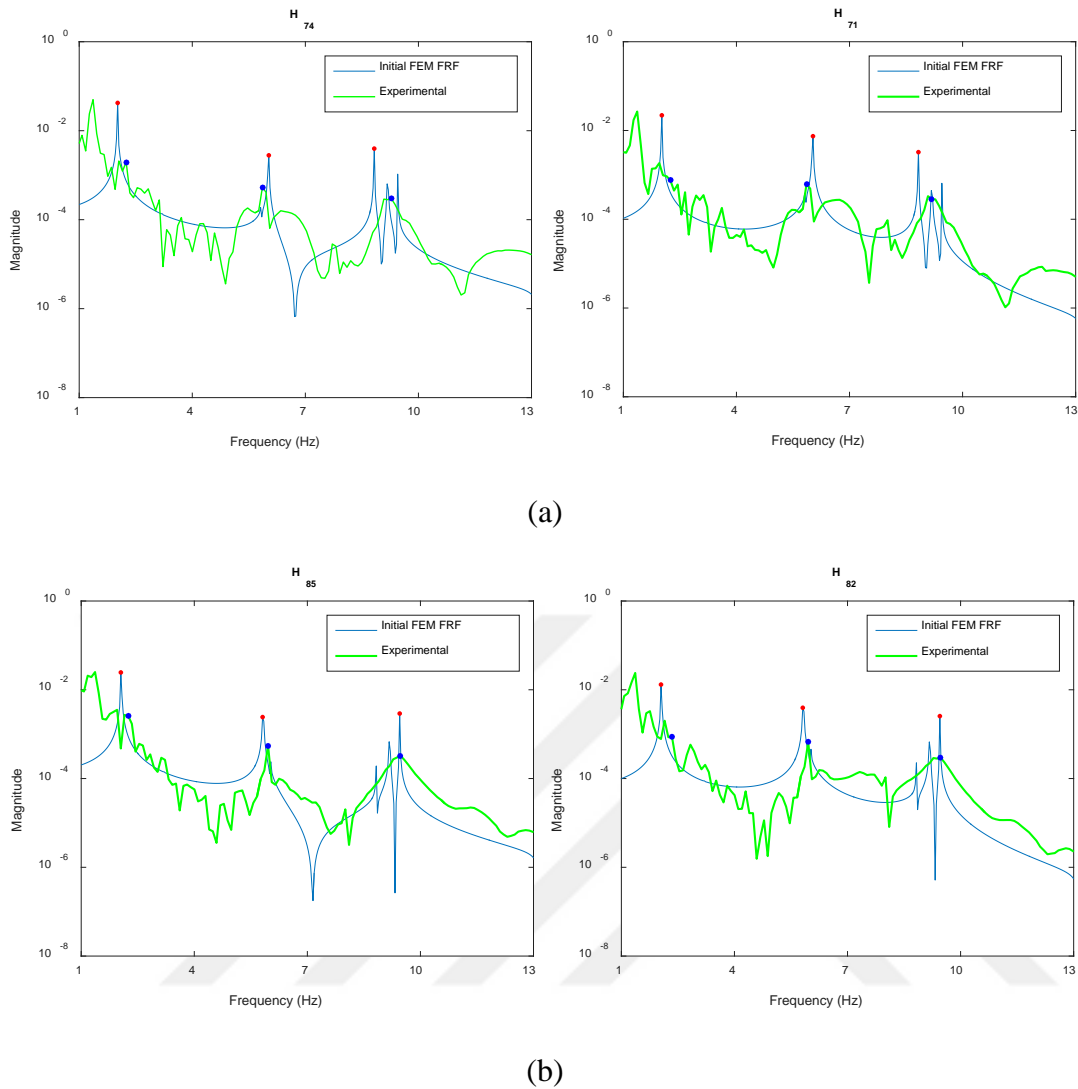


**Figure 3.9 :** Comparison of analytically determined FRF (from initial FEM) and the experimental FRF of the building TB-2, (a)  $x$  direction, (b)  $y$  direction.

When the result of the error function is taken into consideration, it is clear that the  $[M]$  and  $[K]$  required to be updated. To begin with, parameter sensitivity analysis was performed. Because FRFs must be sensitive to changes in selected unknown parameters in order to ensure successful model updating. For this purpose, FRF sensitivity to the changes in young modulus of concrete and unit weight of concrete was displayed in Figure 3.10 to Figure 3.12. As it was expected, the FRF of the initial FEM is sensitive to change in young modulus of the concrete.



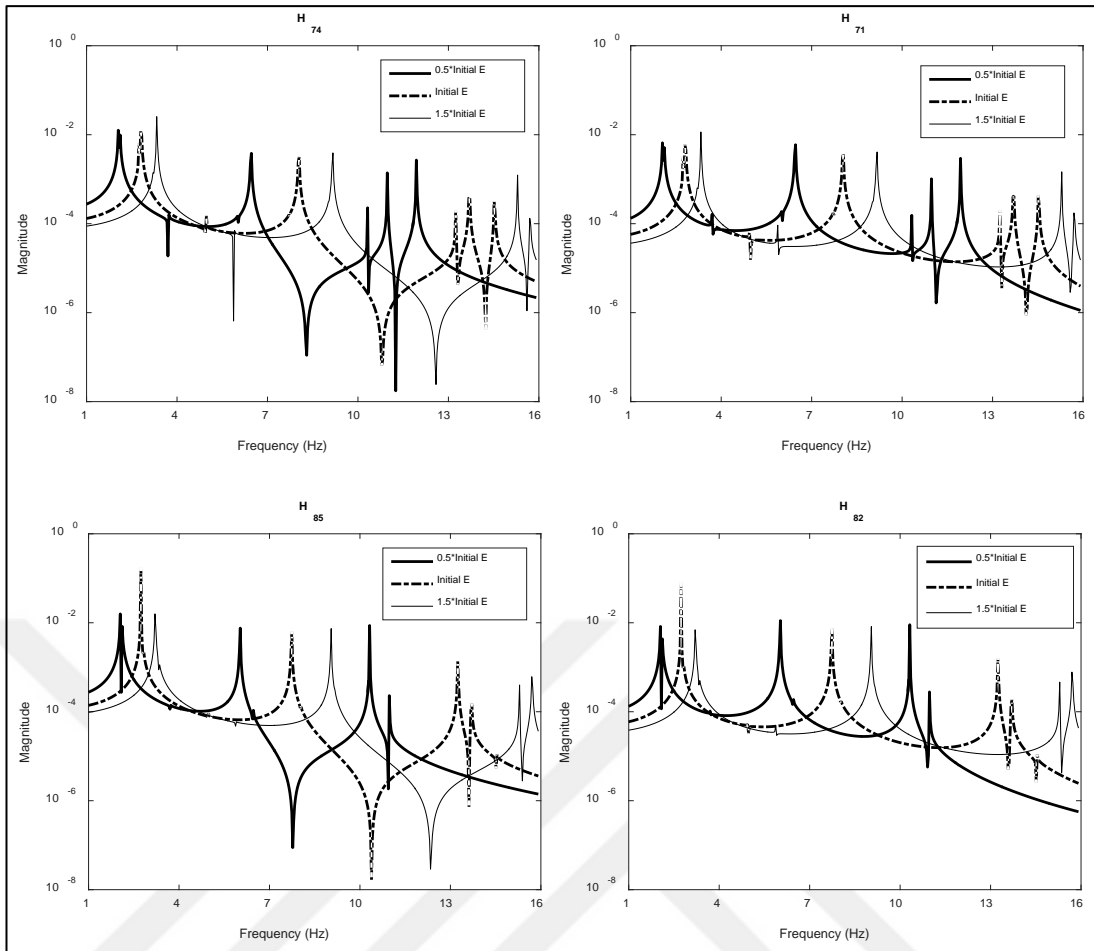


**Figure 3.10 : FRF sensitivity to changes in  $E_c$  (the building TB-1).**

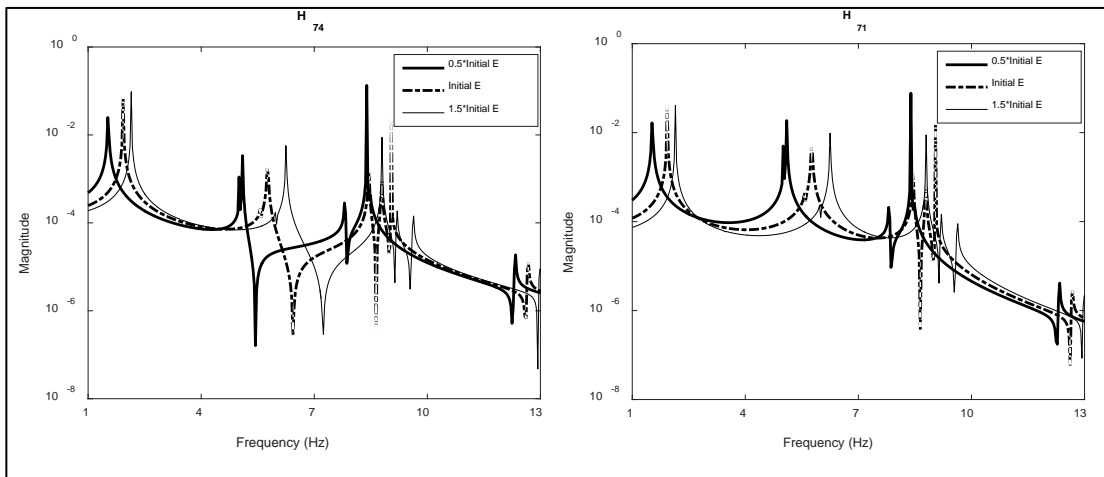


**Figure 3.11 : FRF sensitivity to changes in  $E_c$  (the building TB-2).**

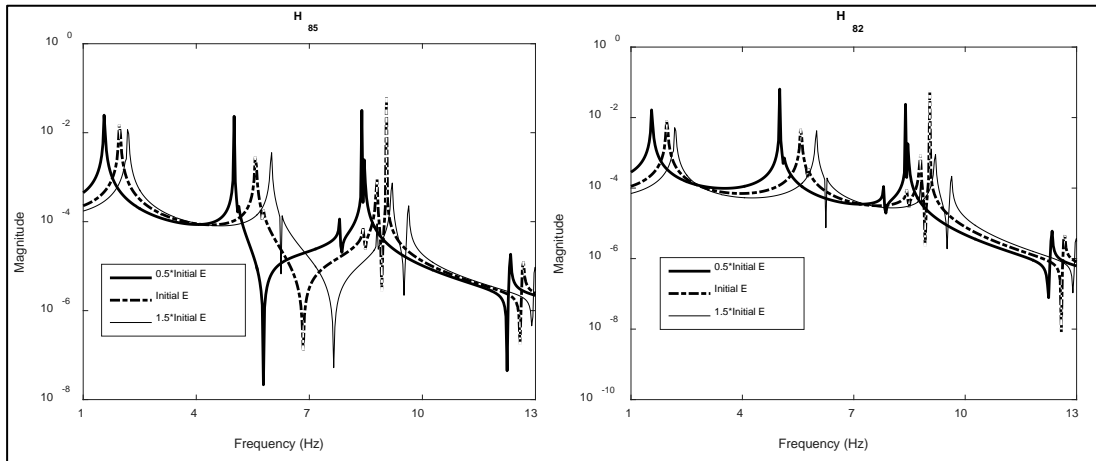


**Figure 3.11 (continued) :** FRF sensitivity to changes in  $E_c$  (the building TB-2).

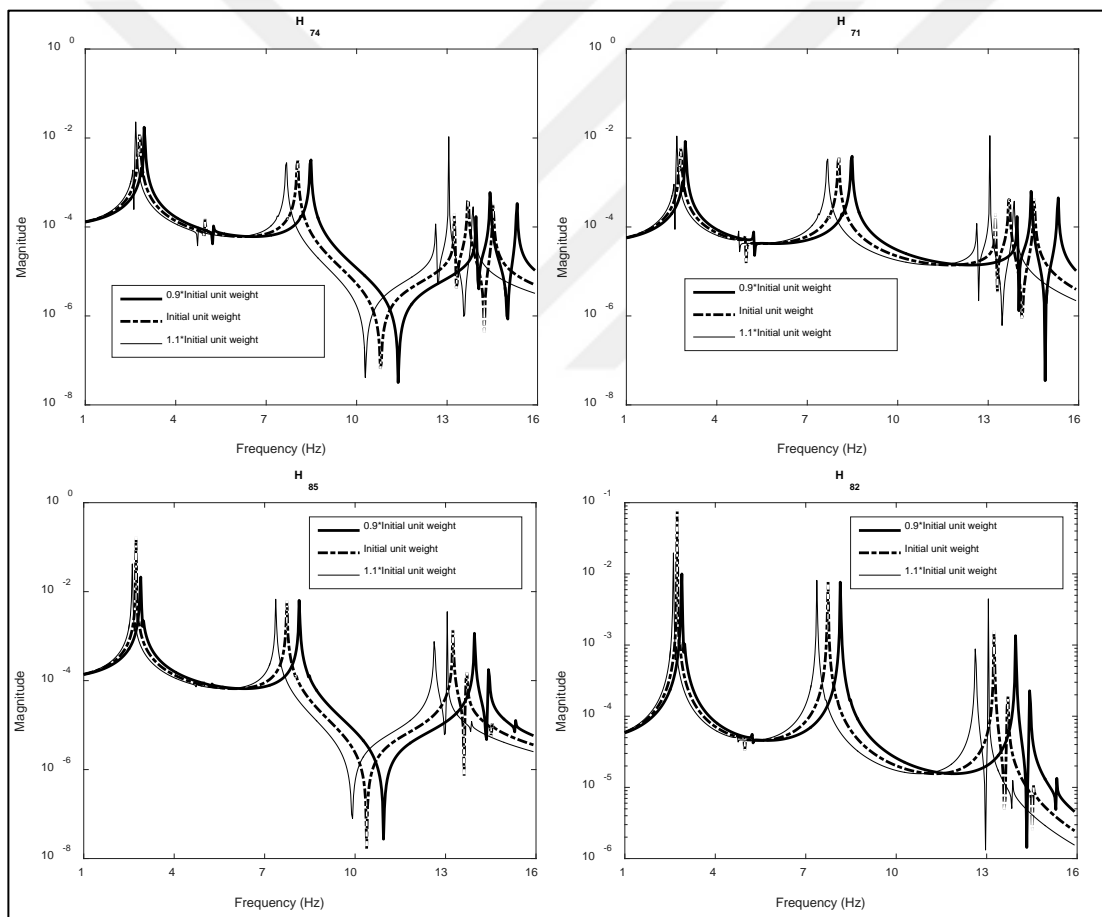


**Figure 3.12 :** FRF sensitivity to changes in unit weight of concrete (the building TB-1).

As seen in the figures, FRFs are sensitive to changes in  $E_c$  and  $\gamma_c$ . Consequently, according to these the sensitivity results, initial FEM was updated by changing the young modulus of concrete ( $E_c$ ) and unit weight of concrete ( $\gamma_c$ ) and keeping the damping coefficients constant (Step 1). Owing to the two-step damage identification

algorithm, model updating is performed by preventing the coupled effects of Stiffness/Mass from damping parameters.

In the model updating process, first the resonance, anti-resonance and noise-suspected points were determined in the experimentally obtained FRF as suggested by (Palencia et al. 2015), then the frequency points located  $\pm 0.3$  Hz were excluded from updating. In fact, since the experimentally obtained FRFs includes lots of noisy components, the modal updating process in Step 1 was mostly performed for the resonant points and their  $\pm 0.4$  Hz wide range of neighbourhoods. Results of the model updating process for the buildings are given in Figure 3.13 and Figure 3.14.

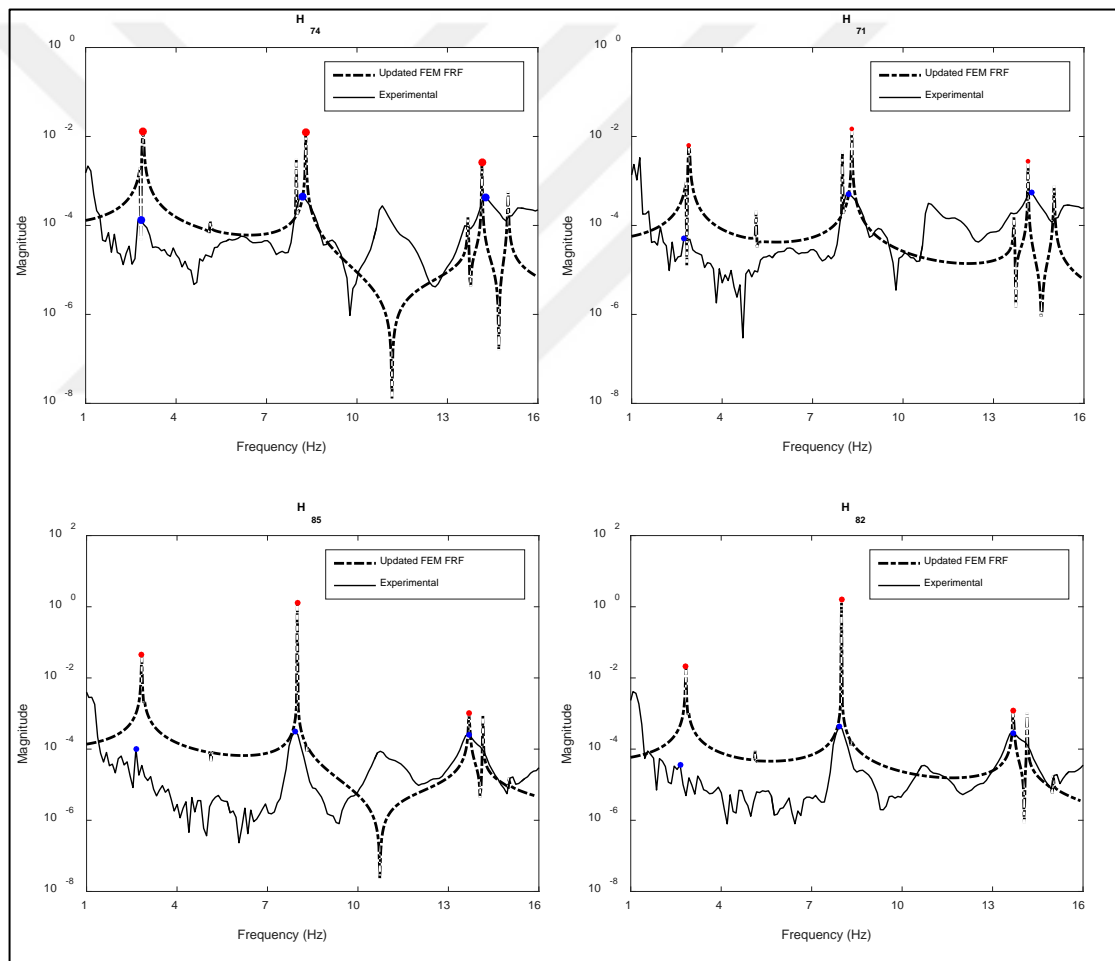


**Figure 3.13 :** Model updating results for the building TB-1 (Step 1: [K] and [M]).

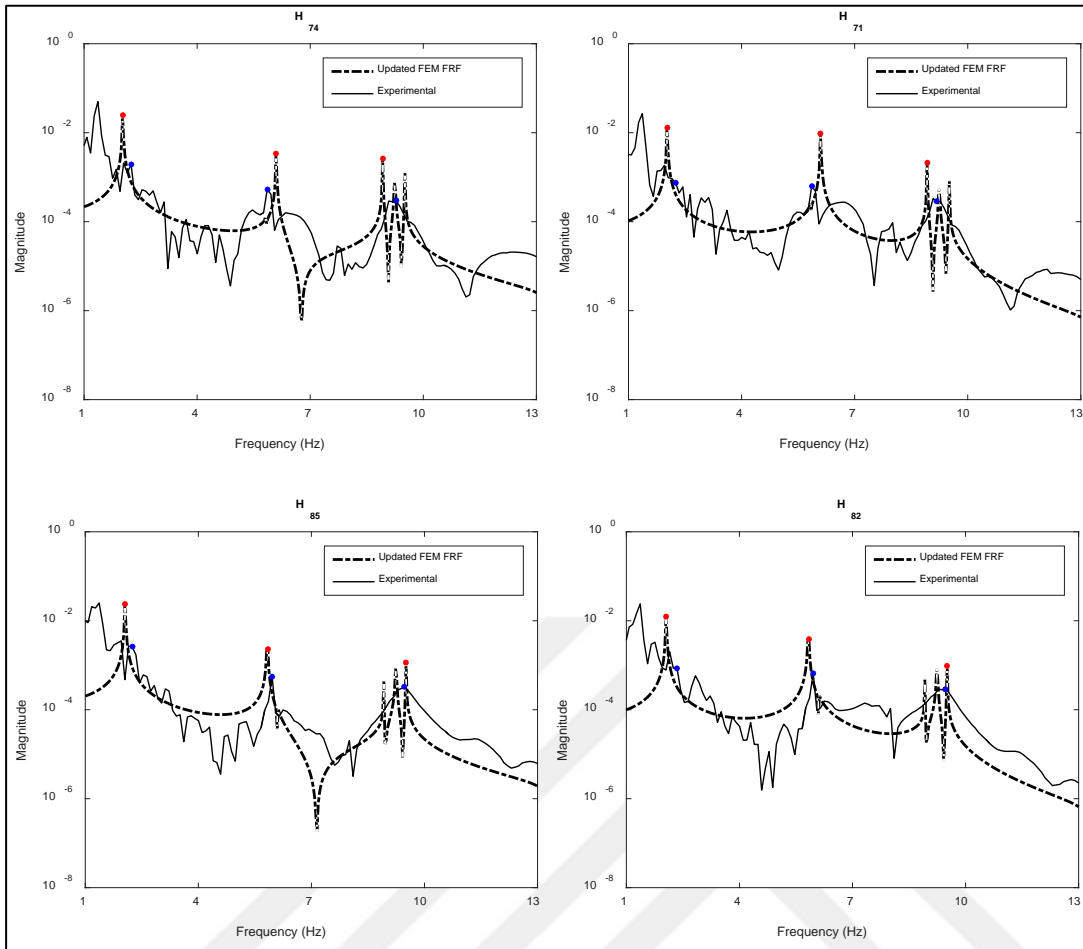


**Figure 3.14 :** Model updating results for the building TB-2 (Step 1: [K] and [M]).

The [M] and [K] matrices of the buildings were updated for the values of  $E_c^{updated}$  and  $\gamma_c^{updated}$  given in Table 3.1 and the first step of the two-step damage identification algorithm (Step 1) is terminated. Although the concrete compressive strength of the building TB-1 was higher than that of building TB-2 (13 MPa and 10 MPa, respectively), the elastic modulus of the building TB-1 was found to be lower than the one found for the building TB-2. This can be attributed the poor workmanship while concrete pouring for the building TB-1.

Followingly, MUP then compute for updating the damping parameters (Step 2). As seen in the Table, since the building TB-1 is an existing structure, the young modulus of concrete was found to be relavely lower then the one calculated considering the suggestion of the design code.

**Table 3.1** : Updated values of young modulus and unit weight of concrete.

Buildings	Initial FEM		Updated FEM		Change	
	$E_c$ (kN/m <sup>2</sup> )	$\gamma_c$ (kN/m <sup>2</sup> )	$E_c^{updated}$ (kN/m <sup>2</sup> )	$\gamma_c^{updated}$ (kN/m <sup>3</sup> )	$E_c$ (%)	$\gamma_c$ (%)
TB-1	25710000	25	17800000	24	9.19	4.00
TB-2	24270000	25	26500000	24.3	1.11	2.80

### 3.2.2 Updating damping ratio (Step 2)

Identification of the damping matrix was performed via changes on the modal damping ratios while keeping  $[K]$  and  $[M]$ , which were updated at the previous step, constant. In this step, as it was also considered in Step 1, minimization of the differences between the analytical and experimental FRFs was aimed at the resonant frequencies. As it was given in Figure 3.1b, this is carried out by substituting the iteratively changed damping ratios into the analytical FRF definition.

Calculation process of the analytical FRF was explained in previous sub-steps. In short, the inverse of the system impedance matrix derived in Laplace domain ( $[B(s)] = s^2[M] + s[C] + [K]$ ) is equal to the system transfer function ( $[H(s)] = [B(s)]^{-1}$ ). As aforementioned, in the Step 1,  $[M]$  and  $[K]$  were numerically identified while damping parameters ( $\sigma = \omega\zeta$ ) included in Laplace constant ( $s = \sigma + j\omega$ ) and accordingly  $[C]$  were considered as zero. Subsequently, analytical FRF was calculated for pre-defined frequency range ( $f = 0-16$  Hz and  $\omega = 2\pi f$ ) where the identified resonant frequencies of the buildings were identified in experimental study. At this point, in order to compute the Step 2, it was required to substitute the damping parameters into the FRF equation. However, as previously mentioned, the experimental FRFs include lots of noisy components. Accordingly, this situation creates problem for updating the damping ratio even just for the resonant frequencies. Therefore, it was decided to consider the experimental FRFs calculated using Method 2 (given in Chapter 2) throughout the updating of damping. If it is necessary to remind it again, the building response captured by accelerometers throughout the force vibration test was amplified by dividing it to corresponding square of the shaker operating frequency. At this point, it is the fact that the analytical FRF calculated using 1<sup>st</sup> method (explained in Chapter 2) is not the analytically equivalent of the experimental FRF which is the ratio of acceleration response of the building to corresponding shaker operating frequency square (experimental FRF calculated using 2<sup>nd</sup> method). In order to derive the

analytical FRF equals to the ratio of acceleration response of the building to corresponding shaker operating frequency square, the numerical manipulations followed were listed below;

- First, the equation of FRF updated in Step 1 were determined in Laplace domain. As aforementioned, at the end of the Step 1, analytical FRF of the system was obtained numerically. The second order differential equation of the analytical FRF of the system in Laplace domain was derived using curve fitting technique defined in MATLAB curve fitting toolbox. To put it more explicitly, MATLAB fits a curve for each resonant frequency and produce a second order differential equation in laplace domain for each of them. The algebraic summation of each equation gives the equation of system transfer function. By this way, mathematical description of the buildings is figured out.
- The acceleration response of the building was then produced by assigning the shaker excitation force to the system transfer function in MATLAB (Sine analysis).

Lastly, acceleration responses of the each DOFs were divided to the shaker operating frequency square as it was done to obtain the experimental FRF. Hence analytical FRF which can be compared with the experimental FRF obtained using second method in  $g/Hz^2$  unit, was determined. A schematic view of the revised version of the Step 2 given in Figure 3.1b is displayed in Figure 3.15. In this figure, the revised sub-steps were shown within red outlines. It should be noted that, the model updating process performed for an experimental FRF without so much noisy component does not required to follow these additional sub-steps.

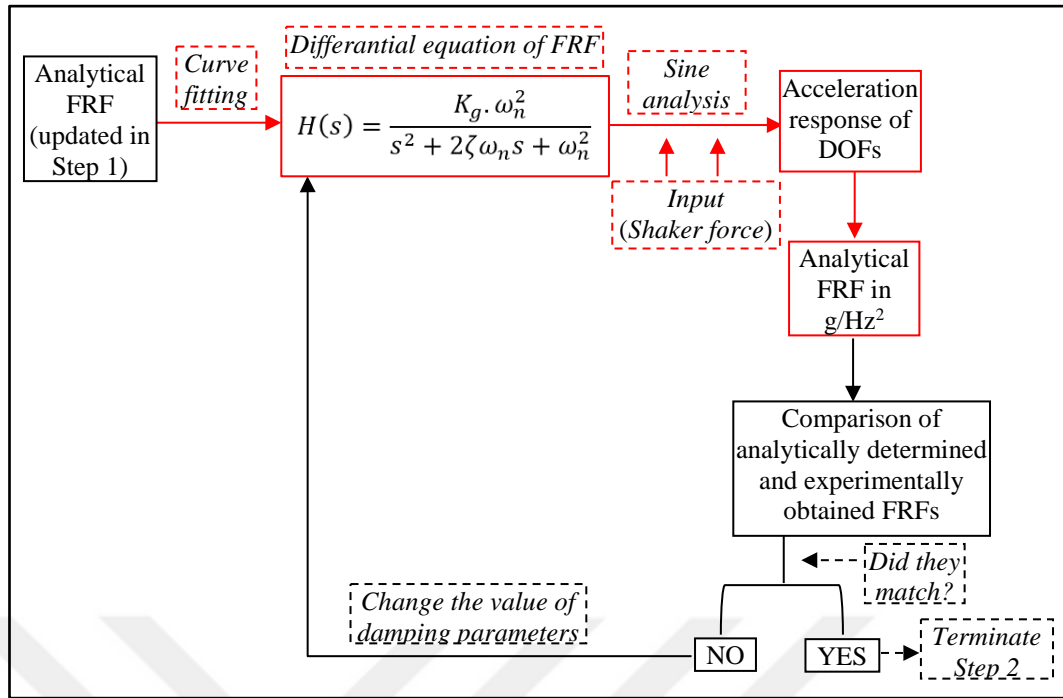


**Figure 3.15 :** Schematic view of revised algorithm for the Step-2.

Consequently, [K] and [M] of the buildings were updated using the first step of the two-step algorithm. For now, the algorithm will be resumed for updating the damping parameters by keeping [K] and [M] constant as alluded above.

### 3.2.2.1 Curve fitting

The differential equation of the analytical FRF updated in Step 1 was obtained using curve fitting technique. A second order differential equation was produced for each resonant frequency which was considered for updating the damping (Equation 3.27). However, since the updated FEM FRFs do not include any damping coefficient, the second term of the denominator ( $2\zeta\omega_n s$ ) will be zero (because  $\zeta$  and  $s$  equal to zero). Application of curve fitting technique for updated FEM FRF is shown in Figure 3.16 and Figure 3.17. As seen in these figures, at the end of a very efficient curve fitting application process, the second-order differential equations produced for each DOF were obtained and given in Table 3.2 and Table 3.3. As seen in tables, although the FRFs, that curves were fitted, have no damping coefficient, some of the produced differential equations have damping coefficients. However, they are reasonable small to be neglected.

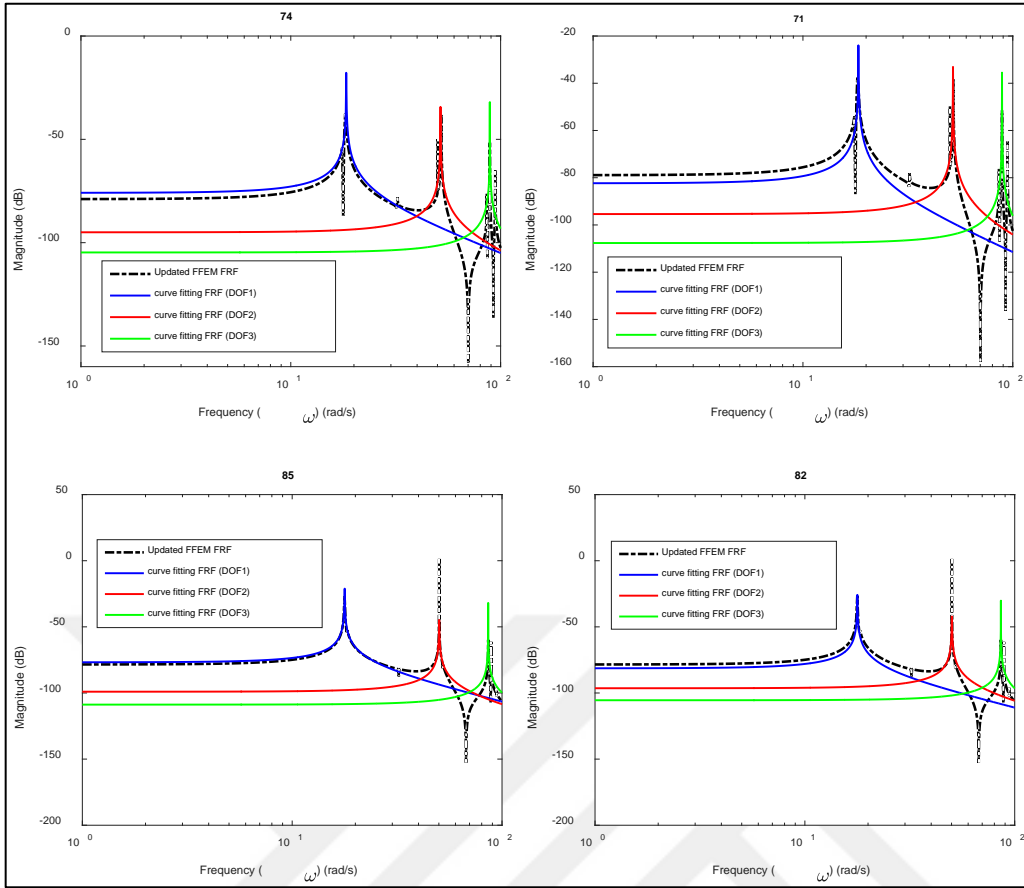


**Figure 3.16 :** Application of curve fitting (the building TB-1).

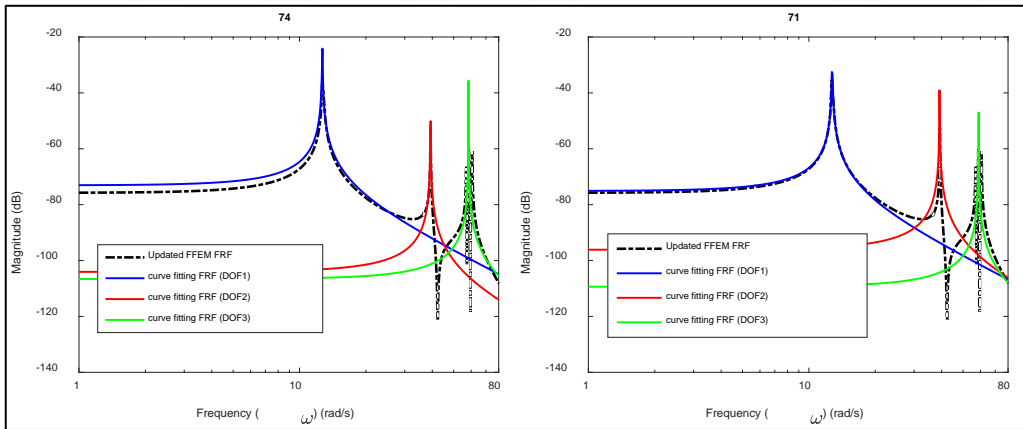


**Figure 3.17 :** Application of curve fitting (the building TB-2).



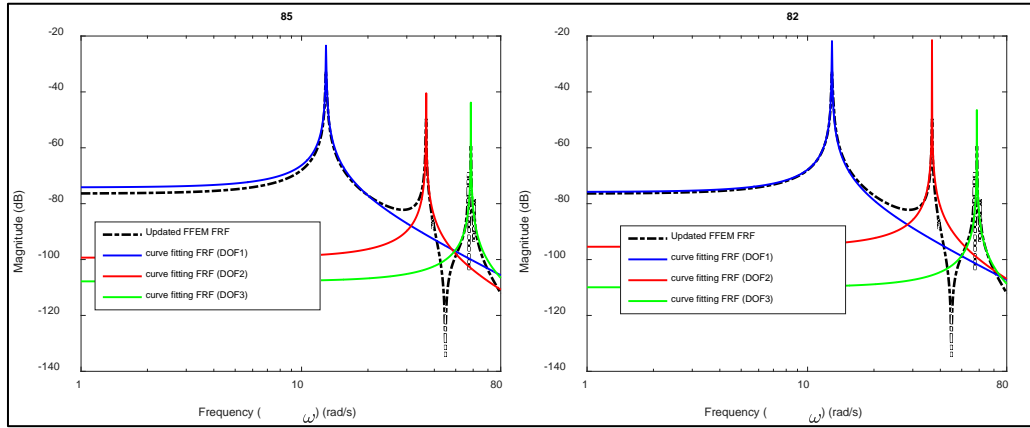


**Figure 3.11 (continued) :** FRF sensitivity to changes in  $E_c$  (the building TB-2).

$$H(s = \sigma + j\omega_n) = \frac{K_g \omega_n^2}{s^2 + 2\zeta \omega_n s + \omega_n^2} \quad (n = \text{number of related DOF}) \quad 3.27$$

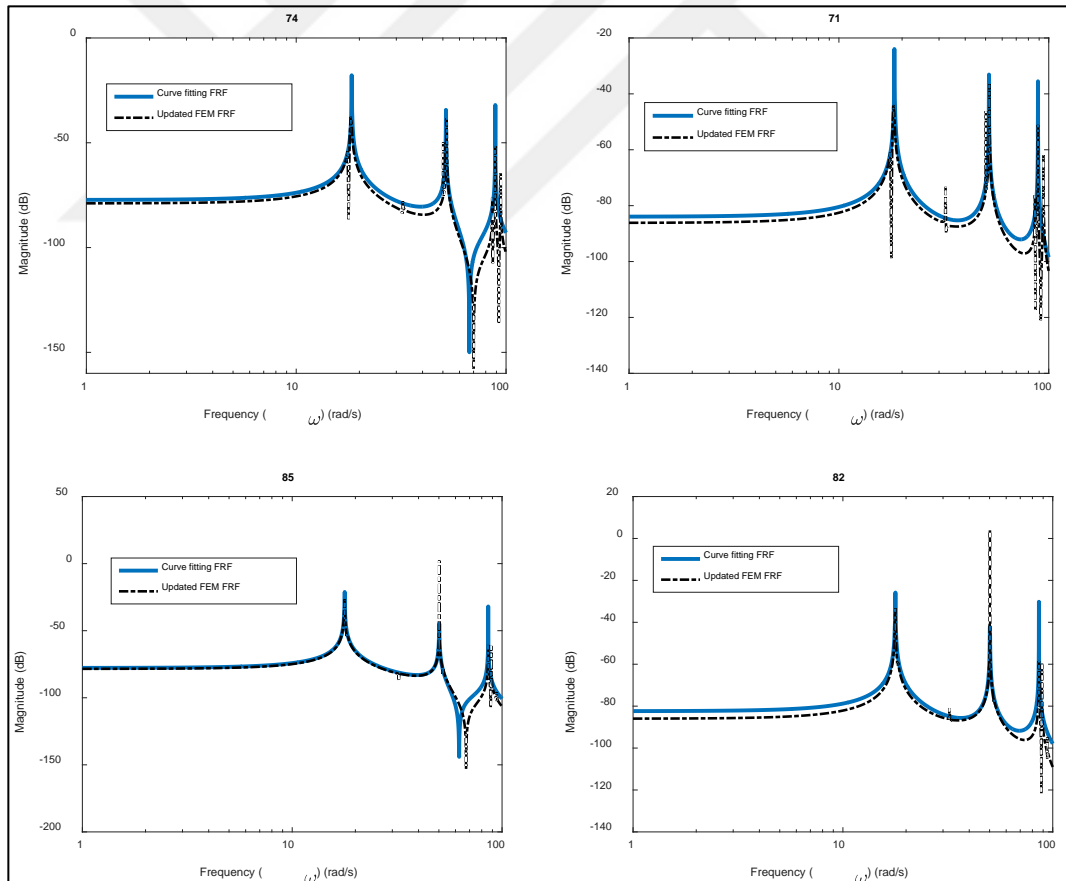


**Figure 3.18 :** FRF of the system (the building TB-1).

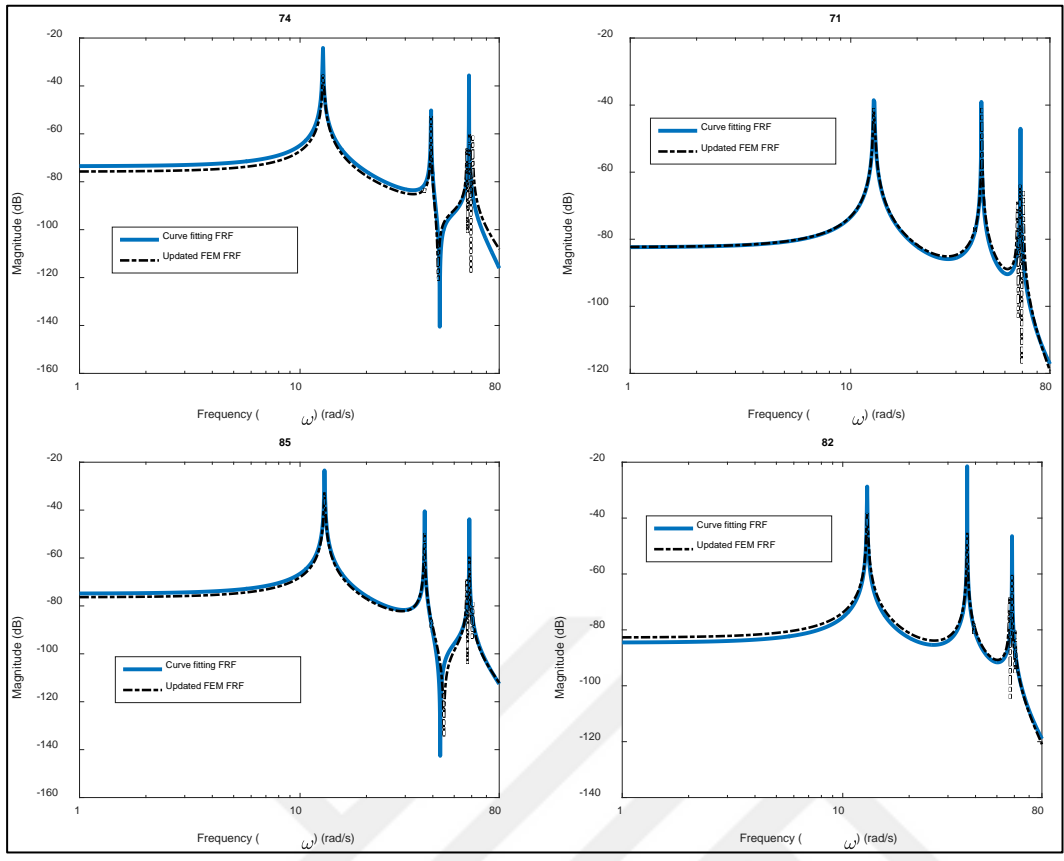


**Figure 3.19 : FRF of the system (the building TB-2).**

**Table 3.2 :** Second-order differential equation of FRFs of updated FEM of the building TB-1.

DOF*	$s=\sigma_1 + j\omega_1$	$s=\sigma_2 + j\omega_2$	$s=\sigma_2 + j\omega_2$
$H_{74}$	$\frac{0.05429}{s^2 + 1.043e-19 s + 338.1}$	$\frac{-0.04762}{s^2 + 2672}$	$\frac{-0.04579}{s^2 + 7897}$
$H_{71}$	$\frac{0.02578}{s^2 + 3.935e-19 s + 338.1}$	$\frac{-0.04574}{s^2 + 2692}$	$\frac{0.03271}{s^2 + 7897}$
$H_{85}$	$\frac{0.0456}{s^2 + 316}$	$\frac{0.0281}{s^2 + 8.716e-28 s + 2520}$	$\frac{-0.02675}{s^2 + 4.751e-18 s + 7384}$
$H_{82}$	$\frac{0.02709}{s^2 + 3.594e-22 s + 316}$	$\frac{0.03808}{s^2 + 1.766e-25 s + 2520}$	$\frac{-0.03927}{s^2 + 2.053e-20 s + 7384}$

\*  $\sigma_n = \zeta_n \omega_n$ , n: number of degree of freedom (n=1,2,3)

**Table 3.3 :** Second-order differential equation of FRFs of updated FEM of the building TB-2.

DOF*	$s=\sigma_1 + j\omega_1$	$s=\sigma_2 + j\omega_2$	$s=\sigma_2 + j\omega_2$
$H_{74}$	$\frac{-0.03568}{s^2 + 160.9}$	$\frac{-0.009653}{s^2 + 2.545e-21 s + 1541}$	$\frac{-0.0159}{s^2 + 3405}$
$H_{71}$	$\frac{0.0143}{s^2 + 162.7}$	$\frac{-0.02391}{s^2 + 1531}$	$\frac{0.01176}{s^2 + 3460}$
$H_{85}$	$\frac{0.03264}{s^2 + 167}$	$\frac{0.01459}{s^2 + 2.548e-20 s + 1349}$	$\frac{-0.01396}{s^2 + 4.25e-20 s + 3431}$
$H_{82}$	$\frac{0.01211}{s^2 + 166.2}$	$\frac{-0.02277}{s^2 + 1344}$	$\frac{-0.01095}{s^2 + 6.243e-21 s + 343}$

\*  $\sigma_n = \zeta_n \omega_n$ , n: number of degree of freedom (n=1,2,3)

**Table 3.4 :** Second-order differential equation of FRFs of updated FEM of the building TB-1.

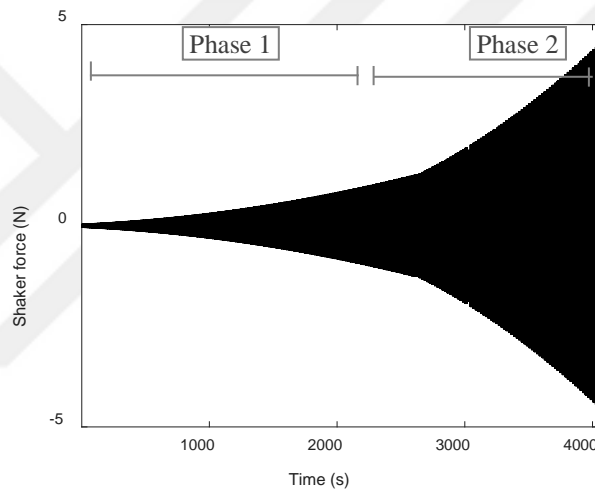
DOF*	FRF of the system
$H_{74}$	$\frac{-0.03911 s^4 - 9.742e-21 s^3 + 43.86 s^2 - 5.198e-17 s + 9.769e05}{s^6 + 1.043e-19 s^5 + 1.091e04 s^4 + 1.102e-15 s^3 + 2.467e07 s^2 + 2.201e-12 s + 7.134e09}$
$H_{71}$	$\frac{0.01275 s^4 - 5.128e-21 s^3 - 4.577 s^2 - 1.075e-16 s + 4.557e05}{s^6 + 3.935e-19 s^5 + 1.093e04 s^4 + 4.167e-15 s^3 + 2.484e07 s^2 + 8.367e-12 s + 7.189e09}$
$H_{85}$	$\frac{-0.009258 s^4 + 8.309e-20 s^3 + 159.3 s^2 + 5.036e-16 s + 7.614e05}{s^6 + 4.751e-18 s^5 + 1.022e04 s^4 + 1.347e-14 s^3 + 2.173e07 s^2 + 3.782e-12 s + 5.879e09}$
$H_{82}$	$\frac{0.02827 s^4 - 2.253e-22 s^3 + 86.35 s^2 + 1.089e-18 s + 4.464e05}{s^6 + 2.089e-20 s^5 + 1.022e04 s^4 + 6.177e-17 s^3 + 2.173e07 s^2 + 2.303e-14 s + 5.879e09}$

**Table 3.5 :** Second-order differential equation of FRFs of updated FEM of the building TB-2.

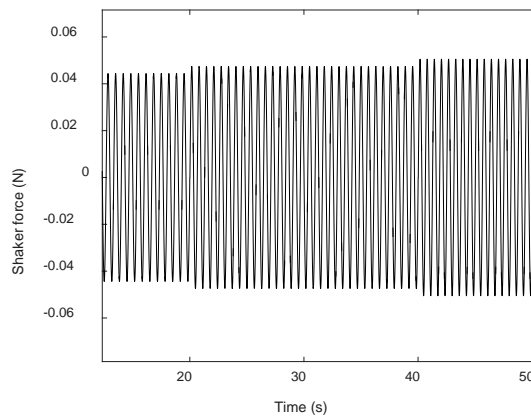
DOF*	FRF of the system
$H_{74}$	$\frac{-0.01012 s^4 - 5.033e-23 s^3 - 115 s^2 - 3.026e-19 s - 1.78e05}{s^6 + 2.545e-21 s^5 + 5107 s^4 + 9.074e-18 s^3 + 6.043e06 s^2 + 1.394e-15 s + 8.443e08}$
$H_{71}$	$\frac{0.002147 s^4 + 4.644 s^2 + 6.52e04}{s^6 + 5154 s^4 + 6.11e06 s^2 + 8.619e08}$
$H_{85}$	$\frac{0.00409 s^4 + 1.243e-21 s^3 + 82.36 s^2 + 4.562e-18 s + 1.396e05}{s^6 + 6.798e-20 s^5 + 4947 s^4 + 1.561e-16 s^3 + 5.427e06 s^2 + 2.417e-14 s + 7.73e08}$
$H_{82}$	$\frac{0.0151 s^4 + 2.591e-23 s^3 + 63.16 s^2 + 2.022e-19 s + 1.136e05}{s^6 + 6.243e-21 s^5 + 4941 s^4 + 9.428e-18 s^3 + 5.404e06 s^2 + 1.394e-15 s + 7.662e08}$

### 3.2.2.2 Sine analysis

Afterward obtaining the FRF equation of the buildings, which clearly means the mathematical based description of the system, a sine analysis was carried out in order to produce the acceleration response of the each DOFs that were considered for model updating process. It was also explained above, shaker sinusoidal force applied in dynamic tests was chosen as input force in sine analysis. After implementing the input force to the transfer function of the system calculated in previous sub-step, the acceleration response of the each DOFs were generated as response of the system throughout MATLAB. The shaker sinusoidal force and the corresponding acceleration response of DOFs are given in Figure 3.20.



(a)



(b)

**Figure 3.20 :** Input force in sine analysis, (a) shaker sinusoidal force, (b) zoomed view.

As aforementioned when giving the details of the experimental study, the frequency range (1.5 Hz-15 Hz) considered in forced vibration test was swept by applying the eccentric mass shaker as 2-phases (e.g.: 1.5-8 Hz and 8-15 Hz). These two phases were also considered in the sine analysis. This is the reason for the increment of the shaker force by time in Figure 3.20a has 2 different trends; in phase 1, the shaker swept 1.5-8 Hz frequency range with 0.05 Hz frequency increment steps while in phase 2, it swept 8-15 Hz frequency range with 0.1 Hz frequency increment steps. Different than the exact forced vibration test in the field, the each increment step was applied for 20-second periods in sine analysis. For the sake of example, for the time period 0-20 s, 20-40 s and 40-60 s, the shaker operating frequency is 1.5 Hz, 1.55 Hz and 1.60 Hz (0.05 Hz increment steps), respectively while corresponding shaker force ( $F=e.\omega^2$ ) equals to 0.044 N, 0.047 N and 0.051 N, respectively (Figure 3.20b).

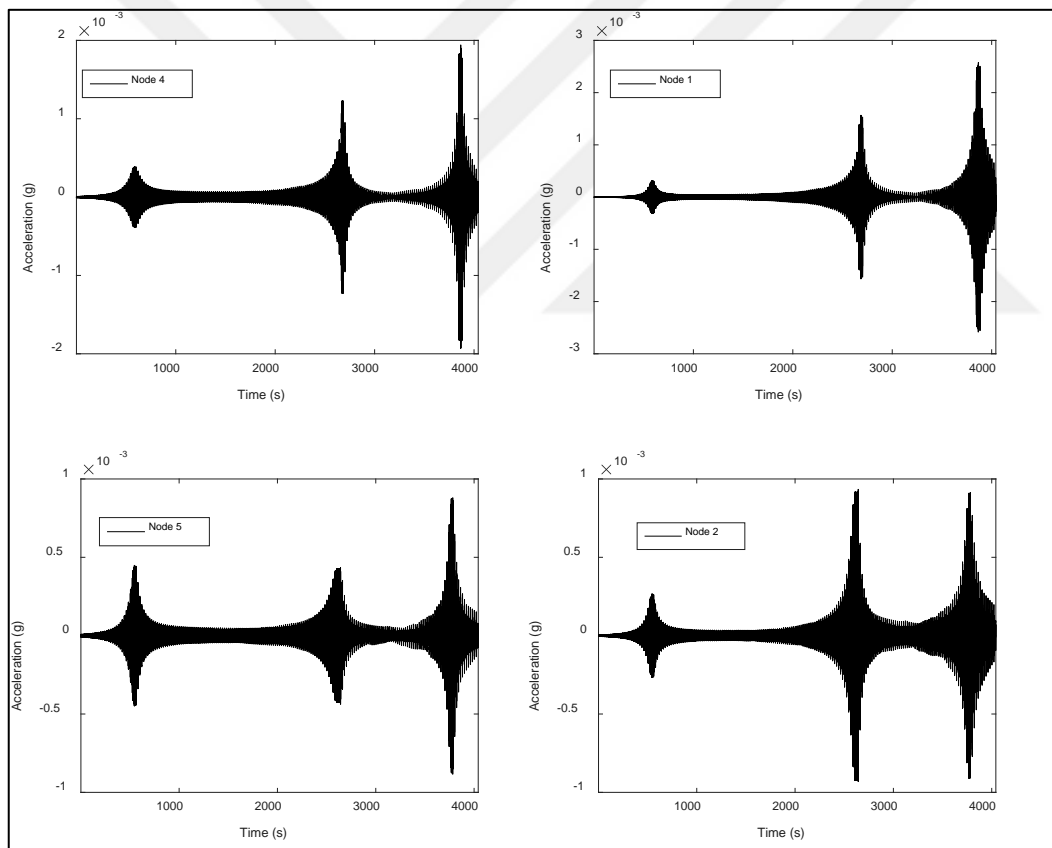


**Figure 3.21 :** Response of the DOFs to sine analysis (The building TB-1).

Hence the response of each DOFs, which were considered for damping updating, corresponds to shaker sinusoidal force is given in Figure 3.21 and Figure 3.22. It should be noted that the given nodes in the figures are corresponding notations of



DOFs previously shown in Figure 3.4. As seen in the figures, acceleration signal includes many spikes. It is attributed that while frequency range was swept step by step (steps as 0.05 Hz between 1.5-8 Hz and steps as 0.1 Hz between 8-15 Hz), a settlement of time was required. In order to disregard the spikes occurred at transition between 2 frequency steps, the first 5 seconds of total implementation time period of each frequency step were neglected throughout the FRF calculation. Apart from that, it is clear that the time of resonant frequencies for each 3 peaks can be figured out in these figures.

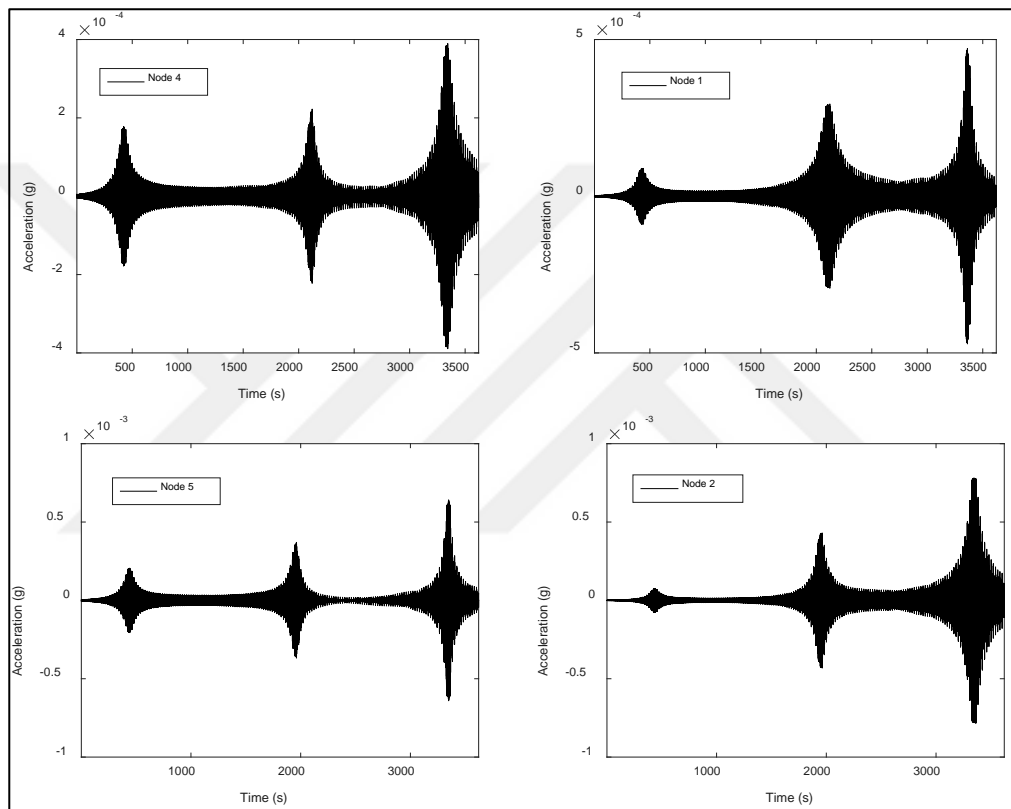


**Figure 3.22 :** Response of the DOFs to sine analysis (The building TB-2).

### 3.2.2.3 Calculation of analytical FRF

In this sub-step, the analytical FRF as the ratio of the corresponding acceleration response of DOFs to shaker operating frequency square was calculated in order to compare with the experimental FRF estimated using the 2<sup>nd</sup> method. In fact, as it has been already understood from the above definition of FRF, it was calculated by dividing the acceleration responses of the each DOFs to the shaker operating frequency square.

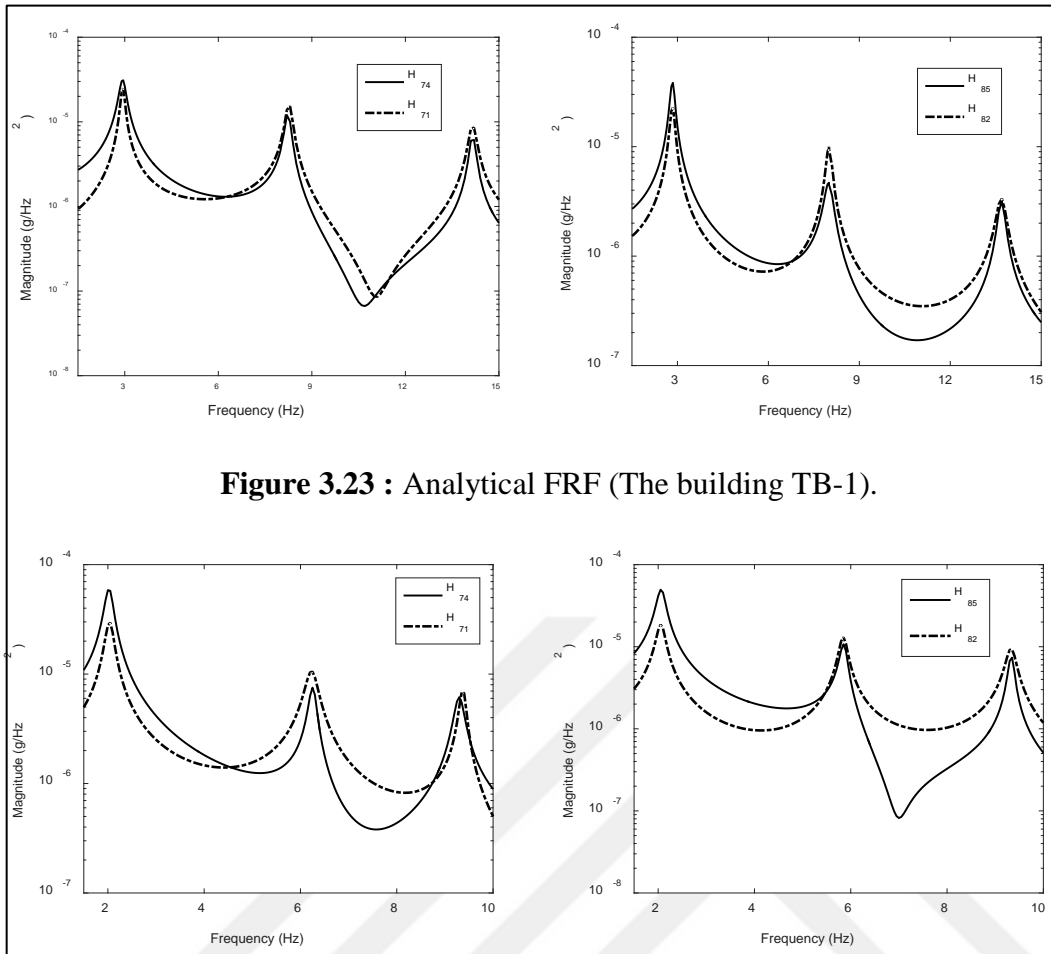


**Figure 3.23 : Analytical FRF (The building TB-1).**

**Figure 3.24 : Analytical FRF (The building TB-2).**

### 3.2.2.4 Comparison of analytically determined and experimentally obtained FRFs

The analytically estimated and the experimentally obtained FRFs were compared in order to perform the model updating of damping parameters. This process was repeated by changing the damping parameters iteratively (by keeping [K] and [M] constant) and substituting them into second-order differential equation of FRF of the system till the analytical and experimental FRFs match. In the case of damping parameters, as it can be seen in the tables, the denominator of the FRF equation includes damping ratio ( $\zeta$ ) as well as the terms of laplace constant  $s$ , which depends also damping ratio and angular frequency. In short, the damping ratio ( $\zeta_n$ ) for each DOF was iteratively changed and substituted into the equation. By this means of this iterative process, the damping ratios are also updated, and the second step of the two-step damage identification algorithm was terminated (Figure 3.25 and Figure 3.26).

Hence, the updating damping ratios through the two-step damage identification algorithm can be seen in Table 3.6.

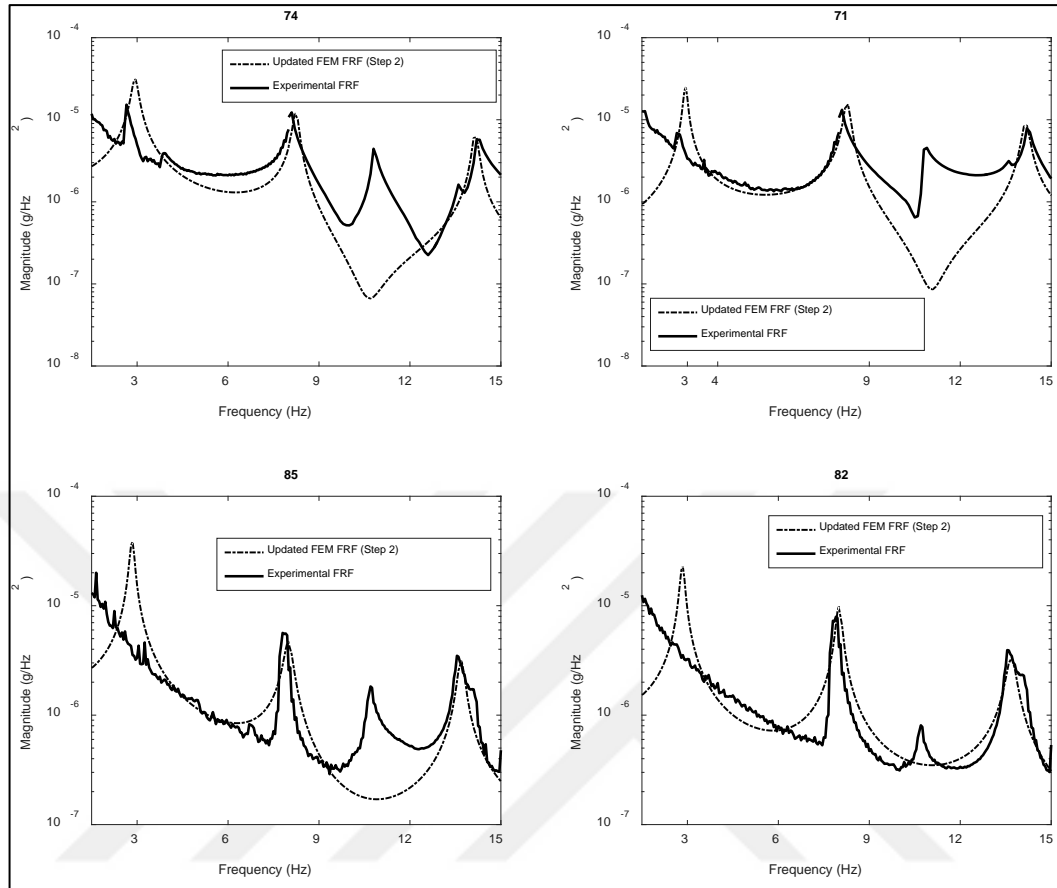


**Figure 3.25 :** Model updating results of the building TB-1 (Step 2: Damping ratio).

Consequently, two-step damage identification algorithm was completed and the initial FEM of the undamaged case of the buildings TB-1 and TB-2 were updated. Hereupon, the updated version of these buildings will be named as ‘baseline model’. The two-step damage identification algorithm will then be implemented to baseline models of the buildings TB-1 and TB-2 with the purpose of damage detection, location and quantification issues of the buildings whose damages were introduced in previous chapter.

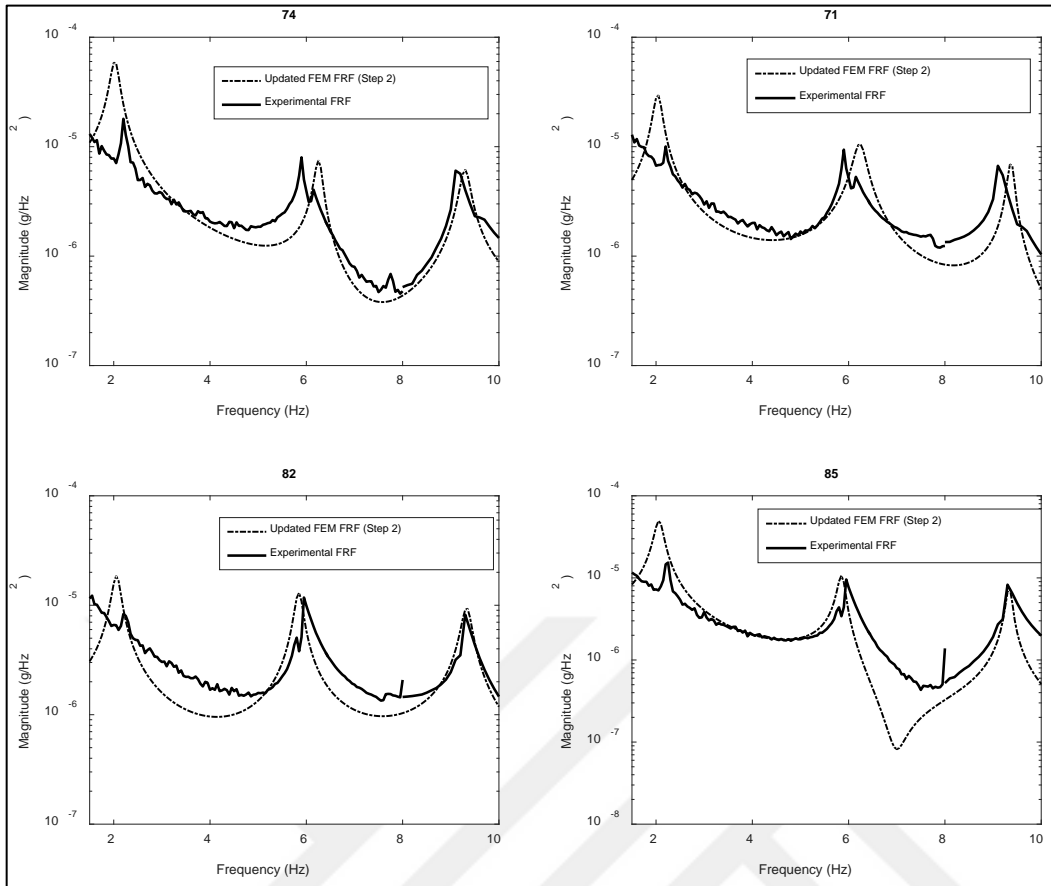


**Figure 3.26 :** Model updating results of the building TB-2 (Step 2: Damping ratio).

**Table 3.6 :** Updated damping ratios for each DOFs.

Buildings	x direction			y direction		
	$\zeta_1$	$\zeta_2$	$\zeta_3$	$\zeta_1$	$\zeta_2$	$\zeta_3$
TB-1	0.035	0.010	0.007	0.025	0.016	0.007
TB-2	0.040	0.011	0.010	0.040	0.011	0.007

### 3.3 Concluding remarks

In this chapter, an automated model updating program (MUP), which was coded in MATLAB and links it with SAP200 through API, was introduced. MUP computed two-step model updating based damage identification algorithm for updating the initial FEM of the buildings TB-1 and TB-2. In this text, the initial FEM definition refers the FEM of the buildings for the undamaged case. The updated version of the initial FEMs were named as ‘baseline model’. The initial FEM of the buildings were updated via changes stiffness, unit weight and damping parameters so that they can capture the dynamic characteristics obtained through forced vibration tests.

The revision in the two-step algorithm in terms of updating the damping parameters provided to obtain the mathematical description of the buildings. Significantly, curve fitting clearly became a useful and practical part of the model updating algorithm and found to be a promising tool in case of the dynamic measurements including noisy components.

The updating of the TB-1 showed that the young's modulus of concrete calculated considering the suggestions given in TS 500 (2000) was relatively high. This can be attributed that the building TB-1 is an existing sub-standard RC structure.





## **4. DAMAGE IDENTIFICATION**

In this chapter, the introduced two-step damage identification algorithm was implemented to detect, localize and quantify the damage in the buildings TB-1 and TB-2. Therefore, a Level 3 damage identification process was achieved. Based on engineering judgment and previous researches (Palencia et al. 2015, Li et al. 2011), it is well known that damage affects the stiffness of the structure and obviously mass (or unit weight) can be excluded from the damage identification process. Therefore, only the parameters related to the stiffness of the baseline model were updated in Step 1. Furthermore, prior to the application of Step 1, a grouping strategy was followed to reduce the unknown parameters in damage identification. For this purpose, the unknown parameters related to stiffness, which are expected to be similar properties, were grouped. This would be a useful methodology when the number of unknown parameters, which lead to degrade the stiffness and consequently lateral load bearing capacity of the buildings, are taken into consideration.

### **4.1 Damage identification of the building TB-1**

As it was explained, the quasi-static cyclic loading was implemented to the building up to 1.5% d.r. (the 1<sup>st</sup> story d.r.). During the quasi-static loading, any shear damage was not experienced on the building while the overall response of the building was governed by nonlinear flexural behavior at the critical end regions of beams and columns (Comert et al. 2016). Furthermore, any significant damage was experienced on the beams and columns of the 2<sup>nd</sup> and the 3<sup>rd</sup> stories. Consequently, approximately 15% strength degradation was observed in the lateral load bearing capacity. The change in FRFs of the building induced by the explained damage was previously given in the Chapter 2. The comparison of the experimentally obtained damaged FRF with baseline FEM FRF, which were obtained in previous chapter, is shown in Figure 4.1. Hence, to detect, localize and quantify the damage of the building TB-1 due to quasi-static cyclic lateral loading (as 1.5% 1<sup>st</sup> story drift ratio), a model updating was implemented by changing the parameters explained below via MUP till the FRFs given

in Figure 4.1 match. As aforementioned, prior to the model updating process, grouping of unknown parameters was carried out.

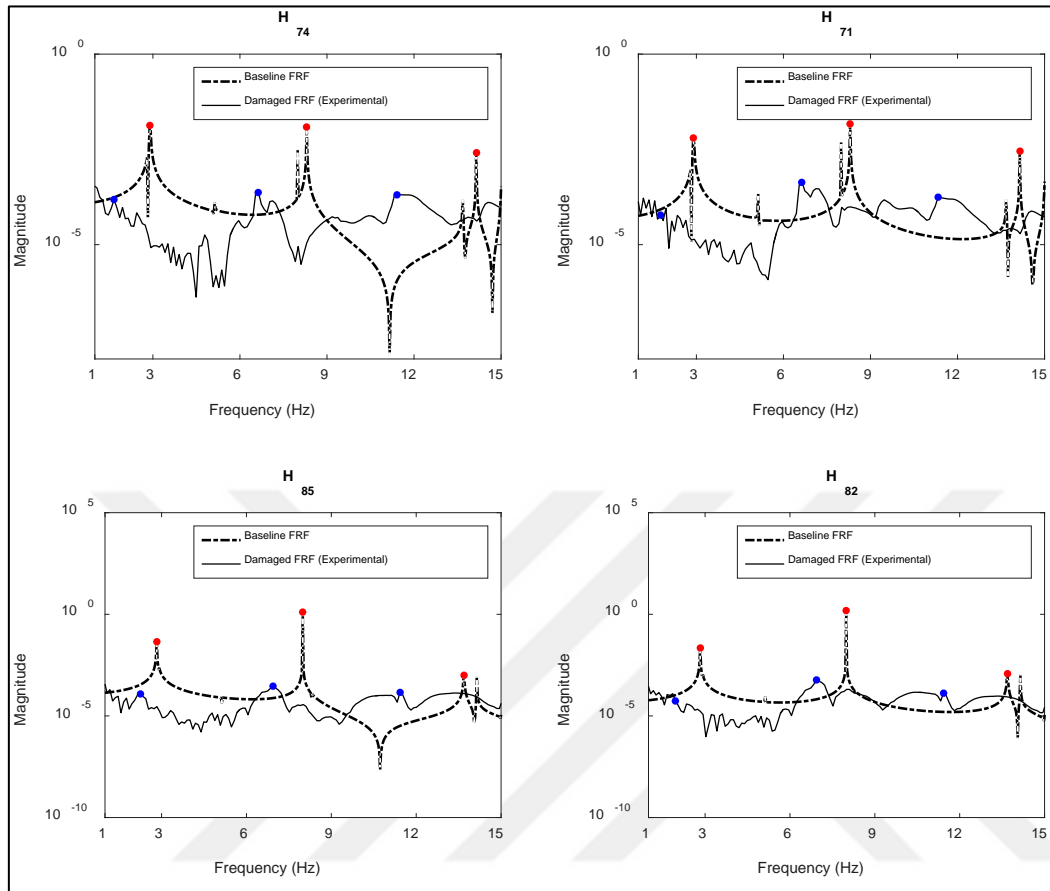


**Figure 4.1** : Baseline and damaged FRFs of the building TB-1.

#### 4.1.1 Updating [K] (Step 1)

##### 4.1.1.1 Grouping of unknown parameters and FRF sensitivity

Based on the engineering judgment leaning on various experiences from the actual damages occurred due to earthquakes as well as controlled laboratory tests, the initial (column-foundation joint) and boundary conditions (column-beam joints) are expected to be affected from the reversed cyclic lateral loading. Similarly, when it is considered that the current seismic performance assessment codes attain to estimate the plastic rotations on the critical end zones (plastic hinge region) of the structural members due to seismic loadings, it would not be an incorrect assumption to select the rotational frame end springs for representing the damage of the structural members achieved due to quasi-static cyclic lateral loading. At the beginning, the initial and boundary conditions of the initial FEMs were not updated since the initial models were established for representing the undamaged situation of the building. Hence the initial



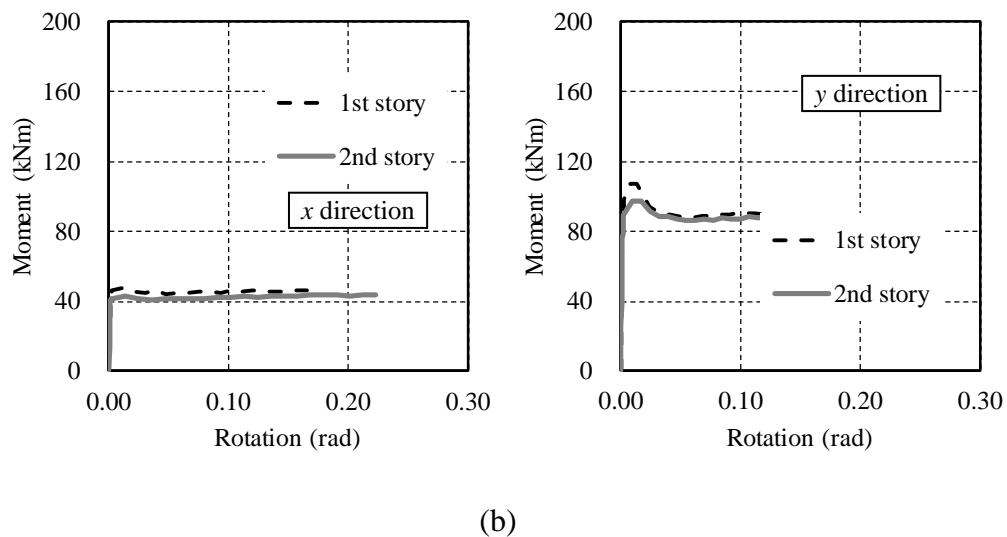
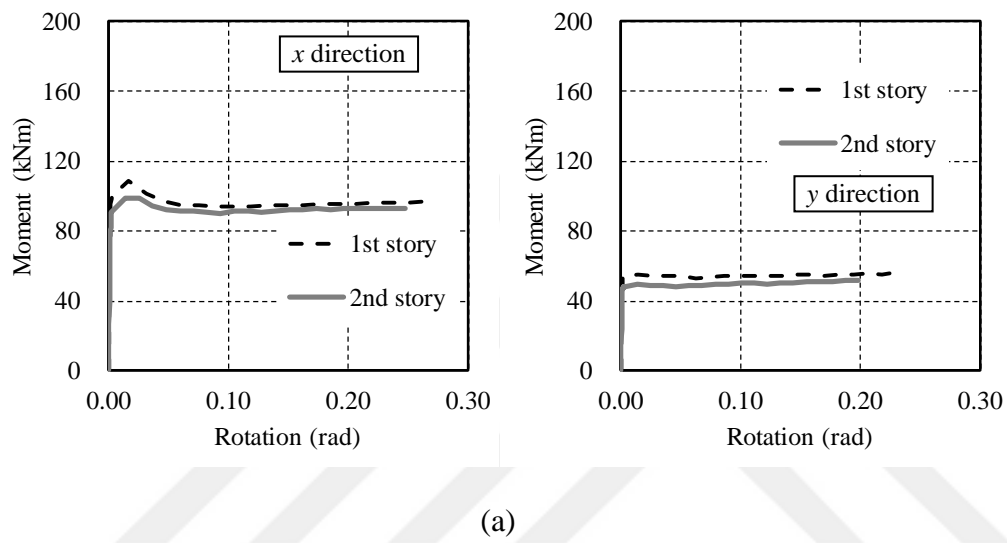
and boundary conditions of the frames were assumed to have full fixity. Attendantly, the full fixity condition was assumed to pass partial fixity condition (or to be released) with the structural damage. Hence, these degrading on the initial fixity value of the initial and boundary conditions was represented by assigning the end springs to the columns and beams.

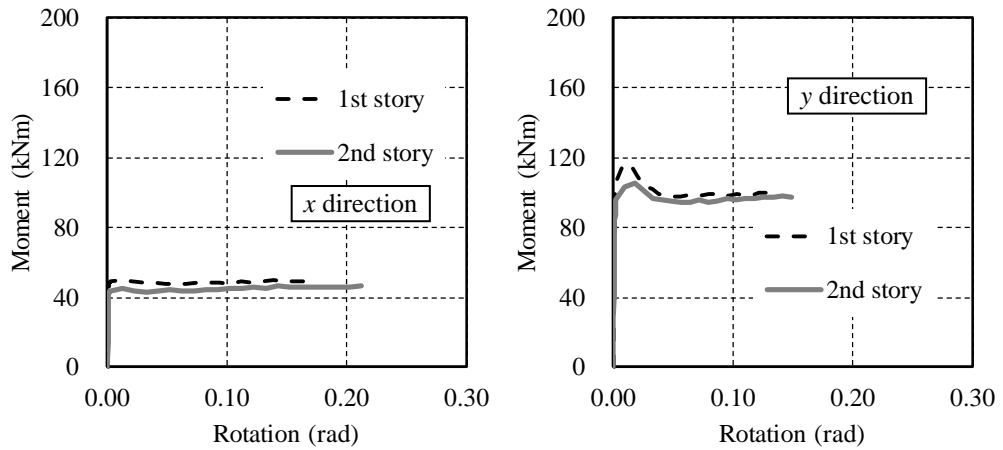
The initial stiffness values of the rotational end springs and their variation with the increasing demanded rotation (Moment ( $M$ )-Curvature ( $\kappa$ ) relationship) were calculated through cross-sectional fiber-analysis approach using the XTRACT 3.0.8 computer program. In the fiber analysis, for the unconfined and confined concrete, based on the uniaxial concrete compressive tests result carried out for the specimens taken out the building (details can be found Comert 2017), the yield, crushing and spalling strain values were taken as 0.002, 0.004 and 0.01, respectively. The cross-sectional properties of the members, dimensions, reinforcing cage, are given in Figure 2.4. For obtaining the rotation values, the curvature values were multiplied by the potential plastic hinge length of the columns. In this study, plastic hinge length was taken as  $H_c/2$  as suggested by TSDC (2007), where  $H_c$  refers the effective depth of the cross-section of the member. The moment-rotation relationships of the columns of the 1<sup>st</sup> and 2<sup>nd</sup> stories are given in Figure 4.2. The  $x$  and  $y$  directions and the corresponding layout plan of the cross-sections of the columns can be seen in Figure 2.4. Accordingly, the initial stiffness values of the rotational end springs equal to the tangent of the trendline drawn from origin to the yield rotation ( $\theta_y$ ) corresponding to maximum concrete strain value as 0.002.

Grouping of the unknown stiffness parameters was carried out as alluded based on engineering judgment and significantly the cross-sectional properties of the columns and given in Table 4.1. In the table, for the demonstration as G1 to G8, the capital letters refer 'Group'.

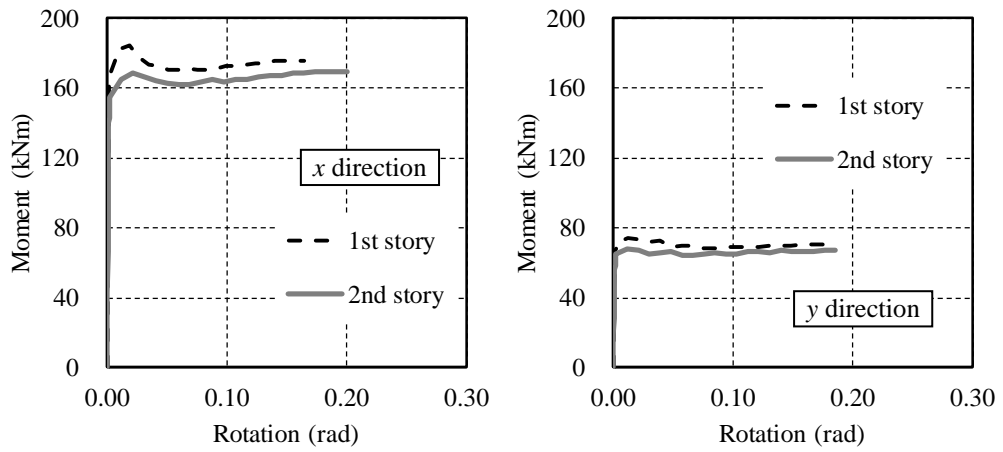
- Since columns S11 and S14 (for the 1<sup>st</sup> story) were stiffer and stronger in the loading direction ( $x$  direction) then the columns S12 and S13 due to their layout on the plan of the building, it was expected that the columns bottom end regions ( $i$ -end) attain severe damage (Group 1).
- Due to the same reason as the layout of the columns on the plan of the building, the top end ( $j$ -end) of the columns S11 and S14 (1<sup>st</sup> story) were assumed to subject similar intense of damage (Group 2).

- Owing to the layout plan of the columns explained in the 1<sup>st</sup> clause, bottom and top ends (*i*-end and *j*-end) of the columns S12 and S13 (1<sup>st</sup> story) were expected to be exposed similar damage intensities (Group 3).
- The 2<sup>nd</sup> story columns were dealt as individual groups (Goups 4, 5, 6 and 7, respectively).
- The 1<sup>st</sup> story beams parallel to the loading direction (K11 and K12) were assumed to be damaged at the support regions (Group 8).





(c)



(d)

**Figure 4.2 :** Moment-rotation relationship of the columns, (a) S11, (b) S12, (c) S13 and (d) S14.

**Table 4.1 :** Grouping the unknown parameters.

1 <sup>st</sup> story			2 <sup>nd</sup> story				1 <sup>st</sup> story beams
G1	G2	G3	G4	G5	G6	G7	G8
S11 <i>i</i> -end	S11 <i>j</i> -end	S12 <i>i</i> -end <i>j</i> -end	S11 <i>i</i> -end <i>j</i> -end	S12 <i>i</i> -end <i>j</i> -end	S13 <i>i</i> -end <i>j</i> -end	S14 <i>i</i> -end <i>j</i> -end	K11 <i>i</i> -end <i>j</i> -end
S14 <i>i</i> -end	S14 <i>j</i> -end	S13 <i>i</i> -end <i>j</i> -end					K12 <i>i</i> -end <i>j</i> -end

Afterward the unknown parameters were grouped as given in Table 4.1, rotational springs were assigned to the frame lower and upper ends (*i*-end and *j*-end, respectively) to provide updating the initial and boundary conditions of the frames for damage

detecting. Prior to compute the damage identification algorithm by iteratively changing rotational stiffness values of the assigned rotational springs to the end regions of the frames (Step 1), the sensitivity of FRF to the selected parameters group was examined.

Effects of change in rotational stiffness values of the bottom end (*i*-end) springs ( $R_x$ : Rotational stiffness in *x* direction,  $R_y$ : Rotational stiffness in *y* direction) of the 1<sup>st</sup> story columns S11 and S14 were examined for their full fixity condition (initial rotational stiffness) and partial fixity condition (0.1\* initial rotational stiffness). Since these columns are stiffer and stronger in *x* direction, shifting on resonant frequencies of the FRFs  $H_{74}$  and  $H_{71}$  are of much more significant comparing to that of the FRFs  $H_{85}$  and  $H_{82}$  (Figure 4.3). Decreasing of  $R_x$  and  $R_y$  values of *i*-end springs of S11 and S14 columns on *y* direction have influence on the higher frequency range of FRFs ( $H_{85}$  and  $H_{82}$ ). In addition to that, the related effect becomes more visible towards higher frequencies. In the case of the top ends (*j*-end) of the same columns (Group 2), like the observed result of change in rotational stiffness values of the (*i*-end) springs, resonant frequencies of the FRFs  $H_{74}$  and  $H_{71}$  are more sensitive than those of the FRFs  $H_{85}$  and  $H_{82}$  (Figure 4.4). However, change of  $R_x$  and  $R_y$  values of *j*-end springs in both *x* and *y* directions have more significant influence on the higher frequency range of FRFs. Even, it is not observed any change in the 1<sup>st</sup> resonant frequencies.

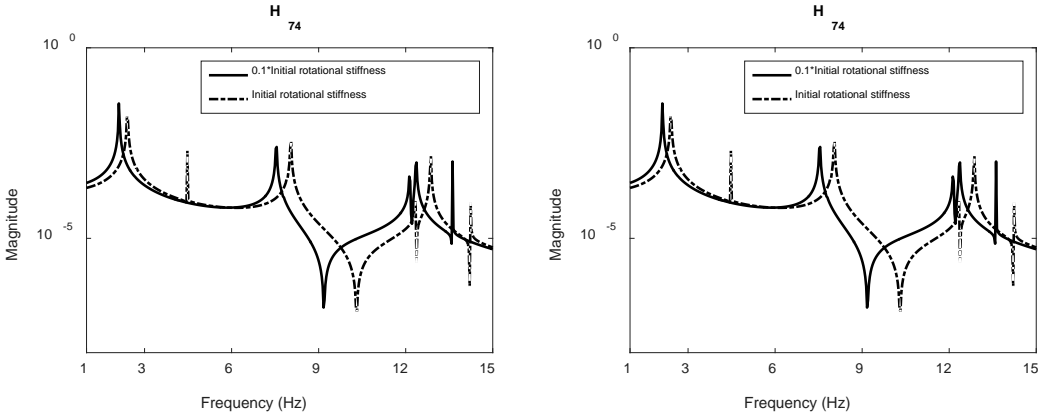


**Figure 4.3 :** FRF sensitivity to change in rotational stiffness ( $R_x$  and  $R_y$ ), Group 1.

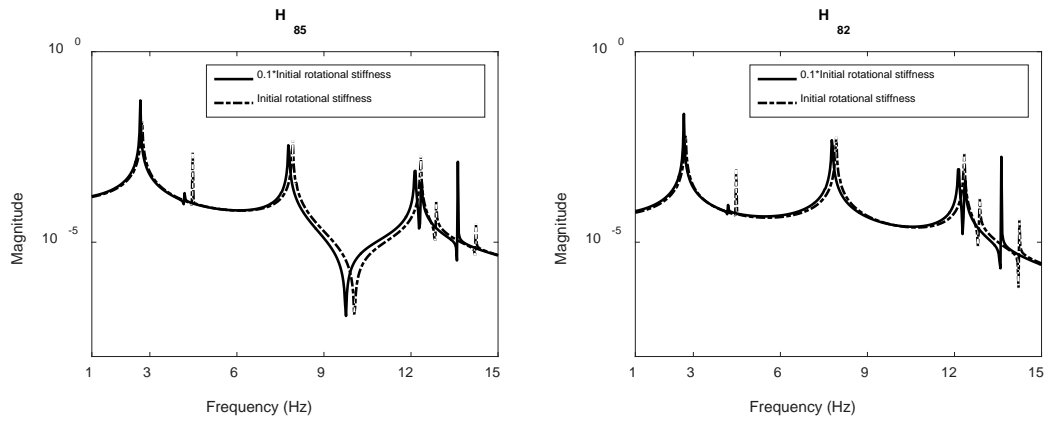


**Figure 4.3 (continued) :** FRF sensitivity to change in rotational stiffness (Rx and Ry), Group 1.

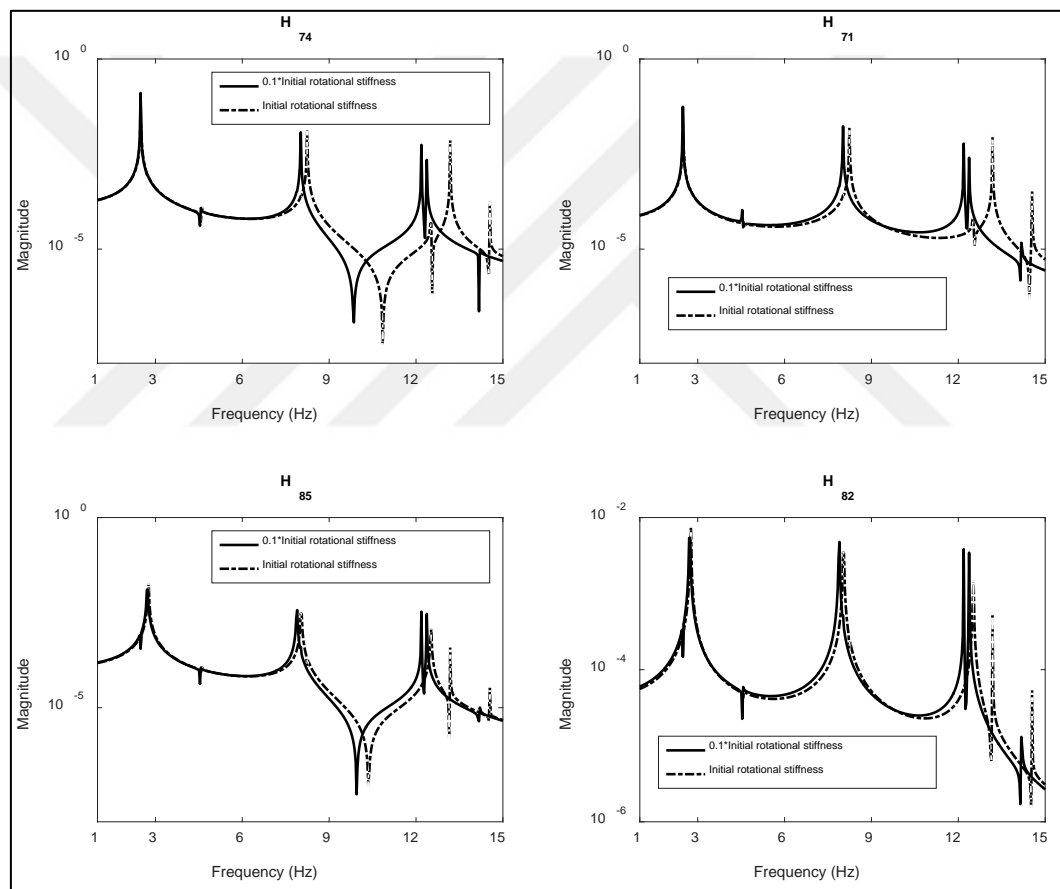


**Figure 4.4 :** FRF sensitivity to change in rotational stiffness (Rx and Ry), Group 2.

The FRF sensitivity to change in rotational stiffness values of the bottom end (*i*-end) springs of the 1<sup>st</sup> story columns S12 and S13 were also checked for their full fixity condition (initial rotational stiffness) and partial fixity condition (0.1\* initial rotational stiffness). Since these columns are stiffer and stronger in *y* direction, as it is expected and in contrary to observed for the effects of stiffness change of *i*-end springs of S11 and S14 columns, shifting on resonant frequencies of the FRFs H<sub>85</sub> and H<sub>82</sub> are

of much more significant comparing to that of the FRFs  $H_{74}$  and  $H_{71}$  (Figure 4.5). As it is also expected, the FRF sensitivity becomes more intense towards higher frequencies. The same results are observed for the  $j$ -end springs of the same columns (Figure 4.6). In case of the of the 1<sup>st</sup> story beams K11 and K12, which are parallel to the loading direction, FRFs in  $x$  direction  $H_{74}$  and  $H_{71}$  are of sensitive to change in rotational stiffness values of the end springs, while that of in  $y$  direction  $H_{85}$  and  $H_{82}$  are not (Figure 4.7). Since comparing to the columns, these beams have marginal contribution to translational stiffness values of the building in  $x$  direction ( $[K_{11}]$ ,  $[K_{14}]$  and  $[K_{17}]$ ), FRFs  $H_{74}$  and  $H_{71}$  have low sensitivity to the change in rotational stiffness of end springs of K11 and K12 comparing to the S11 and S14.

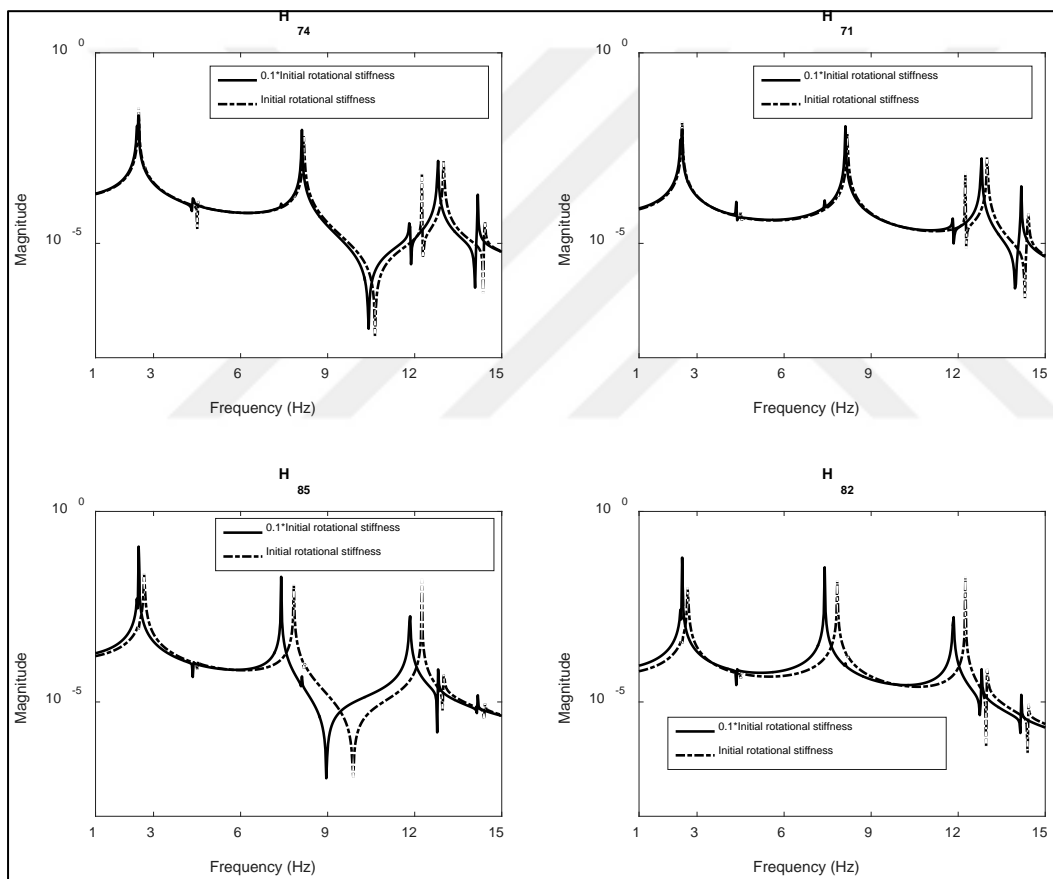


**Figure 4.5 :** FRF sensitivity to change in rotational stiffness (Rx and Ry),  $i$ -end springs in Group 3.

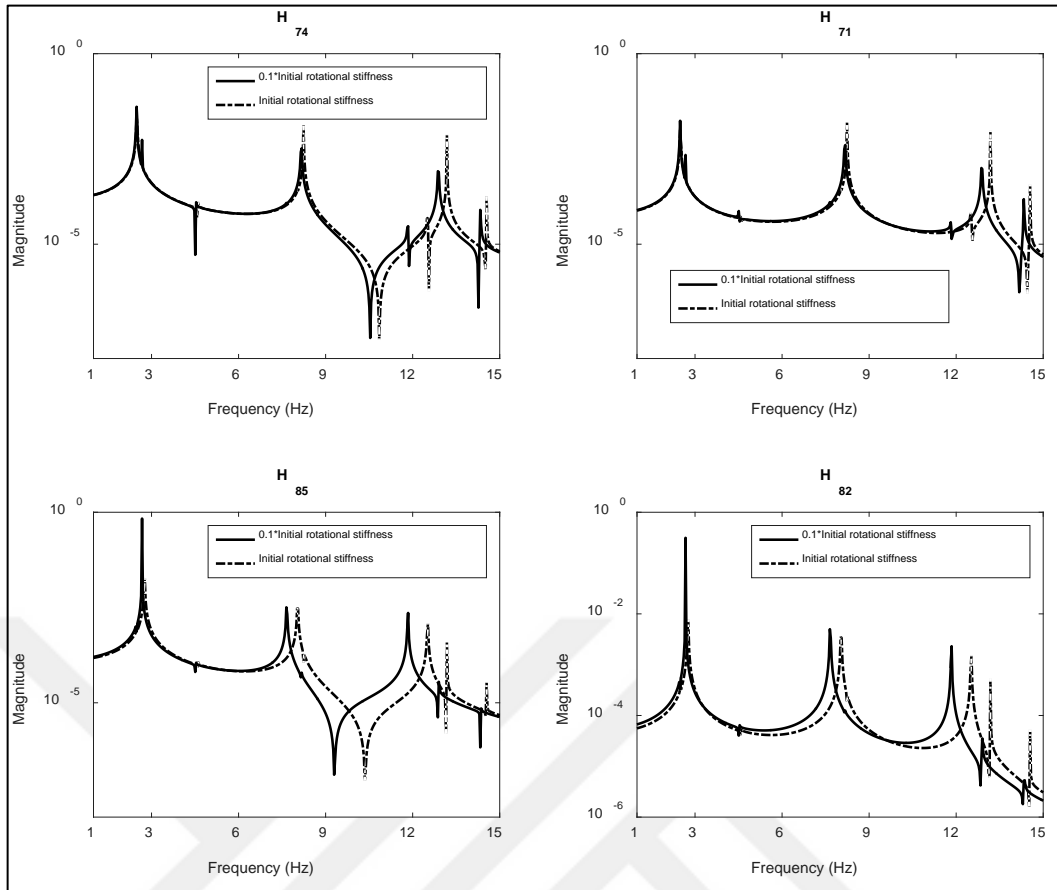


**Figure 4.6 :** FRF sensitivity to change in rotational stiffness (Rx and Ry), *j*-end springs in Group 3.

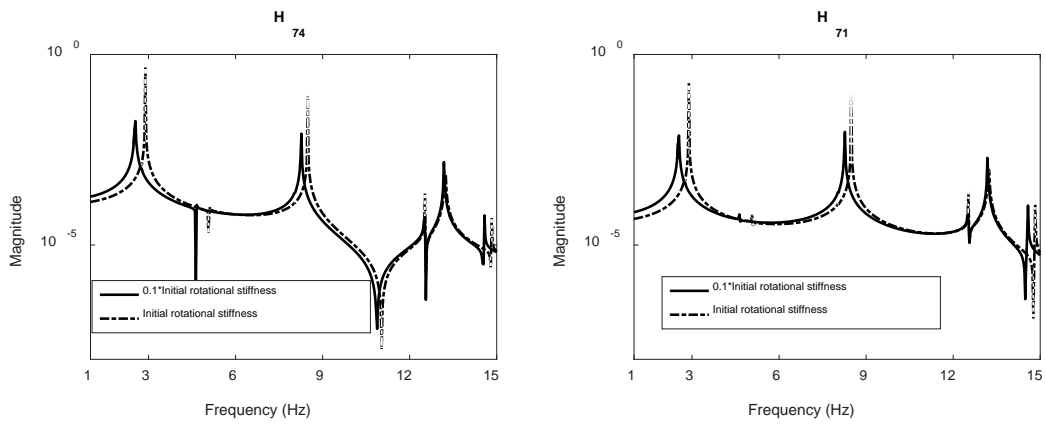


**Figure 4.7 :** FRF sensitivity to change in rotational stiffness (Rx and Ry), Group 8.

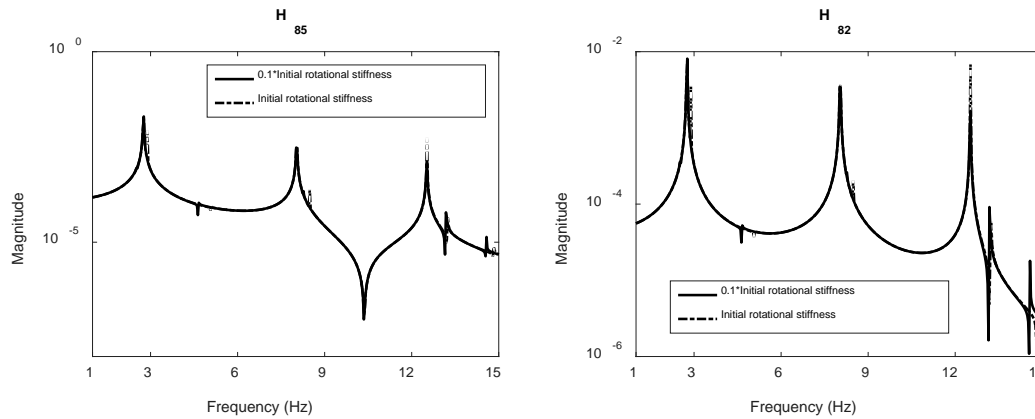


**Figure 4.7 (continued) : FRF sensitivity to change in rotational stiffness (Rx and Ry), Group 8.**

#### 4.1.1.2 Comparison of analytically determined and experimentally obtained FRFs

Consequently, two-step damage identification algorithm was computed by MUP. The rotational stiffness values of the end springs of the frames given above were iteratively changed and the 1<sup>st</sup> Step of the damage identification algorithm was terminated for the FRF based updating results given in Figure 4.8.

The [K] matrix of the building was updated for the stiffness values of the rotational end springs given in Table 4.2 and accordingly the first step of the two-step damage identification algorithm (Step 1) was terminated.

In this table, the intensity of the damage was represented in terms of the ratio determined between updated rotational stiffness value and the initial stiffness value. Accordingly, i-ends of the columns S11 and S14 were found to be more degraded comparing to i-ends of S11 and S13 and j-ends of the all 4 columns in the 1<sup>st</sup> story. These results seem in accordance with the actual damage given in chapter 2. In the case of the damage on the beams, since the FRF was not found to be significantly sensitive to change in the rotational stiffness, the estimated damage level could cause misleading results.



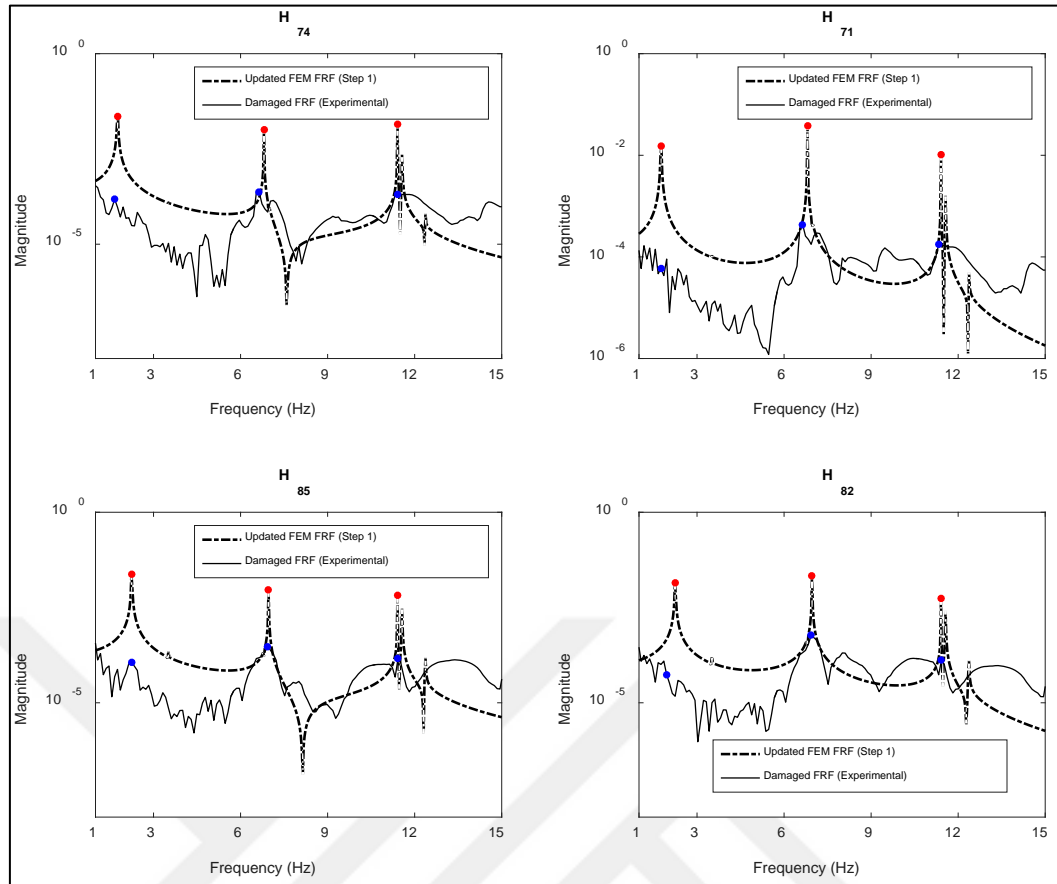


**Figure 4.8** : Model updating results for the building TB-1 (Step 1: [K]).

## 4.1.2 Updating damping ratio (Step 2)

### 4.1.2.1 Curve fitting

For the updating of the damping parameters, as aforementioned, first, the differential equation of the analytical FRF updated in Step 1 (Updated FEM FRF in Figure 4.8) was obtained using curve fitting technique. Thus, a second order differential equation was produced for each resonant frequency which was considered for updating the damping (Equation 3.27) (Figure 4.9). The second-order differential equations produced for each DOF were obtained and given in Table 4.2. As seen in this table, although the Updated FEM FRFs have no damping coefficient, some of the produced differential equations have damping coefficients. However, they are reasonable small to be neglected as also done in model updating of the initial FEM.

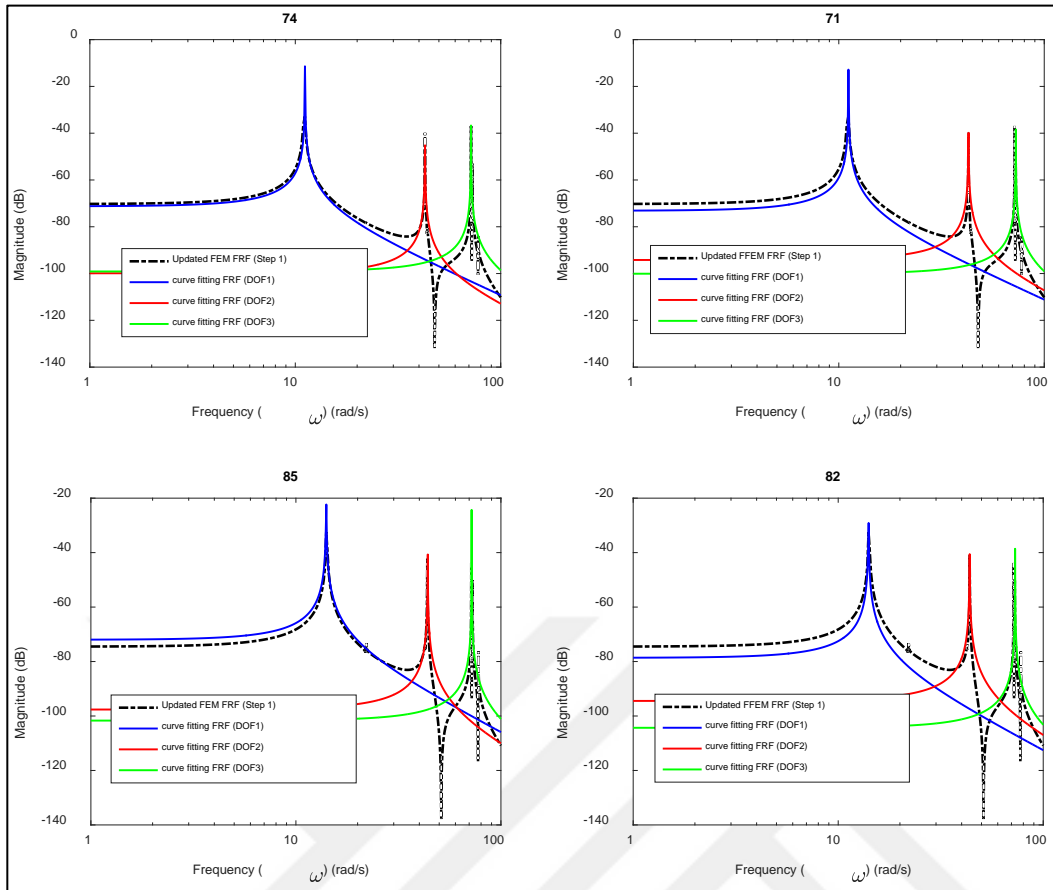


**Figure 4.9 :** Application of curve fitting.

**Table 4.2 :** Updated values of rotational stiffness values of the end springs (Step 1).

Frame	Story	<i>x</i> direction					<i>y</i> direction				
		Initial stiffness (kNm/rad)	Updated stiffness (kNm/rad)		Updated stiffness/Initial stiffness		Initial stiffness (kNm/rad)	Updated stiffness (kNm/rad)		Updated stiffness/Initial stiffness	
			<i>i</i> -end	<i>j</i> -end	<i>i</i> -end	<i>j</i> -end		<i>i</i> -end	<i>j</i> -end	<i>i</i> -end	<i>j</i> -end
S11	1 <sup>st</sup> story	76026.26	4400	20000	0.06	0.26	41276.46	6160	28000	0.15	0.67
	2 <sup>nd</sup> story	70453.09	20000	20000	0.28	0.28	38645.17	20000	20000	0.52	0.52
S12	1 <sup>st</sup> story	33877.30	7600	7600	0.22	0.22	72982.15	8360	*	0.11	*
	2 <sup>nd</sup> story	31977.29	20000	20000	0.63	0.63	68277.40	20000	20000	0.29	0.29
S13	1 <sup>st</sup> story	37047.71	7600	7600	0.21	0.21	80679.07	8360	*	0.10	*
	2 <sup>nd</sup> story	34552.50	24000	24000	0.69	0.69	74581.10	24000	24000	0.32	0.32
S14	1 <sup>st</sup> story	138415.06	4400	42000	0.03	0.30	52541.17	6160	28000	0.12	0.53
	2 <sup>nd</sup> story	129346.52	42000	42000	0.32	0.32	49032.48	42000	42000	0.86	0.86
K11 and K12	1 <sup>st</sup> story	57809.52	3000	3000	0.05	0.05			-		

\* Initial stiffness did not change

**Table 4.3** : Second order differential equations of updated FEM FRFs (Step 1) -curve fitting results-.

DOF*	$s=\sigma_1 + j\omega_1$	$s=\sigma_2 + j\omega_2$	$s=\sigma_3 + j\omega_3$
$H_{74}$	$\frac{0.03401}{s^2 + 2.659e-20 s + 124.3}$	$\frac{0.01852}{s^2 + 1830}$	$\frac{-0.05692}{s^2 + 1.49e-22 s + 5138}$
$H_{71}$	$\frac{0.02734}{s^2 + 124.3}$	$\frac{0.03565}{s^2 + 1830}$	$\frac{0.05238}{s^2 + 2.996e-19 s + 5285}$
$H_{85}$	$\frac{-0.04961}{s^2 + 197.5}$	$\frac{0.02539}{s^2 + 6.013e-19 s + 1932}$	$\frac{0.04263}{s^2 + 5177}$
$H_{82}$	$\frac{-0.02311}{s^2 + 197.5}$	$\frac{-0.03619}{s^2 + 1914}$	$\frac{-0.03475}{s^2 + 5.001e-21 s + 5278}$

\*  $\sigma_n = \zeta_n \omega_n$ , n: number of degree of freedom (n=1,2,3)

**Table 4.4 :** Second order differential equations of updated FEM FRFs (Step 1).

DOF*	FRF of the system
$H_{74}$	$\frac{-0.04143 s^4 - 2.004e-21 s^3 + 28.28 s^2 - 5.291e-18 s + 2.95e05}{s^6 + 2.674e-20 s^5 + 7092 s^4 + 1.856e-16 s^3 + 1.027e07 s^2 + 2.5e-13 s + 1.169e09}$
$H_{71}$	$\frac{0.04407 s^4 - 2.49e-21 s^3 + 104 s^2 + 1.366e-17 s + 2.528e05}{s^6 + 2.996e-19 s^5 + 7239 s^4 + 5.854e-16 s^3 + 1.055e07 s^2 + 6.814e-14 s + 1.202e09}$
$H_{85}$	$\frac{0.01841 s^4 - 4.195e-21 s^3 - 125.4 s^2 - 1.494e-16 s - 4.54e05}{s^6 + 6.013e-19 s^5 + 7307 s^4 + 3.232e-15 s^3 + 1.141e07 s^2 + 6.148e-13 s + 1.975e09}$
$H_{82}$	$\frac{-0.01922 s^4 - 35.65 s^2 - 2.095e05}{s^6 + 7432 s^4 + 1.161e07 s^2 + 2.011e09}$

As aforementioned, the algebraic summation of each second-order differential equation given in Table 4.3 gives the equation of system transfer function (Table 4.4 and Figure 4.10). Hence, the updated FEM of the buildings in Step 1 represented as a mathematical based formulation.

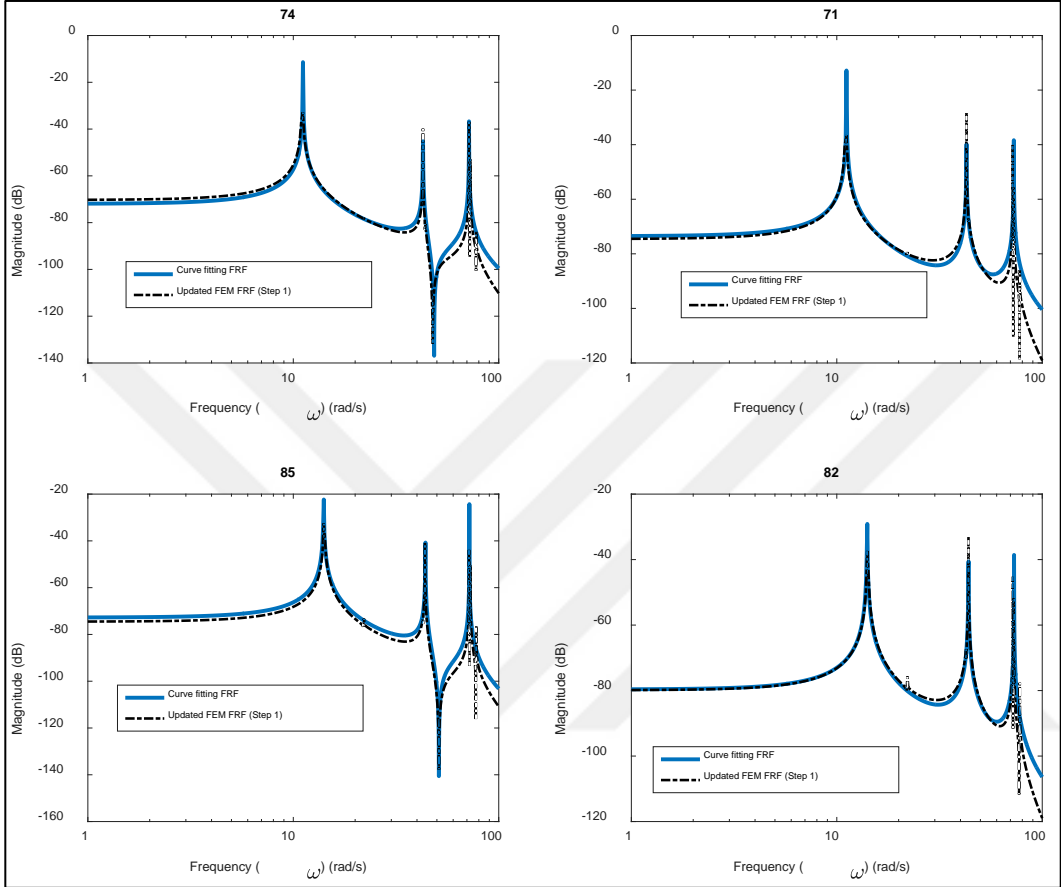


**Figure 4.10 : FRF of the system.**

**4.1.2.2 Sine analysis and Calculation of analytical FRF**

Following the obtaining the FRF equation for damaged case, a sine analysis was performed to produce the acceleration response of the each DOFs and subsequently the analytical FRF as the ratio of the corresponding acceleration response of DOFs to shaker operating frequency square was calculated. Finally, for the sake of completeness, the model updating process was concluded with the well-matching of analytically determined and experimentally obtained damaged FRFs in terms of their amplitudes in resonants (Figure 4.11). As a reminder, this was provided by iteratively changing the damping parameters in the FRF equation. Details of the Step 2 was given in Chapter 3.2.2. It should ben noted that this damping ratio updating process do not provide any additional information about the damage detection, localization and

quantification. The obtained damping ratio values at this step, the experimental ones and the damping ratio values found for baseline model are given in Table 4.5.

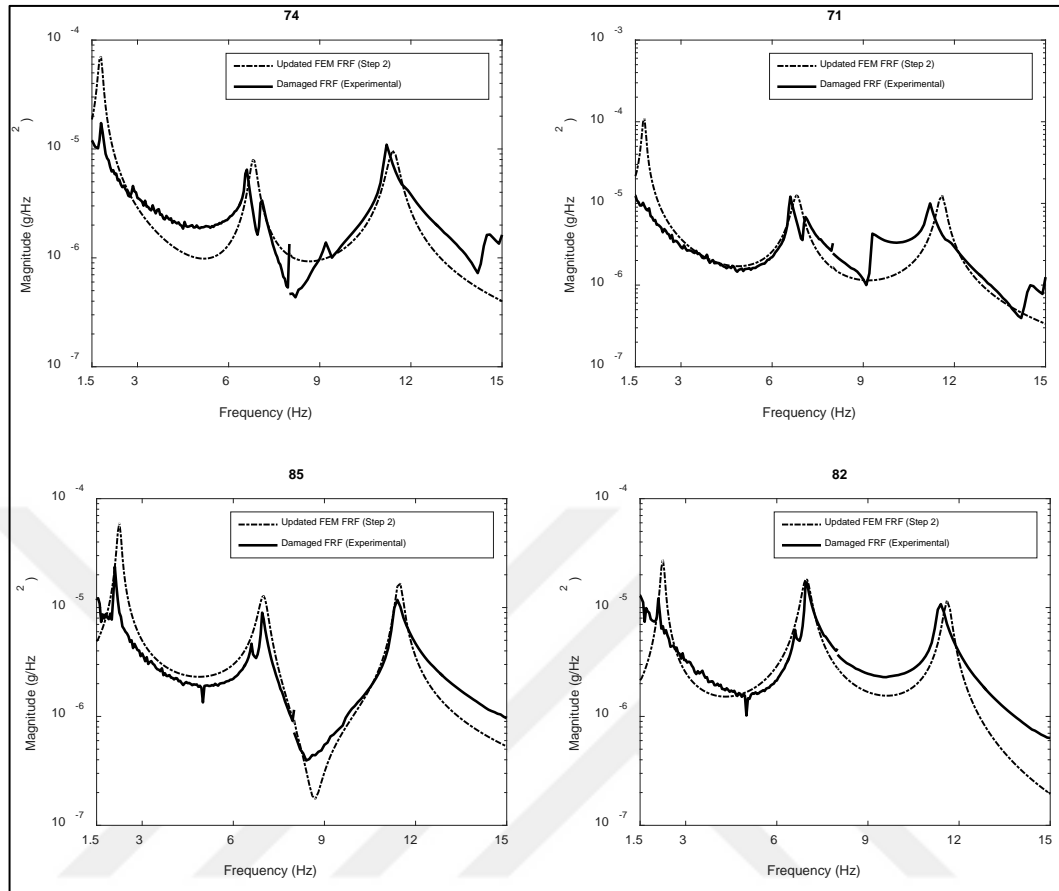


**Figure 4.11** : Model updating results of the building TB-1 (Step 2).

**Table 4.5** : Updated values of damping ratio.

Buildings	x direction			y direction		
	$\zeta_1$	$\zeta_2$	$\zeta_3$	$\zeta_1$	$\zeta_2$	$\zeta_3$
Updated FEM FRF	0.035	0.017	0.015	0.025	0.021	0.010
Damaged FRF (experimental)	-	0.009	0.024	0.028	0.014	0.021
Baseline FEM FRF	0.035	0.010	0.007	0.025	0.016	0.007

As it can be seen in the table, some of the damping ratio values found to be close to the determined through experimental study. Apart from that, some model damping ratios increased comparing to the baseline model at the end of the algorithm. Although the experimental and analytical results were not found to be in perfect match for the damping ratios of the damaged case, the increasing with the damage was identified both for experimental and analytical cases.

## **4.2 Damage identification of the building TB-2**

As mentioned in Chapter 2, the quasi-static reversed cyclic loading was implemented to the building TB-2 up to 4% d.r., yet, the forced vibration test was terminally performed at 3% d.r. due to the safety reasons. In addition to that, the test was also performed in  $x$  direction at a set of certain damage levels with the aim of quantifying the rate of change of dynamic characteristics with gradually increasing structural seismic damage. The test program was given in Table 2.1. As a reminder, the tests were performed for undamaged condition of the building and at the certain damage levels introduced in terms of the 1<sup>st</sup> story drift ratio as 0.5% (Damaged Case 1: DC1), 1.0% (Damaged Case 2: DC2), 1.5% (Damaged Case 3: DC3), 2.0% (Damaged Case 4: DC4) and 3.0% (Damaged Case 5: DC5). The tests were implemented in  $x$  and  $y$  direction for the cases UC and DC5 while only in  $x$  direction for the cases DC1, DC2, DC3 and DC4. Throughout the quasi-static loading, the flexural cracks, concrete crushing and subsequently cover spalling were observed on the 1<sup>st</sup> story columns S11 and S13 while almost no damage without minor flexural cracking was observed on the columns and beams of the 2<sup>nd</sup> story and beams of the 1<sup>st</sup> story. Because of the replacement of the actuators, no damage was observed on the columns and the beams of the 3<sup>rd</sup> story. In short, a distributed damage evolution achieved, and the lateral load bearing capacity of the building was degraded approximately 40%.

Hence, to detect, localize and quantify the damage of the building TB-2 induced by quasi-static cyclic lateral loading, a model updating was implemented by changing the parameters explained below via MUP. As aforementioned, prior to the model updating process, grouping of unknown parameters was carried out.

### **4.2.1 Updating [K] (Step 1)**

#### **4.2.1.1 Grouping of unknown parameters and FRF sensitivity**

With the similar reasons explained in the damage identification case of the building TB-1, the initial and boundary conditions were expected to be affected from the reversed cyclic lateral loading. Therefore, the degrading on the initial fixity value of the initial and boundary conditions was represented by assigning the end springs to the columns.



The initial stiffness values of the rotational end springs were determined through Moment-Curvature relationship of the columns which were obtained via cross-sectional fiber-analysis approach using the XTRACT 3.0.8 computer program. In the fiber analysis, for the unconfined and confined concrete, based on the uniaxial concrete compressive tests result carried out for the specimens taken out the building (details can be found Comert 2017), the yield, crushing and spalling strain values were taken as 0.002, 0.004 and 0.01, respectively. The cross-sectional properties of the members, dimensions, reinforcing cage, are given in Figure 2.4. For obtaining the rotation values, the curvature values were multiplied by the potential plastic hinge length of the columns. In this study, plastic hinge length was taken as  $H/2$  as suggested by TSDC (2007), where  $H$  refers the effective depth of the cross-section of the member. The moment-rotation relationships of the columns of the 1<sup>st</sup>, 2<sup>nd</sup> and 3<sup>rd</sup> stories are given in Figure 4.12. The  $x$  and  $y$  directions and the corresponding layout plan of the cross-sections of the columns can be seen in Figure 2.4. Accordingly, the initial stiffness values of the rotational end springs equal to the tangent of the trendline drawn from origin to the yield rotation ( $\theta_y$ ) corresponding to maximum concrete strain value as 0.002.

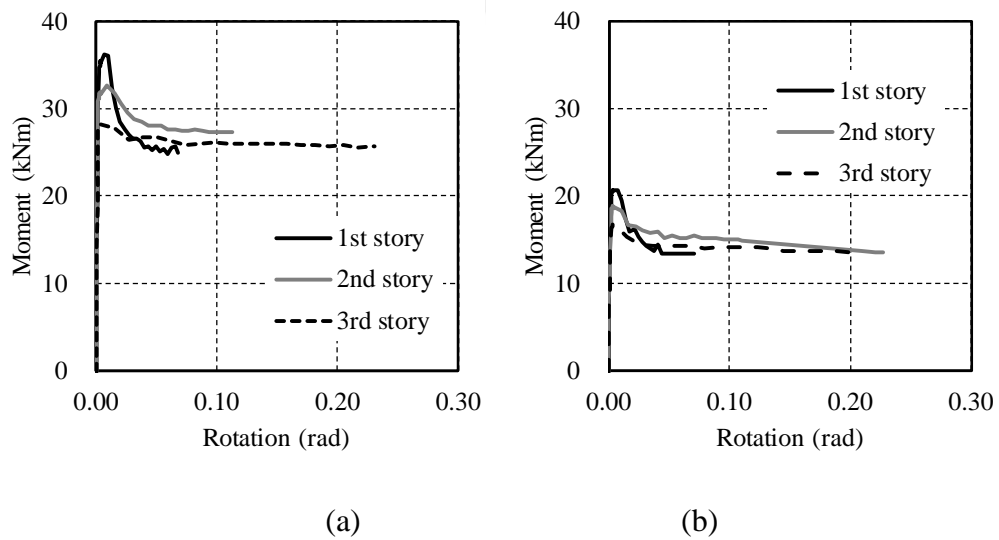


**Figure 4.12 :** Moment-rotation relationship of the columns, (a) S11-S14 for  $x$  direction and S12-S13 for  $y$  direction, (b) S12-S13 for  $x$  direction and S11-S12 for  $y$  direction.

By taking into consideration the cross-sectional properties of the columns and the weak column-strong beam mechanism of the building, it was anticipated that the columns would be affected by the quasi-static reversed cyclic loading forced the building

beyond its elastic limits. In brief, the bottom and top ends of the 1<sup>st</sup> and 2<sup>nd</sup> story columns and the bottom end of the third story columns were assumed to be affected. Grouping of the unknown stiffness parameters can be in Table 4.6.

**Table 4.6 :** Grouping the unknown parameters.

1 <sup>st</sup> story		2 <sup>nd</sup> story		3 <sup>rd</sup> story	
G1		G2		G3	
S11	S12	S11	S12	S11	S12
<i>i</i> -end	<i>i</i> -end	<i>i</i> -end	<i>i</i> -end	<i>i</i> -end	<i>i</i> -end
<i>j</i> -end	<i>j</i> -end	<i>j</i> -end	<i>j</i> -end		
S14	S13	S14	S13	S14	S13
<i>i</i> -end	<i>i</i> -end	<i>i</i> -end	<i>i</i> -end	<i>i</i> -end	<i>i</i> -end
<i>j</i> -end	<i>j</i> -end	<i>j</i> -end	<i>j</i> -end		

The rotational springs were then assigned to the frame lower and upper ends (*i*-end and *j*-end, respectively) for the 1<sup>st</sup> and 2<sup>nd</sup> story columns while to the frame bottom end (*i*-end) for the 3<sup>rd</sup> story columns. Prior to compute the damage identification algorithm by iteratively changing rotational stiffness values of the assigned rotational springs to the end regions of the frames (Step 1), the sensitivity of FRF to the selected parameters group was examined (Figure 4.13 to Figure 4.17).

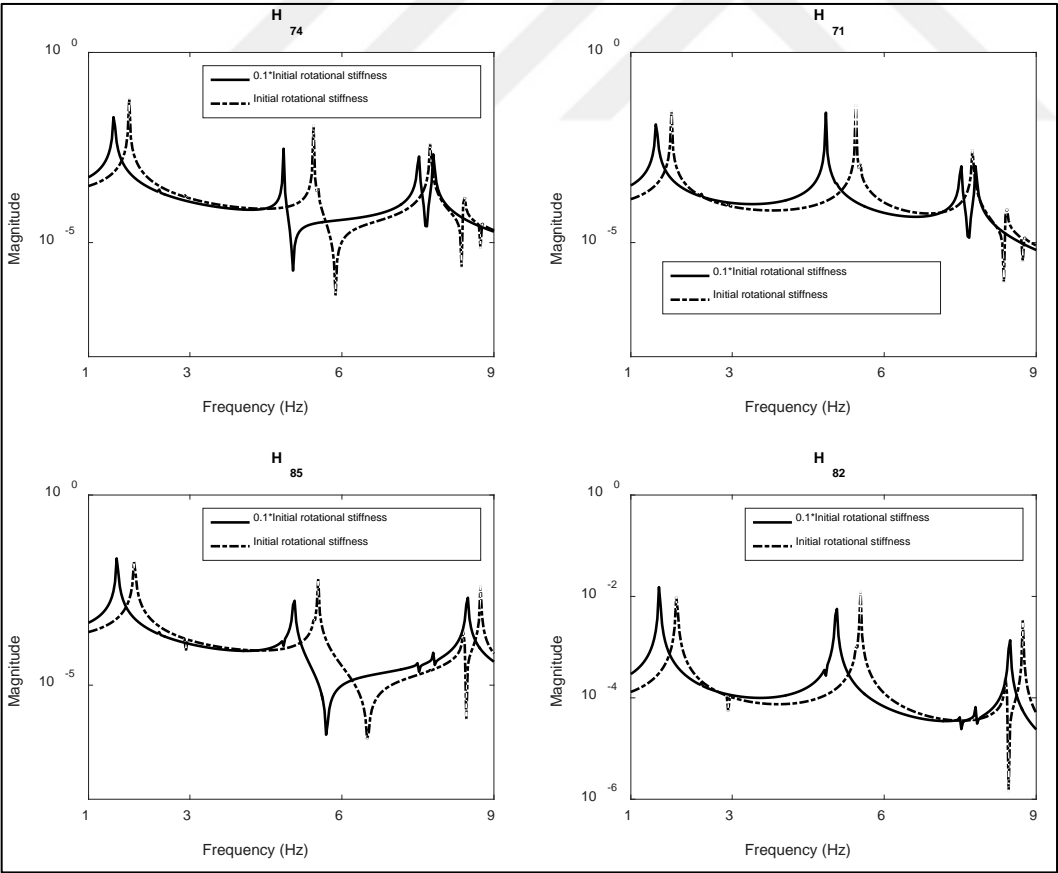


**Figure 4.13 :** FRF sensitivity to change in rotational stiffness (Rx and Ry), *i*-end springs in Group 1.

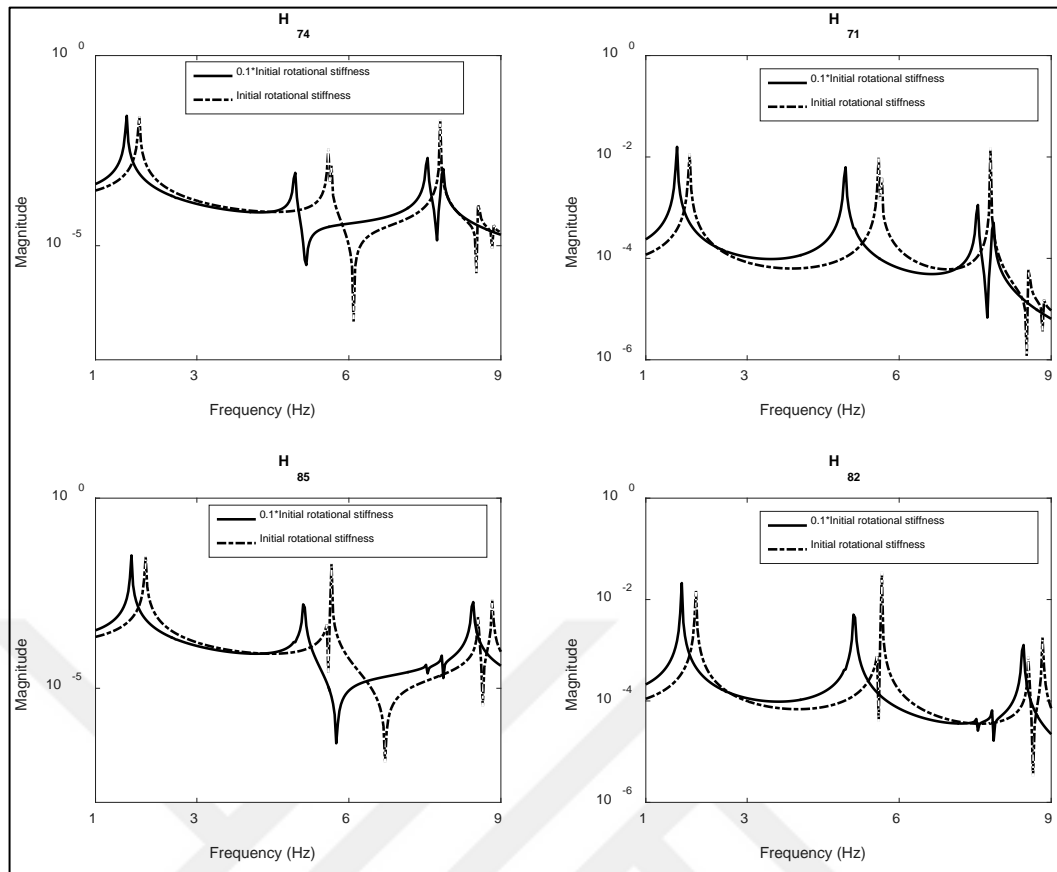


**Figure 4.14 :** FRF sensitivity to change in rotational stiffness ( $R_x$  and  $R_y$ ),  $j$ -end springs in Group 1.

Effects of varying of rotational stiffness values (full fixity condition -initial rotational stiffness- and partial fixity condition -0.1\* initial rotational stiffness-) of the bottom end ( $i$ -end) and top end ( $i$ -end) springs of the 1<sup>st</sup> story columns are displayed in Figure 4.13 and Figure 4.14, respectively. The degradation in bottom and top ends of the columns were taken to be equal, and accordingly, FRF sensitivity to these degradations in bottom and top ends of the columns were found to be almost similar. In the case of the the 2<sup>nd</sup> story columns, although like in the 1<sup>st</sup> story columns there was not found remarkable difference between the FRF sensitivity to the change of the rotational stiffness of  $i$ -end and  $j$ -end of the columns, it is obvious that the FRFs are more sensitive to change of boundary conditions of the 1<sup>st</sup> story columns than that of the second story columns (Figures 4.16 and 4.16) In addition to that, the change in boundary conditions of the 2<sup>nd</sup> story columns has an influence on the high frequency range of FRFs.

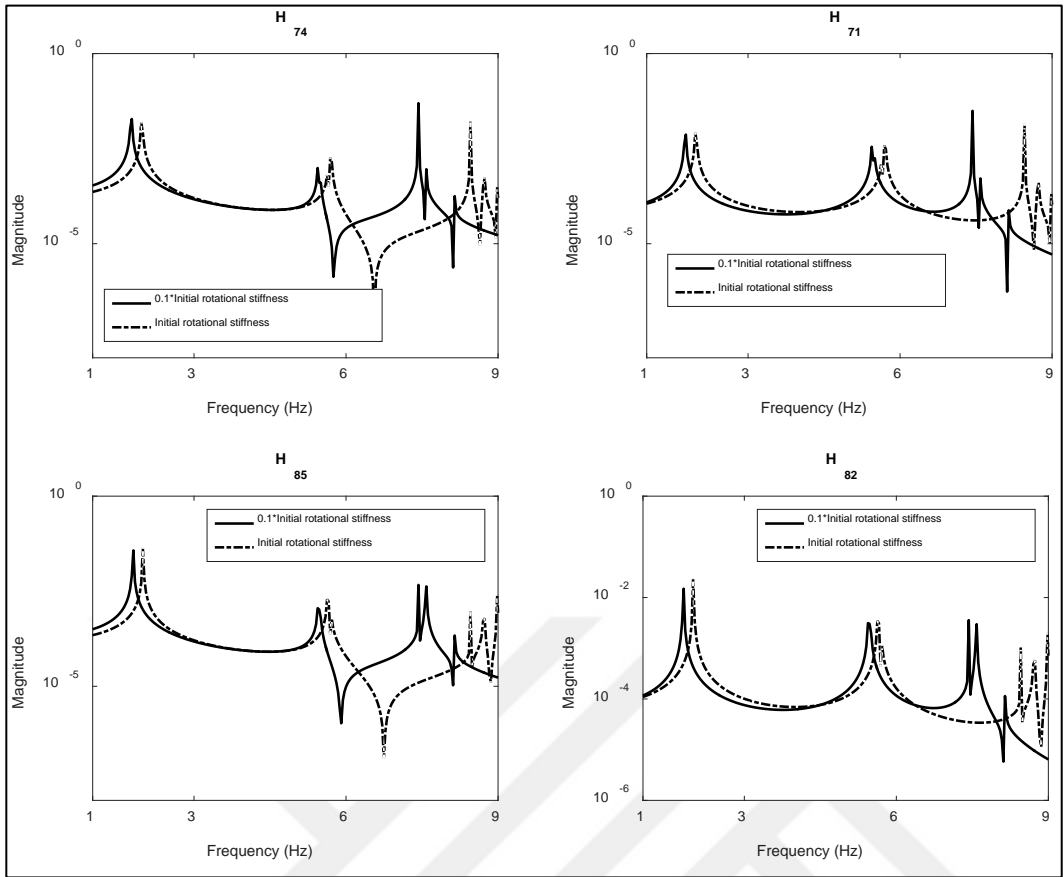


**Figure 4.15 :** FRF sensitivity to change in rotational stiffness (Rx and Ry), *i*-end springs in Group 2.

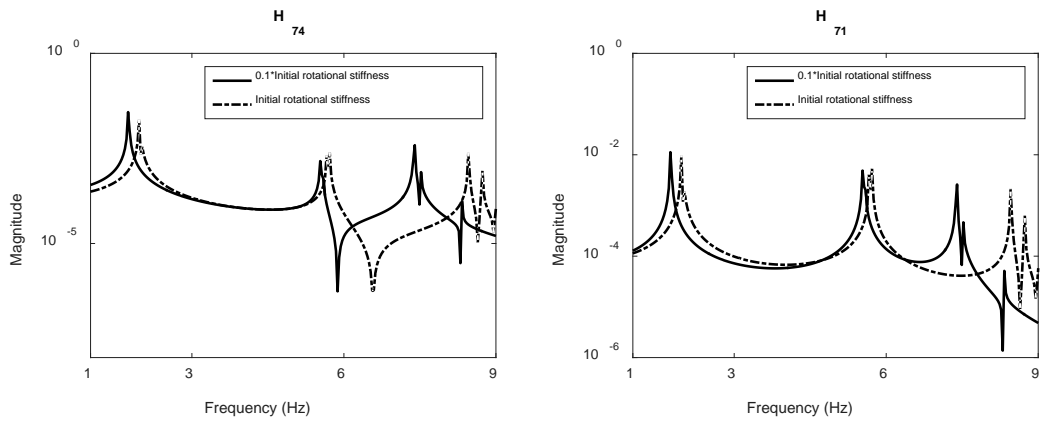


**Figure 4.16 :** FRF sensitivity to change in rotational stiffness (Rx and Ry), *j*-end springs in Group 2.

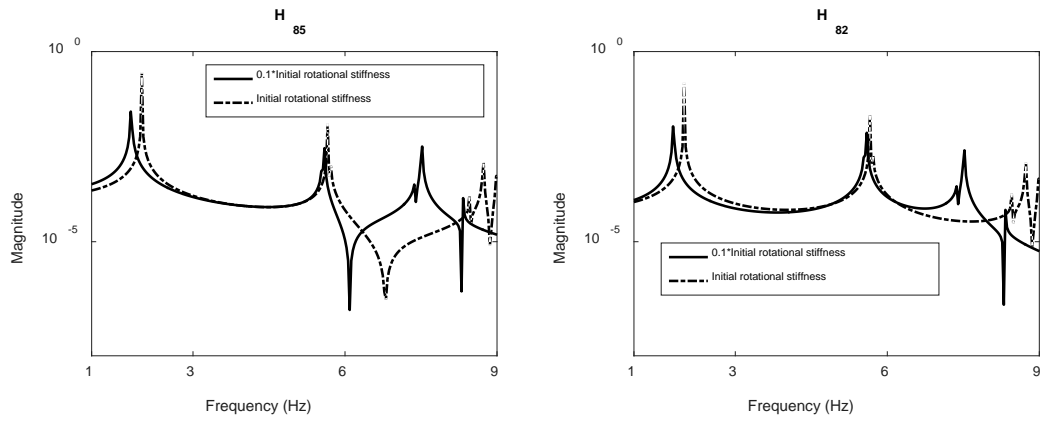


**Figure 4.16 (continued) :** FRF sensitivity to change in rotational stiffness (Rx and Ry), *j*-end springs in Group 2.

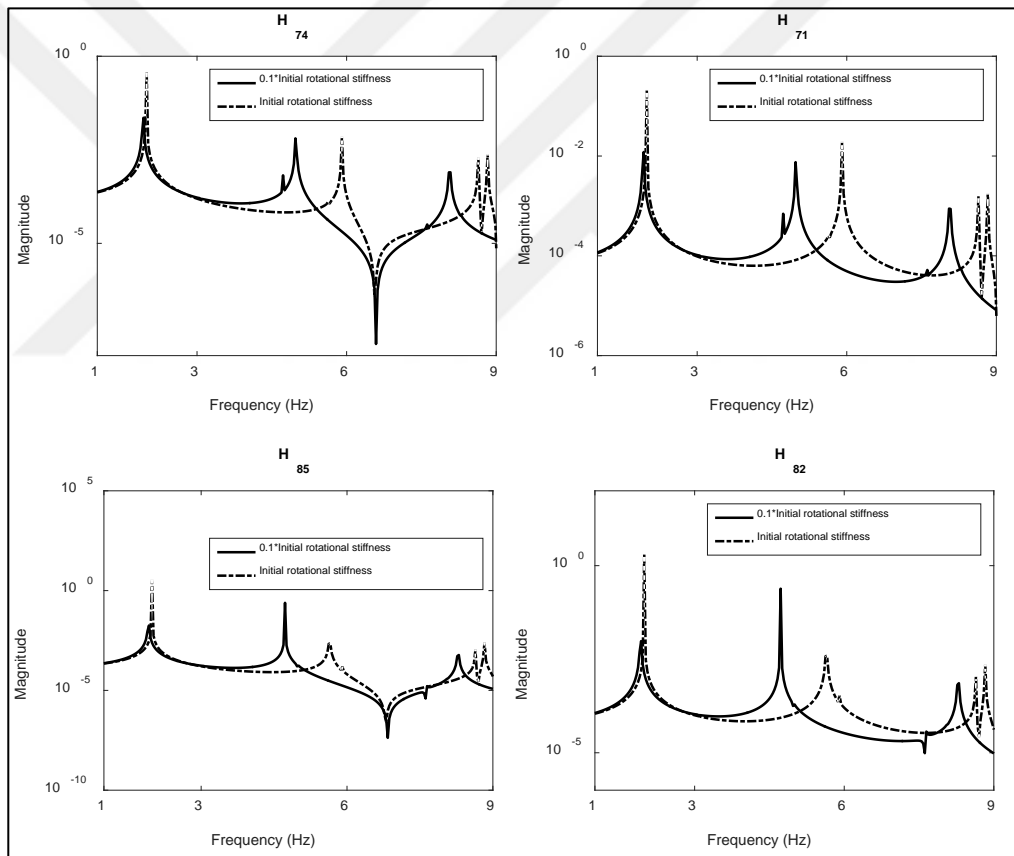


**Figure 4.17 :** FRF sensitivity to change in rotational stiffness (Rx and Ry), Group 3.

#### 4.2.1.2 Comparison of analytically determined and experimentally obtained FRFs

In this sub-section, two-step damage identification algorithm was computed for the damaged cases of DC1, DC2, DC3, DC4 and DC5 by MUP. The rotational stiffness values of the end springs of the frames given above were iteratively changed and the

1<sup>st</sup> Step of the damage identification algorithm was terminated for the FRF based updating results given for all damage cases Figure 4.18 to 4.22.

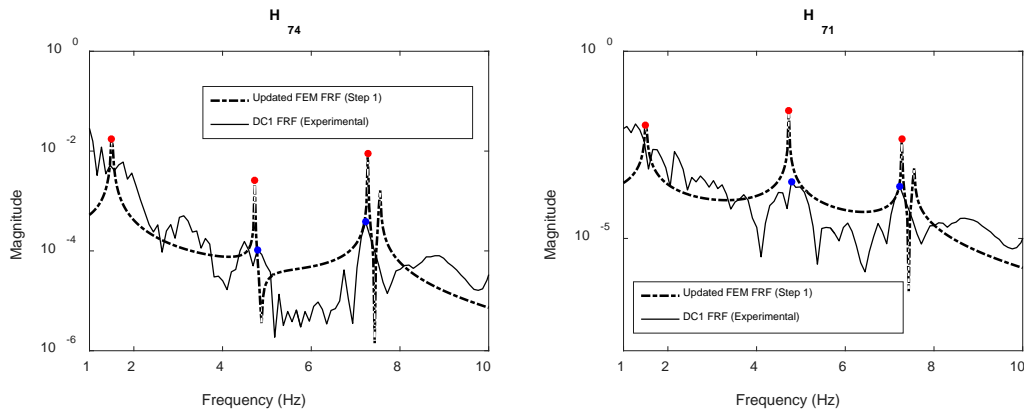


**Figure 4.18 :** Model updating results for the building TB-2 for DC1 (Step 1: [K]).

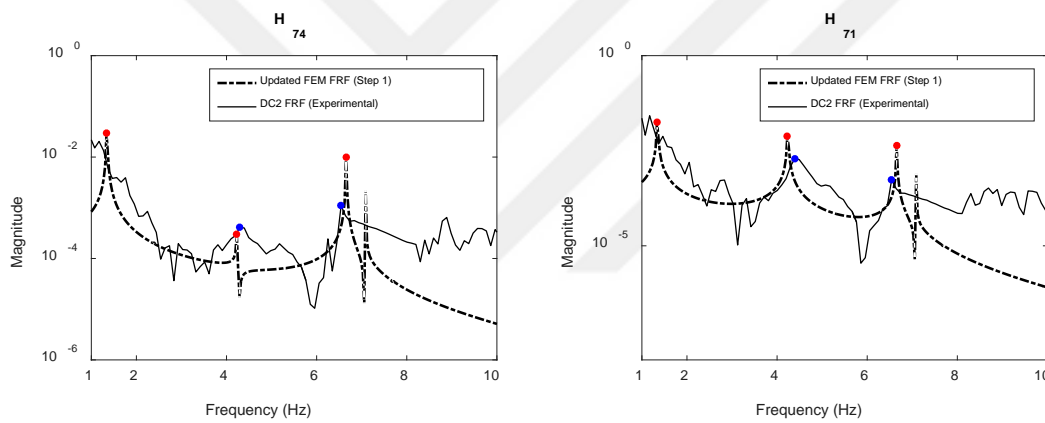


**Figure 4.19 :** Model updating results for the building TB-2 for DC2 (Step 1: [K]).

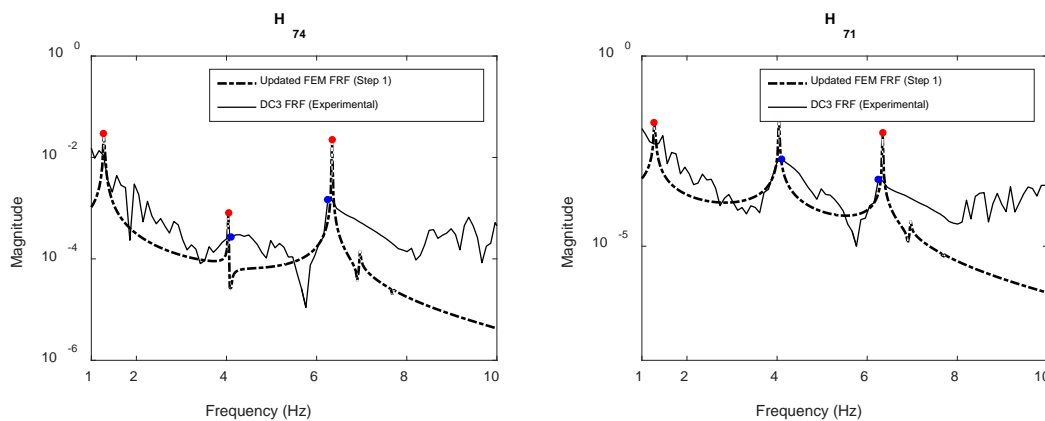


**Figure 4.20 :** Model updating results for the building TB-2 for DC3 (Step 1: [K]).

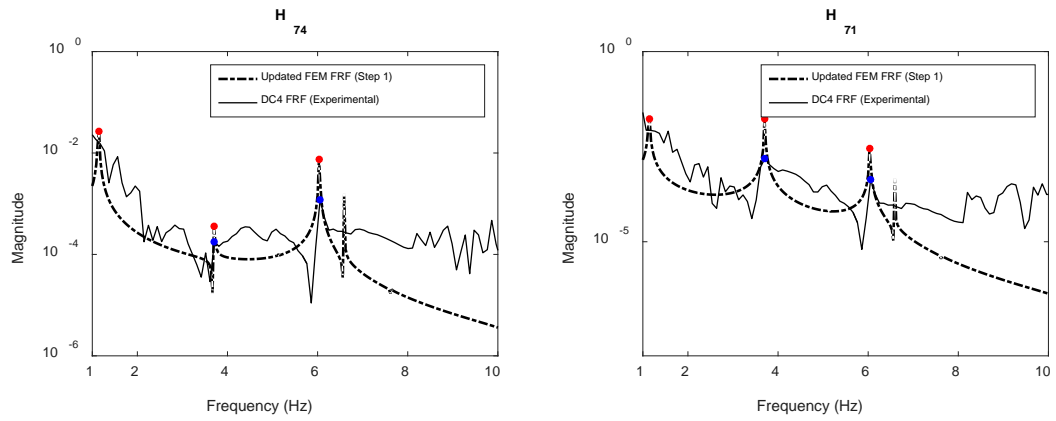


**Figure 4.21** : Model updating results for the building TB-2 for DC4 (Step 1: [K]).

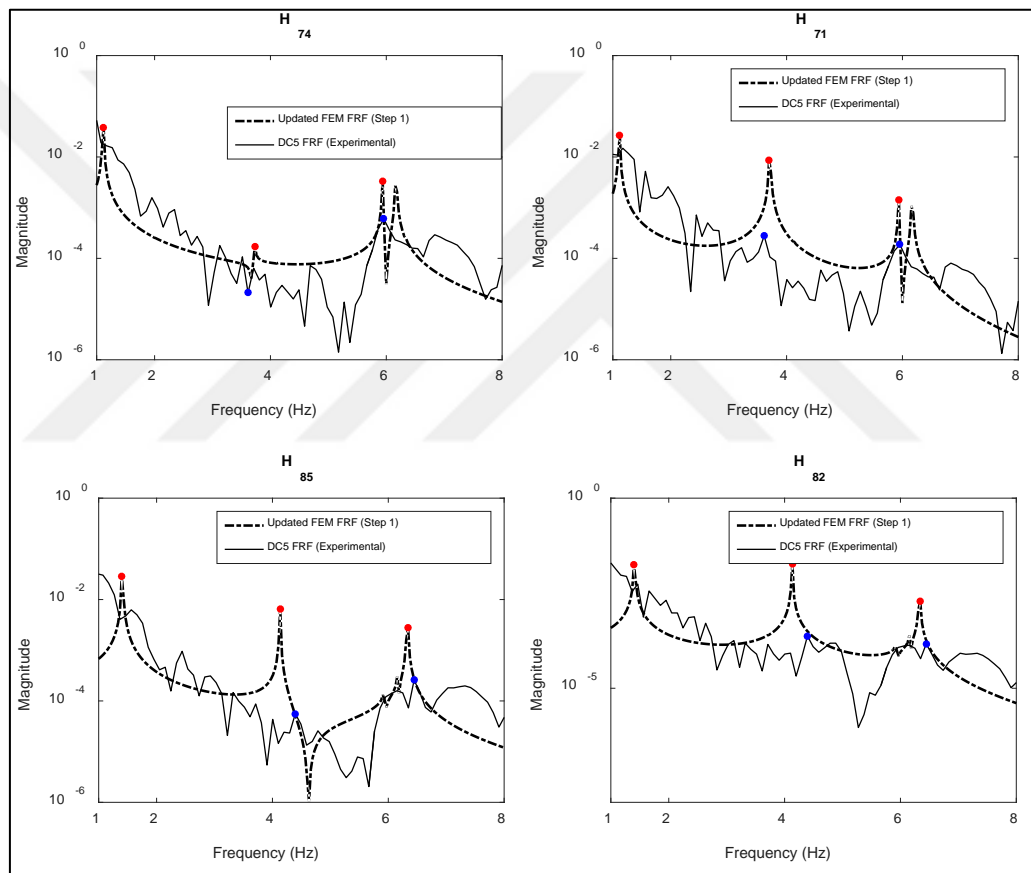


**Figure 4.22** : Model updating results for the building TB-2 for DC5 (Step 1: [K]).

The [K] matrix of the building and accordingly frequency component of the FRF was updated for the stiffness values of the rotational end springs given in Table 4.7. The degradation of the initial and boundary conditions of the columns are given in terms of the ratio of updated rotational stiffness to initial rotational stiffness of the end-springs in Table 4.8 and Table 4.9. Hence the first step of the two-step damage

identification algorithm (Step 1) is terminated. Followingly, MUP then compute for updating the damping parameters (Step 2).





**Table 4.7 :** Updated values of rotational stiffness values of the end springs (Step 1).

		x direction						y direction			
		1 <sup>st</sup> story		2 <sup>nd</sup> story		3 <sup>rd</sup> story	1 <sup>st</sup> story		2 <sup>nd</sup> story		3 <sup>rd</sup> story
		<i>i</i> -end	<i>j</i> -end	<i>i</i> -end	<i>j</i> -end	<i>i</i> -end	<i>i</i> -end	<i>j</i> -end	<i>i</i> -end	<i>j</i> -end	<i>i</i> -end
Initial stiffness (kNm/rad)	S11										
	S14	35469.12		33180.92		25157.34	21693.28		17977.90		17537.67
	S12										
	S13	21693.28		17977.90		17537.67	35469.12		33180.92		25157.34
	DC1	9600	9600	10400	10400	14250					
	DC2	6300	6300	5500	6000	11050					
	DC3	5040	5530	4800	4800	7800			*		
	DC4	3000	3000	3750	3800	5856					
	DC5	2730	3120	4830	4970	5612	9000	9900	6000	6500	8850

\* There is not dynamic test

**Table 4.8 :** Change of the rotational stiffness values for the columns S11 and S14 (Updated stiffness/Initial stiffness) (Step 1).

	x direction					y direction				
	1 <sup>st</sup> story		2 <sup>nd</sup> story		3 <sup>rd</sup> story	1 <sup>st</sup> story		2 <sup>nd</sup> story		3 <sup>rd</sup> story
	<i>i</i> -end	<i>j</i> -end	<i>i</i> -end	<i>j</i> -end	<i>i</i> -end	<i>i</i> -end	<i>j</i> -end	<i>i</i> -end	<i>j</i> -end	<i>i</i> -end
DC1	0.27	0.27	0.31	0.31	0.57					
DC2	0.18	0.18	0.17	0.18	0.44			*		
DC3	0.14	0.16	0.14	0.14	0.31					
DC4	0.08	0.08	0.11	0.11	0.23					
DC5	0.08	0.09	0.15	0.15	0.22	0.41	0.46	0.33	0.36	0.50

\* There is not dynamic test

**Table 4.9 :** Change of the rotational stiffness values for the columns S12 and S13 (Updated stiffness/Initial stiffness) (Step 1).

	x direction					y direction				
	1 <sup>st</sup> story		2 <sup>nd</sup> story		3 <sup>rd</sup> story	1 <sup>st</sup> story		2 <sup>nd</sup> story		3 <sup>rd</sup> story
	<i>i</i> -end	<i>j</i> -end	<i>i</i> -end	<i>j</i> -end	<i>i</i> -end	<i>i</i> -end	<i>j</i> -end	<i>i</i> -end	<i>j</i> -end	<i>i</i> -end
DC1	0.44	0.44	0.58	0.58	0.81					
DC2	0.29	0.29	0.31	0.33	0.63			*		
DC3	0.23	0.25	0.27	0.27	0.44					
DC4	0.14	0.14	0.21	0.21	0.33					
DC5	0.13	0.14	0.17	0.28	0.32	0.25	0.28	0.18	0.20	0.35

\* There is not dynamic test

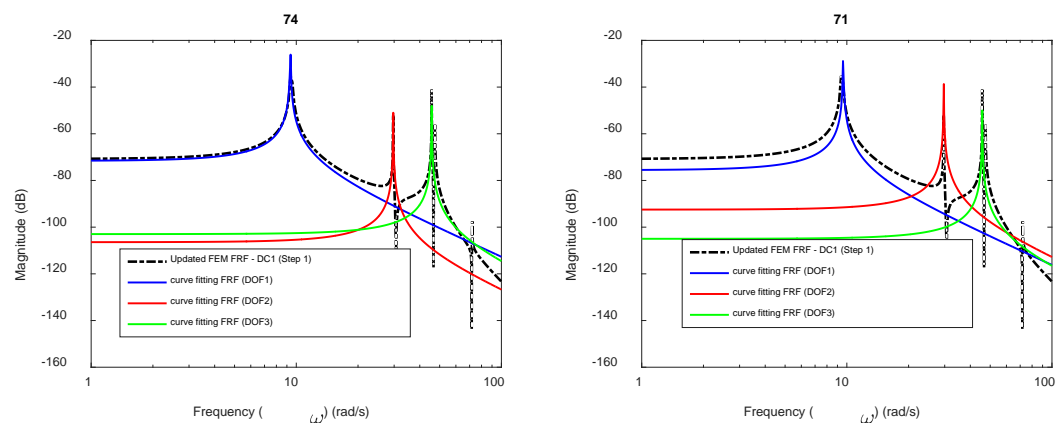
In case of the damage indication as the ratio between updated and the initial rotational stiffness values of the springs, it can be said that since it was not found significant damage indications in the field, a comparison between analytically determined and visually inspected damage could not be clearly carried out. However, this result shows the importance of the vibration based damage identification which indicates significant stiffness degradation comparing to the visual inspection.

#### 4.2.2 Updating damping ratio (Step 2)

For the updating of the damping parameters, the same procedure applied for the updating the damping parameters of the damaged case of the building TB-1 for as well the undamaged cases of the buildings TB-1 and TB-2 was adopted for the damaged cases of the building TB-2.

##### 4.2.2.1 Curve fitting

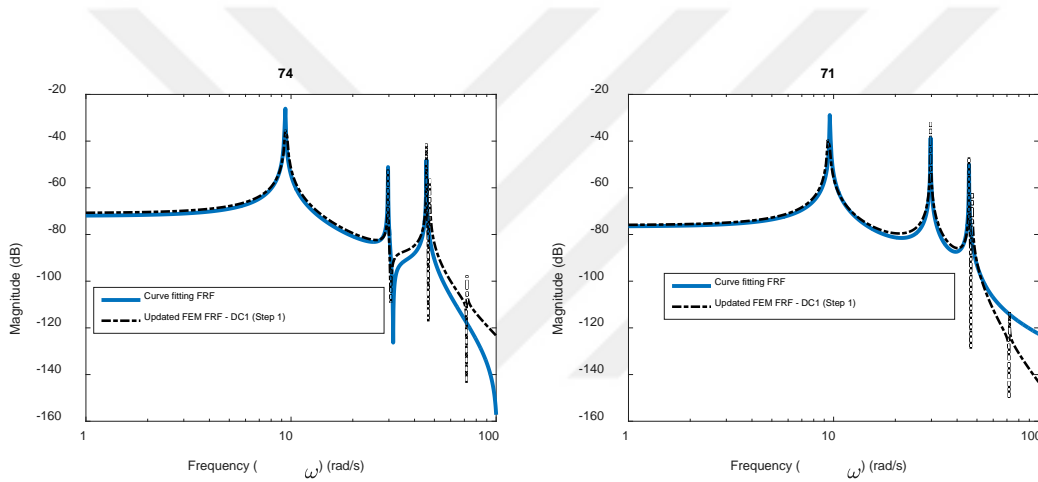
The second order differential equations were produced for each resonant frequency by fitting a curve to the each DOFs of the analytical FRFs which updated in Step 1 (can be seen in Figure 4.18 to Figure 4.22). Figure 4.23 to Figure 4.32 displays the curve fitting applications and their algebraic summation as FRF of the system. The produced second-order differential equations by curve fitting are given in Table 4.10 to Table 4.14.



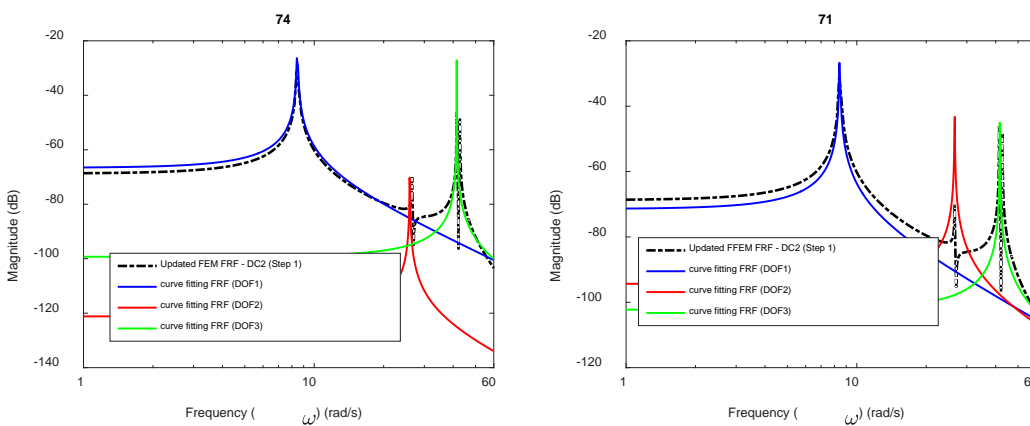
**Figure 4.23 :** Application of curve fitting (Damaged Case 1).

**Table 4.10** : Second order differential equations of updated FEM FRFs (Step 1) – Damaged Case 1.

DOF*	$H_{74}$	$H_{71}$
$s=\sigma_1 + j\omega_1$	$\frac{-0.02222}{s^2 + 87.63}$	$\frac{0.01611}{s^2 + 6.353e-20 s + 92.24}$
$s=\sigma_2 + j\omega_2$	$\frac{-0.005606}{s^2 + 868.1}$	$\frac{0.02234}{s^2 + 1.331e-19 s + 882.1}$
$s=\sigma_3 + j\omega_3$	$\frac{-0.01239}{s^2 + 2.794e-18 s + 2071}$	$\frac{-0.01038}{s^2 + 4.908e-18 s + 2071}$



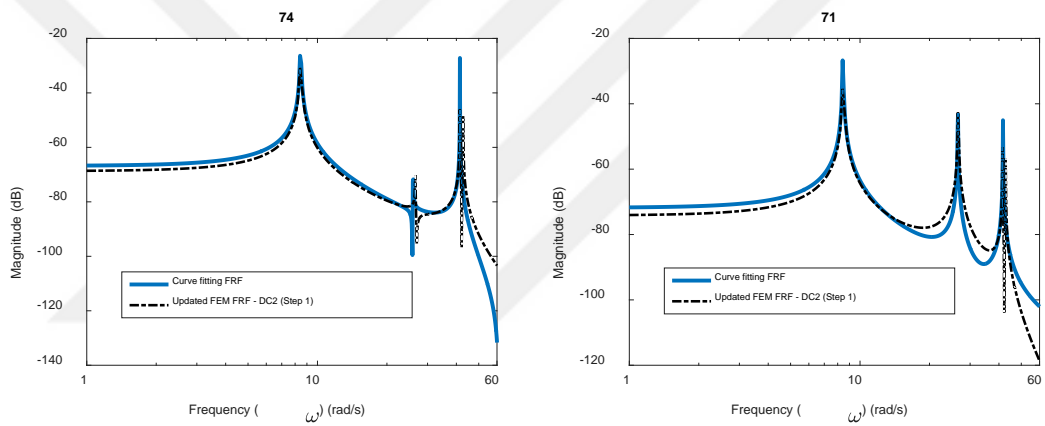
**Figure 4.24** : FRF of the system - Damaged Case 1.



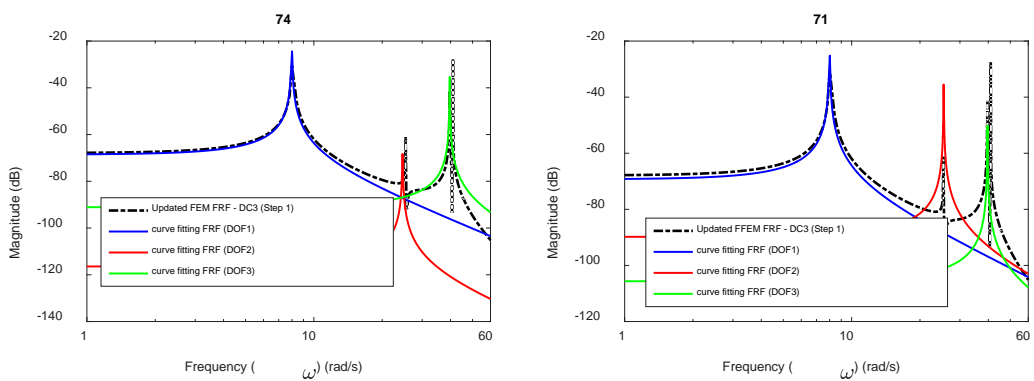
**Figure 4.25** : Application of curve fitting (Damaged Case 2).

**Table 4.11** : Second order differential equations of updated FEM FRFs (Step 1) - Damaged Case 2.

DOF*	$H_{74}$	$H_{71}$
$s=\sigma_1 + j\omega_1$	$\frac{-0.03332}{s^2 + 71.36}$	$\frac{-0.01904}{s^2 + 71.08}$
$s=\sigma_2 + j\omega_2$	$\frac{-0.0005869}{s^2 + 672.9}$	$\frac{-0.01352}{s^2 + 5.35e-18 s + 705}$
$s=\sigma_3 + j\omega_3$	$\frac{0.01865}{s^2 + 1718}$	$\frac{0.01338}{s^2 + 1736}$



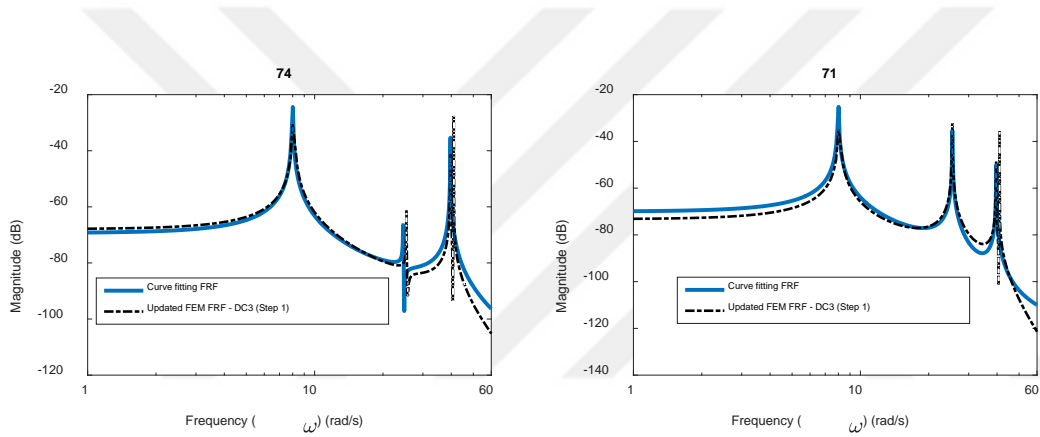
**Figure 4.26** : FRF of the system - Damaged Case 1.



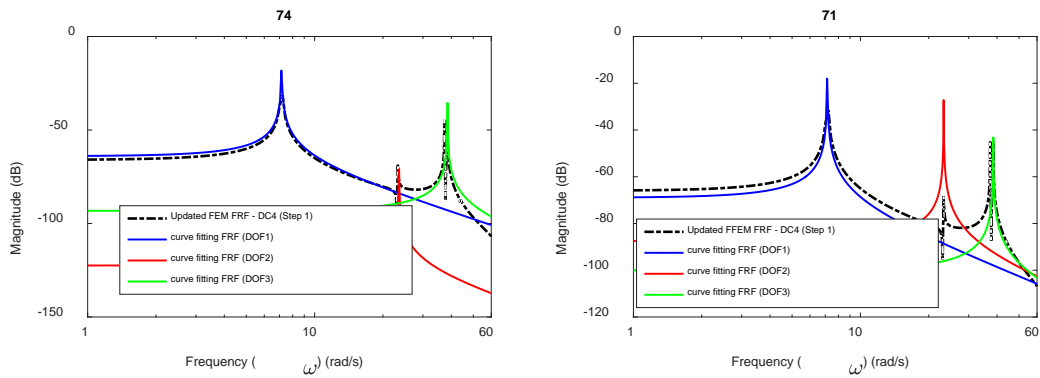
**Figure 4.27** : Application of curve fitting (Damaged Case 3).

**Table 4.12 :** Second order differential equations of updated FEM FRFs (Step 1) - Damaged Case 3.

DOF*	$H_{74}$	$H_{71}$
$s=\sigma_1 + j\omega_1$	$\frac{-0.00396}{s^2 + 63.86}$	$\frac{-0.003406}{s^2 + 1.667e-20 s + 63.85}$
$s=\sigma_2 + j\omega_2$	$\frac{-0.0002598}{s^2 + 604.4}$	$\frac{-0.005229}{s^2 + 647.2}$
$s=\sigma_3 + j\omega_3$	$\frac{0.002196}{s^2 + 1573}$	$\frac{0.002737}{s^2 + 1572}$



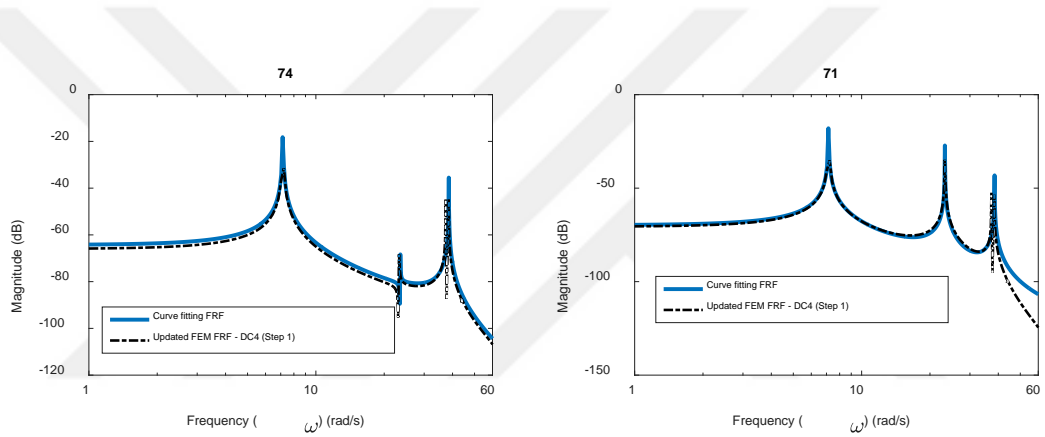
**Figure 4.28 :** FRF of the system - Damaged Case 3.



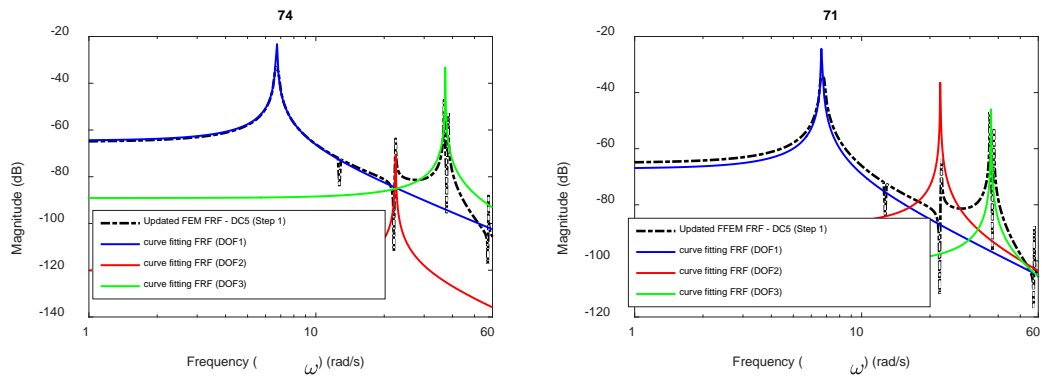
**Figure 4.29 :** Application of curve fitting (Damaged Case 4).

**Table 4.13** : Second order differential equations of updated FEM FRFs (Step 1) - Damaged Case 4.

DOF*	$H_{74}$	$H_{71}$
$s=\sigma_1 + j\omega_1$	$\frac{-0.03222}{s^2 + 51.18}$	$\frac{-0.01817}{s^2 + 51.06}$
$s=\sigma_2 + j\omega_2$	$\frac{0.0004161}{s^2 + 2.574e-18 s + 553.5}$	$\frac{0.02279}{s^2 + 541.8}$
$s=\sigma_3 + j\omega_3$	$\frac{0.01672}{s^2 + 1481}$	$\frac{0.0147}{s^2 + 1.881e-18 s + 1481}$



**Figure 4.30** : FRF of the system - Damaged Case 4.



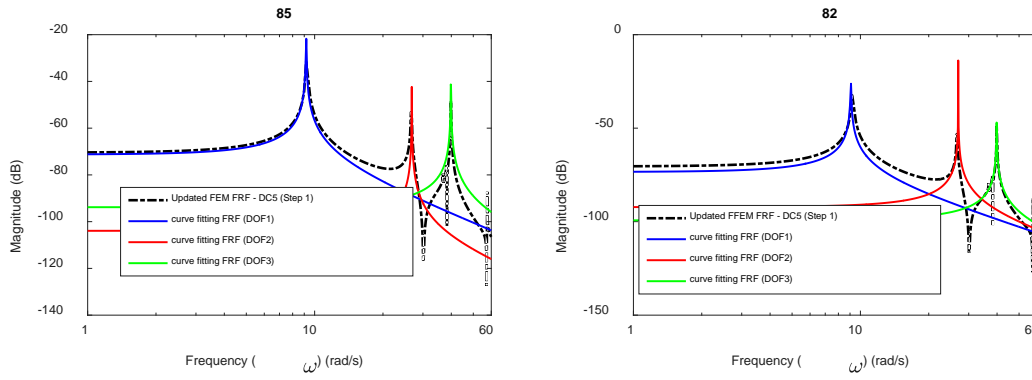


**Figure 4.31 : Application of curve fitting (Damaged Case 5).**

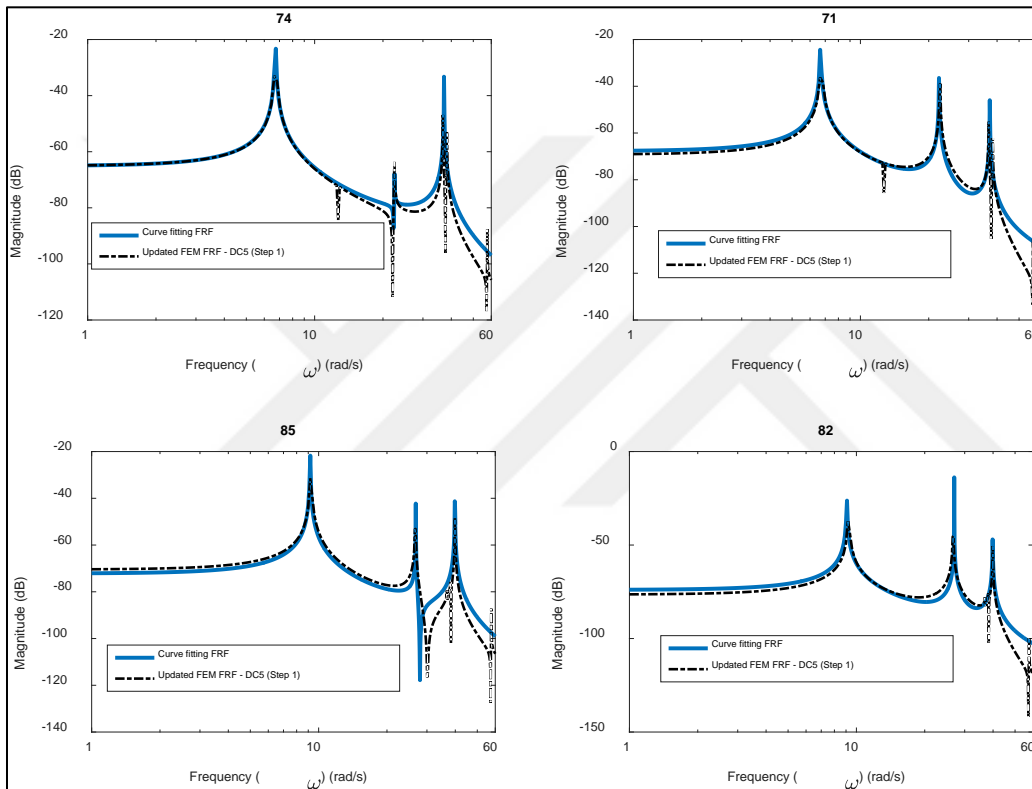


**Figure 4.32 : FRF of the system - Damaged Case 5.**



**Table 4.14 :** Second order differential equations of updated FEM FRFs (Step 1) - Damaged Case 4.

DOF*	$s=\sigma_1 + j\omega_1$	$s=\sigma_2 + j\omega_2$	$s=\sigma_3 + j\omega_3$
$H_{74}$	$\frac{-0.02668}{s^2 + 45.1}$	$\frac{-0.0004968}{s^2 + 503.8}$	$\frac{0.02908}{s^2 + 1.288e-18 s + 1382}$
$H_{71}$	$\frac{-0.01968}{s^2 + 44.51}$	$\frac{-0.02063}{s^2 + 493.8}$	$\frac{0.01186}{s^2 + 1382}$
$H_{85}$	$\frac{-0.02295}{s^2 + 84.15}$	$\frac{0.004564}{s^2 + 718}$	$\frac{-0.0323}{s^2 + 1587}$
$H_{82}$	$\frac{-0.01754}{s^2 + 82.29}$	$\frac{0.01782}{s^2 + 728}$	$\frac{-0.01721}{s^2 + 6.87e-21 s + 1587}$

#### 4.2.2.2 Sine analysis and calculation of analytical FRF

As it was introduced in previous chapters, a sine analysis was performed to generate the acceleration response of the each DOFs with the aim of obtaining the analytical FRF as the ratio of the corresponding acceleration response of DOFs to shaker operating frequency square. This process was repeated by iteratively changing the damping parameters in the equation of the system FRF and finally was concluded with the well-matching of analytically determined and experimentally obtained damaged FRFs in terms of their amplitudes in resonants (Figure 4.33 to Figure 4.37). The obtained damping ratio values at this step and the experimental ones were given for each damaged case in Table 4.15. Although the experimental and analytical results were not found to be in perfect match for the damping ratios of the damaged case, the increasing in damping ratio with the increasing in damage was identified for analytical cases which was observed in the experimental study. This was an expected result due to the difficulties and uncertainties for determination and calculation of the damping parameters.

**Table 4.15 :** Updated values of damping ratio.

Damage case	Buildings	x direction			y direction		
		$\zeta_1$	$\zeta_2$	$\zeta_3$	$\zeta_1$	$\zeta_2$	$\zeta_3$
DC1	Updated FEM FRF	-	0.020	0.010			
	Damaged FRF (experimental)	-	0.024	0.014			
DC2	Updated FEM FRF	-	0.029	0.016			
	Damaged FRF (experimental)	-	0.034	0.015			
DC3	Updated FEM FRF	-	0.038	0.015			
	Damaged FRF (experimental)	-	0.036	0.015			
DC4	Updated FEM FRF	-	0.045	0.020			
	Damaged FRF (experimental)	-	0.036	0.012			
DC5	Updated FEM FRF	-	0.040	0.021	-	0.029	0.025
	Damaged FRF (experimental)	-	0.035	0.014	-	0.022	0.012

\*

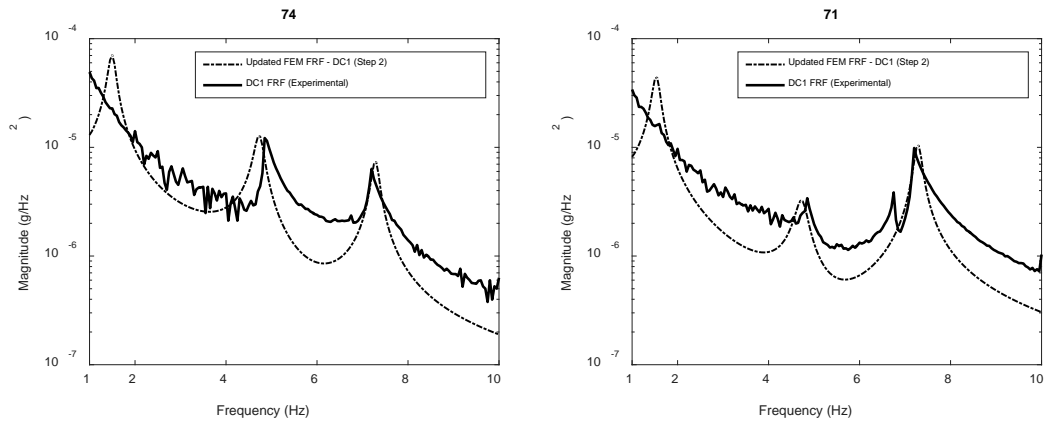


**Figure 4.33 :** Model updating results of the building TB-2 (Step 2) - DC1.

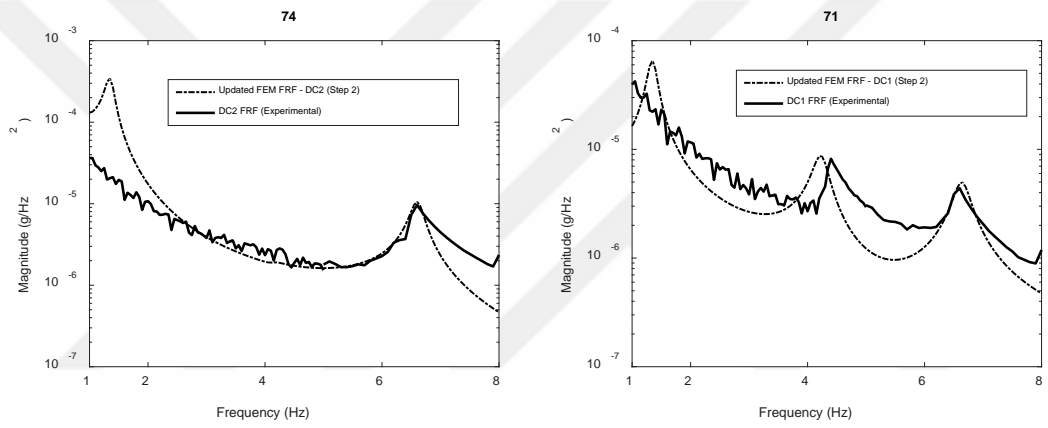


**Figure 4.34 :** Model updating results of the building TB-2 (Step 2) – DC2.

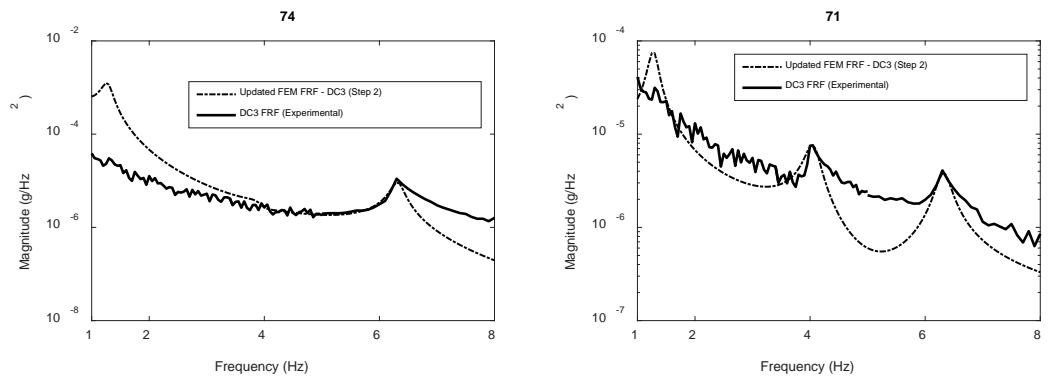


**Figure 4.35 :** Model updating results of the building TB-2 (Step 2) – DC3.

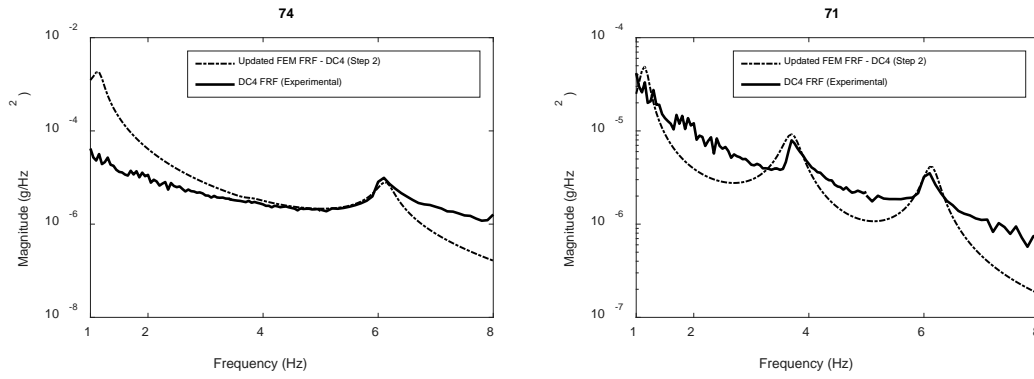


**Figure 4.36 :** Model updating results of the building TB-2 (Step 2) – DC4.

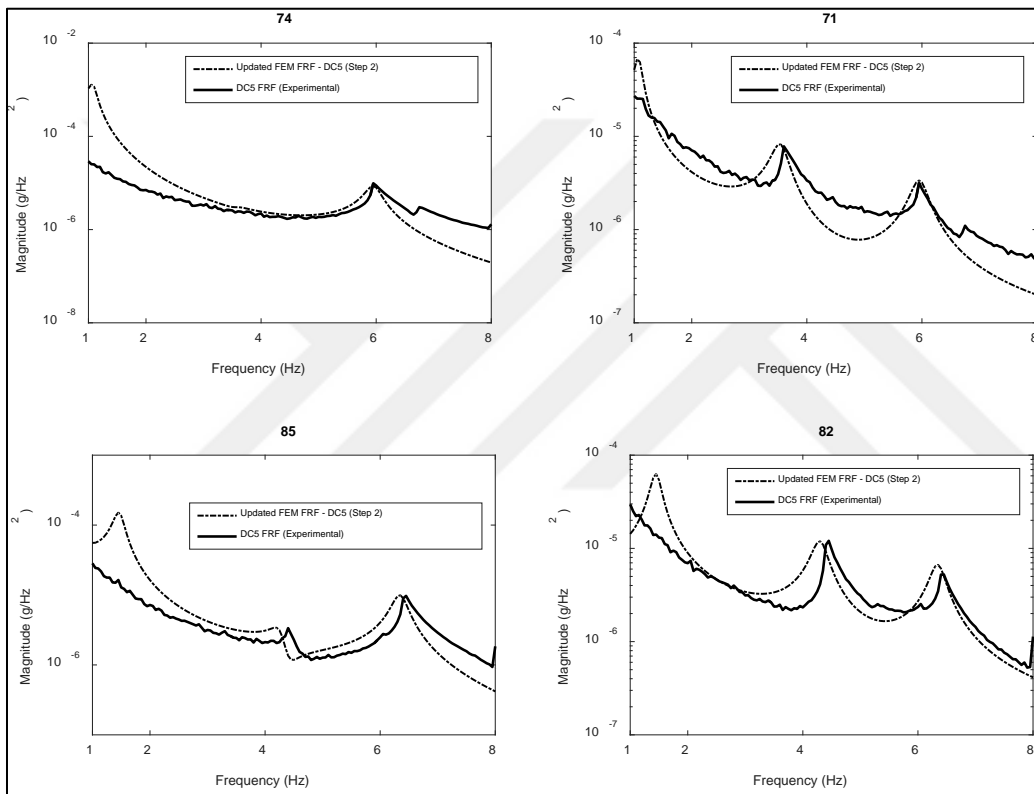


**Figure 4.37 :** Model updating results of the building TB-2 (Step 2) – DC5.

### 4.3 Concluding Remarks

In this chapter, the FRF based model updating algorithm, which was introduced in previous chapter, was adopted for damage detection, localization and quantification using experimentally collected data from the building TB-1 and TB-2. At the end of the application of algorithm, following results were extracted;

Step 1 provided a successful damage detection, localization and quantification process. Although Step 2 also provided to match the experimental FRFs and FEM FRFs in

terms of their amplitudes, it is basically have not any contribution for Level 3 damage identification purpose.

Selection of unknown parameters and grouping them that cause significant changes in the measured FRFs was the most critical issue for damage identification algorithm. In this study, this selection was carried out by glancing over the resisting mechanism of the frames against lateral loadings. In short, the selection of unknown parameters depends on the engineer's judgment which clearly somehow makes the protocol subjective. Therefore, a more automated parameter selection protocol could be dealt as a forward problem.

The algorithm identified the correct location of damage in a blind "scenario" by predicting the decrease in stiffness values of the frame-end springs that is representing the initial and boundary conditions.



## **5. DEMONSTRATION OF EFFICIENCY OF SIMPLIFIED FINITE ELEMENT MODEL FOR DAMAGE IDENTIFICATION**

Since the damage identification algorithm, introduced above, follows a model-based approach, it requires establishing the finite element model of the concerned structures to run the modal analysis and subsequently to derive the dynamic equation of motion. Although it is not a modelling process as complex as the nonlinear modelling of a structure which requires the definition of nonlinear stress-strain relationships of concrete and reinforcing bars for describing the nonlinear behavior of the structure, it still concerns establishing full-scale model of the target structure. Hence, the present chapter examines the efficiency of the predictions of a simple and practical finite element model of the test buildings concerning the damage identification. In brief, a simplified modelling of the buildings TB-2 were established and considered while computing the damage identification algorithm. The efficiency of this approach was then discussed.

### **5.1 Simplified modelling approach**

Previously, a matrix condensation was processed in the background of the damage identification algorithm to decrease the total number of dynamic equation of motions by eliminating the DOFs of the buildings to which zero mass was assigned (Chapter 3.2.1.2). Although the dynamic analysis (modal analysis) was computed for the full-scale 3D model of the buildings, the mass of the buildings was idealized as concentrated in point lumps at the nodes. This matrix condensation method considered throughout the damage identification algorithm is the phenomenon underlying the simplified modelling approach. Therefore, a lumped-mass modelling approach has been considered by subdividing DOFs into the three parts,  $U_x$ ,  $U_y$  and  $R_z$  and 2 numbers of 3DOF lumped mass models were established for building. As seen from the representative view of the simplified models in Figure 5.1, 2-dimensional lumped mass models were considered in  $x$ - $z$  and  $y$ - $z$  spaces. Since the rotational modes were not

identified in this case, a lumped mass model for representing the third DOF ( $R_z$ ) was not established.

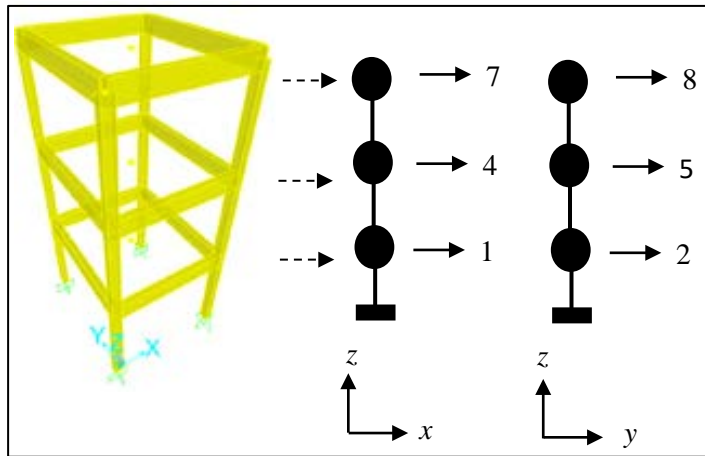


**Figure 5.1 :** Schematic view of simplified FEMs.

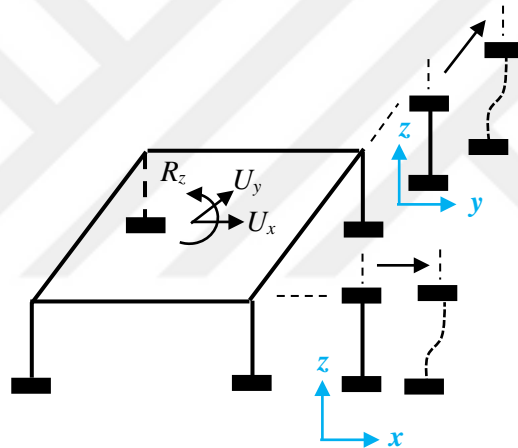


**Figure 5.2 :** Rigid floor diaphragms and corresponding DOFs of 1-story shear frame

As seen in Figure 5.2, as a result of the shear story frame mechanism of the building, a rigid-slab body assumption was considered. Hence, each floor diaphragm composed of slab and beams was able to be assumed rigid so that diaphragm was constrained to move a single unit in the horizontal plane. Since the simplified models were established in two dimensional space ( $x$ - $z$  and  $y$ - $z$ ), out of plane modes were restrained. Due to the rigid-floor body assumption, the both bottom and top ends of vertical members (columns in this case) were assumed fixed.

In the simplified model, a vertical frame member was defined for each story and a moments of inertia value equals to the total moments of inertia values of the columns in the concerned direction was assigned to this member so that the lateral stiffness



values of each story due to vertical members can be calculated by SAP2000 (Equation 5.1 and 5.2).

$$k_{xj} = \frac{12E_c I_{xj}}{H^3} \quad (5.2)$$

$$k_x = \sum_j k_{xj} \quad (5.3)$$

Where  $k_{xj}$  is the lateral stiffness of the  $j$ th member in the story due to relative unit displacement in  $x$  direction (Figure 5.2) and  $E_c$ ,  $I_{xj}$  and  $H$  are the elastic modulus of concrete, moments of inertia of the  $j$ th column in the story and story height respectively. The same mathematical manipulations are valid for calculating the lateral stiffness values in  $y$  direction. It should be noted that the lateral stiffness values of beams and slab were also represented with a unitless lateral member at floor levels. Following the assigning story mass values to considering DOF, model updating of the initial model has been initiated.

## 5.2 Model updating for baseline model

Prior to computing the damage identification algorithm, model updating of the initial model by calibrating the elastic modulus of the concrete was conducted. For this purpose, first, the baseline model was attained by updating the [M] and [K] matrices of the initial model. For this purpose, the values of  $E_c^{updated}$  and  $\gamma_c^{updated}$  found in Chapter 3 while the initial full-scale model of the building TB-2 was updating (Step 1), were considered to examine the efficiency of the utilizing simple model in damage identification algorithm. Figure 5.3 illustrates the comparison of the FRF of simple FEM created using  $E_c^{updated}$  and  $\gamma_c^{updated}$  in Chapter 3 and the experimental FRF of the undamaged state of the building TB-2. Although the analytical FRFs obtained from full-scale model and simple model are not identical, the updating of damping ratio was computed based on the well-matched result in Figure 5.3.

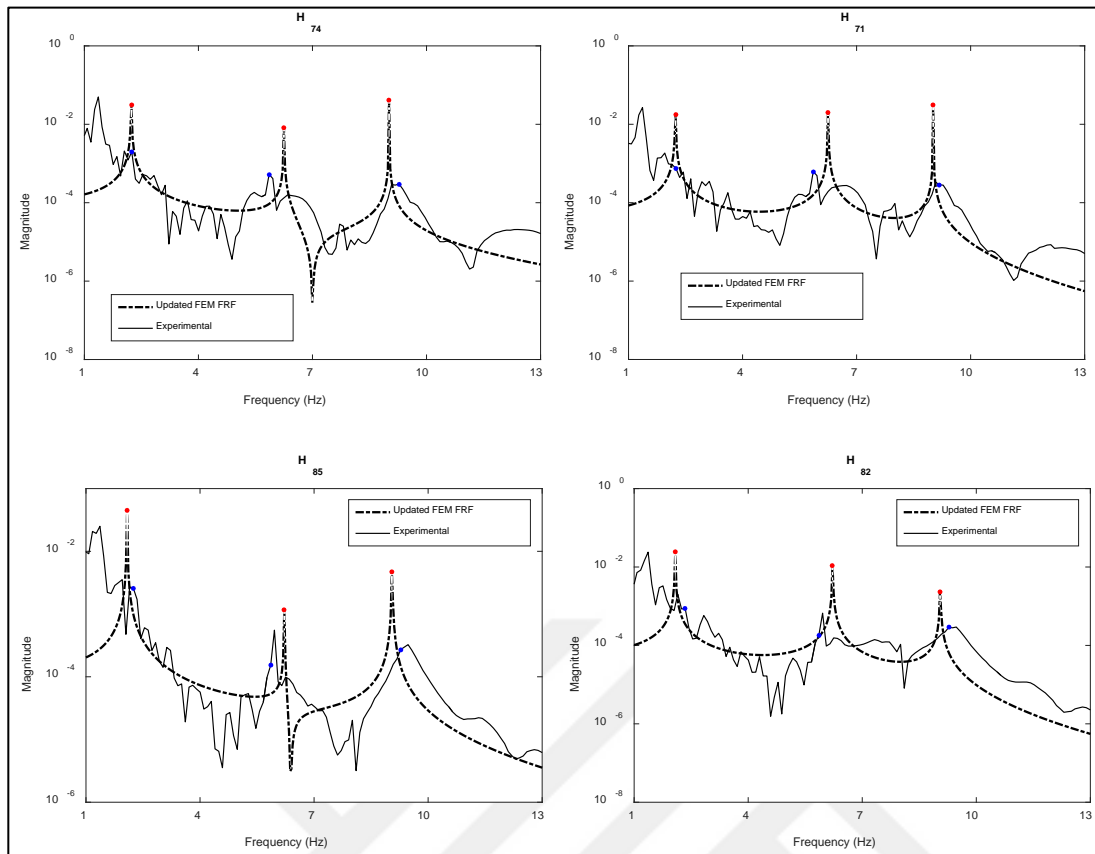


**Figure 5.3 :** Updated FRF of the simple model of the building TB-2 (Step 1:  $[K]$  and  $[M]$ ).

For the updating of damping ratio, second step of the algorithm was computed. First, the differential equation of the analytical FRF updated in Step 1 was determined by the algebraic summation of the 3 numbers of second order differential equation (Table 5.1) attained using curve fitting technique (Figure 5.4 and Figure 5.5). Based on the well-matched result of the curve fitting in Figure 5.5, the equations given in Table 5.2 were concerned as the mathematical description of the simple model of the building TB-2.

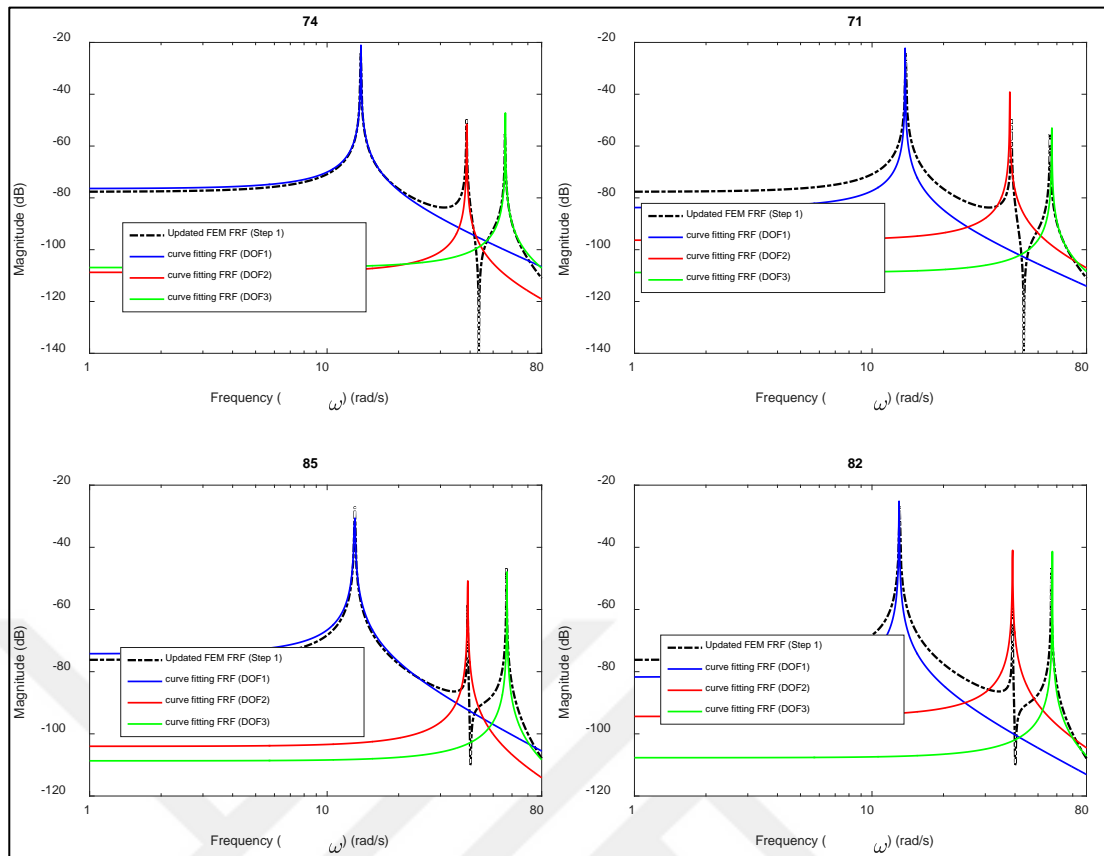


**Figure 5.4 :** Application of curve fitting (the simple model of building TB-2).

Accordingly, a sine analysis was computed by implementing the shaker sinusoidal force as input force to the transfer function of the system (Table 5.2) and the acceleration response of the each DOFs were generated as response of the system throughout MATLAB. Followingly, the analytical FRF as the ratio of the corresponding acceleration response of DOFs to shaker operating frequency square was calculated. The sine analysis and FRF calculation was repeated by iteratively changing the damping coefficients in the differential equation of the system till the amplitudes of the frequency peaks of the analytical and experimental FRF matched (Step 2) (Figure 5.6).

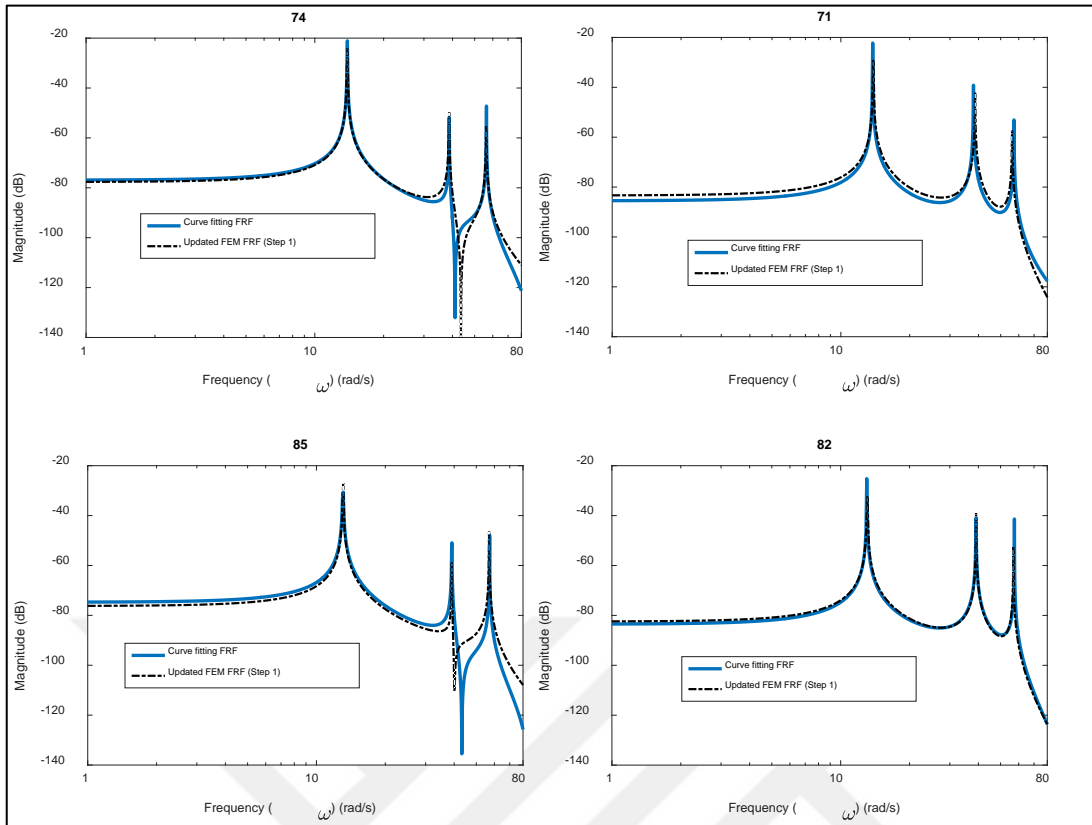


**Figure 5.5 :** FRF of the system (the simple model of building TB-2).

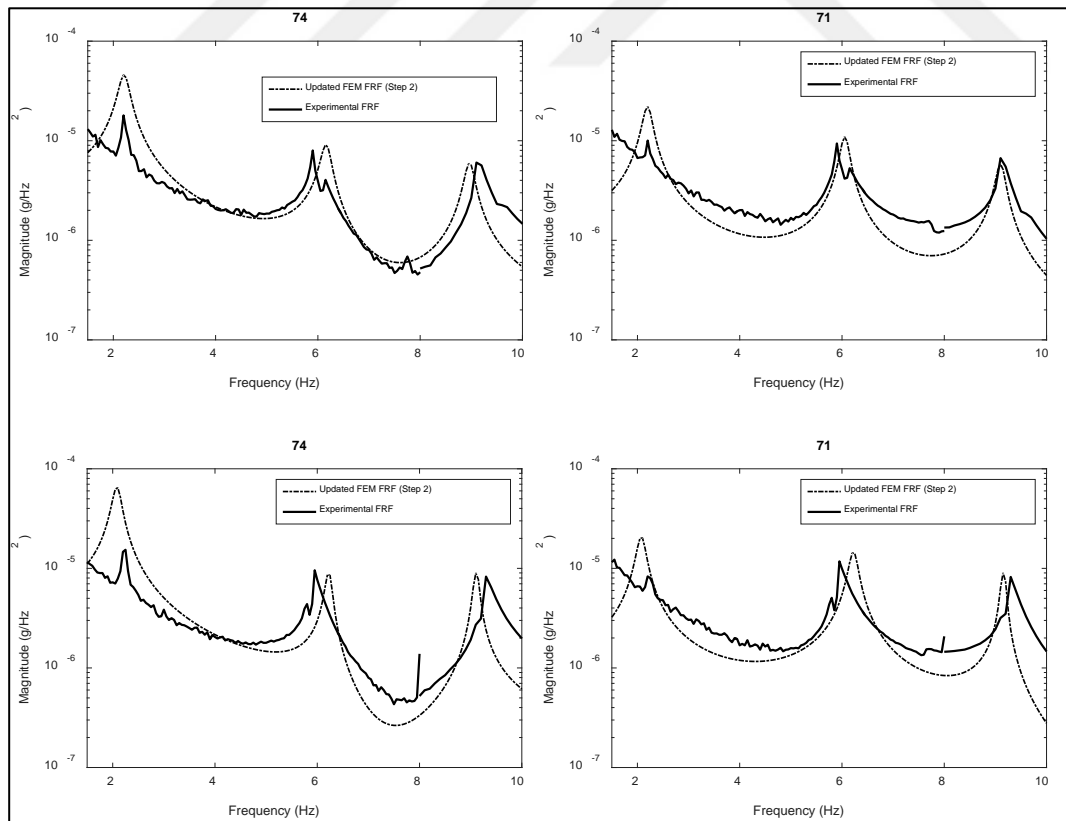


**Figure 5.6 :** Model updating results of the building TB-2 for the simple model (Step 2: Damping ratio).

**Table 5.1** : Second-order differential equation of FRFs of updated simple FEM.

DOF*	$s=\sigma_1 + j\omega_1$	$s=\sigma_2 + j\omega_2$	$s=\sigma_3 + j\omega_3$
$H_{74}$	$\frac{0.02901}{s^2 + 192.3}$	$\frac{0.005458}{s^2 + 9.39e-20 s + 1496}$	$\frac{-0.01432}{s^2 + 3167}$
$H_{71}$	$\frac{0.01228}{s^2 + 189.8}$	$\frac{-0.02203}{s^2 + 1444}$	$\frac{-0.01184}{s^2 + 3265}$
$H_{85}$	$\frac{0.03298}{s^2 + 170.5}$	$\frac{-0.009625}{s^2 + 1.485e-20 s + 1526}$	$\frac{-0.01203}{s^2 + 3267}$
$H_{82}$	$\frac{0.01383}{s^2 + 169.3}$	$\frac{-0.02908}{s^2 + 1526}$	$\frac{-0.01365}{s^2 + 3302}$

\*  $\sigma_n = \zeta_n \omega_n$ , n: number of degree of freedom (n=1,2,3)

**Table 5.2 :** Second-order differential equation of FRFs of updated simple FEM (Algebraic summation).

DOF*	FRF of the system
$H_{74}$	$\frac{0.009233 s^4 + 1.379e-21 s^3 + 92.77 s^2 + 8.368e-18 s + 1.3e05}{s^6 + 9.39e-20 s^5 + 4856 s^4 + 3.154e-16 s^3 + 5.636e06 s^2 + 5.72e-14 s + 9.115e08}$
$H_{71}$	$\frac{0.002092 s^4 + 1.056 s^2 + 4.746e04}{s^6 + 4899 s^4 + 5.608e06 s^2 + 8.948e08}$
$H_{85}$	$\frac{0.01133 s^4 + 3.112e-22 s^3 + 104.6 s^2 + 1.57e-18 s + 1.559e05}{s^6 + 1.485e-20 s^5 + 4963 s^4 + 5.106e-17 s^3 + 5.801e06 s^2 + 8.272e-15 s + 8.496e08}$
$H_{82}$	$\frac{-0.001601 s^4 - 11.05 s^2 + 5.693e04}{s^6 + 4997 s^4 + 5.855e06 s^2 + 8.528e08}$

### 5.3 Damage identification

As previously computed, the two-step damage identification algorithm was implemented to detect, localize, and quantify the damage in the building TB-2 considering its simple FEM. As it was done for the damage identification process of the full-scale model, the simple model was also updated to identify the damage at the certain damage levels introduced in terms of the 1<sup>st</sup> story drift ratio as 0.5% (Damaged Case 1: DC1), 1.0% (Damaged Case 2: DC2), 1.5% (Damaged Case 3: DC3), 2.0% (Damaged Case 4: DC4) and 3.0% (Damaged Case 5: DC5).

With the similar reasons explained in the damage identification case of the building TB-1 in chapter 4, the initial and boundary conditions are expected to be affected from the reversed cyclic lateral loading. Therefore, the degrading on the initial fixity value of the initial and boundary conditions will be represented by assigning the end springs to the columns. However, in the simple model, only two end springs, one for bottom and one for top of the vertical member of each story. Consequently, two-step damage identification algorithm was computed for the damaged cases of DC1, DC2, DC3, DC4 and DC5 by MUP. The rotational stiffness values of the end springs of the vertical members given above were iteratively changed and the 1<sup>st</sup> Step of the damage identification algorithm was terminated for the FRF based updating results given for all damage cases Figure 5.7 to Figure 5.11.

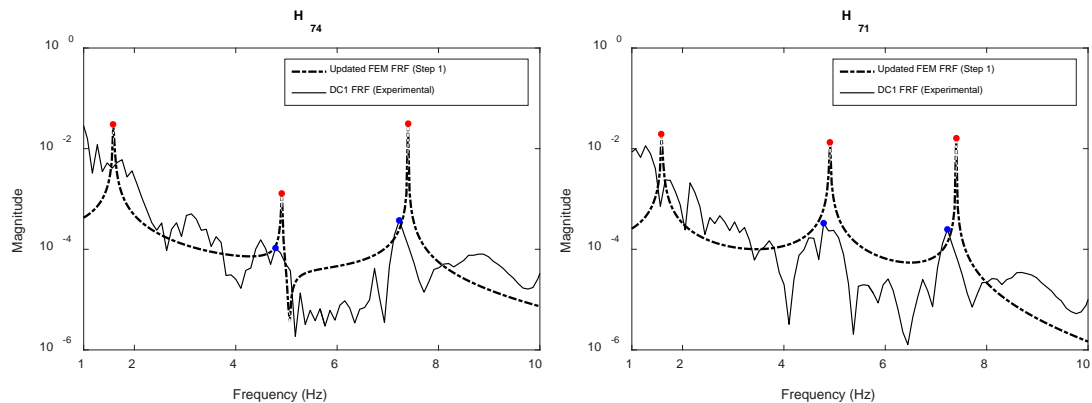


**Figure 5.7 :** Model updating results for the building TB-2 for DC1 (Simple FEM).

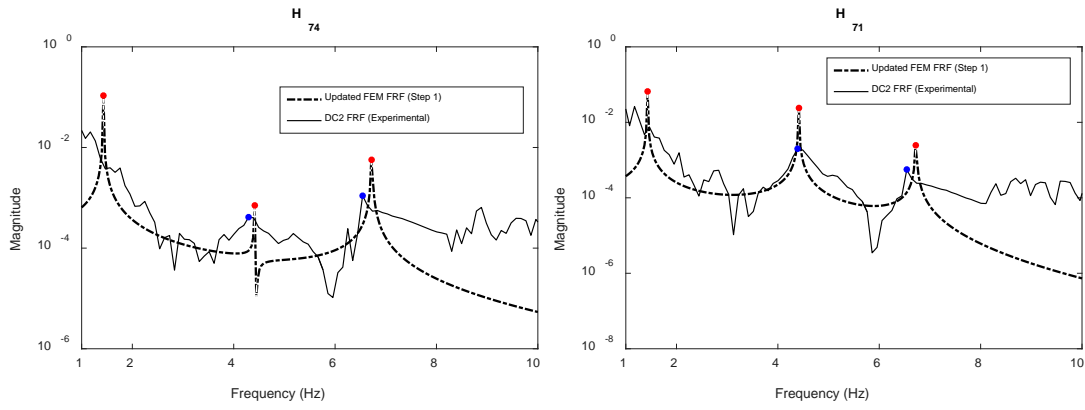


**Figure 5.8 :** Model updating results for the building TB-2 for DC2 (Simple FEM).

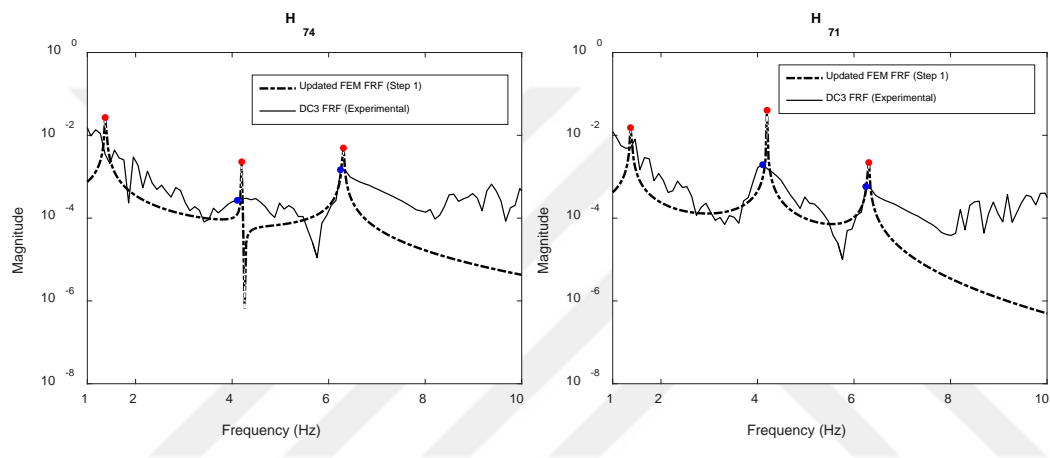


**Figure 5.9 :** Model updating results for the building TB-2 for DC3 (Simple FEM).

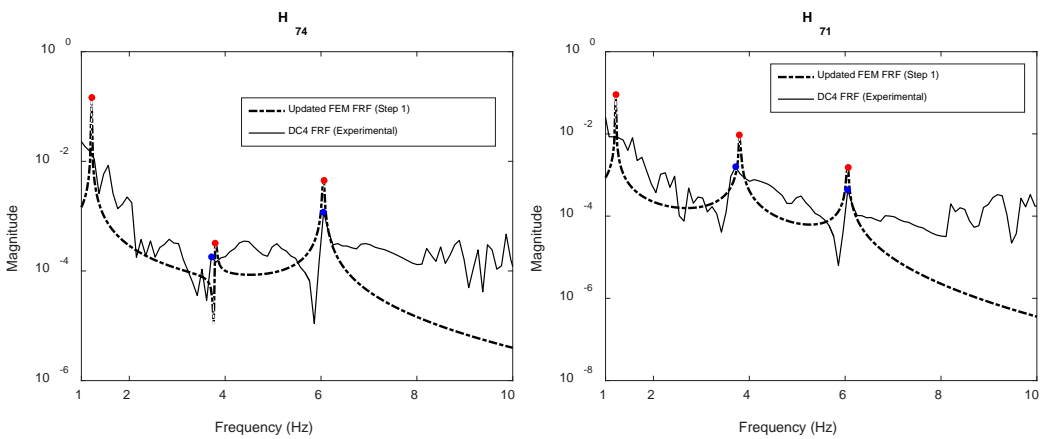


**Figure 5.10 :** Model updating results for the building TB-2 for DC4 (Simple FEM).



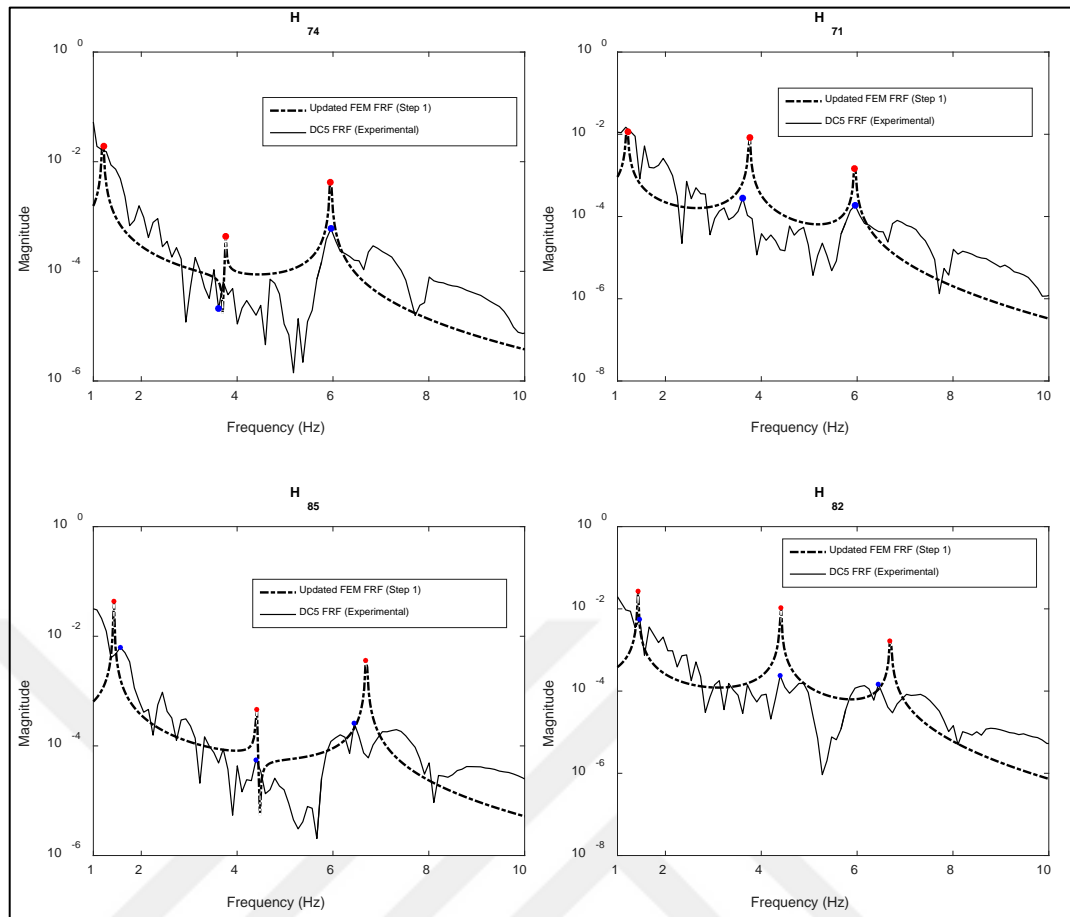


**Figure 5.11** : Model updating results for the building TB-2 for DC5 (Simple FEM).

The well-matched results in the figures in terms of frequency component of the FRF were obtained for the updated values of the  $[K]$  matrice of the building due to the updated initial and boundary conditions which were achieved by changing the stiffness values of the rotational end springs (Table 5.3). Since the all columns in a story were represented by a vertical member with an equivalent lateral stiffness value, the updated stiffness values in Table 5.3 can be compared with the summation of the initial stiffness values of the end spring of each column in a story (Table 5.4). Table 5.4 presents the degradation of the lateral stiffness value of the story which were given in terms of the ratio of updated rotational stiffness values of the simple model to summation of initial rotational stiffness of the end-springs. Similarly, comparison of the updated stiffness values of simple model and the full-scale model was given in Table 5.5. It should be noted that the updated stiffness values of full-scale model were given as the summation of the stiffness values of each end springs in a story (Table 4.7). As seen in Table 5.5, the analytical FRFs obtained from simple model and full-scale model were not matched with the experimental FRFs for the identical stiffness

values. However, it can be extracted that the ratios given in Table 5.5 are relatively close excepting the values of the second story for the DC5.



**Table 5.3 :** Updated values of rotational stiffness values of the end springs (kNm/rad) (Step 1).

	x direction					y direction				
	1 <sup>st</sup> story		2 <sup>nd</sup> story		3 <sup>rd</sup> story	1 <sup>st</sup> story		2 <sup>nd</sup> story		3 <sup>rd</sup> story
	<i>i</i> -end	<i>j</i> -end	<i>i</i> -end	<i>j</i> -end	<i>i</i> -end	<i>i</i> -end	<i>j</i> -end	<i>i</i> -end	<i>j</i> -end	<i>i</i> -end
DC1	36000	36000	40300	45500	55500					
DC2	24500	25550	21500	23250	42900			*		
DC3	18900	19600	17500	17750	29295					
DC4	11280	11400	14000	14000	23790					
DC5	10800	11400	12500	14000	21830	36900	42300	25500	28500	36000

\* There is not dynamic test

**Table 5.4 :** Change of the rotational stiffness values (Updated stiffness/Initial stiffness)

	x direction					y direction				
	1 <sup>st</sup> story		2 <sup>nd</sup> story		3 <sup>rd</sup> story	1 <sup>st</sup> story		2 <sup>nd</sup> story		3 <sup>rd</sup> story
	<i>i</i> -end	<i>j</i> -end	<i>i</i> -end	<i>j</i> -end	<i>i</i> -end	<i>i</i> -end	<i>j</i> -end	<i>i</i> -end	<i>j</i> -end	<i>i</i> -end
DC1	0.31	0.31	0.39	0.44	0.65					
DC2	0.21	0.22	0.21	0.23	0.50			*		
DC3	0.17	0.17	0.17	0.17	0.34					
DC4	0.10	0.10	0.14	0.14	0.28					
DC5	0.09	0.10	0.12	0.14	0.26	0.32	0.37	0.25	0.28	0.42

**Table 5.5 :** Ratio of the updated rotational stiffness values (Simple FEM/Full-Scale FEM).

	<i>x</i> direction					<i>y</i> direction				
	1 <sup>st</sup> story		2 <sup>nd</sup> story		3 <sup>rd</sup> story	1 <sup>st</sup> story		2 <sup>nd</sup> story		3 <sup>rd</sup> story
	<i>i</i> -end	<i>j</i> -end	<i>i</i> -end	<i>j</i> -end	<i>i</i> -end	<i>i</i> -end	<i>j</i> -end	<i>i</i> -end	<i>j</i> -end	<i>i</i> -end
DC1	0.94	0.94	0.97	1.09	0.97					
DC2	0.97	1.01	0.98	0.97	0.97			*		
DC3	0.94	0.89	0.91	0.92	0.94					
DC4	0.94	0.95	0.93	0.92	1.02					
DC5	0.99	0.91	0.65	0.70	0.97	1.03	1.07	1.06	1.10	1.02

Followingly, MUP computed for updating the damping parameters (Step 2). The sine analysis was computed by implementing the shaker sinusoidal force as input force to the transfer function of the system which was obtained through curve fitting. The acceleration response of the each DOFs and the analytical FRF as the ratio of the corresponding acceleration response of DOFs to shaker operating frequency square was then calculated. As it was explained before, the sine analysis and FRF calculation steps were repeated by iteratively changing the damping coefficients in the differential equation of the system till the amplitudes of the frequency peaks of the analytical and experimental FRF matched (Step 2). Accordingly, application of curve fitting and determination of system transfer function are given in Figure 5.12 and Figure 5.13. The updated FRF in terms of its amplitude (Step 2) displayed in Figure 5.14. As it is well known, the updated FRFs was obtained by processing of the acceleration response of the DOFs attained through sine analysis.

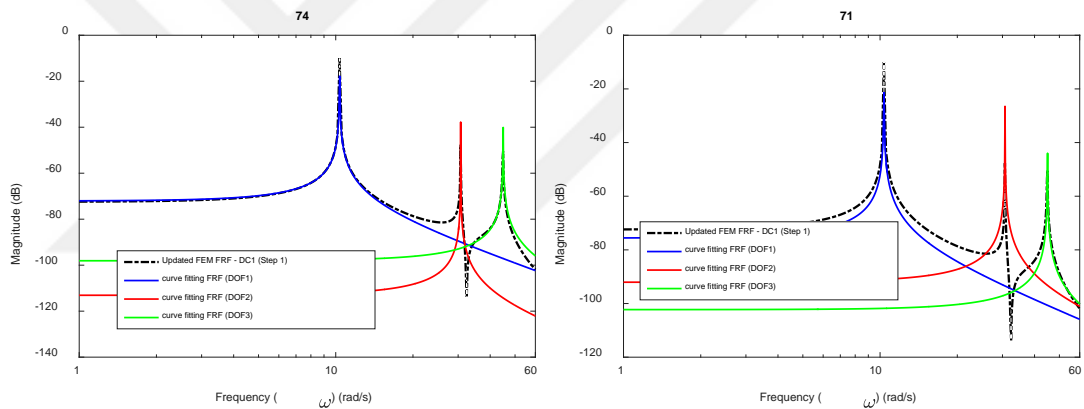


**Figure 5.12 :** Application of curve fitting (DC1-Simple FEM).

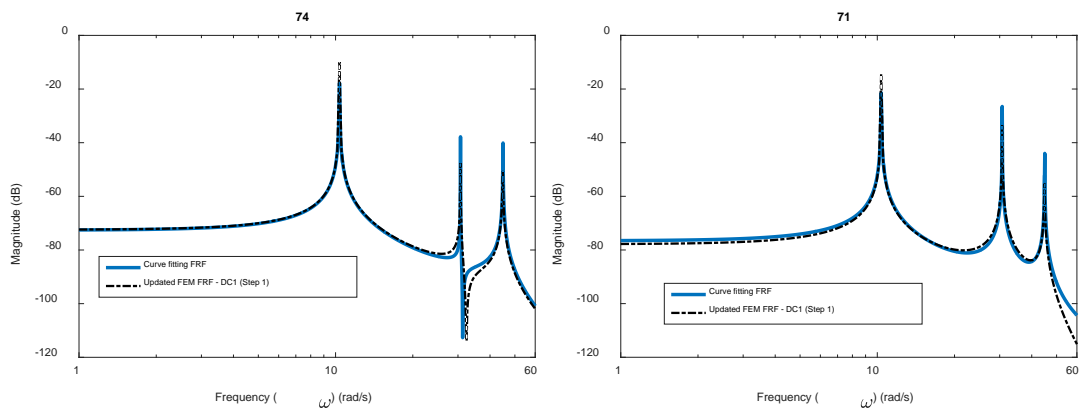


**Figure 5.13 :** FRF of the system - DC1-Simple FEM.

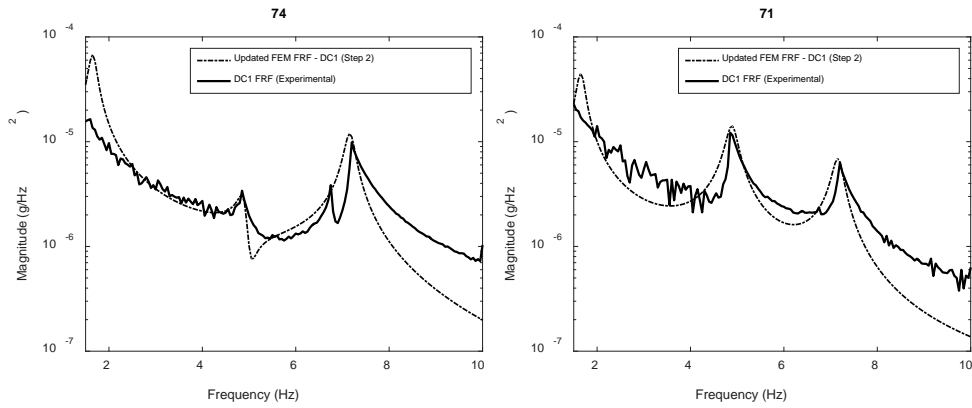


**Figure 5.14 :** Model updating results (Step 2) - DC1-Simple FEM.

Similarly, application of curve fitting, subsequently determination of system transfer function and updating of FRF for minimizing the difference between analytical and experimental FRFs for Damaged Case 2 in terms of their amplitudes are given in Figure 5.15, Figure 5.16 and Figure 5.17, respectively.

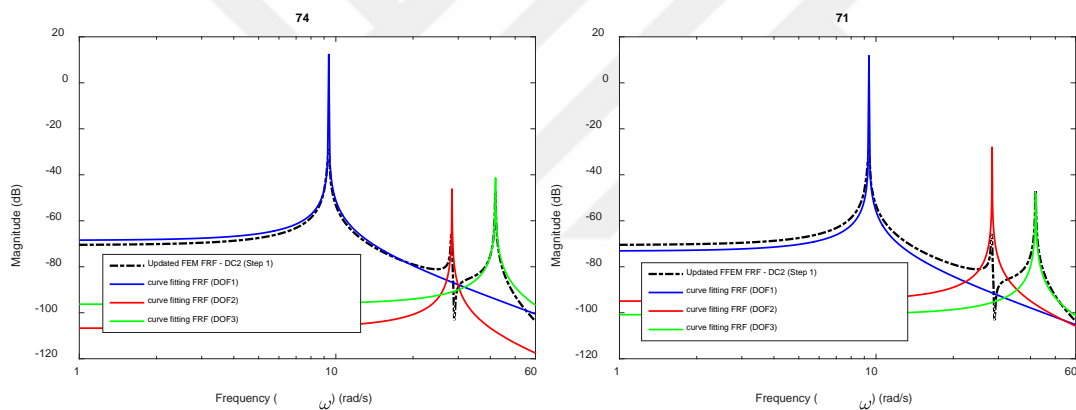


**Figure 5.15 :** Application of curve fitting (DC2-Simple FEM).

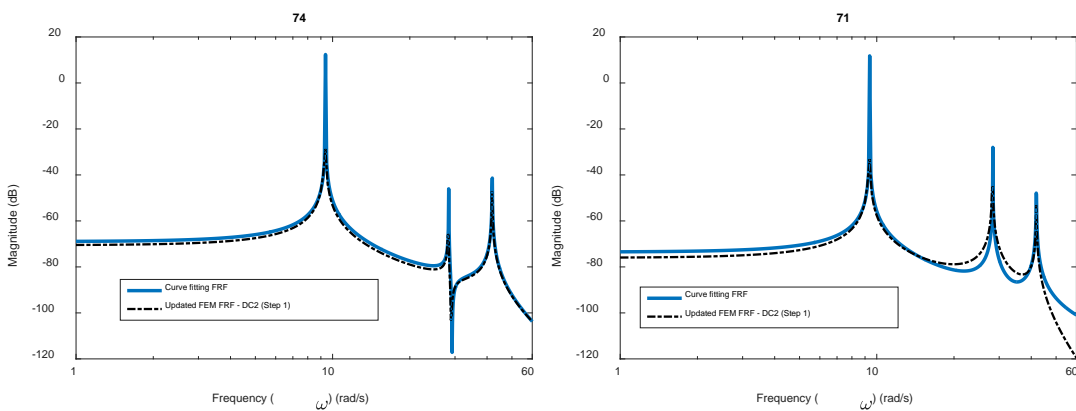


**Figure 5.16 :** FRF of the system – DC2-Simple FEM.

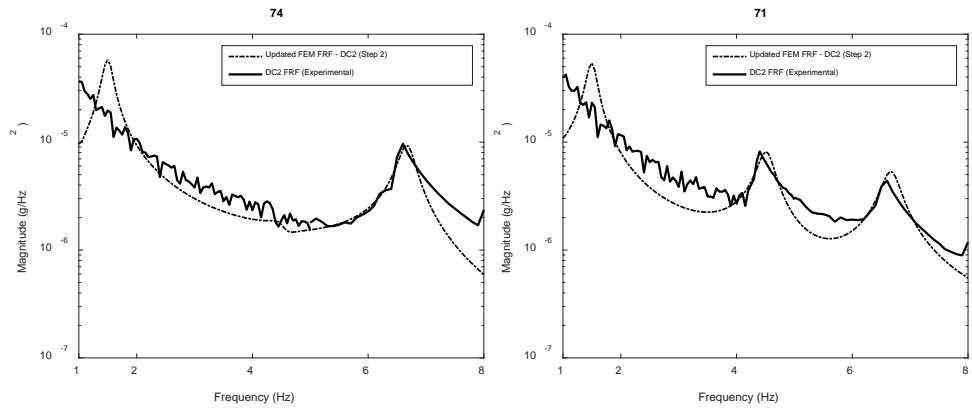


**Figure 5.17 :** Model updating results (Step 2) – DC2-Simple FEM.

The results of the second step of the algorithm for Damaged Case 3 are given in Figure 5.18 to Figure 5.20.

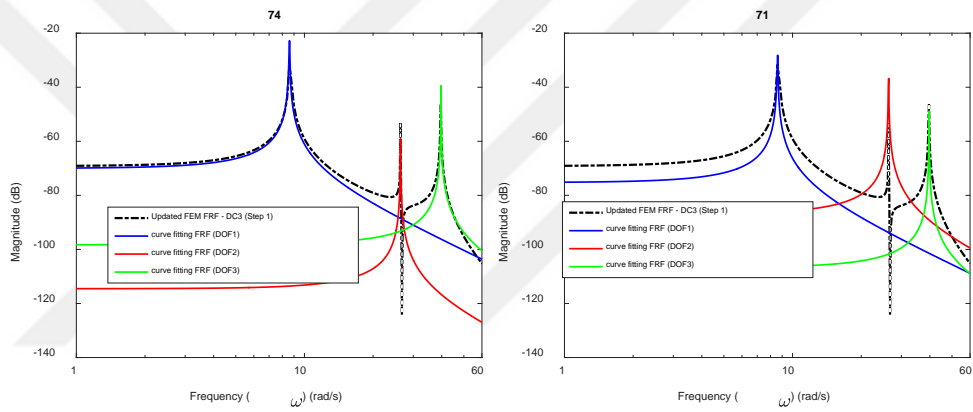


**Figure 5.18 :** Application of curve fitting (DC3-Simple FEM).

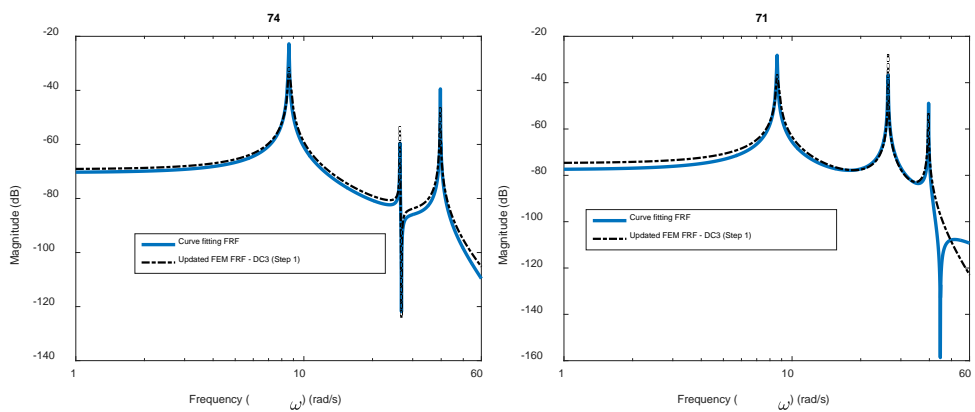


**Figure 5.19 :** FRF of the system – DC3-Simple FEM.

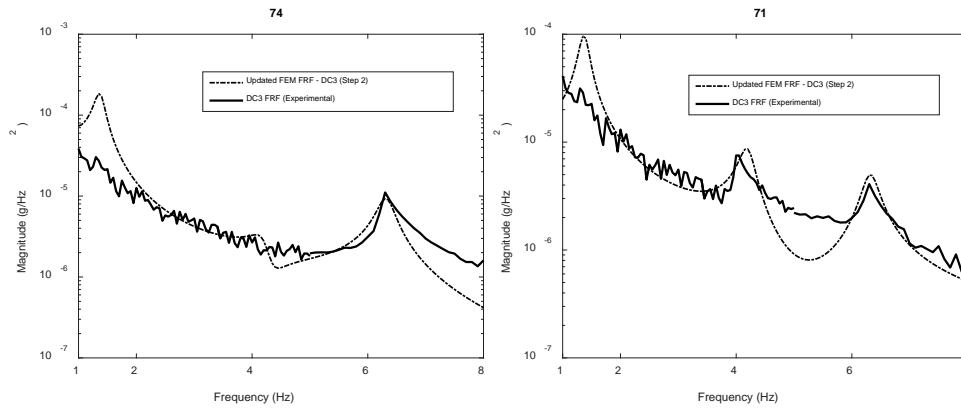


**Figure 5.20 :** Model updating results (Step 2) – DC3-Simple FEM.

The results of the second step of the algorithm for Damaged Case 4 are given in Figure 5.21 to Figure 5.23.

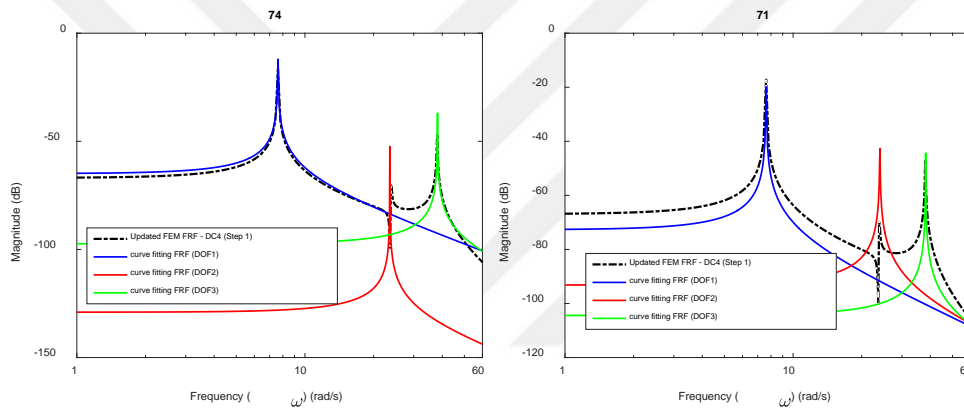


**Figure 5.21 :** Application of curve fitting (DC4-Simple FEM).

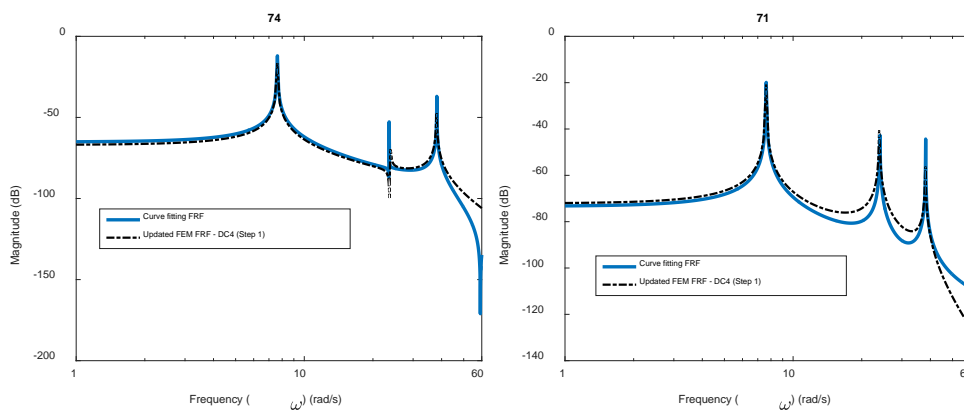


**Figure 5.22 :** FRF of the system – DC3-Simple FEM.



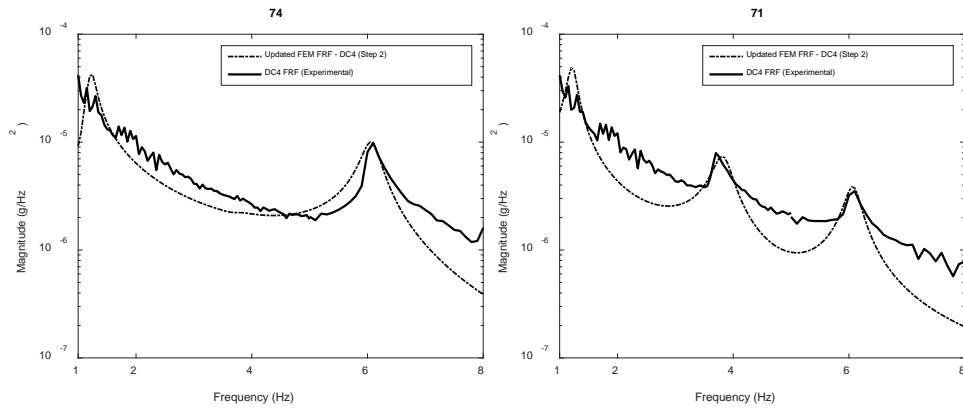


**Figure 5.23 :** Model updating results (Step 2) – DC4-Simple FEM.

Consequently, the results of the second step of the algorithm for Damaged Case 5 are given in Figure 5.24 to Figure 5.26. As seen from the figures, this time the algorithm was also run for estimating the damping ratios of modes in the y direction.

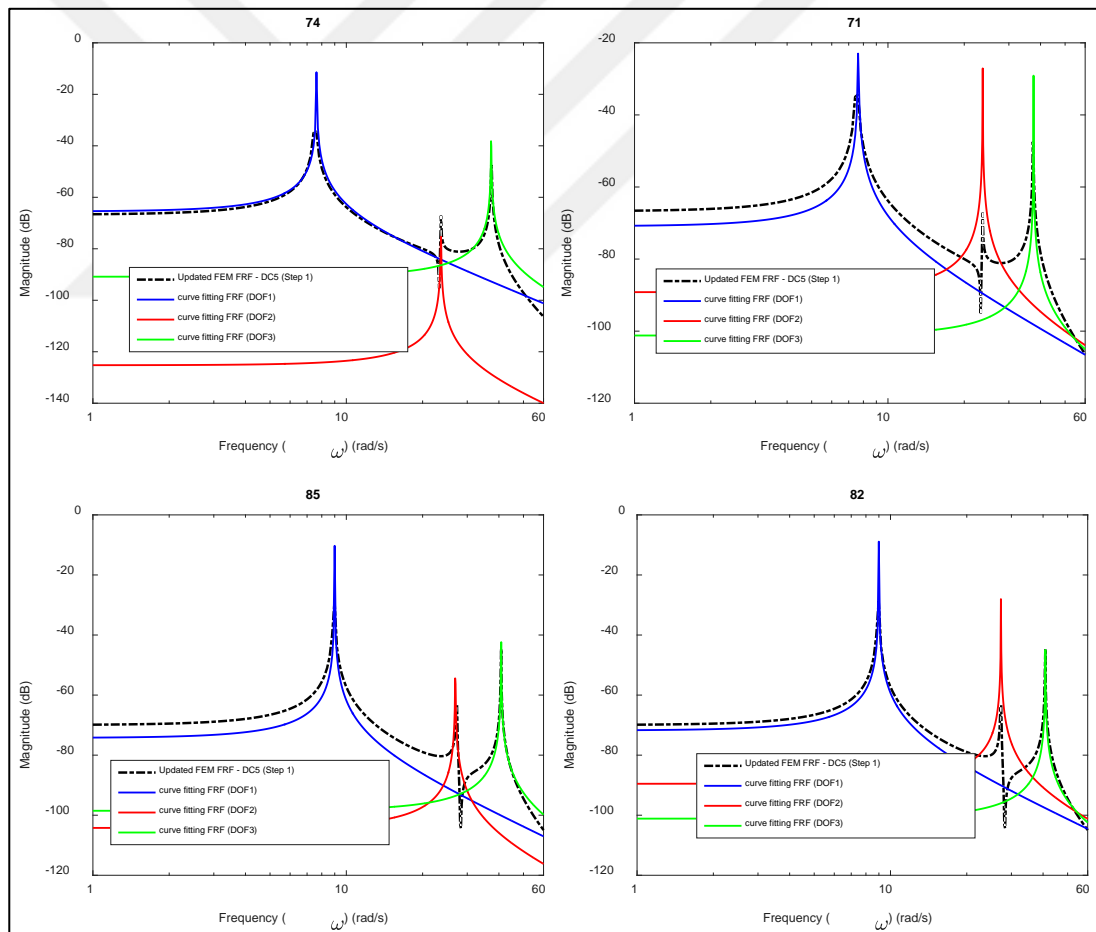


**Figure 5.24 :** Application of curve fitting (DC5-Simple FEM).

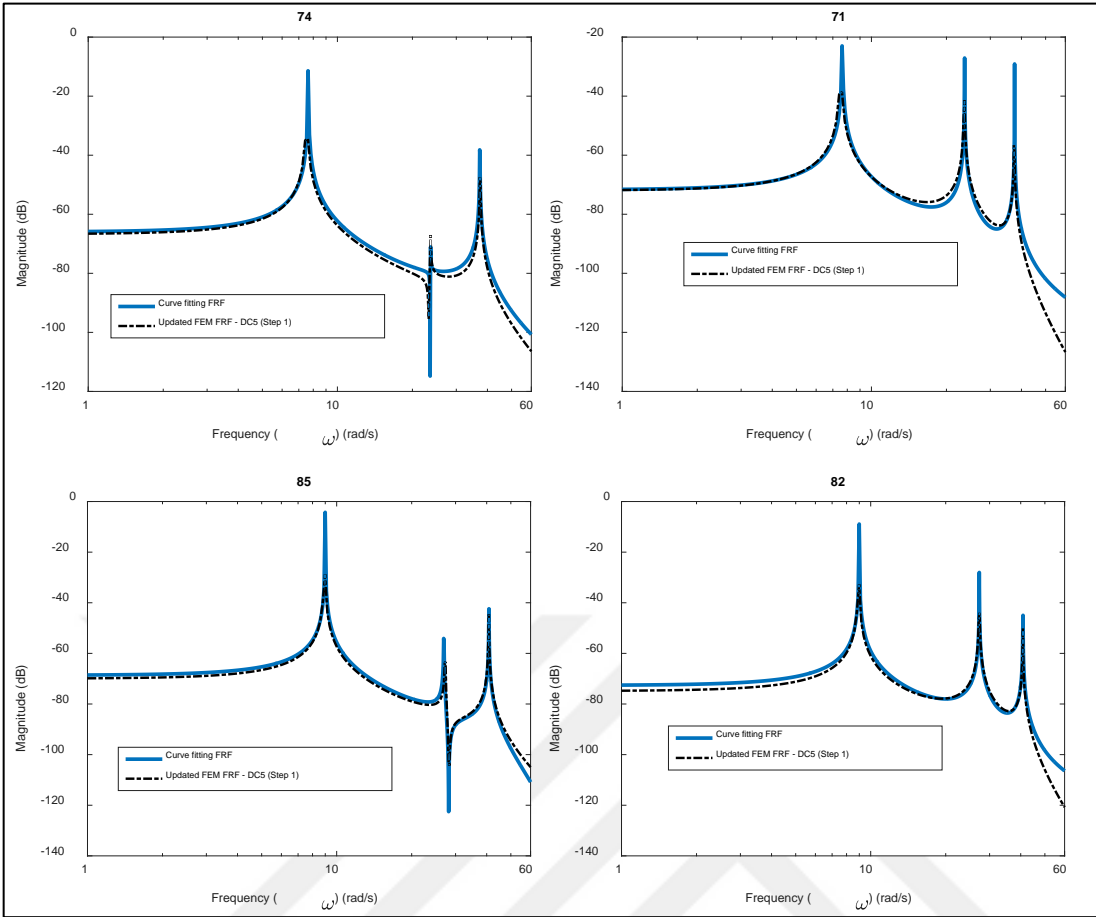


**Figure 5.25 : FRF of the system – DC5-Simple FEM.**

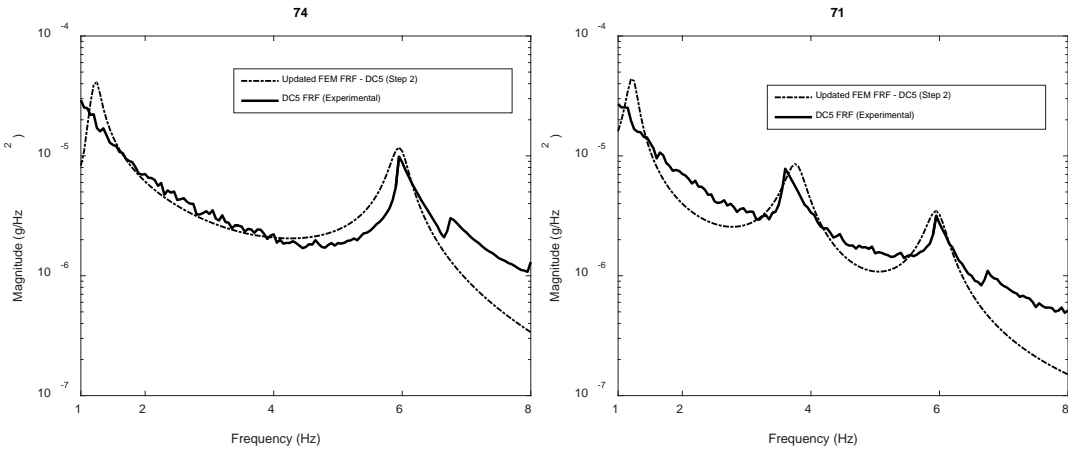


**Figure 5.26 : Model updating results (Step 2) – DC5-Simple FEM.**

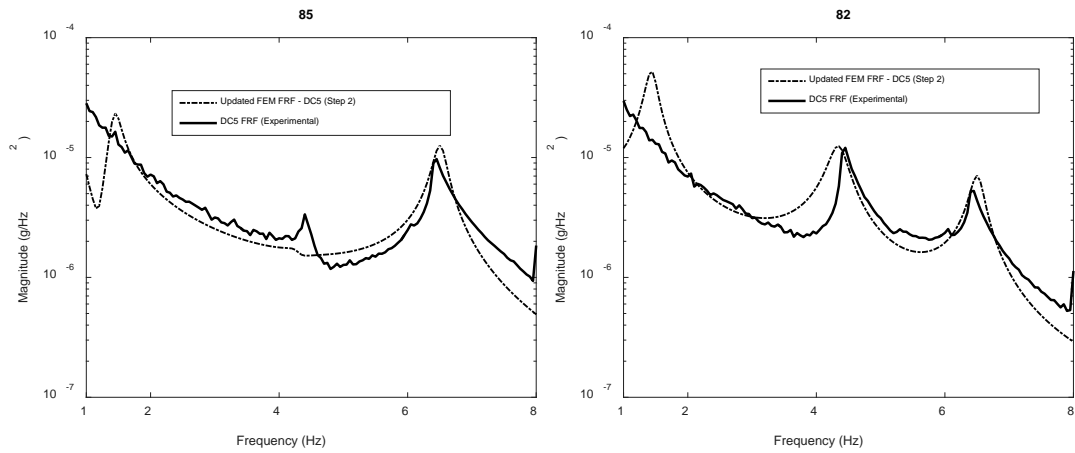


**Figure 5.26 (continued) :** Model updating results (Step 2) – DC5-Simple FEM.

**Table 5.6 :** Updated values of damping ratio.

Damage case	Buildings	x direction			y direction		
		$\zeta_1$	$\zeta_2$	$\zeta_3$	$\zeta_1$	$\zeta_2$	$\zeta_3$
DC1	Updated Simple FEM FRF	-	0.018	0.014	*		
	Updated Full-scale FEM FRF	-	0.020	0.010			
	Damaged FRF (experimental)	-	0.024	0.014			
DC2	Updated Simple FEM FRF	-	0.030	0.020			
	Updated Full-scale FEM FRF	-	0.029	0.016			
	Damaged FRF (experimental)	-	0.034	0.015			
DC3	Updated Simple FEM FRF	-	0.038	0.022			
	Updated Full-scale FEM FRF	-	0.038	0.015			
	Damaged FRF (experimental)	-	0.035	0.013			
DC4	Updated Simple FEM FRF	-	0.045	0.025			
	Updated Full-scale FEM FRF	-	0.045	0.020			
	Damaged FRF (experimental)	-	0.036	0.012			
DC5	Updated Simple FEM FRF	-	0.040	0.021	-	0.025	0.015
	Updated Full-scale FEM FRF	-	0.040	0.021	-	0.029	0.025
	Damaged FRF (experimental)	-	0.035	0.014	-	0.022	0.011

The amplitudes of analytical FRFs obtained through simple FEMs for the 5 different levels of the damage (DC1 to DC5) were matched with the corresponding experimental FRFs for the updated values of damping ratios given in Table 5.6. Furthermore, the updated damping values through the full-scale FEM and the experimental ones are also given in the same table. Hence, although the damping values were found to be close for the full-scale FEM and the simple FEM, for most of the cases, the values obtained through experimental FRFs are relatively different than the analytically determined ones.

#### **5.4 Concluding Remarks**

In this chapter, the FRF based damage identification algorithm was utilized concerning the efficiency of a simplified finite element model to detect, localize and quantify the damage.

The simple model provided similar degradation results with the full-scale model. However, simple model was only able to offer a general degradation in terms of story stiffness not at the member level. This result indicates that the simple model is capable to practice a Level 1 damage identification which means it can prove the existence of the damage.

In the case of damage localization and quantification (Level 2 and Level 3 damage identification), it is not exactly true to say that the simplification in terms of FEM has not ability to cover these needs. Because, degradation level due to damage and the expected locations in terms of type of the damage was pointed out at the story level. This level of knowledge could be beneficial for rapid assessment of multi-story buildings after earth earthquakes.

However, it can be obviously said that the utilization of a simple model would lead to obtain objective results for model updating issues (such as unit volume mass and elastic modulus of material).

## **6. PERFORMANCE BASED DAMAGE ASSESSMENT IN COMBINATION WITH FRF BASED DAMAGE IDENTIFICATION**

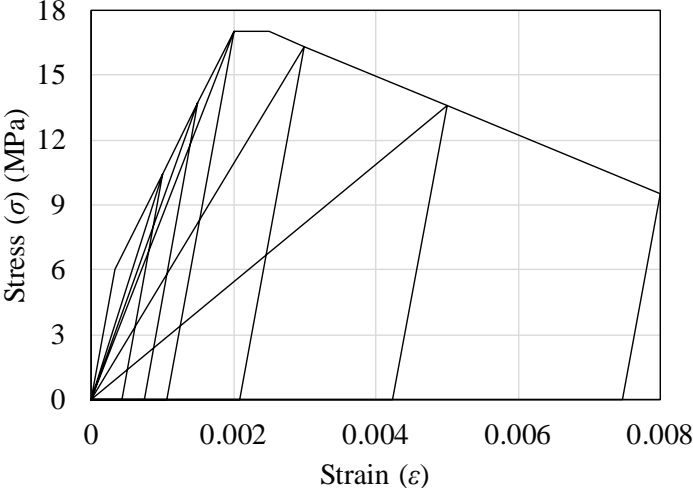
In this chapter, automated damage identification procedure was extended by combining with moment-rotation based nonlinear performance assessment method. By means of the extended damage identification method, serviceability of the structure after seismic structural damage could be estimated using the change of vibration characteristics of the structures due to damage. An additional step for damage identification method was proposed to link it with the moment-rotation based nonlinear performance assessment method specified in ASCE 41-13. For this purpose, first, it was required to create a FEM of a building whose experimental response was already known to verify the estimated of damage level and dynamic results. Accordingly, the test building TB-1 was modeled and analyzed using nonlinear analysis approaches. After obtaining the pushover curve, which is well-matched with the experimental one, dynamic data was generated from the interested DOFs for the undamaged and damaged states of the model with the aim of extracting of natural frequencies. In addition to the well-matched push-over curves, the compatibility between the natural frequencies obtained through generated dynamic signal and vibration tests provided to regard these analytical process as the simulation of the field tests. Thus, the estimation of damage levels of the members through nonlinear performance assessment was linked with the updated initial and boundary conditions of the members given in Chapter 4.

### **6.1 Simulation of the Field Tests**

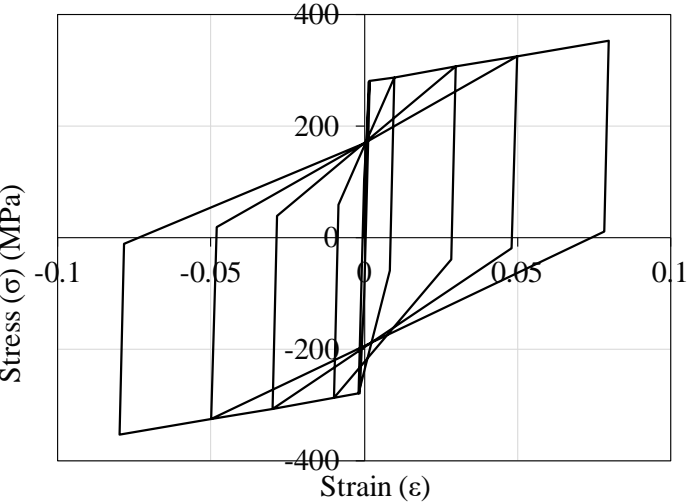
#### **6.1.1 Prediction of pushover curve**

The FEM of the Test Building TB-1 was established using a commercially available software (Perform 3D, 2011) in which the material non-linearity was considered. Based on the lumped plasticity approach, rotational plastic hinges were assigned to the potential plastic hinge regions of the columns and beams. Hence, the nonlinear flexural

behavior of the columns and beams were obtained from cross-section analysis by means of moment–curvature relationships which were determined using fiber modelling approach. The material models for concrete and reinforcement were considered as given in Figure 6.1 based on the material tests described in detail in Comert 2016.



(a)



(b)

**Figure 6.1 :** Stress-strain relationships, (a) concrete, (b) reinforcement.

Furthermore, plastic hinge length ( $L_p$ ) was assumed to be  $L_p = 0.5H$ , as proposed by TSDC (2007), where  $H$  is the effective depth of cross section in bending. In order to catch the experimental response of the building TB-1, the reversed cyclic loading pattern applied throughout quasi-static test was considered (Figure 6.2).

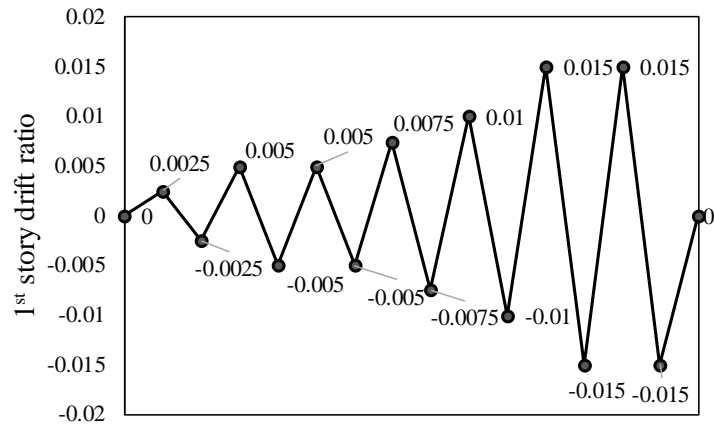


**Figure 6.2 :** Quasi-static test – loading protocol.

In addition, during the push-over analysis, the lateral loads applied at story levels were chosen to be compatible with the field tests. As aforementioned, in the field tests, one actuator was mounted at the first story level while two were at the second story level (Figure 2.6). Accordingly, in the analysis,  $P$  at first story level,  $2P$  at second story level and zero load at third story level were applied. The attained base shear force-first story drift relationship was given with the relationship obtained from the quasi-static test in Figure 6.3. As seen in this figure, the modelling approach well-predicted the experimentally obtained result, significantly for the pushing direction.

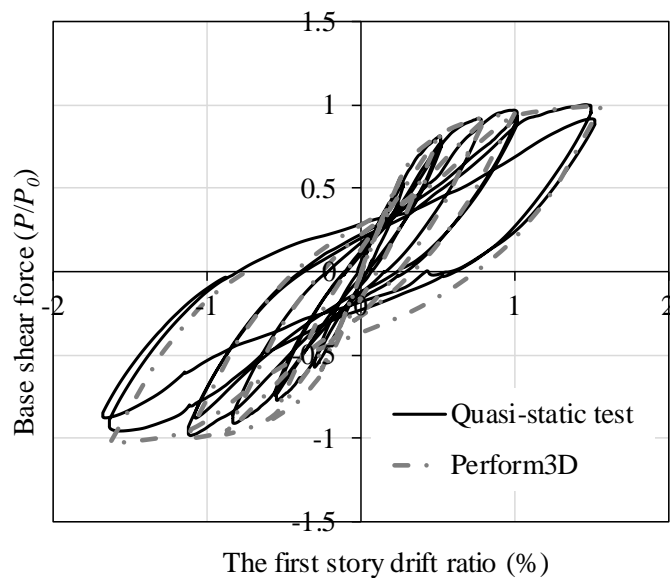


**Figure 6.3 :** Base shear force-first story drift ratio relationship

### 6.1.2 Prediction of member damage states

Following to the well-estimation of the base shear force-first story drift ratio relationship through the nonlinear analysis, the damage states of the first and second

story columns were examined by means of performance limits specified in ASCE 41-13 (Seismic rehabilitation of existing buildings, ASCE/SEI 41-13. ASCE, Reston, 2014). ASCE 41-13 (2014) is the current code in force for the assessment of existing structures in the United States. The damage limits of the members defined by ASCE 41-13 (2014) are given with the typical force-deformation behavior of RC member in Figure 6.4. The damage limits are Immediate Occupancy (IO), Life Safety (LS) and Collapse Prevention (CP).

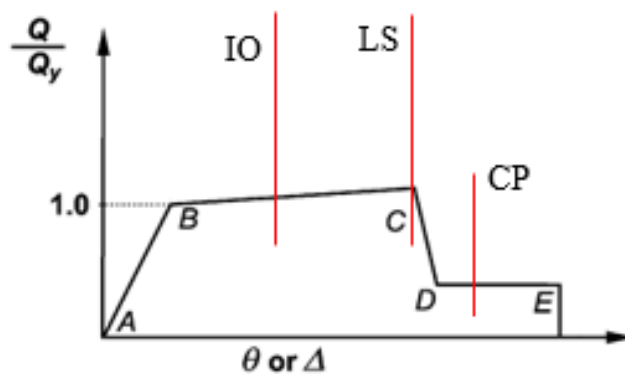


**Figure 6.4 :** Damage limits and response behavior of RC members (ASCE 41-13, 2014).

In addition to that, the damage limits for the nonlinear performance assessment in terms of plastic rotations are given in Table 6.1. In this table,  $\rho$  refers the volumetric ratio of transverse reinforcement. ASCE 41-13 (2014) classifies the columns into 4 groups considering the failure modes (Condition 1 to 4);

Condition 1: Flexure failure;

Condition 2: Flexure-shear failure, where yielding in flexure is expected before shear failure;

Condition 3: Shear failure;

Condition 4: Columns controlled by inadequate development or splicing along clear height.

These failure modes are determined based on the ratio between shear demand at flexural yielding at plastic hinges ( $V_e$ ) and shear capacity on the column ( $V_n$ ) (shear capacity ratio), and the transverse reinforcement detailing (Table 6.2). Shear capacity,  $V_n$  can be calculated using Equations 6.1.



$$V_n = k \left[ \frac{A_v f_{ym} d}{s} + \lambda \left( \frac{0.5 \sqrt{f_{cm}}}{M/Vd} \sqrt{1 + \frac{N}{0.5 \sqrt{f_{cm}} A_g}} \right) 0.8 A_g \right] \quad (6.1)$$

Where  $k$  is the coefficient determined based on the displacement ductility demand.  $k$  is equal 1.0 in regions where displacement ductility demand is less than or equal to 2, and equals to 0.7 in regions where displacement ductility demand is greater than or equal to 6, and it varies linearly for displacement ductility between 2 and 6.  $\lambda$  is equal to 0.75 for lightweight aggregate concrete and 1.0 for normal weight aggregate concrete.  $N_u$  is the axial compression force (set to zero for tension force),  $M / Vd$  is the largest ratio of moment to shear times effective depth under design loadings for the column but shall not be taken greater than 4 or less than 2;  $d$  is the effective depth ( $d = 0.8h$ , where  $h$  is the dimension of the column in the direction of shear) and  $A_g$  is the gross cross-sectional area of the column.

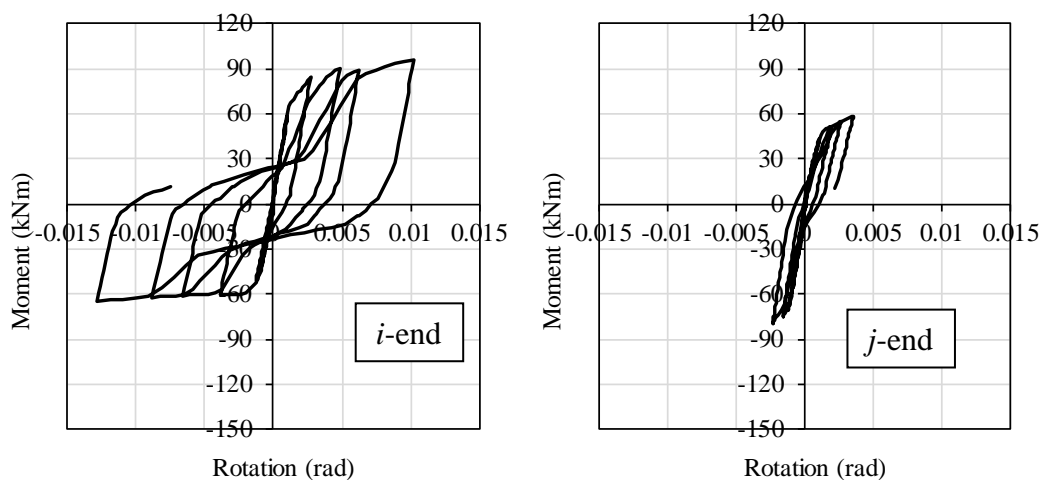
**Table 6.1 :** Damage limits for RC columns for nonlinear procedures (plastic rotation) (ASCE 41-13 2014).

$\frac{N}{A_g f_{cm}}$	$\rho = \frac{A_v}{b_w s}$	$\frac{V_e}{b_w d \sqrt{f_{cm}}}$	IO	LS	CP
<b>Condition 1</b>					
$\leq 0.1$	$\geq 0.006$		0.005	0.045	0.06
$\geq 0.6$	$\geq 0.006$		0.003	0.009	0.01
$\leq 0.1$	$= 0.002$		0.005	0.027	0.034
$\geq 0.6$	$= 0.002$		0.002	0.004	0.005
<b>Condition 2</b>					
$\leq 0.1$	$\geq 0.006$	$\leq 0.25$	0.005	0.045	0.06
$\leq 0.1$	$\geq 0.006$	$\geq 0.5$	0.005	0.045	0.06
$\geq 0.6$	$\geq 0.006$	$\leq 0.25$	0.003	0.009	0.01
$\geq 0.6$	$\geq 0.006$	$\geq 0.5$	0.003	0.007	0.008
$\leq 0.1$	$\leq 0.0005$	$\leq 0.25$	0.005	0.01	0.012
$\leq 0.1$	$\leq 0.0005$	$\geq 0.5$	0.004	0.005	0.006
$\geq 0.6$	$\leq 0.0005$	$\leq 0.25$	0.002	0.003	0.004
$\geq 0.6$	$\leq 0.0005$	$\geq 0.5$	0	0	0
<b>Condition 3</b>					
$\leq 0.1$	$\geq 0.006$		0	0.045	0.06
$\geq 0.6$	$\geq 0.006$		0	0.007	0.008
$\leq 0.1$	$\leq 0.0005$		0	0.005	0.006
$\geq 0.6$	$\leq 0.0005$		0	0	0
<b>Condition 4</b>					
$\leq 0.1$	$\geq 0.006$		0	0.045	0.06
$\geq 0.6$	$\geq 0.006$		0	0.007	0.008
$\leq 0.1$	$\leq 0.0005$		0	0.005	0.006
$\geq 0.6$	$\leq 0.0005$		0	0	0

**Table 6.2 :** Condition to be used for columns in Table 6.1 (ASCE 41-13 2014).

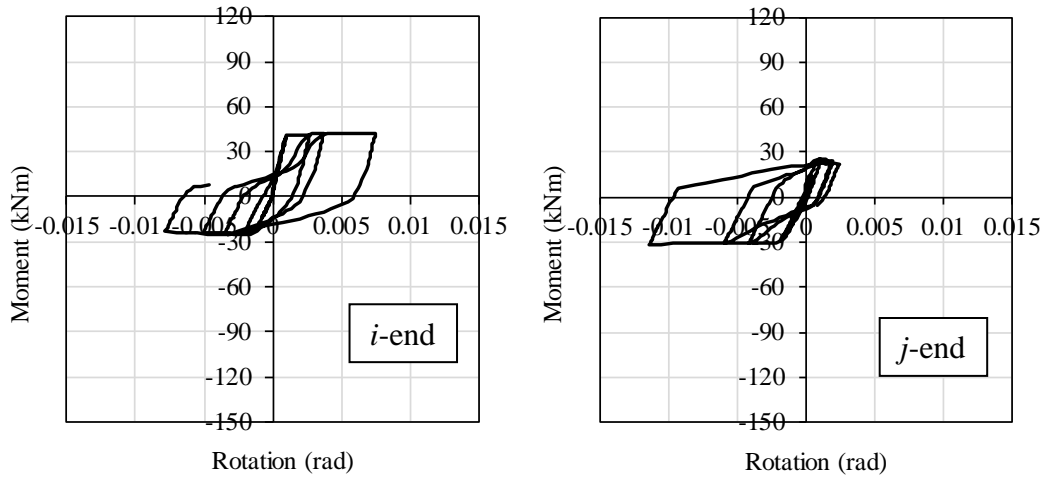
Shear capacity ratio	ACI 318 conforming seismic details with 135-degree hooks	Closed hoops with 90-degree hooks	Other (Including lap-spliced transverse reinforcement)
$V_e/V_n \leq 0.6$	Condition 1	Condition 2	Condition 2
$1.0 \geq V_e/V_n \geq 0.6$	Condition 2	Condition 2	Condition 3
$V_e/V_n > 1.0$	Condition 3	Condition 3	Condition 3

Hence, analytically determined plastic rotation demand at the bottom and top ends of the columns at 1.5% first story drift ratio was calculated by extracting the yield rotations of the cross-sections of the columns from the rotation demands. In addition to that, the analytically obtained moment versus column end rotation relationships of the columns are given columns in Figure 6.5 and Figure 6.6. The yield rotation values of the sections were calculated through cross-sectional fiber analysis. The achieved plastic rotations were compared with the plastic rotation limits given by the ASCE 41-13 (2014) (Table 6.1). Column damage states are listed in Table 6.3. Comparison of the obtained damage states with the damages attained through field tests will be done in next sub-sections.

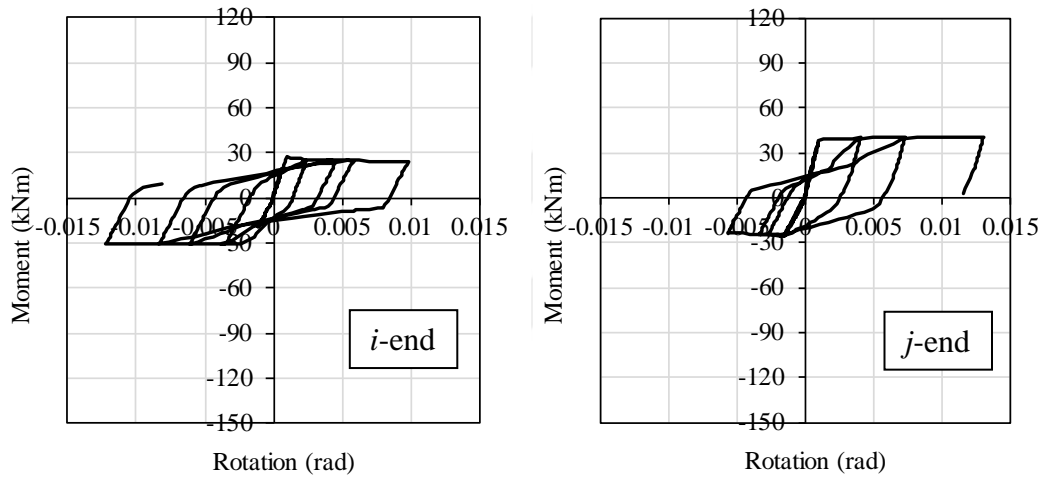


(a)

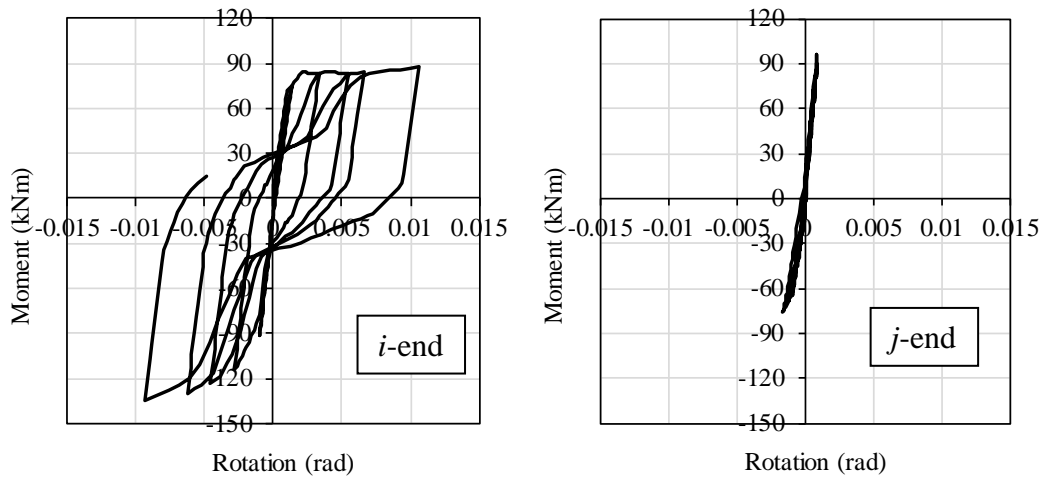
**Figure 6.5 :** Moment-Column end rotations (Perform 3D) (the first story), (a) S11, (b) S12, (c) S13 and (d) S14.



(b)

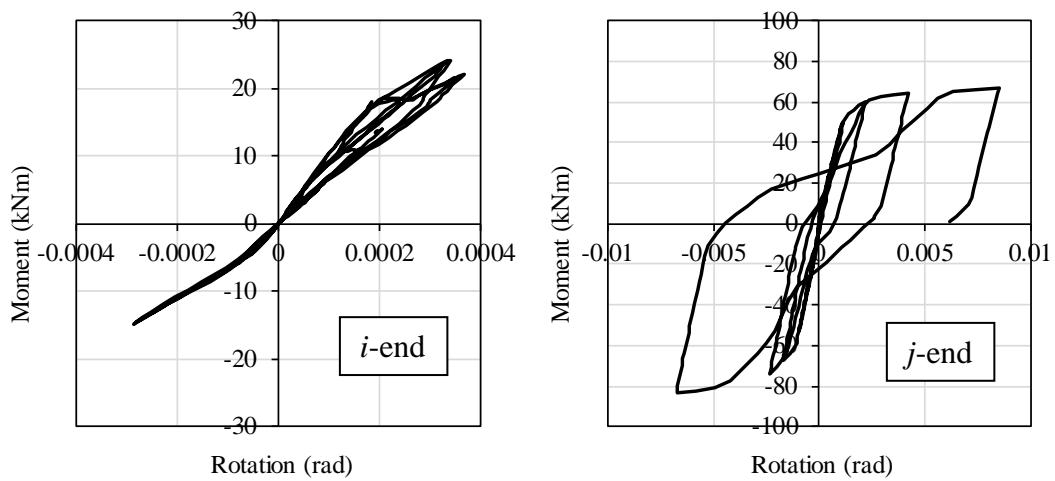


(c)

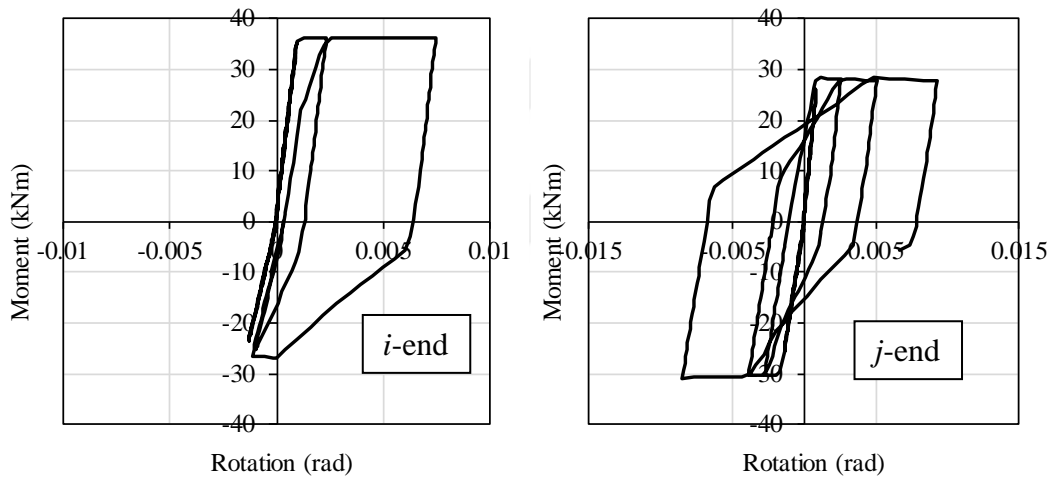


(d)

**Figure 6.5 (continued) :** Moment-Column end rotations (Perform 3D) (the first story), (a) S11, (b) S12, (c) S13 and (d) S14.

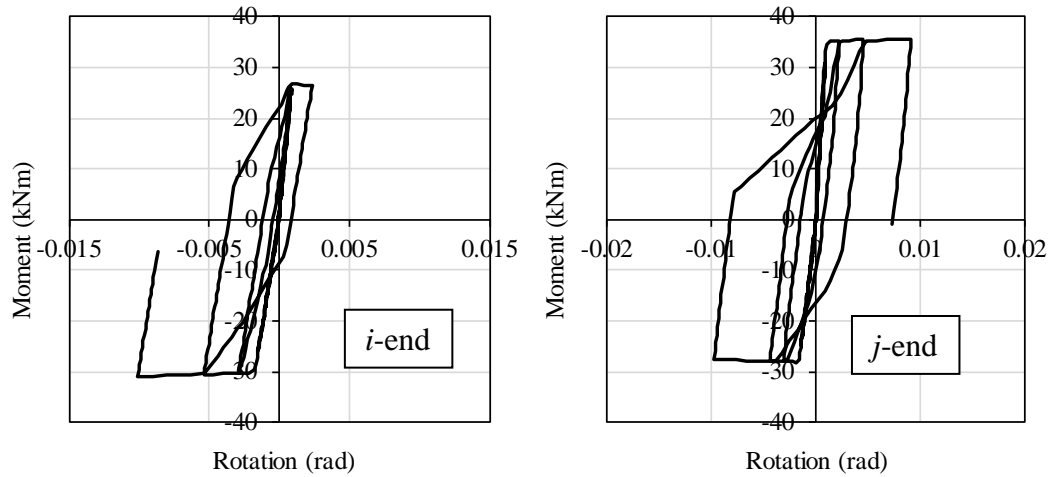


(a)

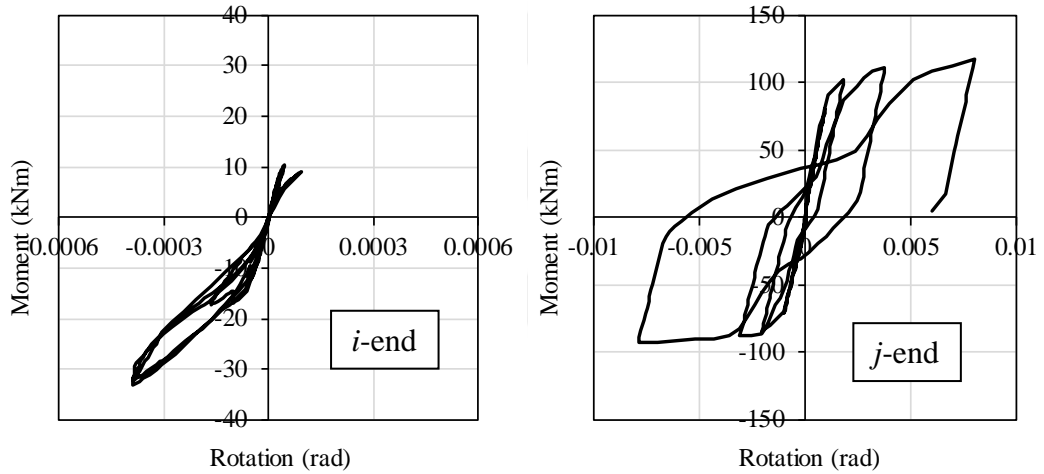


(b)

**Figure 6.6 :** Moment-Column end rotations (Perform 3D) (the second story), (a) S11, (b) S12, (c) S13 and (d) S14.



(c)



(d)

**Figure 6.6 (continued) :** Moment-Column end rotations (Perform 3D) (the second story), (a) S11, (b) S12, (c) S13 and (d) S14.

**Table 6.3 :** Columns damage states.

Columns	Story	i-end	j-end
S11	1 <sup>st</sup> story	Collapse	Minimum damage
	2 <sup>nd</sup> story	Minimum damage	Moderate damage
S12	1 <sup>st</sup> story	Moderate damage	Moderate damage
	2 <sup>nd</sup> story	Moderate damage	Moderate damage
S13	1 <sup>st</sup> story	Collapse	Collapse
	2 <sup>nd</sup> story	Collapse	Moderate damage
S14	1 <sup>st</sup> story	Collapse	Minimum damage
	2 <sup>nd</sup> story	Minimum damage	Moderate damage

## 6.2 Dynamic data generation

Along with the nonlinear modelling of the building TB-1, which estimated a compatible base-shear versus first story drift ratio relationship with the experimental results, acceleration signals as the response of the each DOF, where the accelerometers were mounted in the field tests, were generated. This was achieved by performing a time history analysis by assigning a white noise signal as dynamic force. The white noise signal was generated through MATLAB with the 320 second length. Sampling frequency of the signal was set to be 100 Hz. The amplitude of the signal was scaled with 10000 to limit the peak acceleration value of the signal within the linear elastic range of the lateral load bearing capacity of the building. The first 32 seconds of the signal was displayed in Figure 6.7.

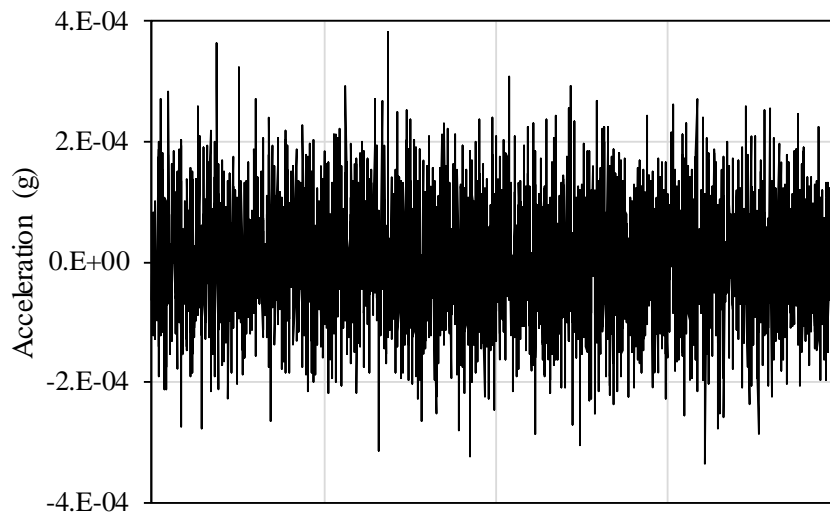
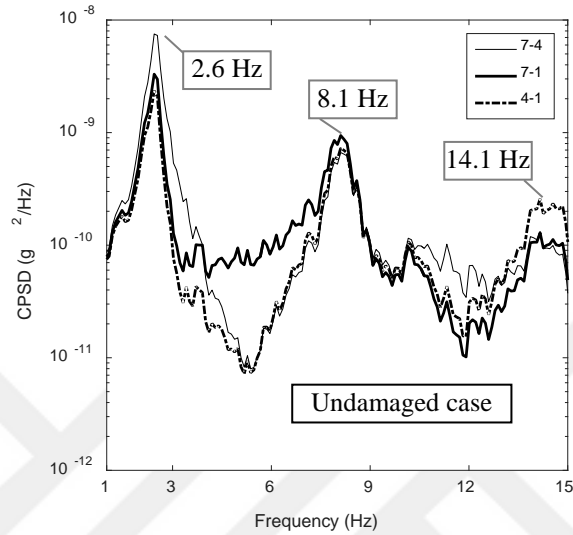


**Figure 6.7 :** White noise signal as dynamic input force

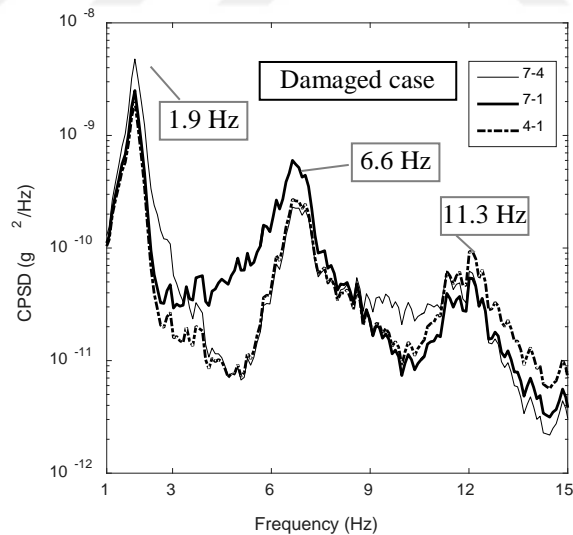
After performing the time history analysis, the acceleration response of the DOFs named as 1, 4 and 7 (see the Chapter 3 and 4) were obtained for the undamaged case and damaged case. It should be noted that the undamaged and damaged cases refer the conditions before and after the nonlinear pushover analysis was implemented.

The frequency content of the vibration responses of the building was examined to verify whether the nonlinear model and the analysis could represent the field tests. Hence, the cross power spectral density functions of the generated vibration signals are given in the Figure 6.8. The experimentally determined and analytically updated frequency responses of the building at both undamaged and damaged cases were obtained using frequency response function in terms of  $g/Hz^2$ , while the simulated

responses were calculated as the CPSD functions (Figure 6.8). Therefore, the frequency response of the simulated model and the experimental one (and analytically updated relationship) did not displayed in the same figure. Instead of that, in addition to Figure 6.8, the experimentally obtained and analytically determined (updated) frequency responses of the building are given in this chapter to remind (Figure 6.9).



(a)



(b)

**Figure 6.8 :** CPSD functions of the generated vibration signal, (a) undamaged case, (b) damaged case.

As seen in the Figure 6.8 and Figure 6.9, dominant frequencies were well-estimated using the generated data. Hence, (i) well-matching of experimentally achieved and analytically estimated base shear-the first story drift relationship, (ii) well-matching of the dynamic responses of the buildings (experimentally identified response, response of the building updated through damage identification algorithm and response of the simulated model) provided to proceed for create the link between the results of the damage identification algorithm and the results of performance based damage assessment.

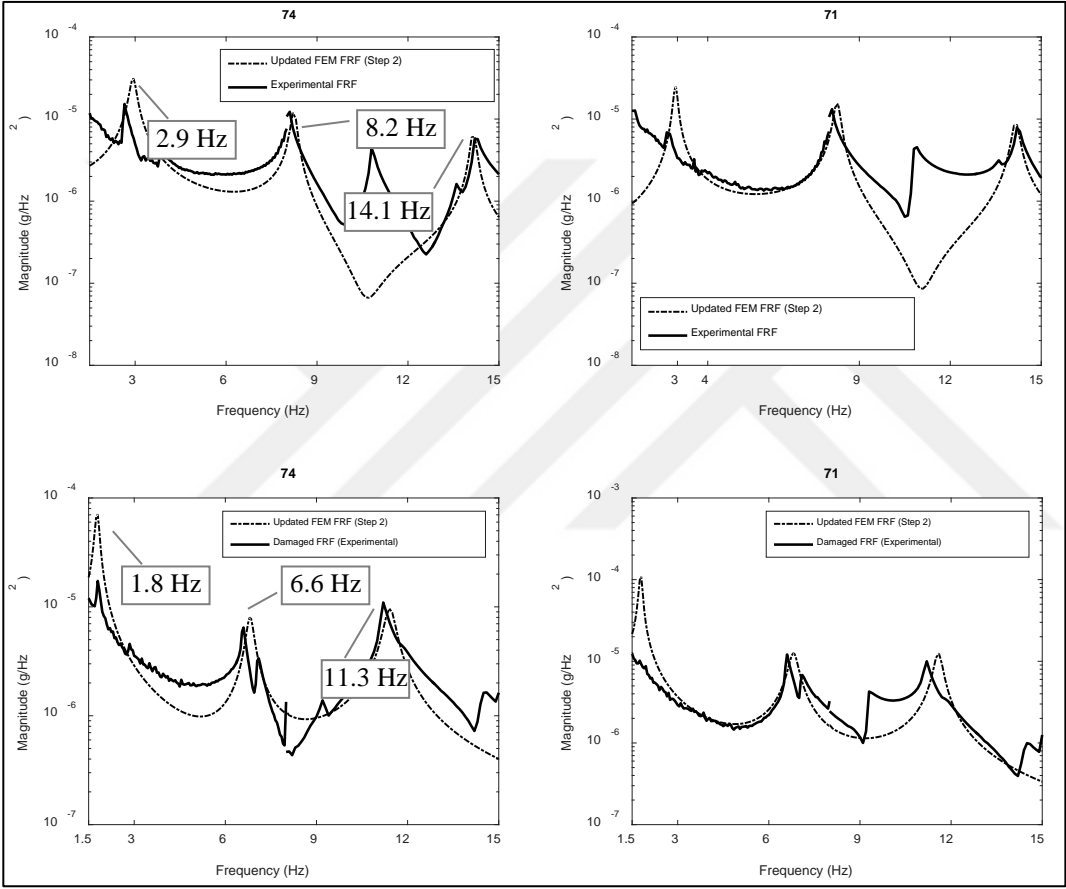


Figure 6.9 : Experimentally obtained and updated FRFs of the building TB-1.

### 6.3 Utilizing of Performance Based Damage Limits on Vibration Based Damage Identification

The damage identification algorithm presented in this dissertation provides to estimate the new rotational stiffness values ( $k_2$ ) of the cross-sections after damage. In this step, the ratio between the new rotational stiffness value and the initial stiffness value ( $k_1$ ), which refers the stiffness degradation, was utilized to simulate the damage state in RC columns that have entered the plastic range due to damage. As aforementioned, ASCE



41-13 (2014) specifies the damage limits in terms of plastic rotations. Accordingly, the rotation demand ( $\theta_d$ ) resulting the new rotational stiffness value ( $k_2$ ) on the cross-section were required to create a link between performance based damage assessment methodology and the vibration based damage identification algorithm. For this purpose, a phenomenon underlying the plastic hinge modification factor, which has been studied by various researchers, was adopted.

### 6.3.1 Plastic hinge modification factor

To evaluate the performance of an earthquake damaged RC building based on the execution of push-over analysis, the moment-rotation plastic hinges of RC columns, which entered the plastic range, requires to be modified. The modification factors for stiffness, strength, and displacement capacity as a function of the rotational ductility demand can be used to simulate the damage state in RC members that have experienced a given ductility demand due to an earthquake. Accordingly, Ludovico et al. 2013 suggested some expressions based on the 36 cyclic tests on non-conforming columns to present seismic design codes (23 RC columns reinforced with deformed bars and 13 with plain ones) extracted from available databases. The selected tests in their study were chosen to be representative of existing members in Mediterranean region and with low normalized axial load. They considered the bilinear moment-rotation relationship which is described by yielding ( $M_y$  and  $\theta_y$ ) and ultimate ( $M_u$  and  $\theta_u$ ) moment-rotation. As suggested in FEMA (1998), the formulations were proposed for modifying the stiffness, strength, and displacement capacity of the hinges (Figure 6.10 and Table 6.4).

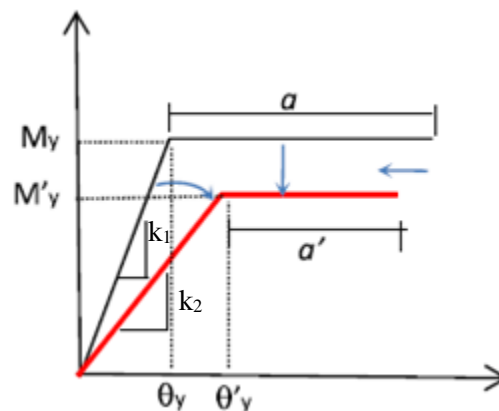


**Figure 6.10 :** Modelling criteria for damaged plastic hinges (Ludovico et al. 2013).

**Table 6.4 :** Modelling criteria for damaged plastic hinges (Ludovico et al. 2013).

	Stiffness	Strength	Plastic rotation
Intact	$k_1$	$M_y$	$a$
Damaged	$k_2 = \lambda_k \cdot k_1$	$M_y' = \lambda_\theta \cdot M_y$	$a' = a - a_d$

As seen in Figure 6.10, to compute the stiffness degradation on the damaged members, a stiffness modification factor ( $\lambda_k$ ) has been introduced. After some mathematical manipulations on the experimental results of the columns on the database, a proper stiffness modification factor has been introduced for columns with plain bars, which allow to compute the stiffness degradation due to damage (Eq. 6.2). In Eq. 6.2,  $\theta$  refers the attained rotation (rotation demand at the achieved displacement level). Details can be found in the study of Ludovico et al. 2013.

$$\lambda_k = 1 - \left[ 1.12 - 1.17 \left( \frac{\theta}{\theta_y} \right)^{-0.77} \right] \quad \text{for } 1.1 < \frac{\theta}{\theta_y} < \frac{\theta_u}{\theta_y} \quad (6.2)$$

### 6.3.2 Determination of rotation demand


Estimation of stiffness degradation on the cross sections due to damage was achieved using the damage identification algorithm. The ductility demand ( $\theta/\theta_y$ ) and accordingly rotation demand on the columns which causes this degradation was also determined using the Eq. 6.2. The yield rotation value of the sections was determined through cross-sectional fiber analysis (Chapter 4, Figure 4.1 and Table 4.2). As aforementioned, the yield rotation was assumed as the value corresponding the tension reinforcement yields, or the maximum concrete strain reached the value of 0.002. The plastic rotation at the columns of building TB-1, due to 1.5% first story drift ratio was calculated by substituting the yield rotation value and the stiffness degradation factor ( $\lambda_k$ ) into the Eq. 6.2. Subsequently, the plastic rotation values were calculated by extracting the yield rotations of the cross-sections of the columns from the rotation demands derived from Eq. 6.2. The plastic rotation values obtained through nonlinear pushover analysis and damage identification algorithm were given with the damage limits derived from the Table 6.1 were given in Table 6.5. Plastic rotation values at the sections and the damage limits were given in Table 6.5. The corresponding damage levels and the observed damage at 1.5% drift ratio are summarized in Table 6.6 to Table 6.9 for the columns S11, S12, S13 and S14, respectively. It should be noted that member damage achieved due to quasi-static tests were given only for the 1st story.

As aforementioned, no significant damage (only a few flexural cracking) was observed in any of the beams or columns located in the second or third stories of the building.


**Table 6.5 :** Comparison of the plastic rotations of the members.

Columns	Story	Damage identification algorithm		Nonlinear analysis		Damage limits (ASCE 41-06 2014)		
		i-end	j-end	i-end	j-end	IO	LS	CP
S11	1 <sup>st</sup> story	0.0120	0.0037	0.0128	0.0024	0.005	0.00883	0.01108
	2 <sup>nd</sup> story	0.0033	0.0033	0	0.0074			
S12	1 <sup>st</sup> story	0.0052	0.0052	0.0062	0.0097	0.005	0.00665	0.00809
	2 <sup>nd</sup> story	0.0010	0.0010	0.0057	0.0077			
S13	1 <sup>st</sup> story	0.0055	0.0055	0.0107	0.0117	0.005	0.006505	0.00789
	2 <sup>nd</sup> story	0.0007	0.0007	0.0128	0.0078			
S14	1 <sup>st</sup> story	0.0142	0.0030	0.0110	0.0050	0.005	0.008503	0.01063
	2 <sup>nd</sup> story	0.0026	0.0026	0	0.0070			


**Table 6.6 :** Comparison of member damage levels (S11).

Story	Damage identification algorithm		Nonlinear analysis		Quasi-static test	
	i-end	j-end	i-end	j-end		
1 <sup>st</sup> story	Collapse	Minimum damage	Collapse	Minimum damage		
2 <sup>nd</sup> story	Minimum damage	Minimum damage	Minimum damage	Moderate damage		


**Table 6.7 :** Comparison of member damage levels (S12).

Story	Damage identification algorithm		Nonlinear analysis		Quasi-static test
	i-end	j-end	i-end	j-end	
1 <sup>st</sup> story	Moderate damage	Moderate damage	Moderate damage	Moderate damage	
2 <sup>nd</sup> story	Minimum damage	Minimum damage	Moderate damage	Moderate damage	

**Table 6.8 :** Comparison of member damage levels (S13).

Story	Damage identification algorithm		Nonlinear analysis		Quasi-static test
	i-end	j-end	i-end	j-end	
1 <sup>st</sup> story	Moderate damage	Moderate damage	Collapse	Collapse	
2 <sup>nd</sup> story	Minimum damage	Minimum damage	Collapse	Moderate damage	

**Table 6.9 :** Comparison of member damage levels (S14).

Story	Damage identification algorithm		Nonlinear analysis		Quasi-static test	
	i-end	j-end	i-end	j-end		
1 <sup>st</sup> story	Collapse	Minimum damage	Collapse	Minimum damage		
2 <sup>nd</sup> story	Minimum damage	Minimum damage	Minimum damage	Moderate damage		

For the 1<sup>st</sup> story columns, the estimated plastic rotations for bottom end of the columns by damage identification algorithm and nonlinear analysis are found to be close each other (except the column S13), while that of for top end of the columns are not. The nonlinear pushover analysis results are of approximately 1.5-2 times greater. For the 2<sup>nd</sup> story columns, both for bottom and top ends of the columns, very limited plastic rotation values are estimated by damage identification algorithm in comparison to the nonlinear analysis. In the case of the observed damages and the estimated damage levels at the columns, for the columns S11, S12 and S14 at the 1<sup>st</sup> story, both damage identification algorithm and the nonlinear analysis provided well-estimated damage level comparing to the quasi-static test (Table 6.6 to Table 6.9). For the columns S13 at the 1<sup>st</sup> story, although nonlinear analysis estimated a damage level as collapse, the estimation of the damage identification algorithm is in good correlation with the test result (Table 6.8). For the second story columns, since no significant damage was observed at the test, it can be said that the damage identification algorithm provided a better estimation for damage level as ‘minimum damage’ for all columns.

#### **6.4 Concluding Remarks**

In this chapter, automated damage identification procedure was extended to represent the rotational stiffness degradation due to damage which was obtained as the extraction of the algorithm, in terms of member damage level specified in ASCE 41-13 (2014).

At the end of a set of analytical process, it was found that the estimated plastic rotations for bottom end of the columns by damage identification algorithm and nonlinear analysis are found to be close each other while that of for top end of the columns are not.

For the 2<sup>nd</sup> story columns, both for bottom and top ends of the columns, very limited plastic rotation values are estimated by damage identification algorithm (in comparison to the nonlinear performance assessment results) and it is more compatible with the observed damage due to quasi-static tests.

Like the plastic rotation values, both damage identification algorithm and the nonlinear analysis provided well-estimated damage level for the columns S11, S12 and S14 at the 1<sup>st</sup> story, comparing to the quasi-static test. For the columns S13 at the 1<sup>st</sup> story, although nonlinear analysis estimated a damage level as collapse, the estimation of the



damage identification algorithm is in good correlation with the test result. For the second story columns, the damage identification algorithm provided a better estimation for damage level as ‘minimum damage’ for all columns.

It can be concluded that the extended damage identification algorithm by combining with nonlinear moment-rotation based performance assessment method, provided well-estimation in terms of damage level of member. It could be said that (i) obtaining the plastic rotation value due to damage and (ii) subsequently estimation of member damage levels can be figured out utilizing the damage identification algorithm. It should be noted that the scope of the study for the rotation estimation from vibration based damage identification algorithm is limited for this type of structures which have flexural failure mechanism.





## 7. CONCLUSION

The main objective of the thesis is to make an investigation about the effects of seismic structural damage on the dynamic characteristics of RC structures and accordingly to propose a damage identification algorithm which can be practically applied for existing RC structures. For this aim, two full-scale, three story substandard RC buildings were considered as a representative of the existing building stock in Turkey and Europe in this dissertation.

Accordingly, the dissertation can be divided into three parts:

In the first part, since it is aimed to quantify the rate of change of dynamic characteristics of typical RC buildings with increasing seismic structural damage, a set of field testing was carried out. In the context of the field tests, vibration-based tests were performed before and after quasi-static lateral loading as well as at a set of certain damage levels.

In the second part, an automated damage identification algorithm to detect, localize and quantify the structural damage was presented. For this purpose, a MATLAB based program (MUP) was developed for automatically computing a damage identification algorithm. In the case of the damage identification, A FRF based algorithm relies on the updating of Finite Element Model (FEM) of the test buildings were developed and adopted for RC structures. Prior to the damage identification process, the algorithm was introduced by updating the initial finite element model of the test buildings. After updating the initial FEM of the buildings and obtaining the baseline model, which has the well-matched FRF with the experimentally obtained FRF of the undamaged case of the buildings, the damage identification algorithm was adopted to detect, localize and quantify the damage of the buildings by minimizing the difference between baseline model and the measured FRFs at the field tests.

In the third part, it is aimed to present an algorithm for predicting the residual capacity of the structures subjected to seismic structural damage. For this purpose, the building TB-1, whose structural damage situation was already known, was considered to

present the algorithm. Hence, the nonlinear model of the building was established, and the model was then subjected to the same lateral loading reversals with the quasi-static tests. Following to verifying the nonlinear model, a set of dynamic data was generated from the model for both undamaged and damaged case. The previously introduced damage identification algorithm was implemented to generated dynamic data and finally damage was detected, localized and quantified. For estimating the residual capacity of the building, the performance based assessment results of the building, which were obtained using ASCE 41-13, were compared with the damage identification results. By this way, the damage identification algorithm was not only examined in terms of efficiency and validity, but also extended to investigate the serviceability of damaged structures. In addition to that an existing RC structure in Istanbul, which is representative of the existing building stock, was considered to investigate the effects of different parameters (such as axial load ratio and volumetric ratio of transverse reinforcing bar) to the residual capacity of the building via the proposed algorithm.

The following results were obtained;

- In the field tests, it was found that the modal frequencies decreased, and the modal damping ratios increased significantly up to the elastic limit. However, the progressing of damage beyond the elastic limit was not accompanied with a similar significant change in the modal frequencies and the modal damping ratios.
- Furthermore, despite a significant degradation in lateral load bearing capacity, as approximately 20%, induced by quasi-static lateral loading at around 3% lateral d.r., no intensified structural damage could be observed by visual inspection in case of building TB-2. However, the forced vibration test results presented that the modal frequencies and the damping ratios changed due to lateral loading in comparison with its undamaged state. These findings indicate a serious risk about the missing the structural damages during visual inspections after earthquakes. Hence, utilization of dynamic testing accompanying with visual inspection could be a promising method for more realistic assessment of structural damages after seismic events.

- The initial FEM of the buildings were updated via changes stiffness, unit weight and damping parameters and the baseline model, which was taken as reference for damage identification, were obtained, successfully.
- The young's modulus of concrete for the building TB-1 was calibrated for a value which relatively lower than the one calculated considering TS 500 (2000). This was attributed to that the building TB-1 was an existing sub-standard RC structure.
- The revision in the two-step algorithm in terms of updating the damping parameters provided to obtain the mathematical description of the buildings. Significantly, curve fitting clearly became a useful and practical part of the model updating algorithm and found to be a promising tool in case of the dynamic measurements including noisy components.
- In the case of proposed damage identification algorithm, it was found that the first step of the algorithm (Step 1) provided a successful damage detection, localization and quantification process. Although the second step (Step 2) also provided to match the experimental FRFs and FEM FRFs in terms of their amplitudes, it is basically have not any contribution for Level 3 damage identification purpose.
- The algorithm identified the correct location of damage in a blind "scenario" by predicting the decrease in stiffness values of the frame-end springs that is representing the initial and boundary conditions.
- The utilization of simple FEM provided similar degradation results with the full-scale model. Differently, simple model was only able to offer a general degradation in terms of story stiffness not at the member level. This result indicates that the simple model is capable to practice a Level 1 damage identification which means it can prove the existence of the damage. However, this level of knowledge could be beneficial for rapid assessment of multi-story buildings after earth earthquakes.
- Furthermore, the utilization of a simple model would lead to obtain objective results for model updating issues (such as unit volume mass and elastic modulus of material).

- The estimated plastic rotations for bottom end of the columns by extended damage identification algorithm and nonlinear analysis are found to be close each other while that of for top end of the columns are not. For the 2<sup>nd</sup> story columns, both for bottom and top ends of the columns, very limited plastic rotation values are estimated by extended damage identification algorithm (in comparison to the nonlinear performance assessment results) and it is more compatible with the observed damage due to quasi-static tests.
- Like the plastic rotation values, both extended damage identification algorithm and the nonlinear analysis provided well-estimated damage level for the columns S11, S12 and S14 at the 1<sup>st</sup> story, comparing to the quasi-static test. For the columns S13 at the 1<sup>st</sup> story, although nonlinear analysis estimated a damage level as collapse, the estimation of the damage identification algorithm is in good correlation with the test result. For the second story columns, the extended damage identification algorithm provided a better estimation for damage level as ‘minimum damage’ for all columns.
- The extended damage identification algorithm by combining with nonlinear moment-rotation based performance assessment method, provided well-estimation in terms of damage level of member. It could be said that (i) obtaining the plastic rotation value due to damage and (ii) subsequently estimation of member damage levels can be figured out utilizing the damage identification algorithm.

By taking into considerations the listed results above, followings are presented as recommendations and future works;

- For the damage identification, selection of unknown parameters and grouping them depends on the engineer’s judgment which clearly somehow makes the protocol subjective. Therefore, a more automated parameter selection protocol could be dealt as a forward problem.
- The damage identificatin protocol could be verified on more complicated structures.

## REFERENCES

- Abdel-Ghaffar, A., and Scanlan, R.H.** (1985). Ambient vibration studies of Golden Gate Bridge: I. Suspended structure, *J Eng Mech*, 111(4):19645.
- Allemang, R.J. and Brown, D.L.** (1982). A correlation coefficient for modal vector analysis, *Proc., 1st Int. Modal Analysis Conf.*, Orlando, Fla., 110–116.
- Apaydin, N., Kaya, Y., Safak, E., & Alcik, H.** (2012) Vibration characteristics of a suspension bridge under traffic and no traffic conditions. *Earthq Eng Struct Dyn* 41(12):1717–1723.
- Asteris, P.G., Chronopoulos, M.P., Chrysostomou C.Z., Varum H., Plevris V., Kyriakides, N., Silva V.** (2014). Seismic vulnerability assessment of historical masonry structural systems. *Eng Struct* 62:118–134.
- Barthorpe, R.** (2011). On model- and data-based approaches to structural health monitoring. (PhD thesis). The University of Sheffield.
- Brownjohn, J.M.W.** (2003) Ambient vibration studies for system identification of tall buildings. *Earthq Eng Struct Dyn* 32(1):71.
- Carden, E.P. and Fanning, P.** (2004). Vibration based condition monitoring: A review. *Structural Health Monitoring*, 3, 355–377.
- Casas, J.R. and Aparicio, A.C.** (1994). Structural damage identification from dynamic-test data, *Journal of Structural Engineering*, 120(8), 2437–2450.
- Catbas, F.N., Kijewski-Correa, T., and Aktan, E.** (2013). Structural Identification of Constructed Systems, American Society of Civil Engineers 1801 Alexander Bell Driv Reston, Virginia, 20191-4400.
- Celik O.C., Sucuoglu H., Akyuz U.** (2013). Forced vibration testing and finite element modelling of a ninestory reinforced concrete flat plate-wall building. *Earthq Spectra* 31(2):1069–1081
- Chang, C.C., Chang, T.Y.P., Zhang, Q.W.** (2001). Ambient vibration of long-span cable-stayed bridge, *J Bridge Eng* 6, 46–53.
- Chen, H.L., Spyrakos, C.C. and Venkatesh, G.** (1995). Evaluating structural deterioration by dynamic response. *Journal of Structural Engineering*, 121(8), 1197–1204.
- Chesné, S. and Deraemaeker, A.** (2013). Damage localization using transmissibility functions: A critical review, *Mech. Syst. Signal Pr.*, 38(1), 569-584.
- Chopra A.K.** (2001). Dynamics of structures: theory and application to earthquake engineering, 3rd edn. Prentice Hall, Upper Saddle River

- Cobb, R.G. and Liebst, B.S.** (1997). Structural damage identification using assigned partial eigenstructure, *AIAA Journal*, 35(1), 152–158.
- Comert, M., Demir, C., Ates, A.O., Orakcal, K. and Ilki, A.** (2016). Seismic performance of three storey full-scale sub standard reinforced concrete buildings, *Bulletin of Earthquake Engineering*, DOI: 10.1007/s10518-016-0023-4.
- De Roeck, G., Peeters, B. and Maeck, J.** (2000). Dynamic monitoring of civil engineering structures. In: *Computational Methods for Shell and Spatial Structures*, IASS-IACM 2000, Chania, Crete, Greece
- Doebling, S.W., Farrar, C.R., Prime, M.B. and Shevitz, D.W.** (1996). Damage Identification and Health Monitoring of Structural and Mechanical Systems from Changes in their Vibration Characteristics: A Literature Review. Los Alamos National Laboratory report, (LA-13070-MS).
- D’Ambrisi A., Mariani V., Mezzi M.** (2012). Seismic assessment of a historical masonry tower with nonlinear static and dynamic analyses tuned on ambient vibration tests. *Eng Struct* 36:210–219
- Esfandiari, A., Bakhthiari-Nejad, F., Rahai, A. and Sanayei, M.** (2009). Structural model updating using frequency response function and quasi-linear sensitivity equation, *J. Sound Vib.*, 326(1), 557–573.
- Ewins, D.J.** (2000). *Modal Testing: Theory, Practice and Application*, 2nd Ed., Baldock, England: Research Studies Press.
- Farrar, C.R., Baker, W.E., Bell, T.M., Cone, K.M., Darling, T.W., Duffey, T.A., Eklund, A., and Migliori, A.** (1994). Dynamic Characterization and Damage Detection in the I-40 Bridge over the Rio Grande, Los Alamos National Laboratory report LA-12767-MS.
- Fan, W., and Qiao, P.** (2011). Vibration-based Damage Identification Methods: A Review and Comparative Study. *Structural Health Monitoring*, Vol 10(1): 83–29.
- Farrar, C.R., Worden, K.** (2007). Introduction to structural health monitoring. *Phil Trans R Soc A* 2007;365(1851):303–15.
- Farrar, C.R. and Doebling, S.W.** (1999). Damage detection II: field applications to large structures.
- Farrar, C.R. and James, G.H.** (1997). System identification from ambient vibration measurements on a bridge. *Journal of Sound and Vibration*, 205, 1–18.
- Fryba, L. and Pirner, M.** (2001). Load tests and modal analysis of bridges, *Engineering Structures* Volume 23, Issue 1, January 2001, Pages 102–109.
- Garcia-Palencia, A., Santini-Bell, E., Gul, M., and Catbas, N.** (2015). A FRF-based algorithm for damage detection using experimentally collected data, *Structural Monitoring and Maintenance*, 2-4, 399-418.
- Garcia-Palencia, A.J. and Santini-Bell, E.** (2013). A two-step model updating algorithm for parameter identification of linear elastic damped structures, *Comput. - Aided Civil Infrastruct. Eng.*, TBD, 28(7), 509-521.



- Garcia-Palencia, A.J., Santini-Bell, E., Sipple, J.D. and Sanayei, M.** (2014). Structural model updating of an in-service bridge using dynamic data, *Struct. Control Health Monit.*, 22(10), 1265-1281.
- Gang, X., Chai, S., Allemang, J.R. and Lijun, L.** (2014). A new iterative model updating method using incomplete frequency response function data, *J. Sound Vib.*, 333(1), 2443-2453.
- Gentile C, Gallino N** (2008). Ambient vibration testing and structural evaluation of an historic suspension footbridge. *Adv Eng Softw* 39:356–366.
- Goksu, C., Inci, P., Demir, U., Yazgan, U., and Ilki, A.** (2017). Field testing of substandard RC buildings through forced vibration tests. *Bulletin of Earthquake Engineering*, 15(8), 3245-3263.
- Gola, M. M., Soma, A. and Botto, D.** (2001). On theoretical limits of dynamic model updating using a sensitivity-based approach, *Journal of Sound and Vibration*, 244(4), 583–595.
- Hou, Z., Noori, M. and Amand, R.S.** (2000). Waveletbased approach for structural damage detection. *Journal of Engineering Mechanics*, 126(7), 677–683.
- Hu, C.S. and Afzal, M.T.** (2006). A statistical algorithm for comparing mode shapes of vibration testing before and after damage in timbers. *Journal of Wood Science*, 52, 348–352.
- Huffman S., Bagchi A., Mufti A., Neale K., Sargent D., Rivera E.** (2006). GFRP seismic strengthening and structural health monitoring of Portage Creek Bridge concrete columns. *Arab J Sci Eng* 31(1C):25–42.
- Inci P., Goksu C., Demir U. and Ilki A.** (2017). Ambient Vibration Testing of a 3-storey Substandard RC Building at Different Levels of Structural Seismic Damage. *International Conference on Earthquake Engineering and Structural Dynamics*, 12-14 June 2017, Reykjavik, Iceland, 2017.
- Ivorra S, Pallares FJ** (2006). Dynamic investigations on a masonry bell tower. *Eng Struct* 28:660–667.
- Jang, J. H., Yeo, I., Shin, S. and Chang, S. P.** (2002). Experimental investigation of system-identificationbased damage assessment on structures, *Journal of Structural Engineering*, 128(5), 673–682.
- Kim, J.T. and Stubbs, N.** (1995). Model-uncertainty impact and damage-detection accuracy in plate girder. *Journal of Structural Engineering*, 121(10), 1409–1417.
- Law, S.S., Shi, Z.Y. and Zhang, L.M.** (1998). Structural damage detection from incomplete and noisy modal test data. *Journal of Engineering Mechanics-Asce*, 124, 1280–1288.
- Liew, K.M. and Wang, Q.** (1998). Application of wavelet theory for crack identification in structures. *Journal of Engineering Mechanics*, 124(2), 152–157.
- Li, G.Q., Hao, K.C., Lu, Y. and Chen, S.W.** (1999). A flexibility approach for damage identification of cantilever-type structures with bending and shear deformation. *Computers and Structures*, 73, 565–572.

- Lieven, N.A.J. and Ewins, D.J.** (1988). Spatial correlation of modespaces: the coordinate modal assurance criterion (COMAC). In: Proceedings of the 6th International Modal Analysis Conference, Kissimmee, Florida, USA, pp. 1063–1070.
- Lu, C. and Hsu, Y.** (2002). Vibration analysis of an inhomogeneous string for damage detection by wavelet transform. *International Journal of Mechanical Sciences*, 44, 745–754.
- Messina, A., Williams, E.J. and Contursi, T.** (1998). Structural damage detection by a sensitivity and statistical-based method. *Journal of Sound and Vibration*, 216(5), 791–808
- Michel C., Gueguen P., Bard P.Y.** (2010). Comparison between seismic vulnerability models and experimental dynamic properties of existing buildings in France. *Bull Earthq Eng* 8(6):1295–1307.
- Montgomery, D.C., Jennings, C.L., and Kulahcı, M.** (2007). Introduction to time series analysis and forecasting, Wiley-Interscience, Hoboken, New Jersey.
- Pakrashi V., B. Basu and O'Connor, A.** (2007). Structural damage detection and calibration using a wavelet–kurtosis technique *Engineering Structures* 29 (2007) 2097–2108.
- Picozzi, M., Milkereit, C., Zulfikar, C., Fleming, K., Ditommaso, R., Fischer, J., Safak, E., Ozel, O. and Apaydin, N.** (2010). Wireless technologies for the monitoring of strategic civil infrastructures: an ambient vibration test on the Fatih Sultan Mehmet suspension bridge in Istanbul, Turkey. *Bull Earthq Eng* 8(3):671–691.
- Rahmatalla, S., Eun, H. C. and Lee, E.T.** (2012). Damage detection from the variation of parameter matrices estimated by incomplete FRF data, *Smart Struct. Syst.*, 9(1), 55-70.
- Ren, W.X. and De Roeck, G.** (2002b). Structural damage identification using modal data. II: Test verification. *Journal of Structural Engineering*, 128(1), 96–104.
- Rytter, T.** (1993). Vibration based inspection of civil engineering structure. (PhD Thesis). Aalborg University, Denmark.
- Saadat, S., Noori, M. N., Buckner, G. D., Furukawa, T. and Suzuki, Y.** (2004). Structural health monitoring and damage detection using an intelligent parameter varying (IPV) technique, *Int J Non-Linear Mech*, 39(10):1678–97.
- Salawu, O.S. and Williams, C.** (1995). Bridge assessment using forced-vibration testing. *Journal of Structural Engineering*, 121(2), 161–173.
- Sanayei, M., Khaloo, A., Gul, M., and Catbas, F.N.** (2015). Automated finite element model updating of a scale bridge model using measured static and modal test data, *Engineering Structures* 102 (2015) 66–79
- Shi, Z.Y., Law, S.S. and Zhang, L.M.** (2000). Damage localization by directly using incomplete mode shapes. *Journal of Engineering Mechanics-ASCE*, 126, 656–660.

- Soyoz, S., Taciroglu, E., Orakcal, K., Nigbor, R., Skolnik, D., Lus, H. and Safak, E.** (2013). Ambient and forced vibration testing of a reinforced concrete building before and after its seismic retrofiting. *J Struct Eng* 139:1741–1752.
- TS 500** (2000). Requirements for design and construction of reinforced concrete structures. Turkish Standards Institute, Ankara
- Turkish Seismic Design Code (TSDC)** (2007). Regulations for buildings to be constructed in earthquake prone areas. Ankara, Turkey.
- Urban Transformation Law (UTL)** (2012). Official Gazette (6306). Ankara, Turkey
- Wahab, M.M.A. and De Roeck, G.** (1999). Damage detection in bridges using modal curvatures: applications to a real damage scenario. *Journal of Sound and Vibration*, 226(2), 217–235.
- Votsis, R.A., Kyriakides, N., Chrysostomou, C.Z., Tantele, E.A., Demetriou, T.** (2012). Ambient vibration testing of two masonry monuments in Cyprus. *Soil Dyn Earthq Eng* 43:58–68.
- Zhao, J. and DeWolf, J.T.** (1999). Sensitivity study for vibrational parameters used in damage detection. *Journal of Structural Engineering*, 125(4), 410–416.



## **APPENDICES**

### **APPENDIX A: Spectrogram views**



## APPENDIX A : Spectrogram views

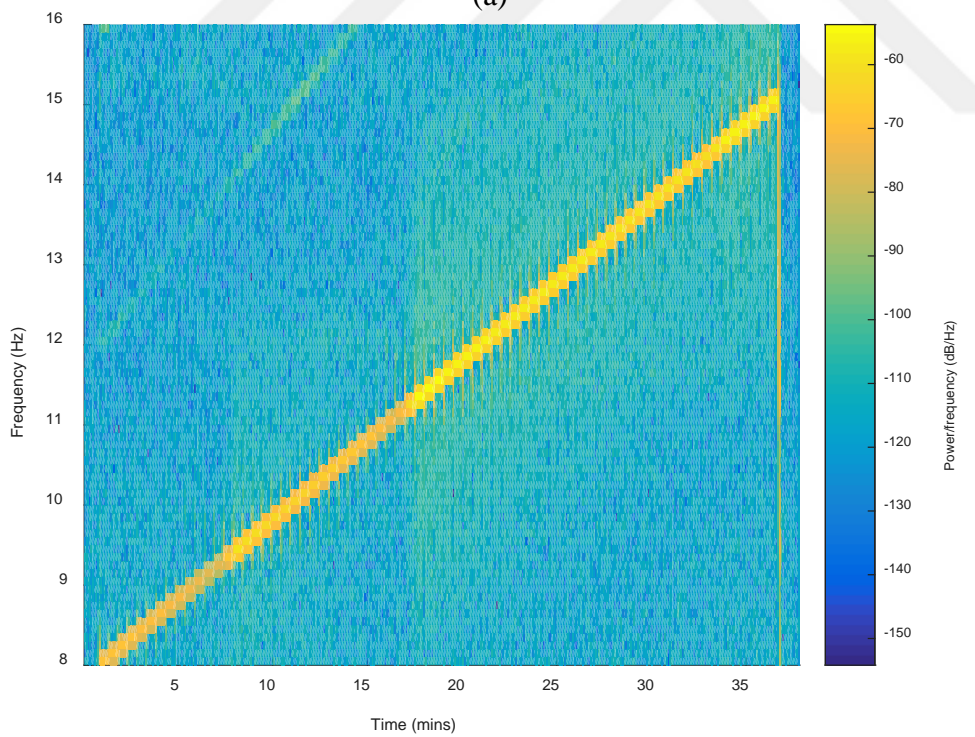
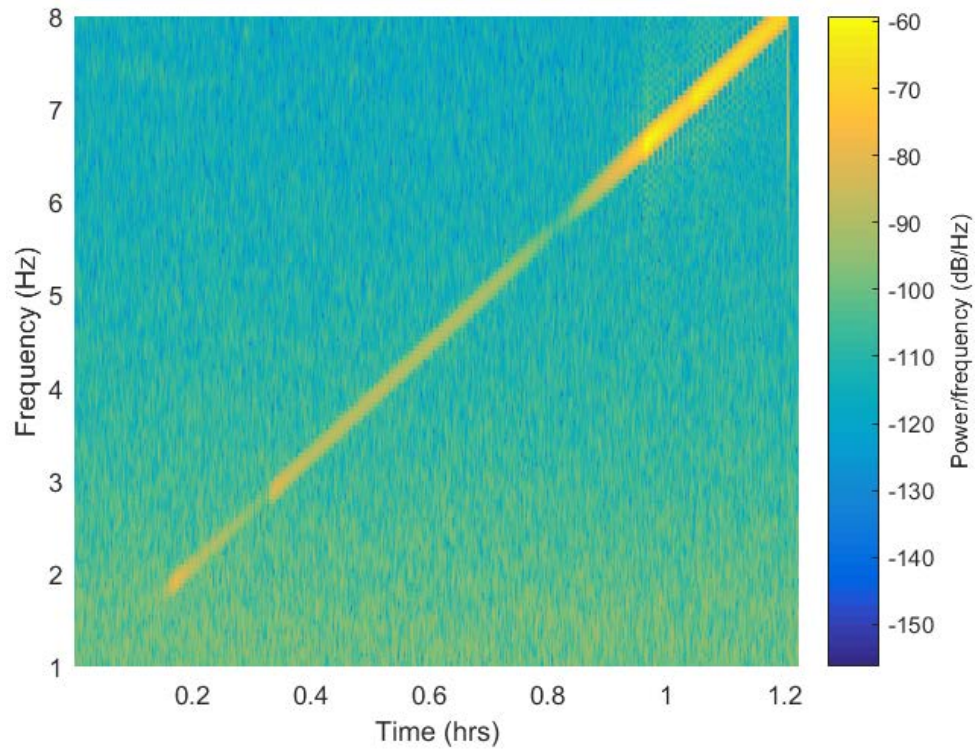
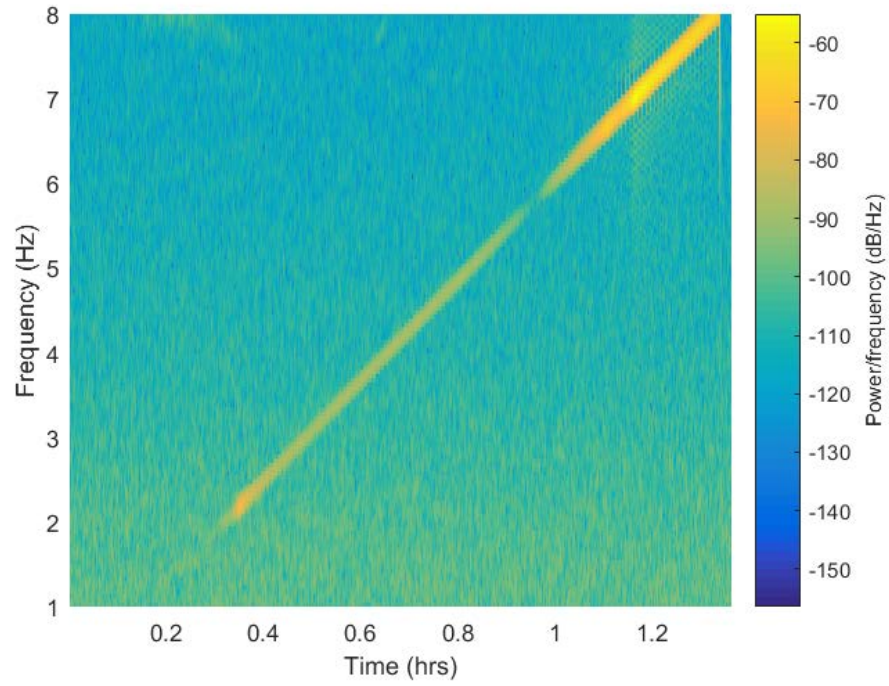
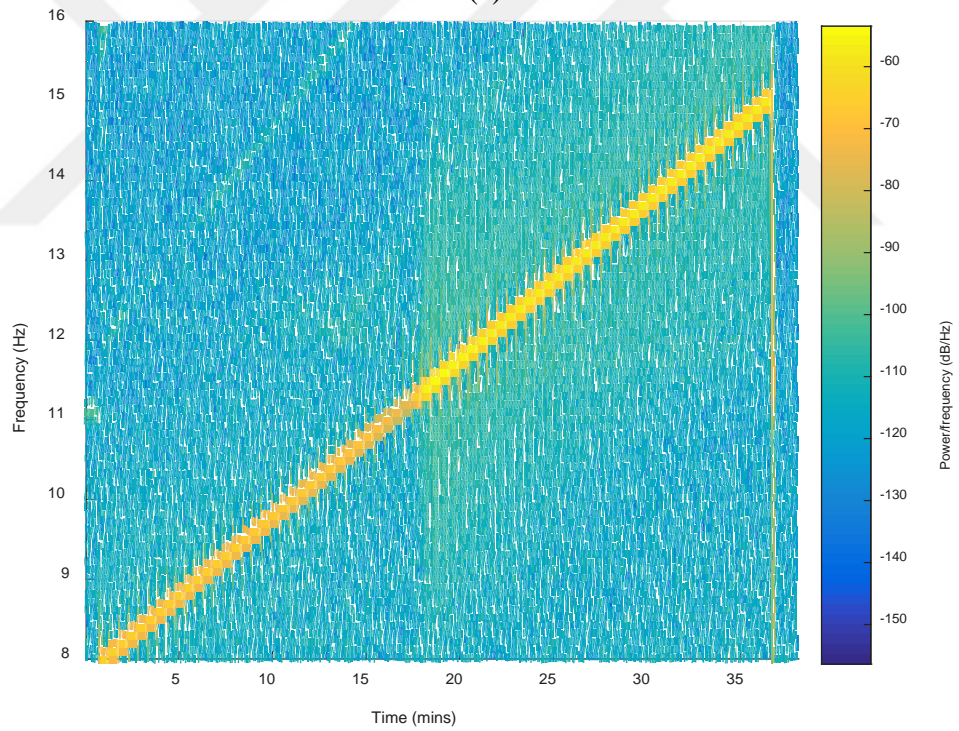


**Figure A.1 :** Spectrogram views for TB-1 Damaged case –  $x$  direction testing, (a) shaker frequency range as 1.5-8Hz, (b) shaker frequency range as 8-15 Hz.

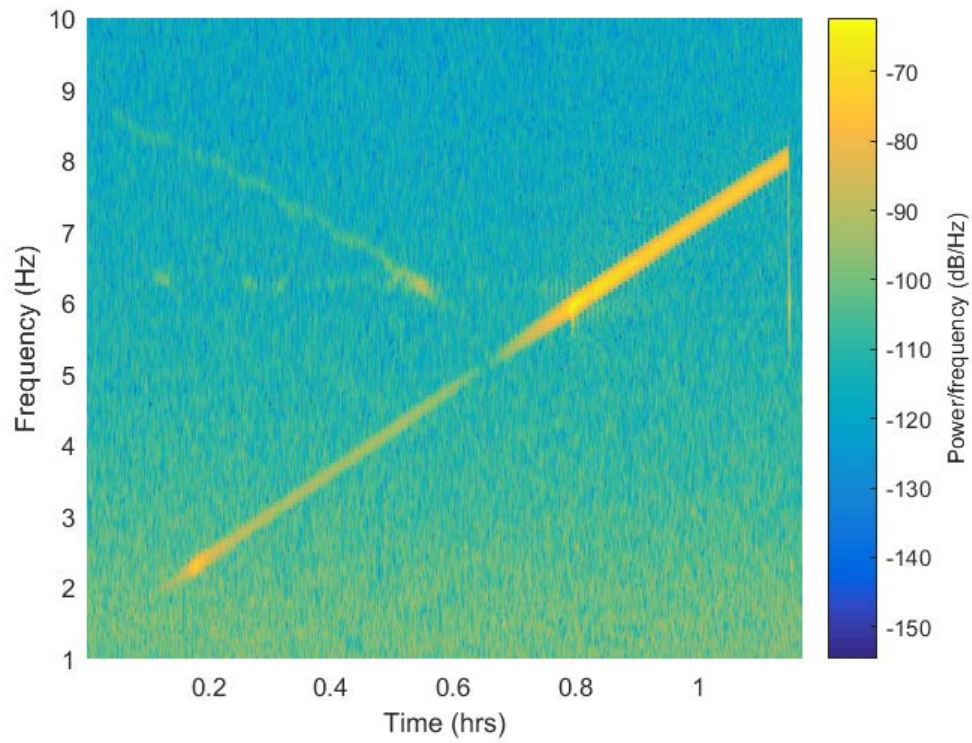


(a)

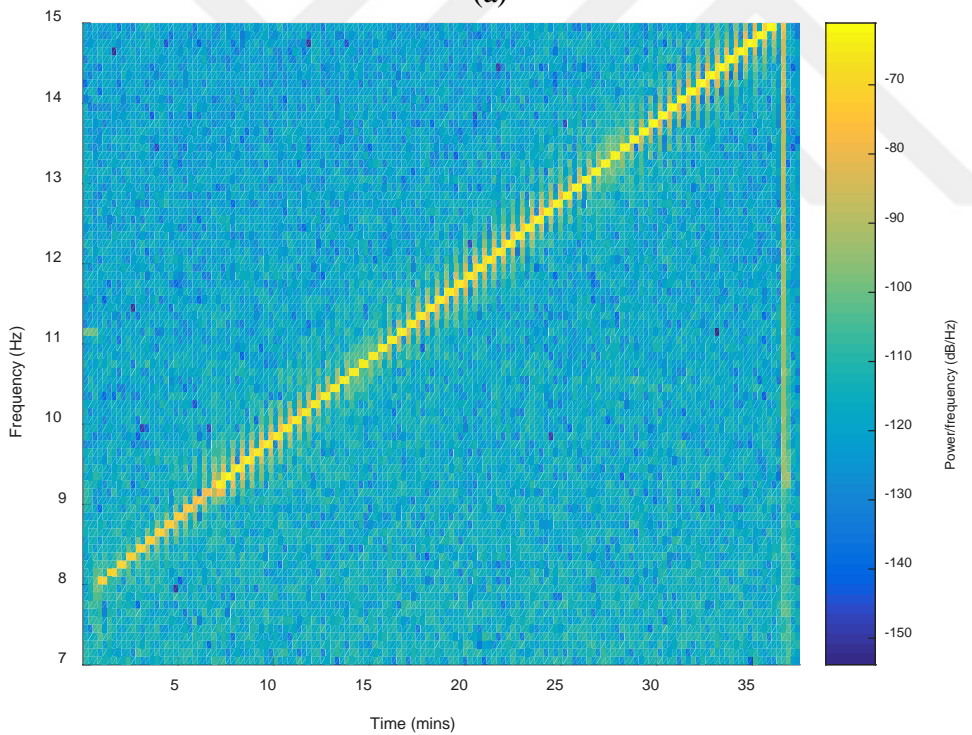


(b)

**Figure A.2** : Spectrogram views for TB-1 Damaged case – y direction testing, (a) shaker frequency range as 1.5-8Hz, (b) shaker frequency range as 8-15 Hz.



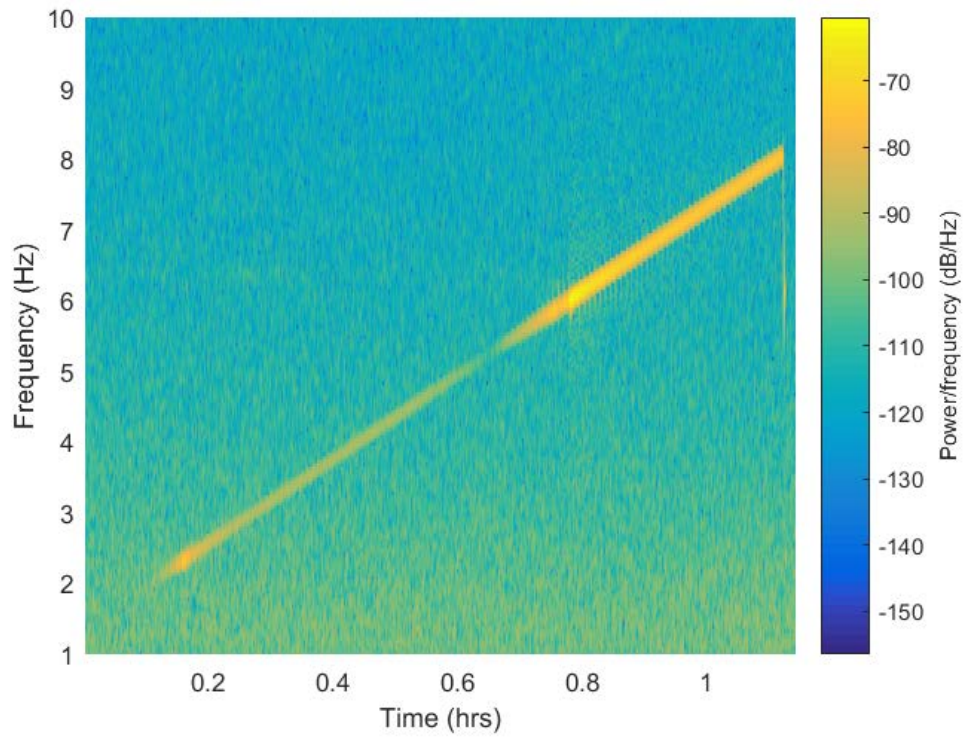
(a)



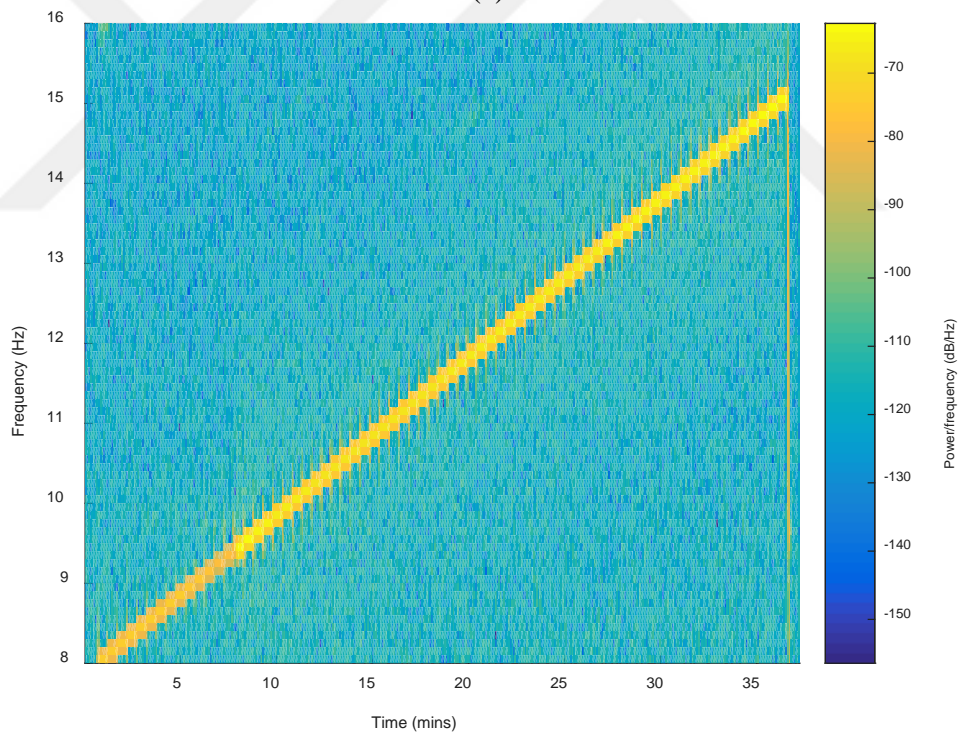
(b)

**Figure A.3** : Spectrogram views for TB-2 Undamaged case – x direction testing, (a) shaker frequency range as 1.5-8Hz, (b) shaker frequency range as 8-15 Hz.





(a)



(b)

**Figure A.4 :** Spectrogram views for TB-2 Undamaged case – y direction testing, (a) shaker frequency range as 1.5-8Hz, (b) shaker frequency range as 8-15 Hz.

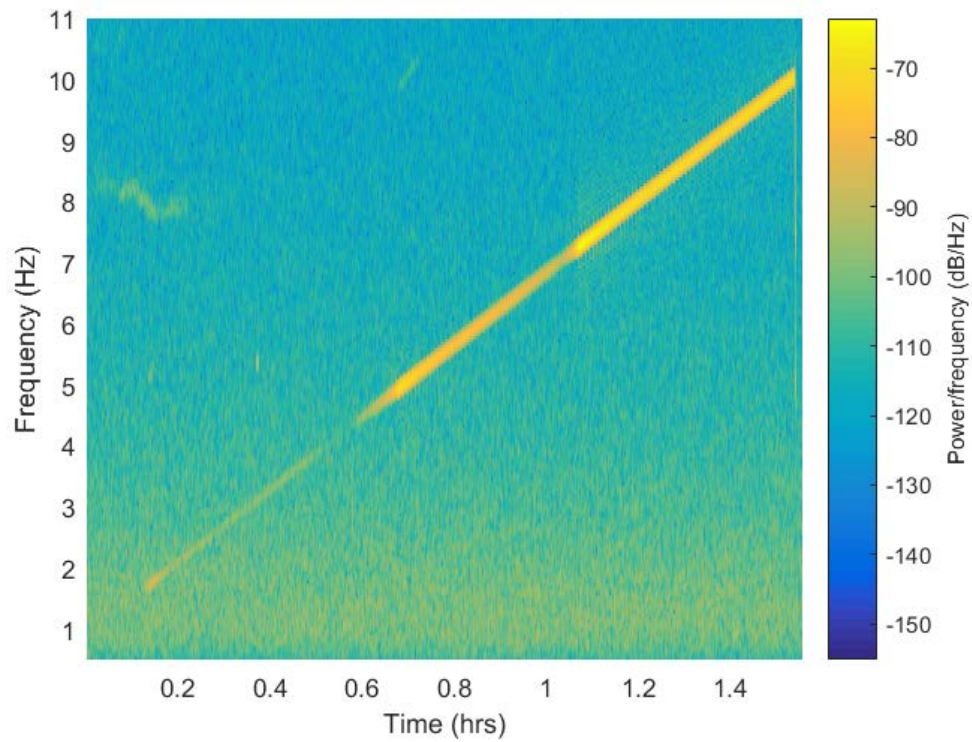
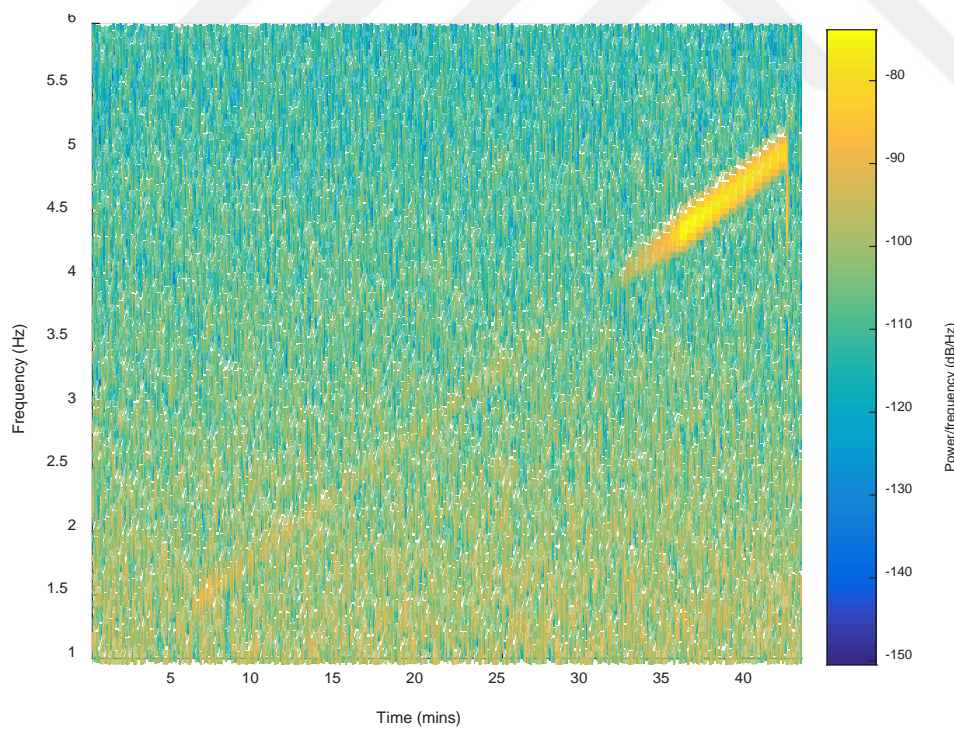
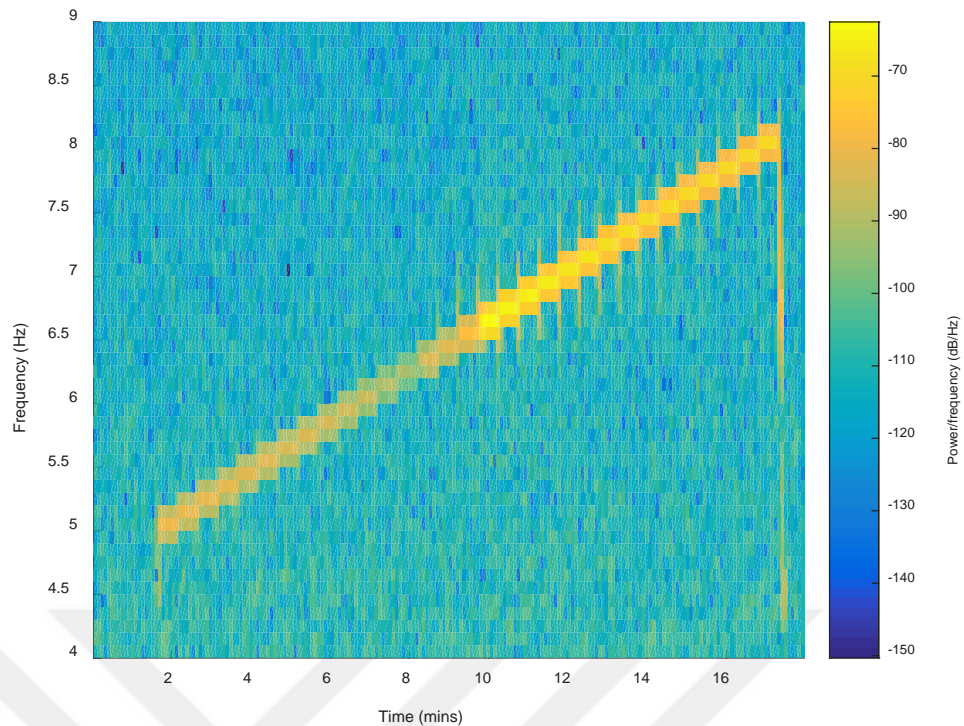


**Figure A.5 :** Spectrogram views for TB-2 Damaged case 1 –  $x$  direction testing (shaker frequency range as 1-10Hz).



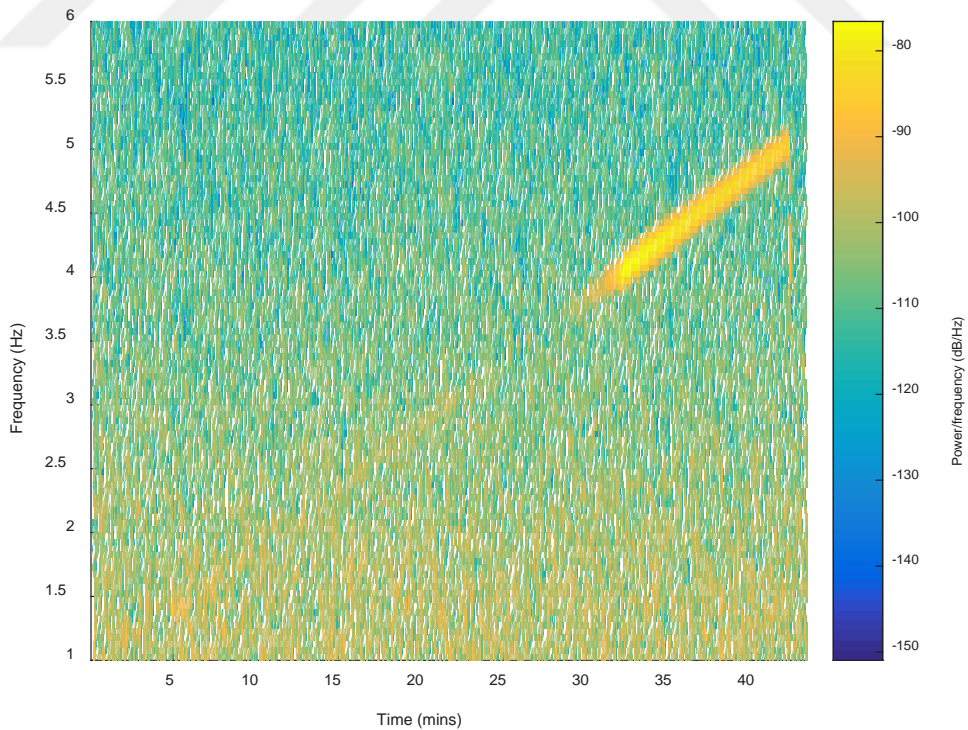
(a)

**Figure A.6 :** Spectrogram views for TB-2 Damaged case 2 –  $x$  direction testing, (a) shaker frequency range as 1-5Hz, (b) shaker frequency range as 5-8 Hz.



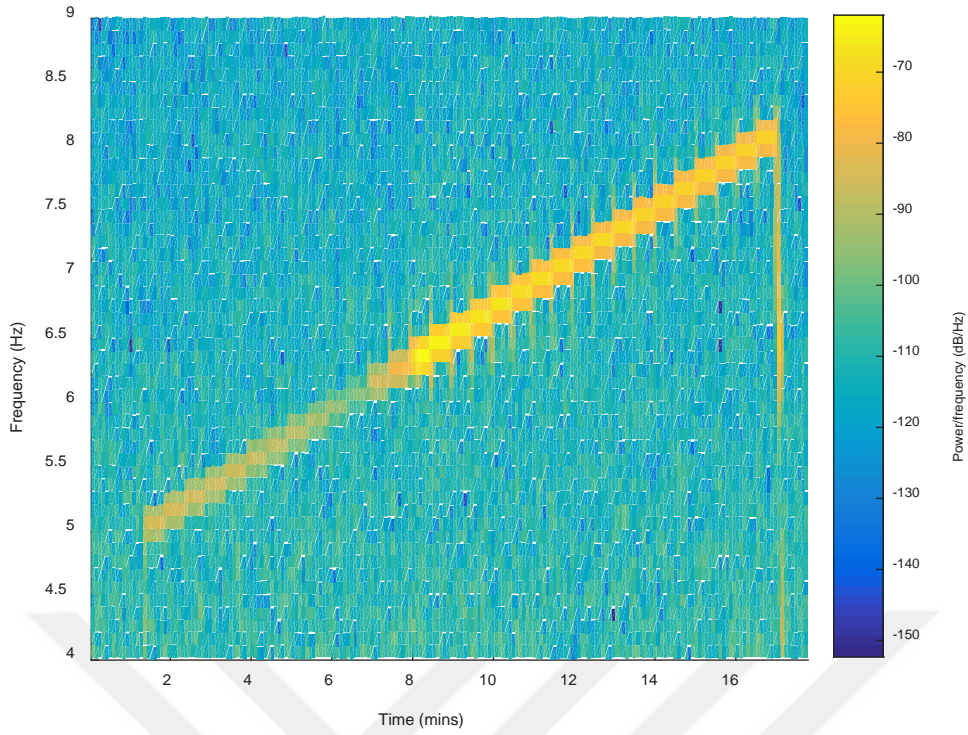
(b)

**Figure A.6 (continued)** : Spectrogram views for TB-2 Damaged case 2 –  $x$  direction testing, (a) shaker frequency range as 1-5Hz, (b) shaker frequency range as 5-8 Hz.



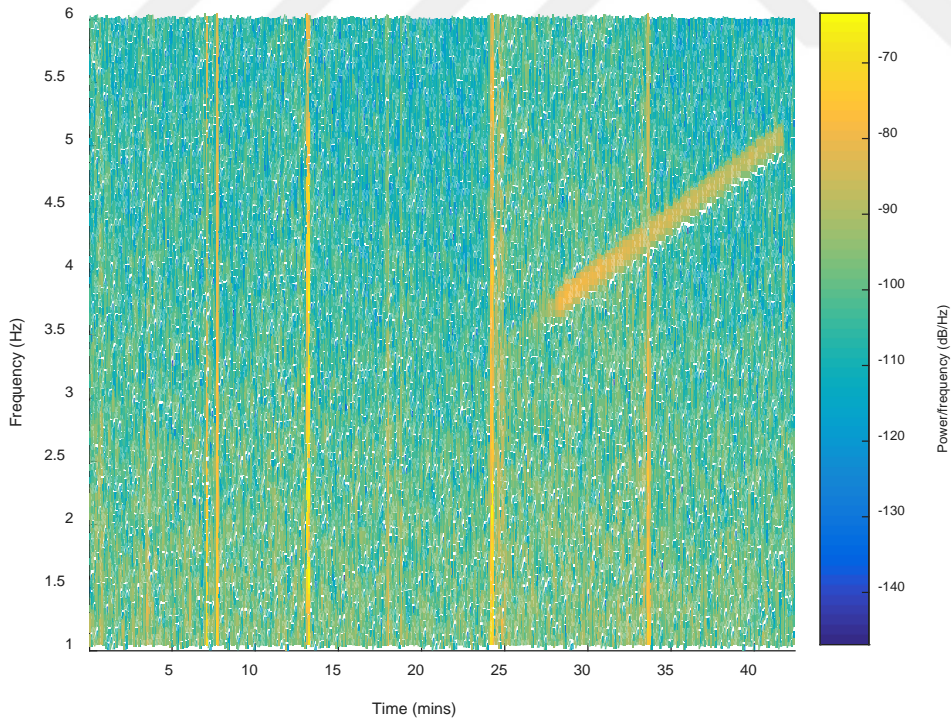
(a)

**Figure A.7** : Spectrogram views for TB-2 Damaged case 3 –  $x$  direction testing, (a) shaker frequency range as 1-5Hz, (b) shaker frequency range as 5-8 Hz.



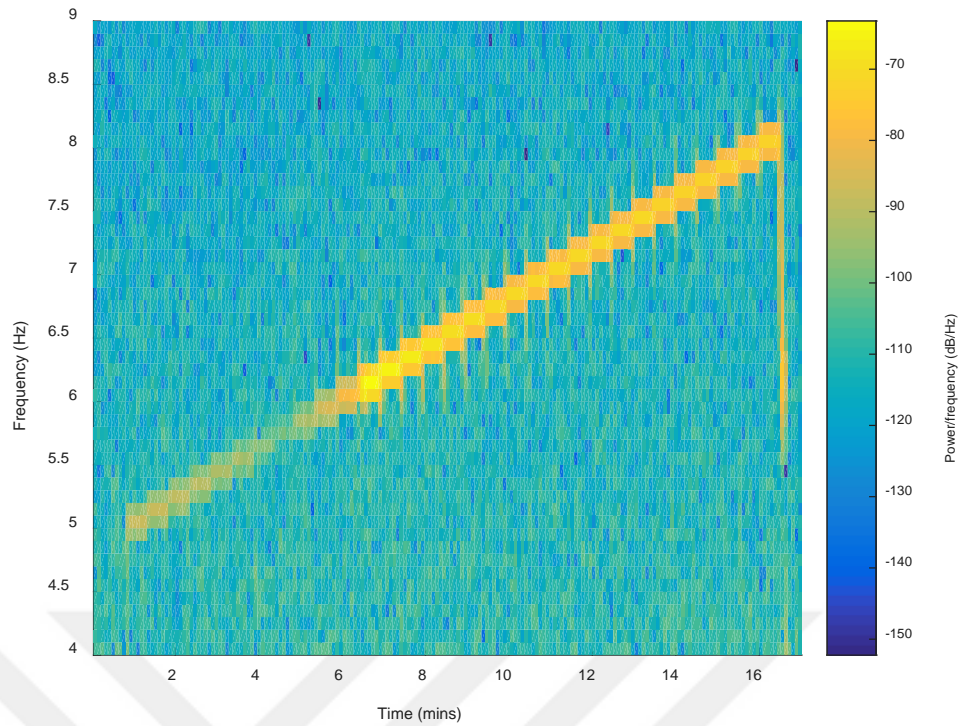
(b)

**Figure A.7 (continued)** : Spectrogram views for TB-2 Damaged case 3 –  $x$  direction testing, (a) shaker frequency range as 1-5Hz, (b) shaker frequency range as 5-8 Hz.



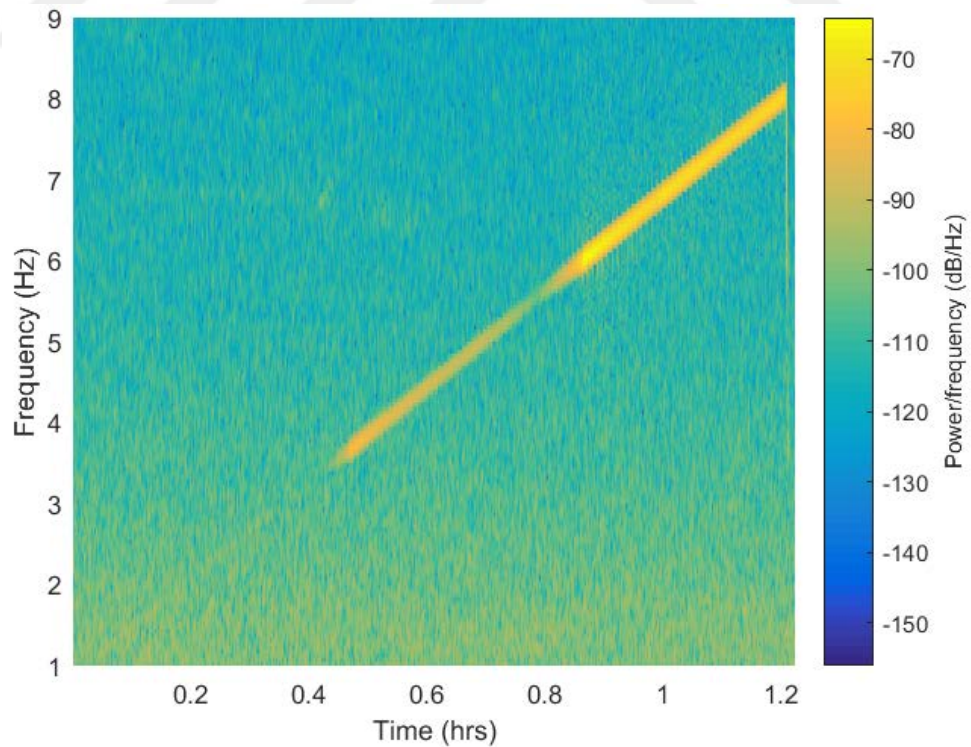
(a)

**Figure A.8** : Spectrogram views for TB-2 Damaged case 4 –  $x$  direction testing, (a) shaker frequency range as 1-5Hz, (b) shaker frequency range as 5-8 Hz.



(b)

**Figure A.8 (continued)** : Spectrogram views for TB-2 Damaged case 4 –  $x$  direction testing, (a) shaker frequency range as 1-5Hz, (b) shaker frequency range as 5-8 Hz.



(a)

**Figure A.9** : Spectrogram views for TB-2 Damaged case 5 –  $x$  direction testing, (a) shaker frequency range as 1.5-8 Hz, (b) shaker frequency range as 8-15 Hz.

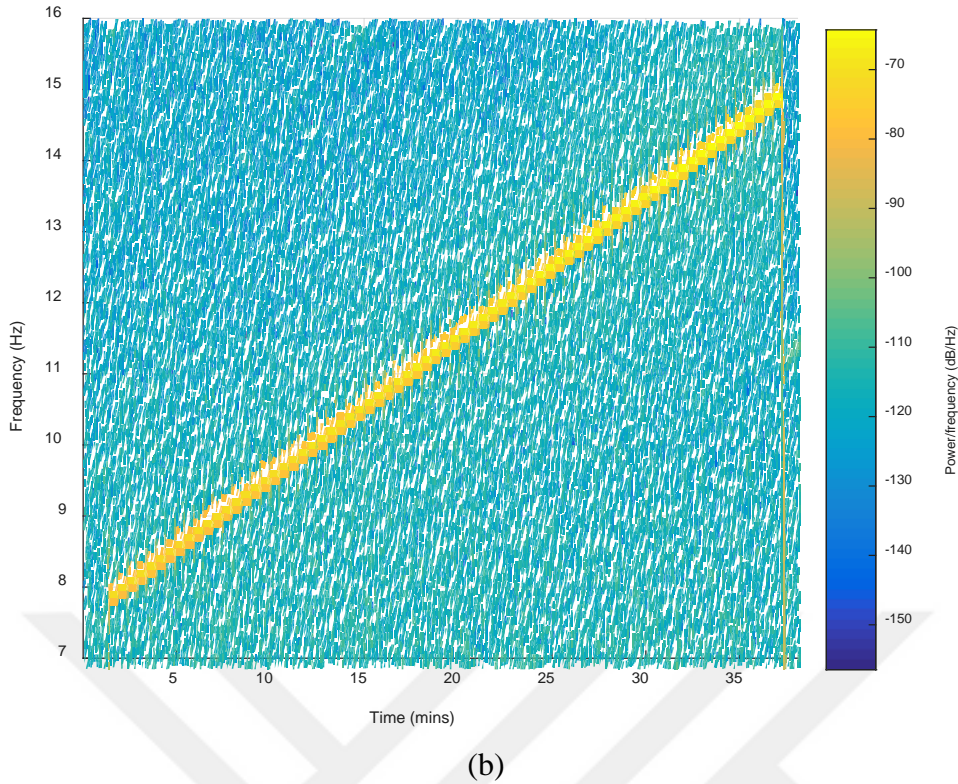


**Figure A.9 (continued)** : Spectrogram views for TB-2 Damaged case 5 –  $x$  direction testing, (a) shaker frequency range as 1.5-8 Hz, (b) shaker frequency range as 8-15 Hz.

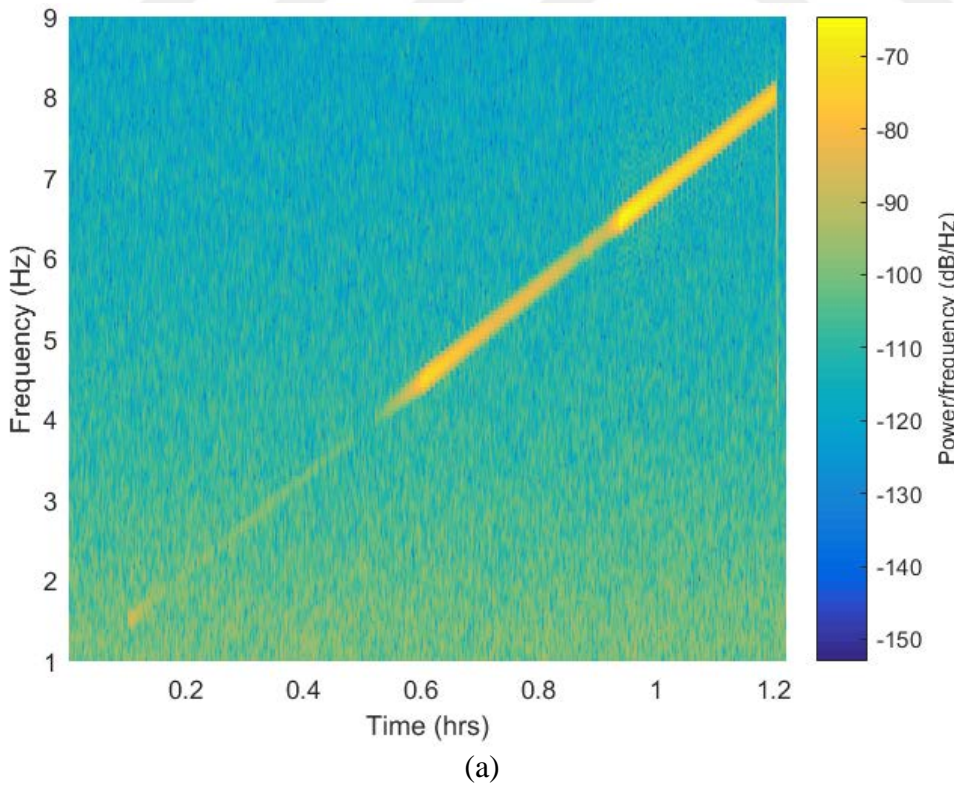
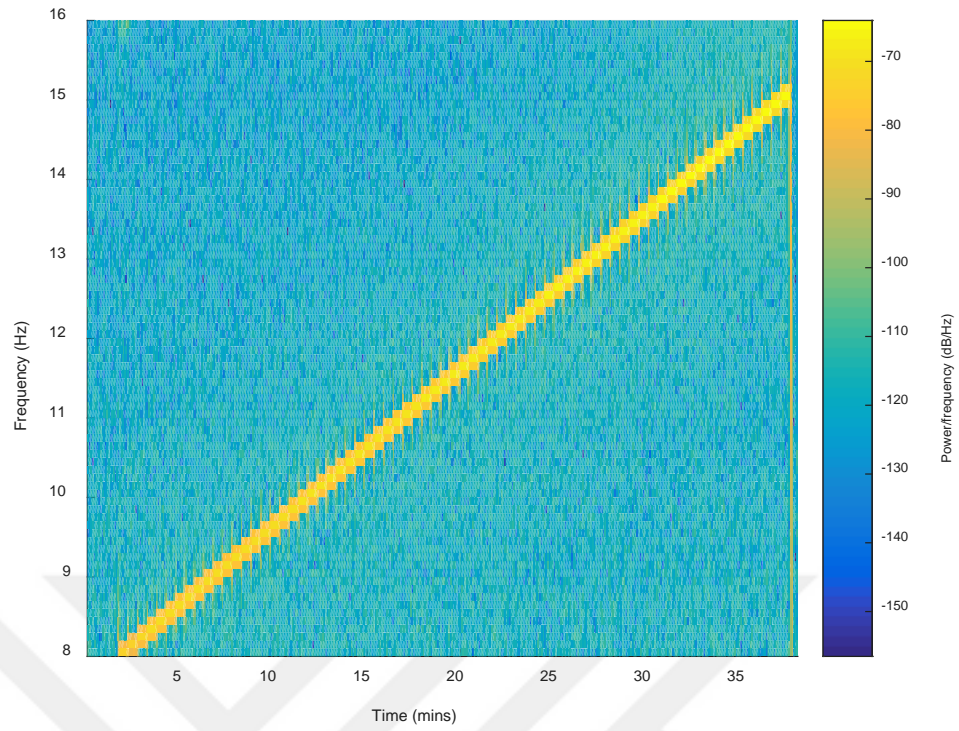


**Figure A.10** : Spectrogram views for TB-2 Damaged case 5 –  $y$  direction testing, (a) shaker frequency range as 1.5-8 Hz, (b) shaker frequency range as 8-15 Hz.



(b)

**Figure A.10 (continued)** : Spectrogram views for TB-2 Damaged case 5 – y direction testing, (a) shaker frequency range as 1.5-8 Hz, (b) shaker frequency range as 8-15 Hz.





## CURRICULUM VITAE



**Name Surname** : Pınar İNCİ KOÇAK  
**Place and Date of Birth** : Malatya/23.10.1985  
**E-Mail** : pinarinci@gmail.com

### EDUCATION :

- **B.Sc.** : 2009, Yildiz Technical University, Department of Civil Engineering
- **M.Sc.** : 2011, Istanbul Technical University, Structural Engineering  
2013, Building Research Institute, Japan, Earthquake Engineering
- **PhD** : 2017, Istanbul Technical University, Structural Engineering

### PUBLICATIONS, PRESENTATIONS AND PATENTS ON THE THESIS:

#### Journals

- Goksu C., **Inci P.**, Demir U., Yazgan U., Ilki A., "Field testing of substandard RC buildings through forced vibration tests. " Bull. Earth. Eng. DOI 10.1007/s10518-015-9799-x, 2015.
- Yuksel E., Karadogan H.K., Bal I.E., Ilki A., Bal A., **Inci P.**, "Seismic behavior of two exterior beam–column connections made of normal-strength concrete developed for precast construction." Engineering Structures 99, 157–172, 2015.
- Goksu C., **Inci P.**, and Ilki A., "The effect of corrosion on bond mechanism between extremely low strength concrete and plain reinforcing bars," ASCE J. Perf. Const. Facilities, DOI: 10.1061/(ASCE)CF.1943-5509.0000811, 2015.

- **Inci P.**, Goksu C., Ilki A., Kumbasar N., “Effects of Reinforcement Corrosion on the Performance of RC Frame Buildings Subjected to Seismic Actions,” ASCE J. Perf. Const. Facilities, 27(6), 683-696, 2013.

#### **International Conference Papers**

- Demir C., Comert M., **Inci P.**, Dusak S., Ilki A., “Seismic Assessment and Rehabilitation of Hirka-i Serif Mosque”. 3rd International Conference on Protection of Historical Constructions, 12-15 July 2017, Lisbon, Portugal, 2017.
- **Inci P.**, Goksu C., Demir U., Ilki A., “Ambient Vibration Testing of a 3-storey Substandard RC Building at Different Levels of Structural Seismic Damage”. International Conference on Earthquake Engineering and Structural Dynamics, 12-14 June 2017, Reykjavik, Iceland, 2017.
- **Inci P.**, Goksu C., Ando S., Ilki A., “Comparative evaluation of turkish and japanese policies on post-earthquake building damage inspection”. The 23rd SRA-E conference 16-18 June, Istanbul, 2014.
- Goksu, C., **Inci P.**, Ilki A., “The Bond-Slip Behavior of Extremely Low Strength RC Columns with Corroded Plain Reinforcing Bars”. First International Conference on Performance-Based and Life-Cycle Structural Engineering (PLSE 2012), Hong Kong, 2012.